LLNL-TR-663242

Topics in LIFE Target Survival: 11-SI-004 Final Report

R. Miles, B. Benett, T. Bond, A. Chang, D. Dawson, F. Fornasiero, J. Hamilton, M. Havstad, S. Kucheyev, M. LeBlanc, P. Rosso, G. Schebler, E. Van Cleve, M. Worsley

October 23, 2014

Disclaimer

This document was prepared as an account of work sponsored by an agency of the United States government. Neither the United States government nor Lawrence Livermore National Security, LLC, nor any of their employees makes any warranty, expressed or implied, or assumes any legal liability or responsibility for the accuracy, completeness, or usefulness of any information, apparatus, product, or process disclosed, or represents that its use would not infringe privately owned rights. Reference herein to any specific commercial product, process, or service by trade name, trademark, manufacturer, or otherwise does not necessarily constitute or imply its endorsement, recommendation, or favoring by the United States government or Lawrence Livermore National Security, LLC. The views and opinions of authors expressed herein do not necessarily state or reflect those of the United States government or Lawrence Livermore National Security, LLC, and shall not be used for advertising or product endorsement purposes.

This work performed under the auspices of the U.S. Department of Energy by Lawrence Livermore National Laboratory under Contract DE-AC52-07NA27344.

Topics in LIFE Target Survival: 11-SI-004 Final Report

Robin Miles, Bill Benett, Tiziana Bond, Allan Chang, David Dawson, Francesco Fornasiero, Julie Hamilton, Mark Havstad, Sergei Kucheyev, Mary LeBlanc, Paul Rosso, Greg Schebler, Eli Van Cleve, Marcus Worsley: LLNL

Introduction

The LIFE target design incorporates many considerations to generate the desired fusion gain including the physics design, the cost of manufacturing of the target, the injectability of the target, the aerodynamic flight characteristics of the target, the ability to track and engage the target and to maintain the structural and thermal integrity of the target. This document describes the effort that was made in support of issues of survivability of the target during injection which included issues mass-manufactural materials and processes which could be used in the target. The current LIFE target design is shown in Figure 1. The external shape of the lead hohlraum is designed to be manufactured and handled easily in the production line, compatible with the injection system and provide aerodynamic stability during flight into the chamber as needed. The internal characteristics of the target are largely governed by physics requirements and by thermal/structural integrity considerations which may require thicker membranes and heat mitigation modifications that are not ideal from the physics point of view.

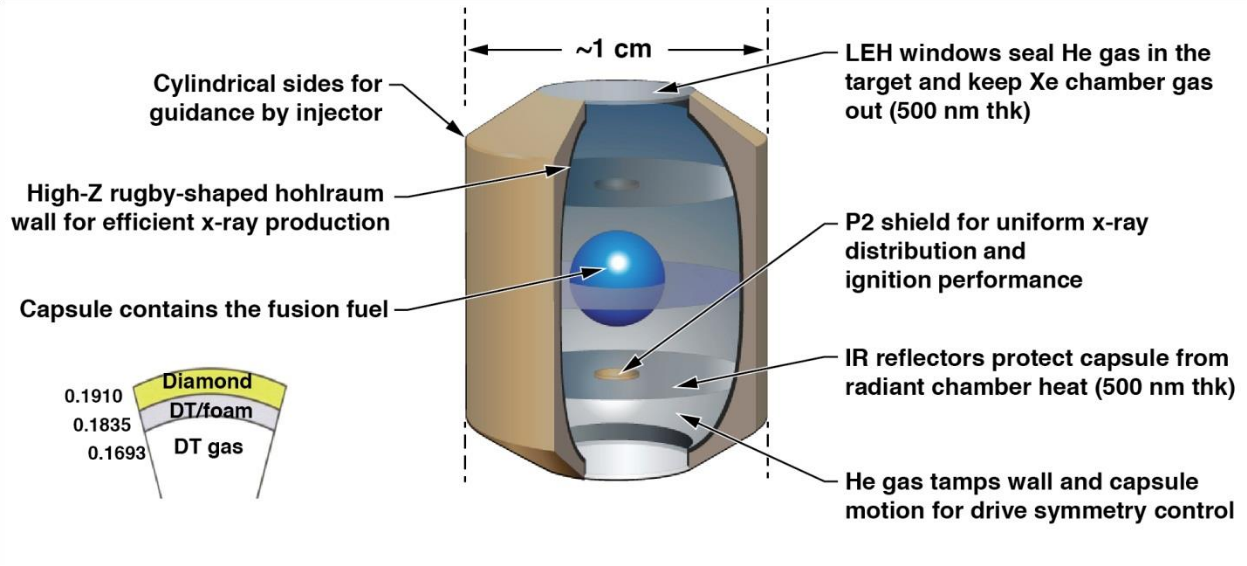
~1 cm
Cylindrical sides for guidance by injector
High-Z rugby-shaped hohlraum wall for efficient x-ray production
Capsule contains the fusion fuel
0.1910
0.1835
0.1693
Diamond
DT/foam
DT gas
LEH windows seal He gas in the target and keep Xe chamber gas out (500 nm thk)
P2 shield for uniform x-ray distribution and ignition performance
IR reflectors protect capsule from radiant chamber heat (500 nm thk)
He gas tamps wall and capsule motion for drive symmetry control

Figure 1. LIFE target design

Engineering design

The primary considerations for engineering design are centered around the robustness of the target, the ability to handle, inject and ensure that the target arrives at chamber center in a physical condition and in a spacial position and orientation such that it will implode as expected consistent with the physics design and laser interactions. The challenges for the target are structural, the ability to survive the forces imposed during manufacturing and injection acceleration, thermal, to ensure that the DT layer be at the design temperature following injection into the chamber center, and aerodynamic, the ability to place the target to be within the allowable spatial position and orientation for successful laser-target interaction near fusion chamber center.

While the following discussion focuses on the specific design aspects of the LIFE target, there has been a long history of studies in inertial fusion confinement target survival for both indirect and direct drive targets. Gooden *et. al.* [3] discussed the thermal and structural requirements during injection for an indirect IFE target and recommended a temperature limit of the DT based on the yield strength of the DT. As the DT approaches its triple point, the layer becomes softer and can distort under the acceleration forces of injection. Several studies [4-8] look at heating of direct drive targets where the temperature rise of the DT layer is expected to be significant as there is no hohlraum to protect the capsule from the hot chamber. Moll *et. al.* [9] placed membrane films internal to the target in order to reduce the convection of the helium gas within the target. Work done by Valmiansk *et. al.* [10] showed that the DT layer could survive a1000g acceleration using 5 um polymer shell and a 5 um capsule support membrane.

Structural design considerations

Structural forces will be applied to the target and target components at several times during the fabrication and injection operations. Forces will be imposed during component formation, assembly operations and handling of the target during transport through the manufacturing line. Although these forces have not yet been fully assessed, estimates have been made based on the geometric requirements of the injection structure and the frequency at which targets will be injected. The greatest accelerations will be applied to the target during loading and injection of the target into the fusion chamber. Accelerations during the loading phase are mainly applied transverse to the axis of the target, while the injection phase is dominated by axial acceleration. The components affected by these forces include the hohlraum, the capsule and the membranes. However, the hohlraum is negligibly affected by these forces, the CVD diamond ablator minimally affected, the DT layer potentially affected by forces transferred from the ablator if in solid form, and the membranes greatly affected. In particular, the capsule support membrane carries the load of the capsule. The capsule mass is dominated by the ablator and is about 17 mg for a DT layer of about 1 mg. The LEH window must bear the differential pressure forces across it even at high temperature. The IR shield must support the accelerated mass of the P2 shield.

Capsule support membrane

The allowable capsule support thickness at the center of the support membrane (where the highest stress is found) is 100 to 200 nm. Finding an appropriate material for this membrane has been a challenge. The specifications for the material were developed through modeling the effects of a 10,000 m/s^2 acceleration on a capsule. For preliminary investigations, the primary specifications are the tensile strength values for determining if the membrane will survive the acceleration forces and the elastic modulus for determining the deflection of the membrane. Ideally, the membrane might deflect elastically a nominal amount such as 50 um then return to near target center to be within the tolerance specification of about ±25 um from hohlraum center at the time of the laser shot. The specification for the initial membrane deflection is not concrete although a large deflection is intuitively undesirable. The end-state at fusion chamber center is most important for implosion performance. An example of the requirements for 100 nm thick capsule support membranes is shown in Figure 2. Membrane films are plotted corresponding to their elastic modulus and tensile strength. Materials with properties above the "strength" line are acceptable. The corresponding capsule deflection can be read from the "deflection" line for the given modulus. A list of the materials considered for the capsule support membrane is tabulated in Table 1. Many of the high strength materials look attractive because the high stiffness and strength imply capsules which remain centered and films which won't break during acceleration but they are brittle materials and experience showed that an even minimal handling led to breakage of the films. It was determined that the use of these brittle films would probably lead to very poor yields during manufacture. Thus, they were eliminated from consideration. The remaining polymers were good but not fantastic. The polyimides were particularly attractive due to their high strength (for a polymer), good flexibility and toughness. Carbon-composites are also attractive.

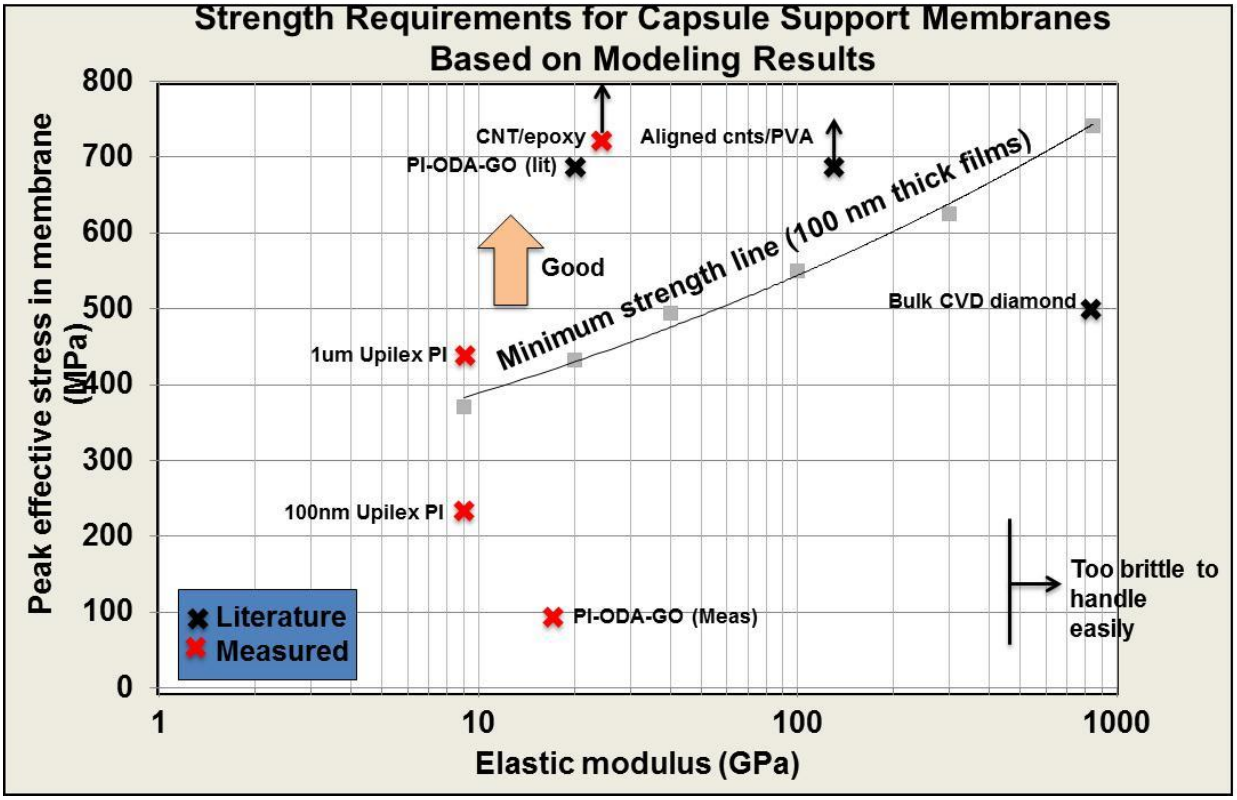

Figure 2. The graph shows desirable material properties for capsule support membranes for 100 nm uniform thickness membranes under a 800g acceleration load. For a given elastic modulus, the minimum material strength and the expected displacement under the acceleration load are plotted. The ideal material strength would be at least a factor of 2 above the "Minimum strength" line. It is preferred to keep the displacement under ~50 um but the displacement at chamber center must be within the specifications of ±25um.

Table 1. A list of the materials considered for the capsule support membrane. The high-strength materials are typically brittle and involve defects which make them very difficult to handle without breakage.

	Material	E (GPa)	Tensile strength (GPa)	Source
Requirement		>~10	>~0.5	
Polymers				
	Polyimide - Upilex	9	0.5	measured
	Reinforced PI-ODA-GO	20	0.844	per Wang (in testing)
	Vapor phase polyimide	3	0.094	per Letts
	CNT (float zone) -epoxy	40	1.25	per Ma
	CNT (Sansung)-epoxy		0.4	in testing
	CNT (float zone) -PVA	30	1	per Ma
	CNT/PVA aligned 60% fill	50	1.8	per Liu
	CNT/BMI aligned 60% fill	120	1.5	per Cheng
	Formvar	2	0.12	per Bhandarkar
	Parylene N	2.4	0.046	
	UHMWPE	120	0.02	
	SU8	2.6	0.052	
	nanoKevlar	8		per Yang
	GDP	2	0.08	per Nikroo
High-strength brittle mat'ls				
	CVD diamond	1000	0.5	per Diamond Mat'ls
	DLC	800	5	
	LPCVD silicon nitride	296	6.4	
	Graphene, single crystal	500	130	
	Graphene-multi cyrstal			
	Graphene-reduced paper	40	0.29	

Flexible polyimide and carbon-composites are favored

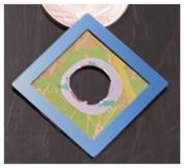

High strength materials too brittle to handle easily

Once the materials have been selected, the material properties are determined through uni-axial, burst tests and ball-indentation tests. The advantage to the uni-axial test is that the stress and strain are measured in one direction making the determination of the elastic modulus and the tensile strength relatively straightforward. The disadvantage is that cracks can initiate at the edges of the material and propagate into the center lowering the measured tensile strength relative to what might be measured without deleterious edge effects. Burst tests measure the deflection and failure of pressurized diaphragms. The stress directions are in both radial and axial directions. The material properties are determined from de-convoluted data which leave some amount of ambiguity if the pressure force is not applied ideally and/or the material is not of uniform thickness. However, edge effects are generally not a concern in these tests. This test is most relevant to LEH windows which operate under pressure loading. The last test is the ball indentation test. The ball is indented into the membrane. The force applied to the ball is measured as a function of displacement. Depending on the friction between the capsule and the membrane, the area of greatest stress is around the ring of contact area at the edge of where the ball touches the membrane. This test is good for measuring the elastic modulus but the values of tensile strength are not as legitimate due to the fact that stresses and strains on the film are not well-defined, in particular in the visco-elastic regime. Edge effects also do not apply and this test loads the membrane in a similar way to the loading of the capsule on the capsule support membrane.

The results of the testing of various membranes are shown in Table 2. Most of the materials exhibited tensile strength values less than the desired minimum strength of ~ 800 MPa for modulii in the range of most polymers or composites (<10 GPa). Polyimide is normally a good choice of material, however, as shown in Figure 3, the strength of polyimide falls with decreased thickness such that the strength of a 200 nm thick film is about half that of a 1 um thick film. Studies of films under cryogenic (80K) conditions (Figure 3) show an increased strength but again brittle failure.

The capsule deflections during the acceleration of the LIFE target could be minimized by using a variable thickness membrane as shown in Figure 4. The thickness of the outer region of the membrane, away from areas that the capsule contact region, is on the order of 1000 nm, a 5-10 fold increase in thickness over the central part of the membrane. The peak stresses and failure mode would not change between the variable thickness and the uniform thickness cases because the film thickness in the high stress part near the capsule ball are the same. The overall membrane stiffness for deflection resistance increases, however, resulting in reduced membrane displacements and the handle-ability of membranes during manufacture is improved.

Table 2. Tabulated results of material tests to date (must be updated)

Material			**Uni-directional;Leblanc**				**Uni-directional;Leblanc**				**2D burst;Lu**
			Room temperature				**Nitrogen temperature**				**Room tem**
	Black = measured directly; blue = measured indirectly; purple = approximate		Modulus (GPa)	Tensile strength (GPa)	Nominal strain rate (s-1)	Tensile strain at failure (%)	Modulus (GPa)	Tensile strength (GPa)	Nominal strain rate (s-1)	Tensile strain at failure (%)	Modulus (GPa)
Polyimide - Kapton	McMaster-Carr	25 um	0.032	0.281	0.01	79	0.051	0.465	0.01	46	
Polyimide - Upilex	Luxel	1 um	7.9	0.413	0.01	46	8.7	0.505	0.01	12.6	
	Luxel	100 nm	8.7	0.18	0.001	2.5					
Polyimide - variable thickness	Luxel:spin coat/vacuum form:center etch	1000/200 nm									
Polyimide - ODA - GO	LLNL:Worsley	1 um									
GO	LLNL:Hamilton										
GO-with vapor-phase polyimide	LLNL:Hamilton/Ellis	3.65 um total	2.7	0.048	0.001	3.5					
Silicon nitride - trampoline	LLNL:Hamilton	Broke every time									
Graphene - multi-crystal	Graphene Supermarket	10 nm									
Graphene - multi-crystal	Graphene Supermarket	100 nm									
Graphene - multi-crystal	LLNL:Francesco										
Graphene - w/ parylene - single la	Graphene Supermarket/LLNL:Olund:Hamilton: Witstock										
Graphene - w/ parylene - double	Graphene Supermarket/LLNL:Olund:Hamilton:Witstock										
CNT - epoxy	thickness varies widely	aprox 48um	4.7	0.103	0.001	4.5					
CNT - Sansung - plain											
CNT - Sansung - cross-linked	LLNL										
CNT-carbon foam	LLNL:Worsley										
nanocrystalline diamond	Diamond Materials	1 um									
		5 um	1110	1.59	0.0002	0.14					

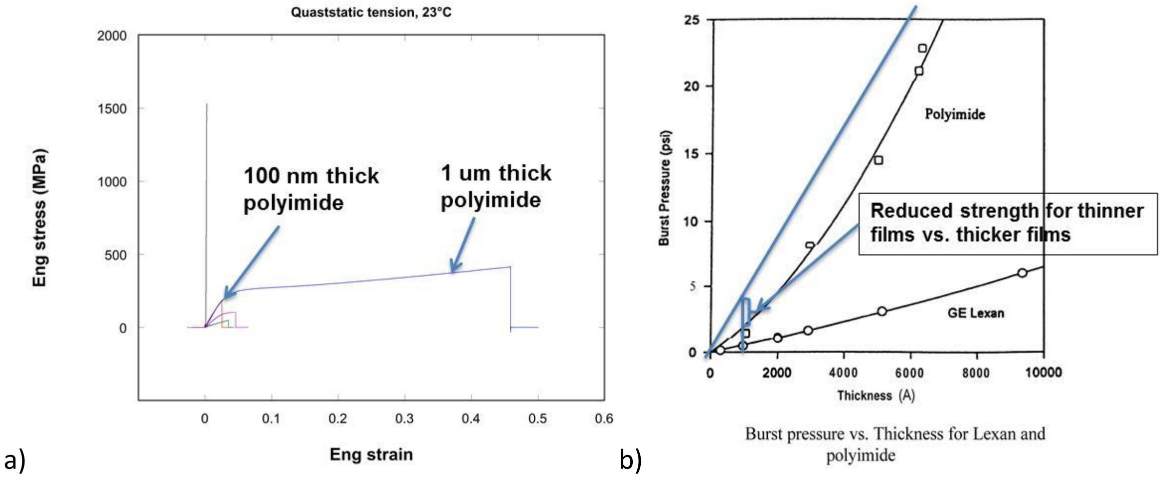

Figure 3. Tests of upilex polyimide film show a decrease in strength for films less than about 500 nm thick a) tensile test results b) burst pressure data from Luxel [10]

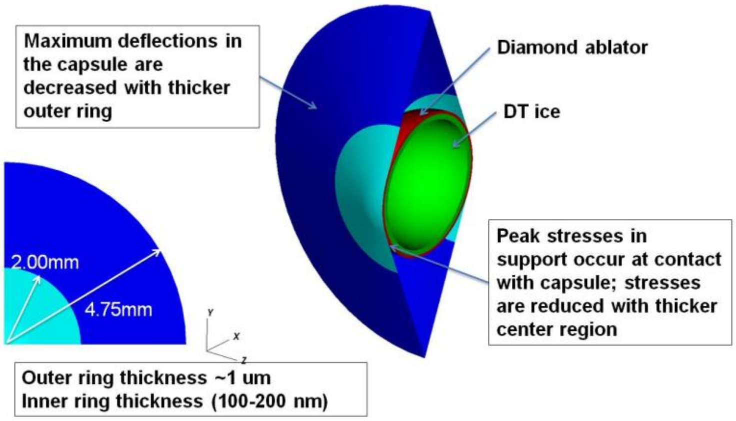
Maximum deflections in the capsule are decreased with thicker outer ring
Diamond ablator
DT ice
Peak stresses in support occur at contact with capsule; stresses are reduced with thicker center region
2.00mm
4.75mm
Y
X
Z
Outer ring thickness ~1 um
Inner ring thickness (100-200 nm)

Figure 4. Variable thickness capsule support membrane geometry for minimizing deflection and improving handleability

Because of the reduced strength with thickness and because of the large predicted deflection with polyimide films, carbon-based composites were also considered. After studying the literature, a couple of promising materials were found that merited testing. These were graphene–oxide and carbon nanotube/polymer composites. Simple mixing of graphene and nanotubes into polymer matrices enhance the strength and modulus of the composite by at most about 50% which is not very exciting. The work done by Wang *et. al.* [11] showed that if you functionalize graphene-oxide with ODA, one of the precursors of polyimide, then the graphene oxide becomes co-valently incorporated into the polyimide matrix increasing the strength by a factor of ~15 over the neat polyimide. However, studies of this material have proven disappointing thus far. PI-ODA-GO (polyimide with ODA functionalized graphene oxide) and neat PI resins were produced at LLNL per the Wang paper and shipped to Luxel for spin-casting into thin membranes and burst pressure testing. Unfortunately, as seen in Figure 5, the 1 um GO flakes agglomerated into larger ~50 um carbon clumps which acted as stress concentrators. The burst pressure data shows that the results for the neat and the GO polyimide are roughly similar. Future tests will be conducted with better dispersed GO flakes.

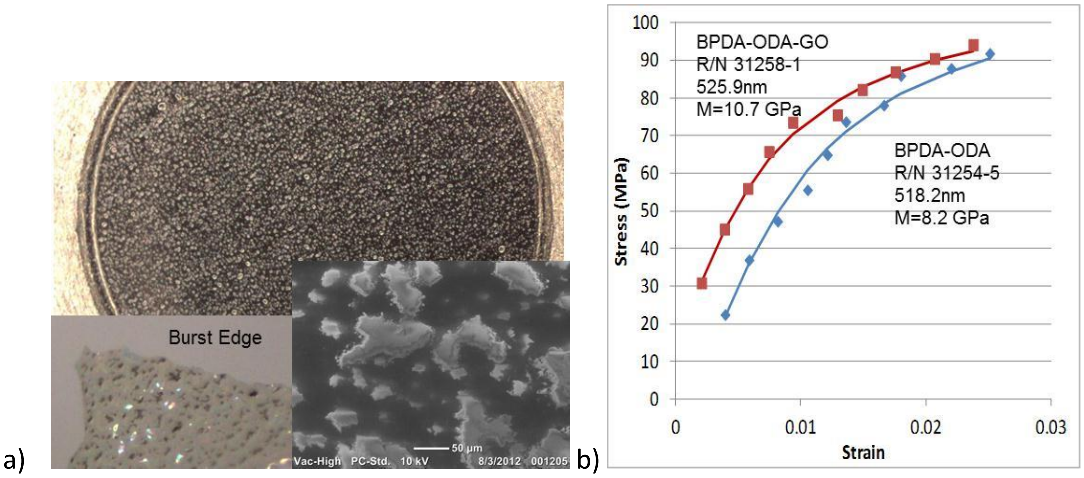

Figure 5. ~500 nm thick PI-ODA-GO films (resin per Wang) (a) and burst pressure data from Luxel (b)

Ma *et. al.* [12] wrote a paper which describes a carbon nanotube "sponge" which is deposited using a vapor-phase iron catalyst on the walls of the CVD reaction tube. The resulting carbon nanotubes are millimeter–long and interlocked with each other, thus forming a reticulated architecture which allows a more effective, continuous load-transfer within the CNT network and to the polymer when incorporated into a polymer matrix. Unfortunately, we don't have access to this type of CVD-reactor but we are able to work with researchers at Samsung who are depositing entangled-CNT sheets on filter paper with a nearly identical process. To produce high-strength films of a few hundred–nm thickness, we pursued several routes including: a) a solvent-assisted densification of the CNT sheets to promote stress transfer among the CNTs in the network (Figure 6); b) CNT film intercalation with epoxy which is expected to further enhance the mechanical properties by preventing CNT interfacial slippage during loading; c) ion-irradiation treatment to induce damage within the composite CNT-epoxy films followed by annealing to repair and create cross-links at the damaged sites ; d) combination of strategies a)-c). Improvement of the mechanical properties has been observed by irradiating the CNT/epoxy thin films with helium ions, as shown in Figures 7 and 8. The enhanced mechanical properties of the epoxy-CNT composite may derive from the effect of irradiation on the matrix, on the CNT, or on the CNT-epoxy interface (by covalent bonds/crosslinks formation). Additional work on the CNTs are shown in the Appendix.

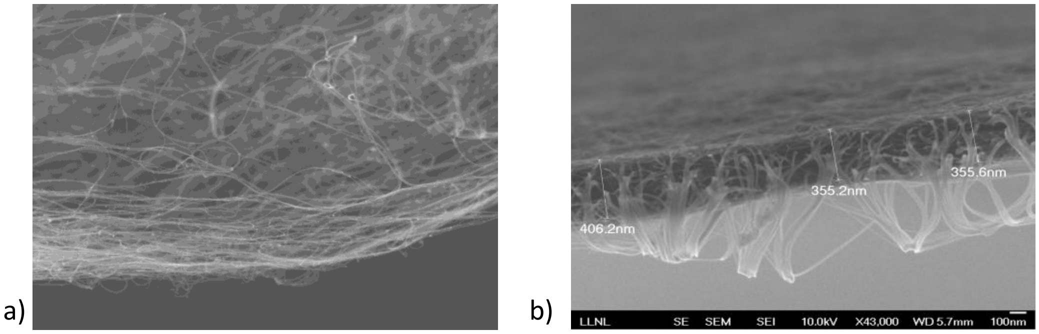
a)
b)
406.2nm
355.2nm
355.6nm
LLNL SE SEM SEI 10.0kV X43,000 WD 5.7mm 100nm

Figure 6. Modified Samsung CNTs-composite films a) CNT film as grown b) condensed, crosslinked and inflitrated with epoxy (EpoThin)

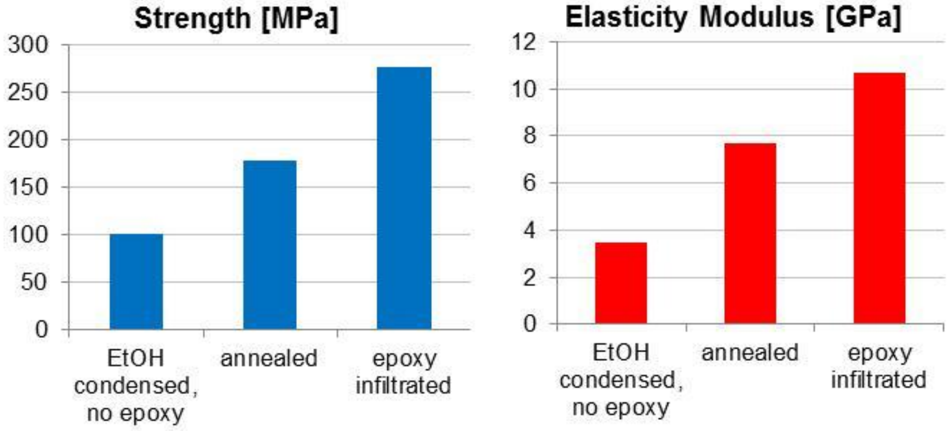

Figure 7. Increase in material properties of CNT-composite films following indicated processign steps

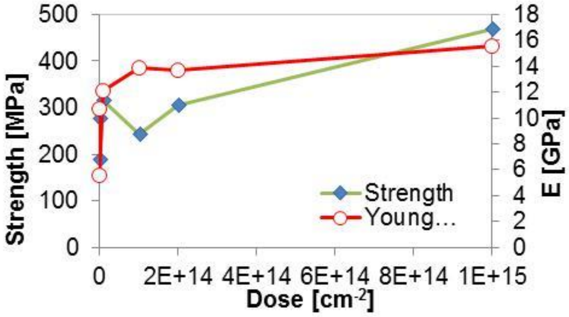

Figure 8. Improvements in material properties of CNT/epoxy composites with increasing ion-damage then annealing repair to increase cross-linking level.

Additional studies of CNT/epoxy composites have shown that increasing CNT fraction (to 60%) and increasing directionality of the CNTs in the composite film, for example, by mechanical stretching significantly improve stiffness and strength of the composites. [13, 14] *Modeling of capsule support deflections*

During periods in which the target is accelerating, the capsule support membrane experiences stresses due to the inertia of the capsule. The membranes are specifically designed to support the capsule during high axial accelerations found during injection, though moderate transverse accelerations are expected during the loading of the target into the injector. Only the elastic behavior of the various components was considered; to ensure the proper placement and shape of the capsule upon reaching chamber center, it is expected that stresses in the capsule support membrane should ideally remain well below the yield and/or failure stresses of the material. Axial accelerations up to 10,000 m/s^2 and transverse accelerations of around 100 m/s^2 were considered.

The primary metrics taken from the simulations were the peak effective stress in the capsule and the maximum deflection of the membrane relative to the hohlraum. These metrics for simulations using properties from a carbon/polymer composite are shown in Table 3. During the injection phase, the force applied to the capsule is almost entirely carried by the aft membrane, as can be seen in Figure 9, and the peak stress occurs near to the center of the aft membrane. For simulations in which the material properties are held constant, the peak stress and maximum deflection are most directly a function of the maximum axial acceleration. However, for acceleration profiles in which there are sharp changes in acceleration (high jerk), oscillations of the capsule can be induced which will increase both the peak stress and the maximum deflection (Figure 10). Tailoring of the acceleration profile to reduce these sharp transitions can effectively reduce or eliminate these oscillations.

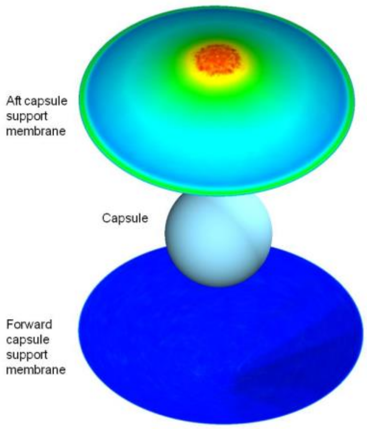
Aft capsule support membrane
Capsule
Forward capsule support membrane

Figure 9. During acceleration the aft capsule support membrane carries the load from the capsule.

Table 3. Modeling results for carbon/CNT composite capsule support membranes

Material	Elastic modulus (GPa)	Tensile strength (MPa)	Outer ring thickness (nm)	Center thickness (nm)	Peak displacement (micron)	Peak effective stress in support (MPa)
PI-ODA-GO 3%	10	790 (thick film)	1000	200	71.81	183
	20		1000	200	39.45	201
			1000	100	66.79	365
			100	100	105.31	358
			200	200	56.94	201
CNT	40	?	100	100	56.72	401
			200	200	30.29	217

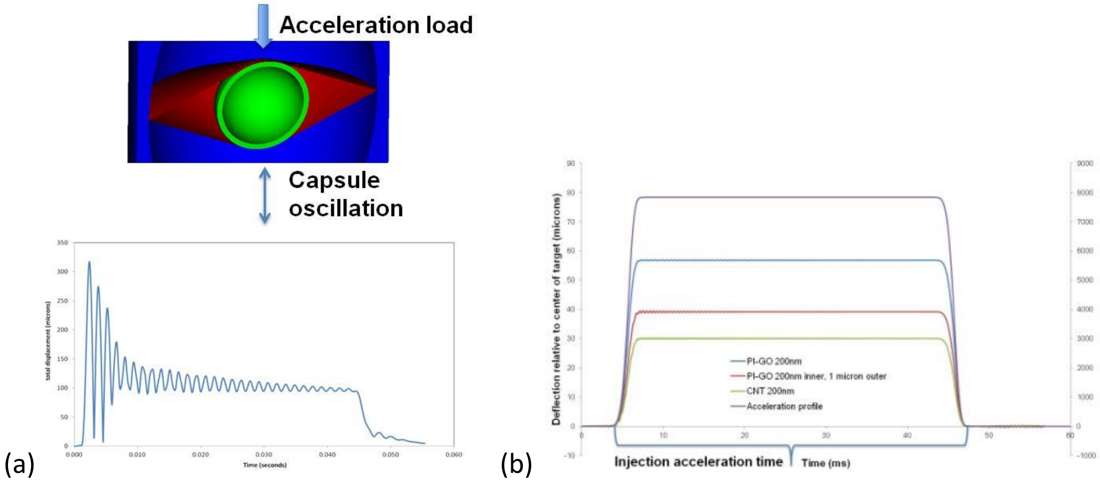

Figure 10. Jerk (changes of acceleration rate with time) can cause oscillations which can be damped by friction between the capsule and the capsule support membrane(a). Acceleration profiles can be designed to induce minimal oscillations on the target (b).

Since the accelerations that the target will be subjected to will likely be more complicated than strictly the axial accelerations the support membranes were designed to address, it is important to investigate the effect of transverse accelerations as well. Transverse accelerations that are orders of magnitude less than the anticipated axial accelerations can induce significant stresses in the support membranes due to the lack of capsule support in the tensile direction. Also, these transverse accelerations can result in unacceptable transverse deflections and oscillations of the capsule relative to the hohlraum (Figure 10). In the case in which no prestress is applied to the membranes, the capsule is initially unrestricted in its transverse motion; only once the membrane has deformed significantly is the capsule's transverse motion impeded.

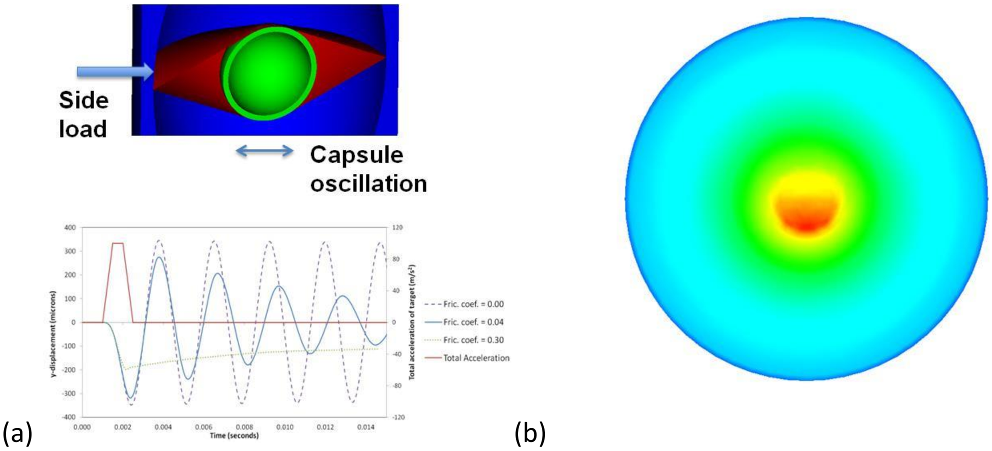

Figure 10. *A side load of ~80 m/s^2 from loading can cause 300 um oscillations of the capsule if there is no friction but damps down if there is some friction (a). Stresses in the membrane can be high due to side loads. Stresses of ~240 MPa are seen with even 10 g accelerations. (b)*

To reduce these deflections, studies were conducted in which prestress was applied to the capsules by including an initial gap between the forward and aft membranes that was closed at the beginning of the simulations. Figure X shows the peak measured deflection as a function of prestress. The 40 MPa prestress configuration was subjected to the full axial acceleration profile prior to the initial transverse acceleration, showing that the addition of the prestress does not appreciably impact the peak effective stress in the membrane or the maximum deflection during the injection. In fact, results from the simulations suggest that the total axial deflection of the capsule will be reduced by the addition of prestress, as can be seen in Figures 11 an 12. Figure 13 shows that the maximum effective stress in the support remains about the same after the addition of the prestress, though the magnitude of the oscillations of the effective stress do appear to decrease somewhat.

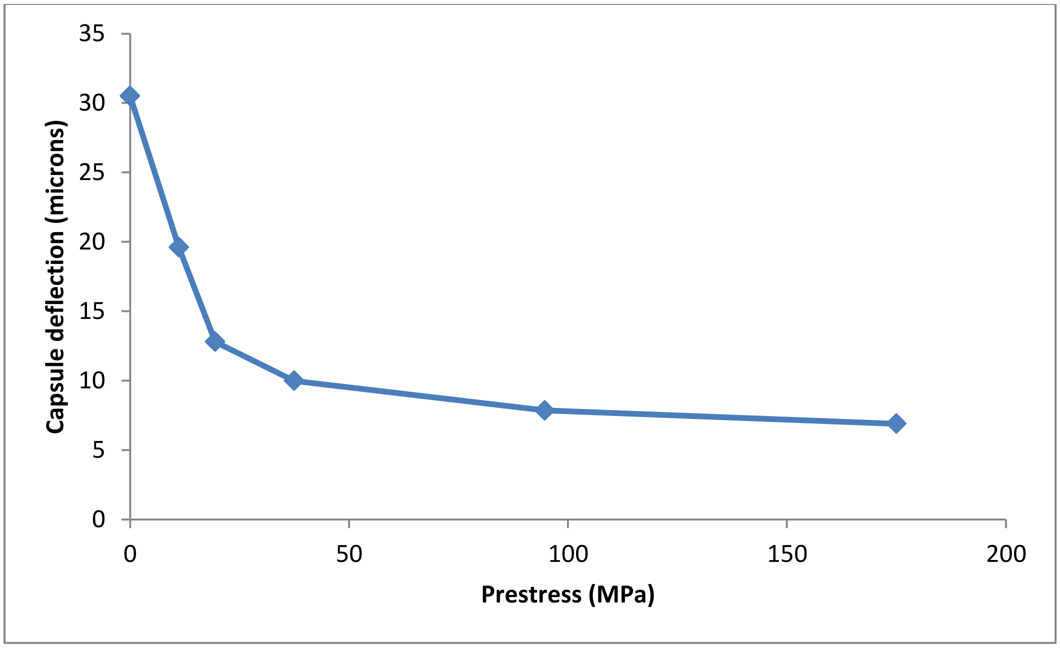

Figure 11. Transverse capsule deflections for varying levels of prestress when the target is subjected to a 100 m/s^2 acceleration pulse.

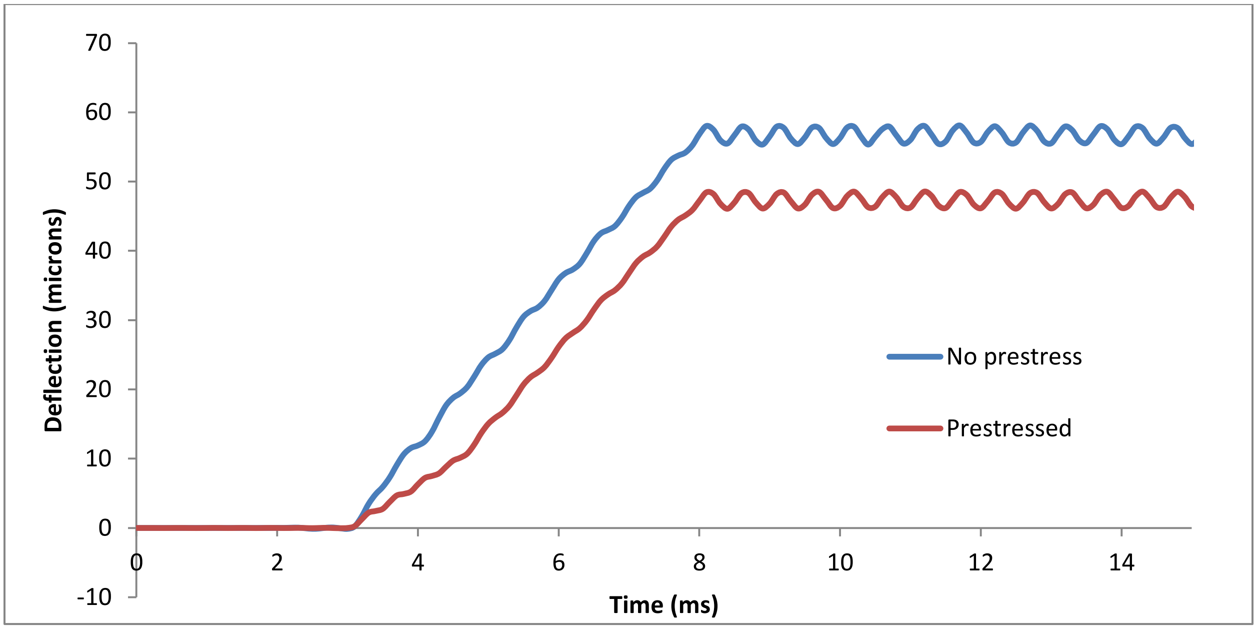

Figure 12. Axial displacement of the capsule for no prestress and 40 MPa prestress.

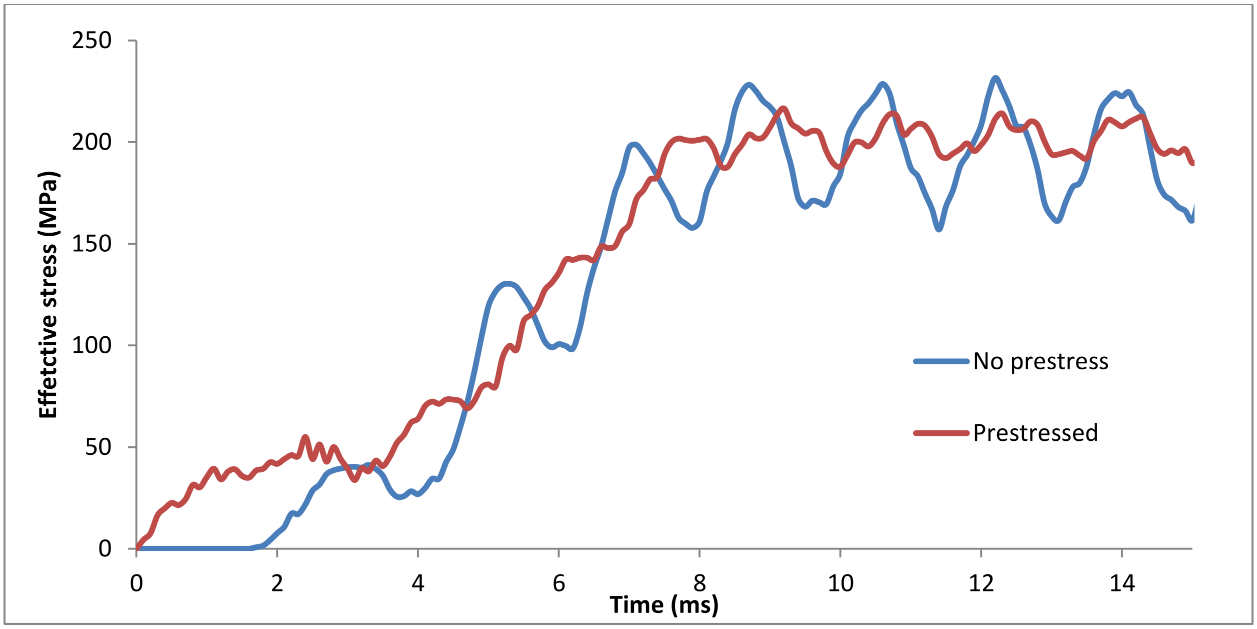

Figure 13. Peak effective stress in capsule support for no prestress and 40 MPa prestress.

LEH windows

The LEH windows must be able to withstand the differential pressure across them resulting from the helium inside the target the density of which is ~1 mg/cc at ~18K. This corresponds to a pressure of about 1/3rd atm. The outer pressure changes depending on the phase of manufacturing and injection. A gas gun injector may require a 3 atm gas pressure for target acceleration. Table 4 shows the maximum pressure differential which can be sustained across the LEH window as calculated using a Timoshenko equation [15]. For the candidate materials shown, the results indicate that polyimide is a good material for this component. Higher differential pressures and/or additional safety margin can be accommodated with a thicker window if allowable by the target physics. Thermal considerations for the LEH window are important as this component heats up quickly in the hot xenon chamber atmosphere. The helium behind the window also heats up which increases its temperature and pressure as it helps to limit the peak LEH window temperature. The increased helium pressure could potentially rupture the LEH window or the IR shield. The increase in pressure can be relieved by allowing helium flow around the periphery of the IR shield into the inner helium compartment. The hohlraum heat sinks this gas to minimize heating of the capsule by the heated helium.

Table 4. Materials considered for the LEH window

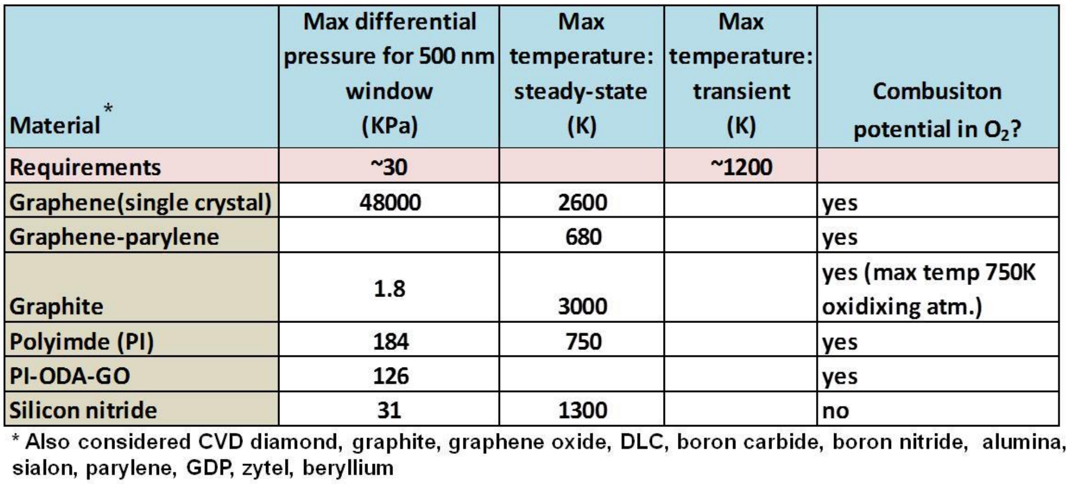

Material*	Max differential pressure for 500 nm window (KPa)	Max temperature: steady-state (K)	Max temperature: transient (K)	Combusiton potential in O_2?
Requirements	~30		~1200	
Graphene(single crystal)	48000	2600		yes
Graphene-parylene		680		yes
Graphite	1.8	3000		yes (max temp 750K oxidixing atm.)
Polyimde (PI)	184	750		yes
PI-ODA-GO	126			yes
Silicon nitride	31	1300		no

* Also considered CVD diamond, graphite, graphene oxide, DLC, boron carbide, boron nitride, alumina, sialon, parylene, GDP, zytel, beryllium

Care must also be taken during the manufacturing process to ensure that the differential pressure across the LEH window is within acceptable limits. The helium is sealed in the target at room temperature to permit a high-quality glue seal. At this temperature, the pressure for the desired 1 mg/cc helium is about 5 atm. A high pressure helium environment may be used to minimize the pressure differential across the window post sealing. The ambient pressure can be reduced as the capsule temperature is reduced. Another method for helium fill could be diffusion-fill through the thin LEH windows even at lower temperatures. The advantage of this type of fill is that the final assembly operations need not be done under high pressure helium but rather under ambient pressure conditions, thus reducing the design demands for vacuum/pressure operation on the manufacturing equipment. The fill-time could be reduced by heating the LEH window to increase its permeability, preferably without heating the entire target. A minimized fill-time is needed to keep the plant tritium inventory low.

IR shield

The IR shield must support the lead P2 shield during acceleration (Figure 14). A simple calculation of the ~10,000 m/s^2 acceleration of a 4 g; 2.8 mm diameter lead P2 shield applies the force through the 500 nm thick IR shield at the periphery of the P2 shield. The stress is about 25 MPa through the thickness, well below the ~300 MPa strength of polyimide.

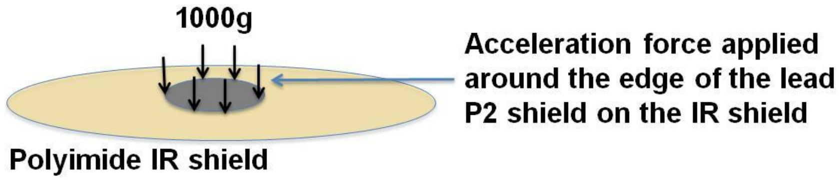
1000g
Acceleration force applied around the edge of the lead P2 shield on the IR shield
Polyimide IR shield

Figure 14. Acceleration of the P2 shield against the thin 500 nm thick IR shield.

Thermal Design

Thermal issues represent a major concern for target engineering. The DT layer must remain in the cyrogenic state during injection into the target chamber. In particular, the vapor pressure of the DT in the center of the capsule must not change significantly otherwise the fusion reaction may be inhibited as the vapor phase DT creates a resistance to the compression of the DT layer. The thermal specification is currently a maximum temperature rise of the inner surface of the DT layer of 100 mK although more work needs to be done to justify this particular number. The primary thermal protection mechanisms are to shield the DT from the thermal environment using the hohlraum and other target features and to minimize the exposure time to the hostile chamber environment. The total flight time of the target is less than 100 ms.

The target will be cooled down to about 18K on its way to the injector. At some point during the operation to load the targets into the injector, the targets will no longer be cooled and instead will begin to warm up. The targets will be heated during the acceleration phase of injection and during flight to and through the chamber on the way to fusion chamber center. The thermal environment that the target will experience will be different for each of the three phases of injection; the injection acceleration, the flight to the chamber (drift region) and the flight within the chamber. Depending on the design of the injector, frictional or induction or convective heat might be applied to the hohlraum wall. The fusion chamber exhibits the most hostile environment with gases as hot as ~6000K and the chamber walls radiating at ~900K. The temperature of the drift region has not yet been defined but the target must be below the transonic region (< 80% of Mach one) for assured aerodynamic stability. The Mach number is a function of the gas temperature and molecular weight of the gas. For xenon gases and targets traveling at ~250 m/s, the required gas temperature is ~700K which can add a significant amount of heat to the target. Lower molecular weight gasses such as argon or helium or a lower flight velocity will allow the reduction of the gas temperature.

Figure 15 shows the basic mechanisms of target heating. The primary mechanism for heat to penetrate the target is through the thin LEH window. The thin LEH window with negligible thermal mass quickly heats up and starts heating the helium near the window. The helium re-circulates due to convection driven by buoyancy and spinning of the target. The hohlraum wall acts as a heat sink to cool this helium. The moving helium in turn heats the IR shield which transfers heat to the helium compartment containing the capsule. The capsule ablator is heated and conducts this heat to the DT layer. A secondary convective thermal path is via the hohlraum side walls. The hohlraum side walls can be heated during injection due to friction between the hohlraum and the injector barrel, or due to convection in the case of the push-rod injector or due to induction in the case of an induction injector. An increased hohlraum temperature near the capsule transfers heat via the helium directly to the capsule. Heat transferred in this way during injection has considerable time to affect the capsule temperature, unlike heat transferred during flight though the chamber with a comparatively short flight time to affect the temperature. Excessive heat from the hohlraum can push the capsule temperature too high.

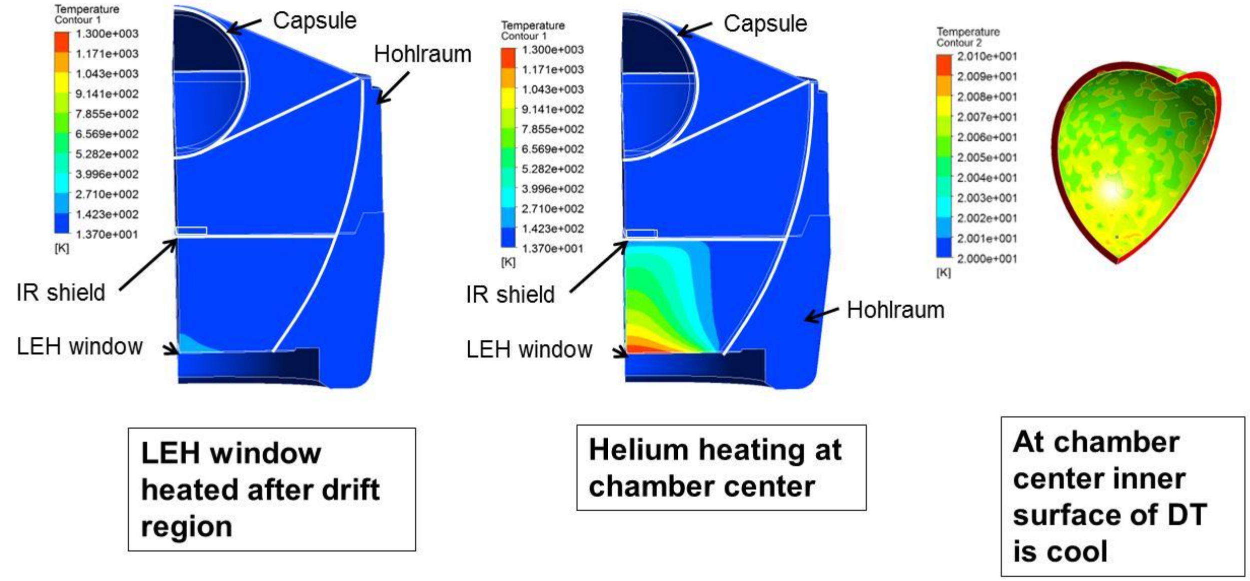

Figure 15. Heat primarily enters through the LEH window and migrates towards the capsule during the flight to chamber center. Some heat does enter the target through the hohlraum walls and can affect the DT temperature especially if the hohlraum is heated during the injection process.

Radiative heat transfer from the ~ 900K chamber walls illuminates the LEH window in addition to the convective heating. The radiation is reflected, absorbed or transmitted through the LEH window depending on the composition of the window. Optical properties of candidate materials were tested in the apparatus shown in Figure 16 described in the Appendix. Polyimide windows, on the other hand, transmit ~85% of the incident light as shown in Figure 17. Graphene layers in the LEH window act as absorbers as shown in Figures 18 and 19. Polyimide LEH windows are structurally preferable to graphene windows as the 100-200 nm thick multi-crystalline graphene windows as discussed in a previous section. A < 100 um thick methane sublimating sacrificial layer is not expected to absorb significantly in the IR [17]. A reflective layer can also be added to the front of the LEH window provided that the optical depth increase significantly thereby decreasing reflectivity at the increased temperatures expected for the LEH window.

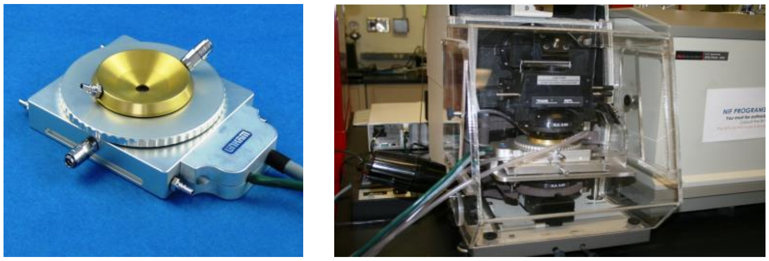

Figure 16. Experimental Setup for IR characterization of polyimide, graphene and aluminum films

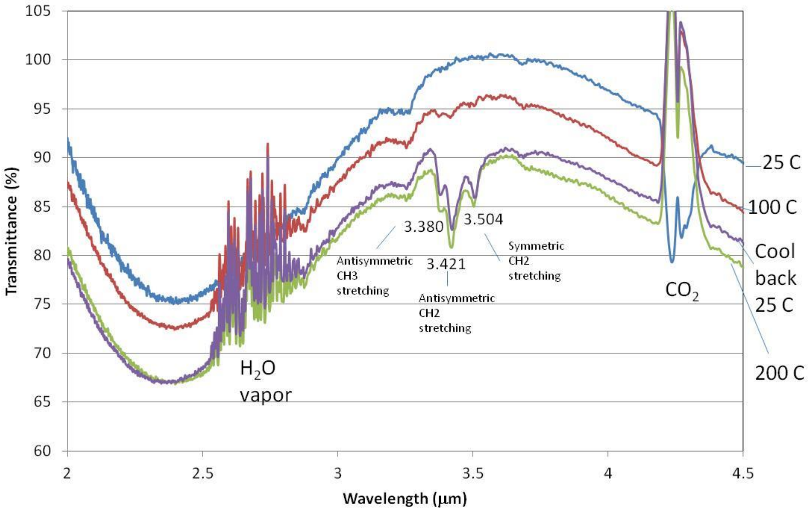

Figure 17. Measured transmission of 1000 nm thick polyimide at room temperature

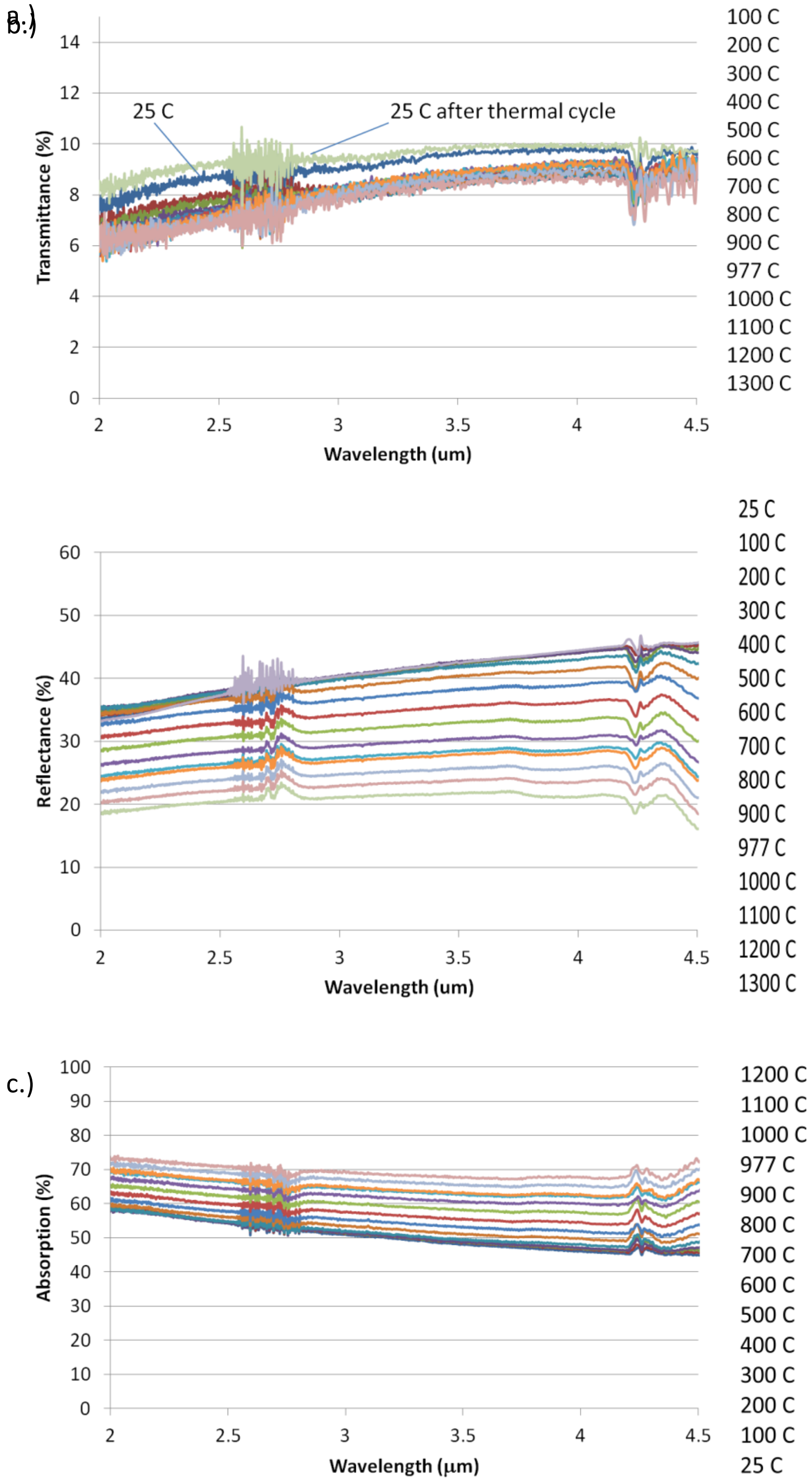

Figure 18. Measured transmission (a) reflection (b) and calculated absorption (c) of 100nm thickness graphene as a function of temperature

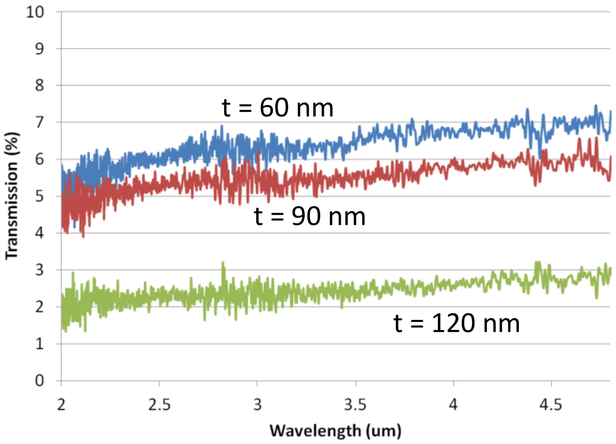

Figure 19. Transmission of graphene as a function of thickness

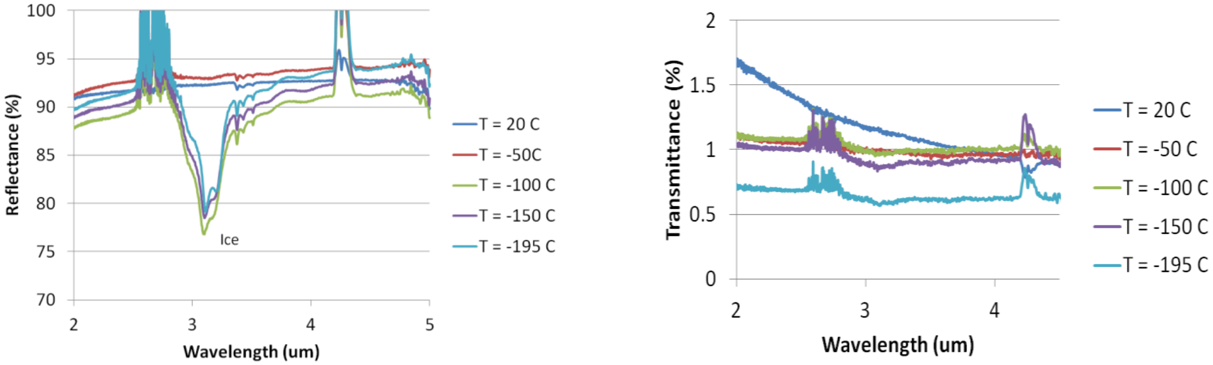

Figure 20. Measured reflection/transmission of 30 nm aluminum on a glass substrate as a function of temperature

Significant radiation passing through the LEH window must be reflected off the IR shield. The IR shield reflective layer thickness is nominally 30 nm thick aluminum. A plot of normal specular reflectivity versus temperature is shown in Figure 20. While this measures specular reflection, there must also be unmeasured diffuse reflection because the measured transmission is only ~1.5% (Figure 20). The absorption for such a thin aluminum film should be negligible.

The average temperature of the target components for the various phases of the target flight is shown in Table 5. Two different injection scenarios were investigated including frictional heating that may result from a gas gun with hohlraum contact to the barrel walls and a push-rod injector where the target may experience a gas at a specific temperature chosen to remain under transonic flight. Design options used to mitigate thermal effects on the target as shown in Figure 21 include a cup design round the LEH window to form a stagnation region to reduce the convective heat flux to the LEH window, addition of a hole at the perimeter of the IR window to relieve the pressure of the helium being heated in the front compartment and allow the gasses flowing from the front compartment to the inner helium compartment to be cooled by the relatively cooler hohlraum, and lastly, addition of a sublimating sacrificial layer on the LEH window to absorb the incoming heat.

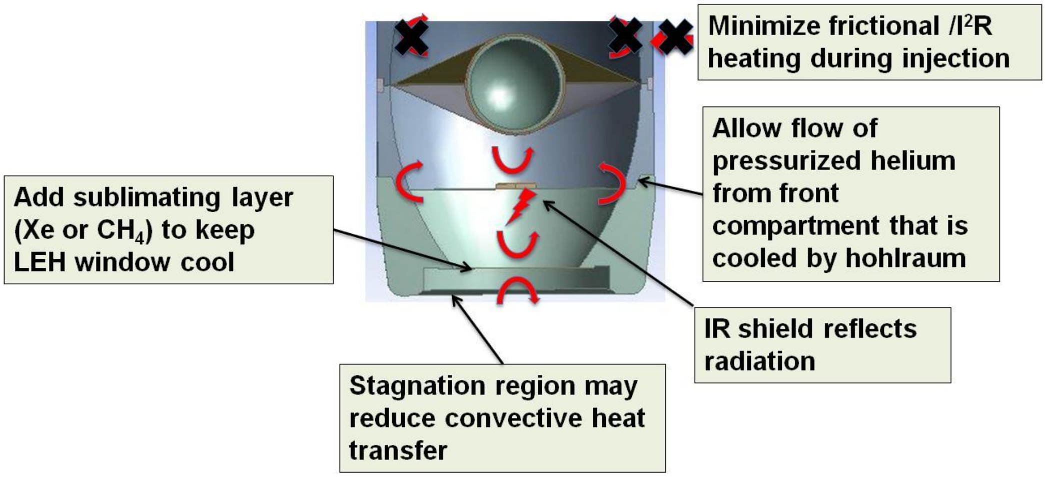
Minimize frictional /I^2R heating during injection
Allow flow of pressurized helium from front compartment that is cooled by hohlraum
Add sublimating layer (Xe or CH_4) to keep LEH window cool
IR shield reflects radiation
Stagnation region may reduce convective heat transfer

Figure 21. Design option to reduce heat load on the DT layer and to reduce the pressure in the forward helium compartment.

Table 5. Thermal modeling results for the targets injected into the chamber

Case No.		LEH average temperature (K)	He front compartment average temperature (K)	He front compartment pressure change (Pa)	P2 shield average temperature (K)	He second compartment average temperature (K)	He second compartment pressure change (Pa)	Capsule ablator max. temperature (K)	DT inner surface max temperature (K)
1	Baseline (rugby) case w/ frictional heating during injection	1268	315	111896	59.5	42.2	21991	22.4	20.3
2	Baseline case w/o frictional heating during injection but with 700 K gas environment instead	1275	312	99052	58.6	40.7	18836	22.4	20.26
3	above case but switch design to recess LEH	563	199	71078	37.1	29.7	11910	20.4	20.08
4	Add helium bypass flow to above	580	90.7	23021	36.6	N/A	N/A	20.6	20.08
5	Baseline with phase change material(methane)	72.9	38.5	26603	22.8	NR	NR	20.4	20.03
6	Baseline with phase change material (pentane)	245	83.6	56922	30.2	NR	NR	20.2	20.04
7	helium bypass with recess LEH and phase change material (pentane)	245	49	23363	26.7	N/A	N/A	20.3	20.05
8	Baseline case w/ frictional heating during injection but 150m/s	1160	296	105161	64.2	43.1	22808	22.7	20.37
9	Helium bypass, recessed LEH window, no friction, 300K gas with 150 m/s	520	87.5	25468	40.9	N/A	N/A	20.8	20.15
10	Baseline with phase change material (pentane) but 300K gas, 150 mps	245	85	56444	35.9	28.5	12806	21	20.14
11	Baseline with phase change material (methane) but 300K gas, 150 mps	73	39.7	27882	26.3	25.2	9230	20.5	20.07
12	Baseline but 420K gas, 200 mps	1224	302.6	97381	56.3	40.4	18589	22.3	20.25
13	baseline but adiabatic LEH, all time	30.75	25.7	9880	20.4	NR	NR	20.3	20.03

Line 1 on table 5 shows the results for the baseline case. The baseline target is shaped as in Figure 1. The target is assumed an initial temperature of 20K and experiences frictional heating during injection acceleration then exits the injector at 250 m/s. The flight path is 10 m long, 6 m of which through a 6000K xenon chamber gas with radiation from 900K chamber walls assume to interact with the LEH window with emissivity of 0.3. In this case, the LEH window reaches a high temperature of ~1300K, the helium pressure in the front chamber increases by roughly 1 atm, and the DT layer heats 300 mK, above the specification. This, the baseline scenario will not meet the current thermal criteria at chamber center. Case 2 shows that removal of the frictional heating during injection but replacing it with flight through a xenon atmosphere, warmed to keep the speed of sound above the target velocity, does not improve the thermal performance significantly. Case 3 shows that the stagnation cup at the LEH window used to reduce the heat transfer coefficient from the hot xenon gas to the LEH is effective in reducing the change in the DT temperature to 80 mK which is within the desired specifications. However, the pressure change of the helium in the front compartment is still high so case 4 shows that this pressure can be relieved with a helium bypass flow around the IR shield which heat sinks the helium to the hohlraum and results in minimal effect on the temperature rise of the DT. Cases 5 through 7 show that a phase change material on the front LEH window which keeps the LEH window temperature at the sublimation temperature of the phase change material is effective at keeping the DT layer cool. Case 8 shows that a slower flight velocity (150 m/s) yields a higher DT temperature due to the longer flight time despite the lower heat transfer coefficient for the hot xenon to the hohlraum, that the DT temperature improves but does not meet specification even with a stagnation cup at the LEH window (case 9) or a pentane sacrificial layer (case 10) but meets specification with a methane sacrificial layer (case11). Case 12 shows that a 200 m/s flight velocity also does not yield an in-specification DT temperature rise but that this can be achieved through use of a methane sacrificial layer (case 13). In summary, for the current scenario, an effort to reduce the LEH temperature is required if the DT temperature rise is to be minimal at chamber center either through the use of a stagnant layer at the higher velocities (~250 m/s) or sacrificial sublimating layer at all velocities. A by-pass flow around the IR shield is required to reduce the helium pressure in the front compartment.

The desired property of the sacrificial layer on the LEH window is that the sublimation temperature be sufficiently low to result in minimal thermal transfer into the target. The second criterion is that the evaporation/sublimation rate be sufficiently high that the material can absorb the incoming heat and dissipate prior to reaching fusion chamber center. It is also desirable to have a material that can be easily applied in liquid phase during the manufacture of the devices. As the target is cooled down to about 20 K there is a point where the phase change material would be dropped onto the LEH window and frozen in place. Some candidate phase change materials are shown in Table 6. Pentane is attractive because it is liquid phase at room temperature and thus the manufacturing process will be easier. Methane, however, sublimates at a much lower temperature and analysis shows that it is necessary to use a low sublimating material if the target flight velocities are going to be reduced to the order of 150 m/s which makes the design of the injector much easier. The extra hydrogen added to the chamber which must be recovered by the hydrogen isotope separation system is on the order of a fraction of the DT isotopes and therefore should not overwhelm the separation system.

Table 6. Some candidate phase change materials for use as sacrificial layers over the LEH window

Material	Thickness needed to absorb convective heat input to LEH (micrometers)	Sublimation or evaporation temperature (K)	Evaporation rate (kg/(ms))	Thickness evaporate-able in 25 msec (micrometers)
Xenon	19.9	125	8.1	570
Methane	31.4	73	0.82	49
Pentane	9.8	243	17.2	685

Manufacturability

DT layer

The layering of the ice DT layer in the NIC campaign is a very time intensive process. The NIC layer is single crystal and is created by first filling the capsule with DT liquid then freeze-plugging the fill-tube then allowing the crystal to grow from the freeze plug. Because of the small dimension of the tube (~ 7 um inner diameter) the crystals which are initiated are single crystals and become the seed crystal for the Bridgeman-like growth. Typical layering time for a NIC shot is on the order of about 10 hours. If the layer is not growing well, the DT layer is remelted and the process begins anew. Automating this process will be very difficult considering the lack of fill tube in the LIFE targets, the current need to manually monitor the freeze over 10 hours and the need for reduced tritium inventory in the plant making short layer times very attractive. A further complication for the LIFE targets is that unlike NIC targets which have temperature sensors and heaters placed around the target to precisely adjust the uniformity of the capsule temperature to prevent beta layering induced thickness changes, the LIFE target will be cooled in a batch process for which precise capsule temperature uniformity may be difficult to achieve.

The alternative approach is to use a low-density foam to act as a sponge for the DT. The shape of the DT layer would be pre-defined by the geometry of the foam. The foam will have to be very low density to prevent interference with the implosion, ~20-25 mg/cc of DCPD or other carbon-based foam or ~5 mg/cc silica aerogel. The DT layer could be either in the liquid or solid phase. The advantage of a liquid DT layer is that beta layering effects do not apply, cracks do not form and the layering process is a straight-forward reduction in temperature wherein the DT in vapor phase will condense and wick into the foam layer. The disadvantages to a liquid DT layer without the foam are that the liquid phase is lower density than the solid phase and the higher vapor pressure over a liquid layer increases the work needed to compress the DT and the liquid layer could possibly distort during the acceleration of the target. The lower density of the liquid can be accommodated by modifications in the physics design.

The reduction of the vapor pressure due to the presence of the foam is a topic of recent research. The premise of the research is that the freezing point and the corresponding vapor pressure are lowered for the DT in nano-porous foams due to the increased surface energy associated with the liquid-solid interface. Studies have born out this premise and D_2 and H_2 liquids in ~340 mg/cc silica foams freeze at ~1 degree K under the neat freezing temperature. In addition, the vapor pressure is lowered to that which would have been above the solid phase at the same temperature as shown in Figure 23. Unfortunately, the desired freezing point depression which would meet NIC specifications is about 1.8 K as suggested in Figure 22.

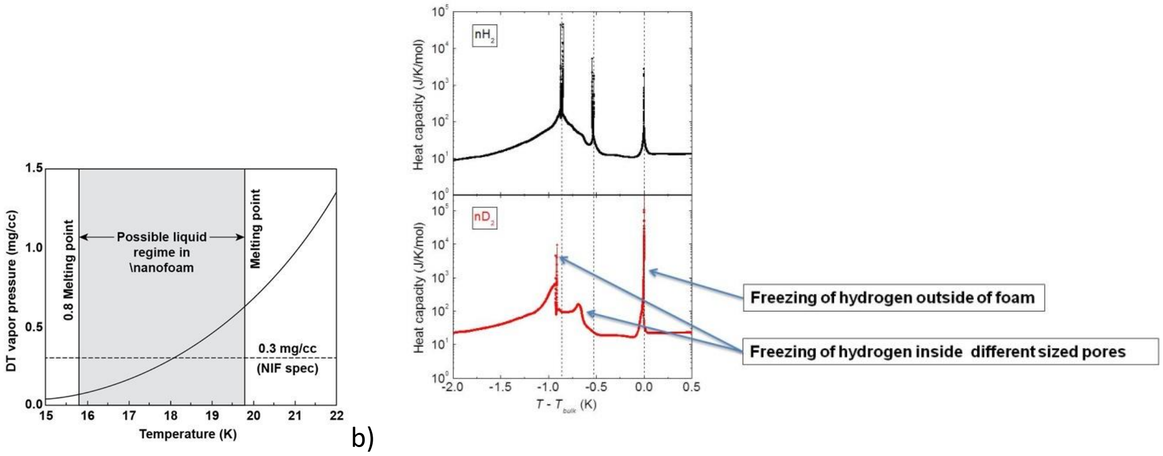

a) b)

Figure 22. Desired melting point for liquid DT in foam is about 1.8 K below the freezing point of neat DT to lower the vapor pressure to NIC levels (a). Heat capacity measurements of hydrogen isotopes in foams shows liquid to solid transition temperatures at about 1 degree below the neat freezing point (b).

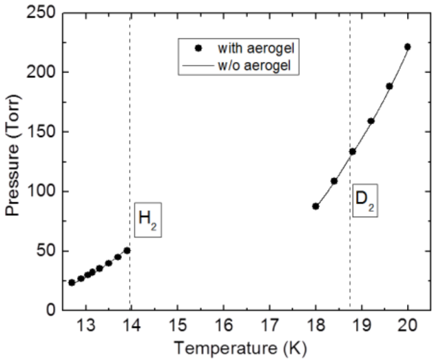

Figure 23. Plots of the measured vapor pressures of the hydrogen isotopes in with and without the foam (aerogel) show that the vapor pressure is a function of temperature only and not of state. The hydrogens without the foams are in slid state at temperatures below the freezing point whereas they are in liquid state inside the foams at the same temperature.

Tests of the lower density ~ 25 mg/cc DCPD and carbon nanotube carbon aerogels (CNT-CA) foams showed very little depressed freezing temperature as shown in Figure 24 due to the low surface to volume ration associated with such low density foams.   A plot of surface area to pore volume shown in Figure 25 suggests this correlation.

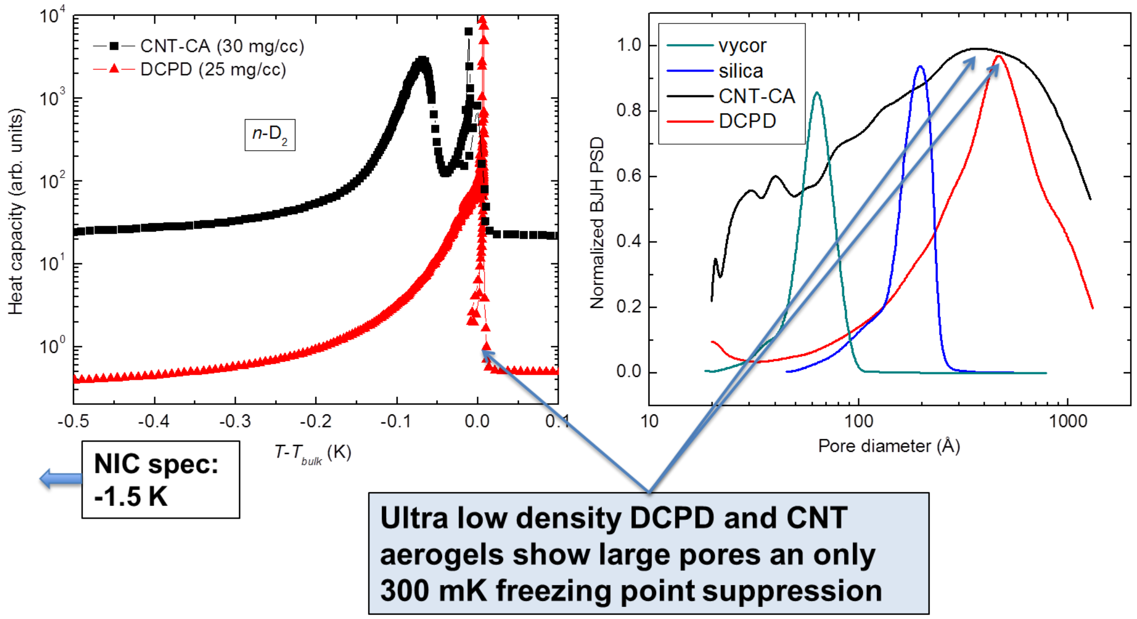

NIC spec: -1.5 K

Ultra low density DCPD and CNT aerogels show large pores an only 300 mK freezing point suppression

Figure 24. The pore sizes of the low density DCPD and CNT foams are large with a larger size distribution (b). The resulting depressed freezing temperature is minimal (a).

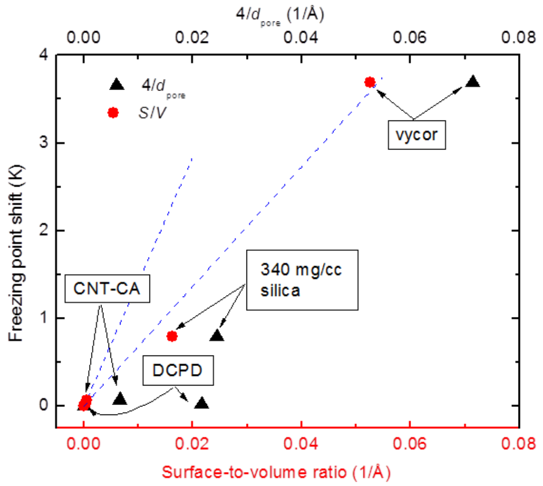

Figure 25. The depression of the freezing point correlates better to the surface to volume ratio (red dots) than to the pore size (black triangles)

It is also important that the DT layer maintain its integrity during the flight into the fusion chamber. Modeling results indicate that a liquid DT layer will not be distorted more than 1 um from its round shape as shown in Figure 26. A full report of these studies are included in the Appendix.

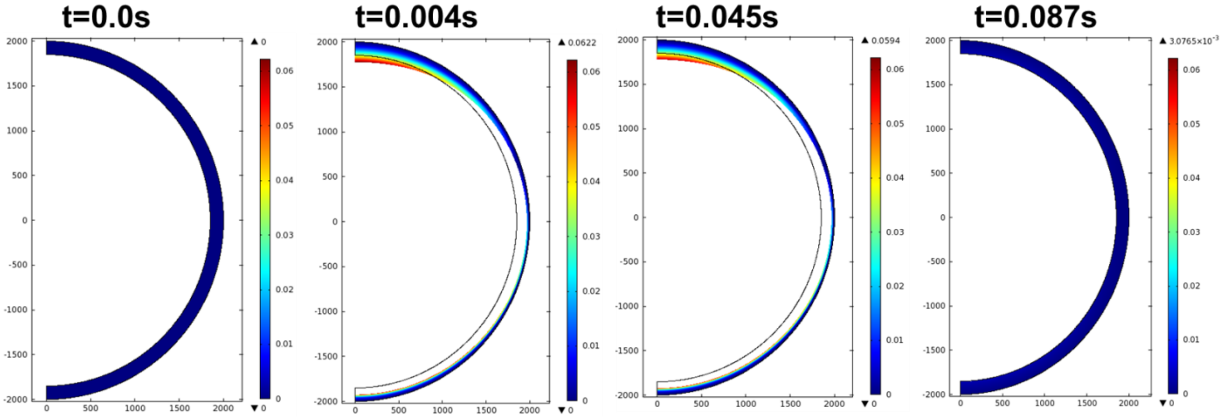

Figure 26. Displacement of liquid-foam (scaled by a factor of 1200) showing a 1 um disturbance in the shape of the layer during acceleration followed by recovery during flight into chamber center.

High Growth Rate Diamond Material

It is important to consider the material used as the ablator. Because the CVD diamond ablator comprises the highest cost component of the target, methods for decreasing this cost must be found and the corresponding mechanical properties ultimately measured. To reduce cost, either the deposition rate of the diamond carbon must be increased or the numbers of capsules per run must be increased. A reports in the Appendix show that deposition rates of ~ 5 um/hr, up from ~1 um/hr can be achieved (although the material properties and uniformity must be investigated) and large numbers of capsules can be coated uniformly in a large microwave plasma reactor. In a 915 MHz microwave plasma coater an inclined rotating disk was installed and tested. This concept was very successful as the movement of the balls was very stable. Two deposition runs were performed, with 3300 and 3600 balls respectively. These balls were homogeneously coated with 34 microns of diamond.

References

1. Amendt, P., Dunne, M., Ho, D., Lasinski, B., Meeker, D., Ross, J.S., “Status of the Laser Inertial Fusion Energy (LIFE) Hohlraum Point Design”, Conference on Laser Inertial Fusion Energy (CLIFE 2012), Yokohama, Japan, Apr. 26 - Apr. 27, 2012.
2. Amendt, P., Dunne, M., Ho, D.D., Lindl, J.D., “LIFE pure fusion target designs: Status and prospects”, *Fusion Science and Technology*, **60**, 49 (2011).
3. Goodin, D.T., Gibson, C.R., Petzoldt, R.W., Siegel, N.P., Thompson, L., Nobile, A., Besenbruch, G.E., Schultz, K.R., “Developing the basis for target injection and tracking in inertial fusion energy power plants”, *Fusion Engineering and Design*, 60 (2002) 27–36.
4. Raffray A.R., Petzoldt R., Pulsifer J., Tillack M.S., Wang, X., “Thermal behavior and operating requirements of IFE direct-drive target”, *Fusion Science and Technology*, 44, 1, 111-116 (2003).

5. Gosnell, T., Hoffer, J., “Effect of thermal radiation on melting times of DT ice layers in polymer-capsule targets for IFE reactors”, *Fusion Science and Technology*, 45, 4, 567-572 (2004).
6. Christensen, B.R., Raffrey, A.R., Tillack, M.S., Thermal loading of a direct drive target in rarefied gas”, *Fusion Science and Technology*, 47, 4, 1175-1179 (2005)
7. Christensen, B.R., Raffrey, A.R., Tillack, M.S., Modeling D.T., vaporization and melting in a direct drive target”, *Fusion Science and Technology*, 47, 4, 1180-1186 (2005)
8. Petzolt, R.W., Goodin, D.T., Nikroo, A., Stephens, E., Siegel, N., Alexander, N.B., Raffray, A.R., Mau, T.K., Tillack, M., Najmabadi, F., Krasheninnikov, S.I., Gallix, R.,”Direct drive target survival during injection in an inertial fusion energy power plant”, *Nuclear Fusion*, 42, 12, 1351-1356 (2007).
9. Moll, G., Martin, M., Collier, R., “Thermal simulations of the intermediate step laser megajoule cryogenic target *parameter study)”, *Fusion Science and Technology*, 55, 3, 283-289 (2009).
10. Valmianski, E., Petzoldt, R. W., “ Mechanical response of DT target to acceleration for a laser power plant”, *Fusion Science and Technology*, 51, 4, 800-803 (2007)
11. Luxel PI paper: attached in bundle
12. Wang J-Y., Yang, S-Y., Huang, Y-L., Tien,H-W., Chin, W-K., Ma C-C. M., “Preparation and properties of graphene oxide/polyimide composite films with low dielectric constant and ultrahigh strength via in situ polymerization” *J. of Materials Chemistry*, DOI: 10.1039/c1jm11766a.
13. Ma, W. ,Song, L. , Yang, R., Zhang, T., Zhao, Y., Sun L., Ren,Y., Liu,D., Liu,L.,Shen,J., Zhang, Z., Xiang,Y., Zhou,W., SiShen Xie, S.,“ Directly Synthesized Strong, Highly Conducting, Transparent Single-Walled Carbon Nanotube Films”, *Nano Letters*, 7 (8), 2307-2311 (2007).
14. Cheng, Q., Bao,J., Park, J., Liang, Z., Zhang, C., WangHigh, B., “ Mechanical Performance Composite Conductor: Multi-Walled Carbon Nanotube Sheet/Bismaleimide” *NanocompositesAdv. Funct. Mater*. 2009, 19, 3219–3225
15. Liu, W., Zhang, X., Xu, G., Bradford, P. D., Wang, X., Zhao, H., Zhang, Y., Jia, Q., Yuan, F-G., Li c, Q., Qiu, Y., Zhu, Y., “Producing superior composites by winding carbon nanotubes onto a mandrel under a poly(vinyl alcohol) spray”, *Carbon*, 49, 4786 –4791, (2011).
16. Timoshenko, S.P. and Goodier, J.N., Theory of Elasticity, 2nd edn, McGraw-Hill, New York, 1951.
17. Grundy, W.M., Schmitt, B., Quirico, E., “The Temperature-Dependent Spectrum of Methane Ice I between 0.7 and 5 μm and Opportunities for Near-Infrared Remote Thermometry”, *Icarus*, **155**, 486–496 (2002).
18. McCoy, R. L., Modern Exterior Ballistics, Schiffer Publishing Ltd, Atlglen, PA, 1999.

Appendix: Thermal Studies of the Laser Inertial Fusion Energy (LIFE) Target during Injection into the Fusion Chamber

Miles, R., Havstad, M., LeBlanc, M., Chang, A., Golosker, I., Rosso, P.

1.0 Introduction

The Laser Inertial Fusion Energy (LIFE) commercial electrical generating plant was conceptualized at LLNL [1-1]. Like many inertial fusion energy (IFE) plant concepts[1-2,1-3], the target is expected to be injected into the fusion chamber at repetition rates of 5-20 per second and velocities of about 250 m/s. During the ~100 ms injection acceleration and flight time into chamber-center where implosion occurs, the target experiences intense heat fluxes to its surfaces. During injection, the target experiences frictional heating if the injector is a gas gun or I^2R energy from currents induced in the hohlraum if induction acceleration is used. The target also experiences convective heating from the hot chamber gases and infrared (IR) radiation heating from the chamber walls. Implosion will be unsuccessful if the target components lose structural integrity (e.g. melt) or the DT overheats inhibiting successful compression of the fuel. This study looks at the thermal profile of the LIFE target as it is injected into the fusion chamber to ensure a target design which meets the thermal requirements for successful implosion at chamber center.

The candidate LIFE target is shown in Figure 1-1 [Ref. 1-4, 1-5]. The LIFE target is an indirect drive target consisting of a hollow spherical capsule with a diamond ablator and an inner layer of solid DT held in the center of a lead hohlraum by two <100 nm thick carbon-composite capsule support membranes. A ~500 nm thick polyimide LEH window seals each axial end of the target. A 500 nm thick polyimide membrane coated with ~30 nm of aluminum serves as the IR shield and support for the lead P2 shield which is ~5mm in diameter and ~ 200 um thick. Helium at a density of ~1 mg/cc at ~18K fills the target.

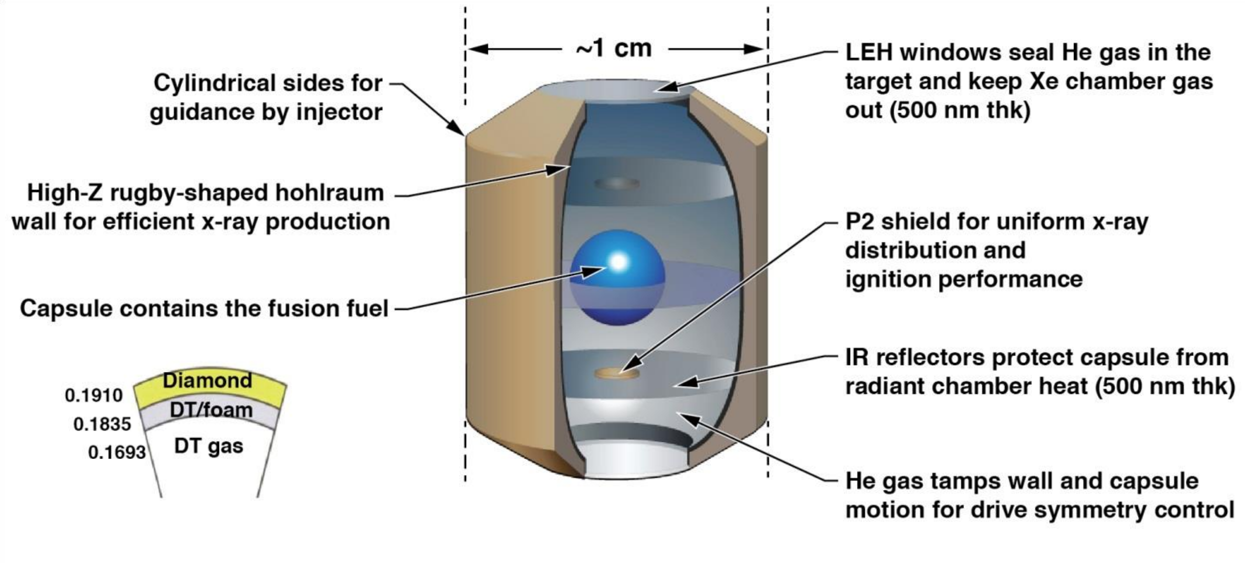
~1 cm
Cylindrical sides for guidance by injector
High-Z rugby-shaped hohlraum wall for efficient x-ray production
Capsule contains the fusion fuel
0.1910
0.1835
0.1693
Diamond
DT/foam
DT gas
LEH windows seal He gas in the target and keep Xe chamber gas out (500 nm thk)
P2 shield for uniform x-ray distribution and ignition performance
IR reflectors protect capsule from radiant chamber heat (500 nm thk)
He gas tamps wall and capsule motion for drive symmetry control

Figure 1-1. LIFE target design

As shown in Figure 1-2, the target experiences three phases of environmental conditions during the injection process. The first phase is the acceleration injection phase during which time the target is accelerated up to its flight velocity by the injector. The injector mechanism has not been specified but leading candidates include a gas gun and an induction accelerator. During this time, the target hohlraum could be subjected to external thermal loads resulting from the hot gas of a gas gun, possible friction with the injector barrel or induced electrical I^2R heating. The second phase is called the drift phase named for the drift through the gas between the muzzle of the injector and the inner chamber wall. Lastly, the target flies through the chamber to chamber-center where implosion occurs. The chamber contains low density (~6 ug/cc), hot (~6000K) xenon gas. The chamber walls are hot (~900K) and emit infrared radiation though the target laser entrance hole (LEH) window. The flight times through each phase of the target flight are ~42 ms in the injector, ~16 ms in the drift region and ~24 ms in the chamber which yields a total flight time of ~82 ms. Beyond the obvious requirement to maintain structural integrity (i. e. no softening or melting) during flight, the primary thermal requirement of the target is derived from the desire to limit the increase in vapor pressure of the DT beyond a point where implosion would be inhibited due to back-pressure during implosion. Max Tabak estimated that this represented a requirement for a temperature increase of no more than 0.1 K at the surface of the DT layer. While this numerical requirement needs to be reconsidered in more detail, we used this as the assumed requirement for this analysis. In essence, the capsule is thermally protected using the hohlraum and the IR shields as barriers to heat transfer and by limiting the exposure time.

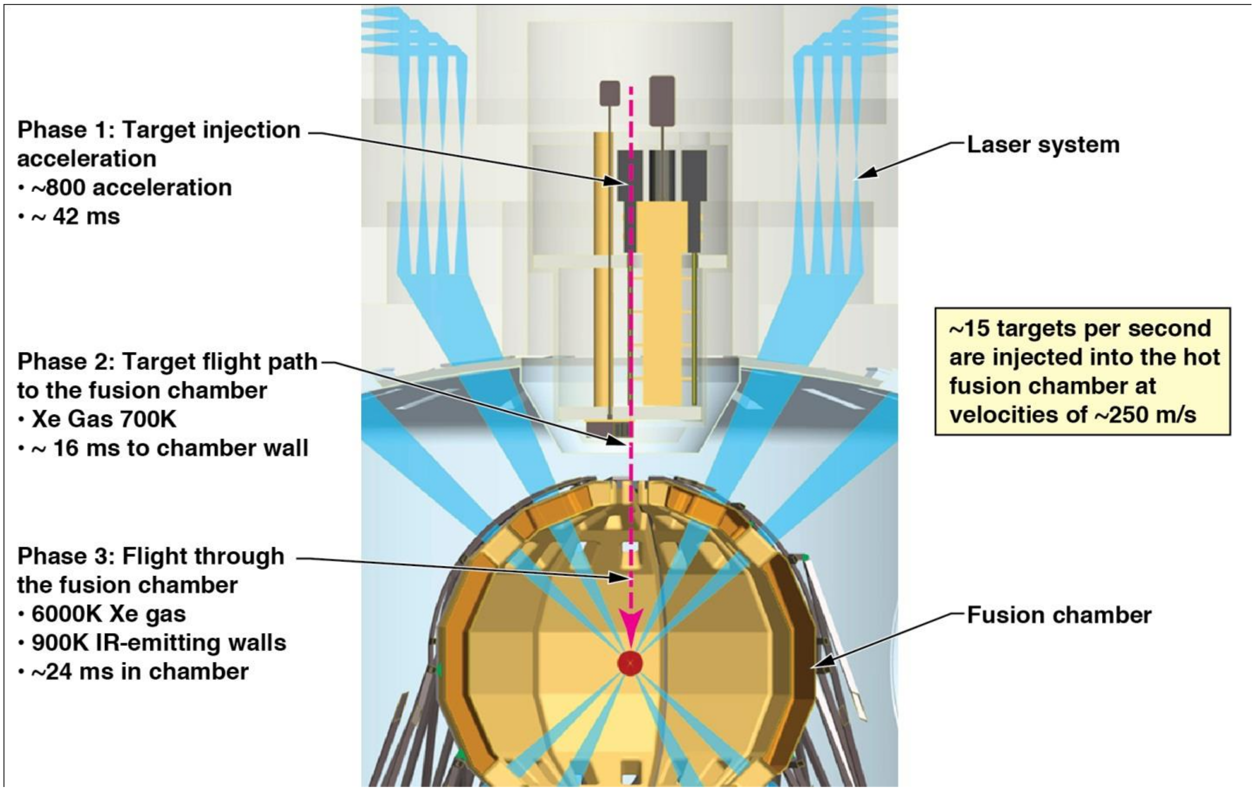
Phase 1: Target injection acceleration
• ~800 acceleration
• ~ 42 ms
Laser system
~15 targets per second are injected into the hot fusion chamber at velocities of ~250 m/s
Phase 2: Target flight path to the fusion chamber
• Xe Gas 700K
• ~ 16 ms to chamber wall
Phase 3: Flight through the fusion chamber
• 6000K Xe gas
• 900K IR-emitting walls
• ~24 ms in chamber
Fusion chamber

Figure 1-2. Schematic of LIFE target flight into the fusion chamber

To determine whether or not a LIFE target would survive the injection process, a series of analytical models were developed. The results of this work were published in reference 1-6. This document discusses tests which were conducted to validate the results of this analysis. The tests were not conducted in the extreme environmental conditions expected in a fusion chamber due the difficultly of duplicating these conditions but were used to emulate essential aspects of the heat transfer phenomena. This task consists of measuring the convection heat transfer coefficients internal and external to the target and the parameters of radiative heat transfer.

1.1 Thermal models of the target in the LIFE plant

The results of the modeling efforts for flight into the fusion chamber are summarized in Figures 1-3 and 1-4 and in Table 1-1 below. The major ingresses of heat into the target are heat absorbed by the hohlraum during the process of injection acceleration and convective heat from the chamber gasses to the thin LEH window which heats the helium behind the window establishing convection currents which in turn heat the capsule. The injection-acceleration heat source is a lower intensity source than the chamber heat source but has a longer period of time to penetrate through the hohlraum and migrate towards the capsule. The hohlraum acts as a heat sink for the intense heat of the chamber. Nearly all the IR radiation from the chamber walls is reflected off the IR shield. The heat transfer coefficient at the LEH window can be reduced by adding a cup geometry in front of the LEH window which creates a stagnation region as shown in Figure 1-4. At some target velocities the specification of a maximum temperature increase of 0.1 K increase at the DT inner surface will be exceeded unless stronger measures are taken to reduce the heat absorbed at the LEH window by, for example, adding a 10 um solid methane sublimation layer to the window. In either case, the heating of the helium behind the LEH window increases the internal helium pressure in the adjacent compartment to such a degree that rupture of the LEH window and IR shield would result were the pressure not relieved by adding by-pass ports around the IR shield to vent the gas from the first compartment near the LEH window into the second compartment near the capsule. Although this increases the temperature in the second compartment by some small degree, the gas is largely cooled by the hohlraum as it is vented, reducing the thermal threat to the capsule.

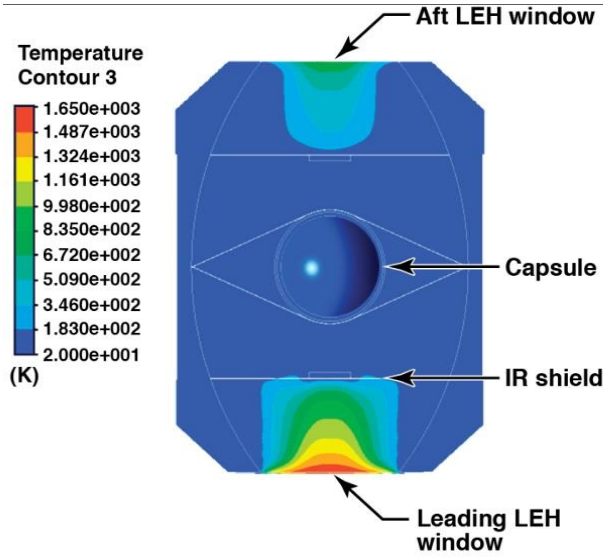

Figure 1-3. Thermal distribution in target at chamber center

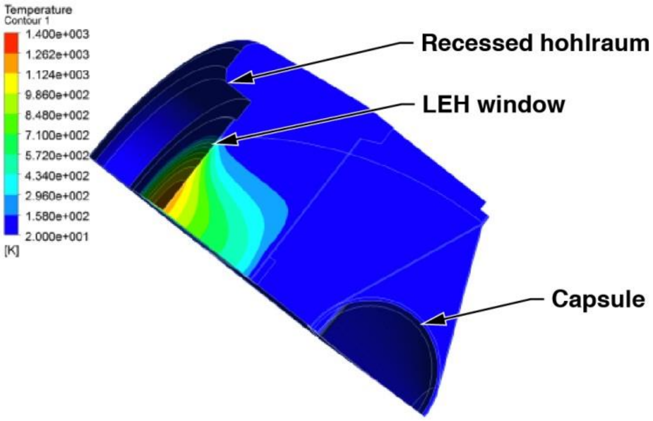

Figure 1-4. Thermal distribution in target with recessed leading edge at chamber center

Table 1-1. Summary of thermal analysis for a variety of cases (Initial target temperature is 20K)

Case No.		LEH average temperature (K)	He front compartment average temperature (K)	He front compartment pressure change (Pa)	P2 shield average temperature (K)	He second compartment average temperature (K)	He second compartment pressure change (Pa)	Capsule ablator max. temperature (K)	DT inner surface max temperature (K)
1	Baseline (rugby) case w/ frictional heating during injection	1268	315	111896	59.5	42.2	21991	22.4	20.3
2	Baseline case w/o frictional heating during injection but with 700 K gas environment instead	1275	312	99052	58.6	40.7	18836	22.4	20.26
3	above case but switch design to recess LEH	563	199	71078	37.1	29.7	11910	20.4	20.08
4	Add helium bypass flow to above	580	90.7	23021	36.6	N/A	N/A	20.6	20.08
5	Baseline with phase change material(methane)	72.9	38.5	26603	22.8	NR	NR	20.4	20.03
6	Baseline with phase change material (pentane)	245	83.6	56922	30.2	NR	NR	20.2	20.04
7	helium bypass with recess LEH and phase change material (pentane)	245	49	23363	26.7	N/A	N/A	20.3	20.05
8	Baseline case w/ frictional heating during injection but 150m/s	1160	296	105161	64.2	43.1	22808	22.7	20.37
9	Helium bypass, recessed LEH window, no friction, 300K gas with 150 m/s	520	87.5	25468	40.9	N/A	N/A	20.8	20.15
10	Baseline with phase change material (pentane) but 300K gas, 150 mps	245	85	56444	35.9	28.5	12806	21	20.14
11	Baseline with phase change material (methane) but 300K gas, 150 mps	73	39.7	27882	26.3	25.2	9230	20.5	20.07
12	Baseline but 420K gas, 200 mps	1224	302.6	97381	56.3	40.4	18589	22.3	20.25
13	baseline but adiabatic LEH, all time	30.75	25.7	9880	20.4	NR	NR	20.3	20.03

1.2 Tests

Three sets of experimental tests were pursued. These tests were used to 1) measure the heat transfer coefficient on the external surface of the target subjected to chamber gas 2) verify the existence of convection currents internal to the target and measure the internal heat transfer coefficients between the LEH window and the helium target gas and 3) measure the absorption, reflectance and transmittance of IR radiation through the IR shield and carbon-composite membrane. In each case, the relevant heat transfer elements were emulated and the test conditions modeled. The expectation is that agreement between the model and the test results will increase the confidence in the model of the target flight in the chamber.

1.3 References

1-1 Latkowski, J. F. et. al., "Chamber Design for the Laser Inertial Fusion-based Energy (LIFE) Engine," *Fusion Science and Technology,* **60**, 54 (2011).

1-2 Meier, W. R. et. al., "OSIRIS and SOMBRERO Inertial Confinement Fusion Power Plant Designs: Volume 1 Executive Summary and Overview," WSJA-92-01, DOE/ER/54100-1 (1992).

1-3 Sethan, J. D. et. al., "Fusion Energy with Lasers, Direct-drive Targets, and Dry Wall Chambers," *Nuclear Fusion*, **43**, 1693 (2003).

1-4 Amendt, P., et. al., "LIFE Pure-Fusion Target Designs: Status and Future," *Fusion Science and Technology,* **60**, 49, (2011).

1-5 Miles, R., et. al,. "Challenges Surrounding the Injection and Arrival of Targets at LIFE Fusion Chamber Center," *Fusion Science and Technology,* **60**, 61 (2011).

1-6 Miles, R., et. al. "Thermal and Structural Issues of Target Injection into a laser-Driven Inertial Fusion Energy Chamber", *Fusion Science and Technology*, 66, Oct 2014.

2.0 Measurement of the external heat transfer coefficient

The objective of the external heat transfer coefficient section was to validate the models for the external heat transfer conditions as best as possible given that the exact fusion chamber environment cannot be easily reproduced. The test was conducted using a flow of gas through a pipe into which a dummy target was placed with external dimensions similar to the actual LIFE target as shown in the diagram of Figure 2-1. Initially, heated nitrogen gas (~700K) was forced over the target while the gas temperature and target surface temperatures were measured so that the heat transfer coefficient could be calculated from the difference of these temperatures over time according to Equation 2-1 in Section 2.2. The pressure of the gas in the pipe was low, ~23 torr, similar to that expected in the fusion chamber. Originally we planned to heat the gas flowing through the pipe. Unfortunately, the heater broke before good data was obtained so the test was reversed. The target was pre-heated to temperatures of about 865 K then ambient air was drawn over the dummy-target and the heat transfer coefficient was measured by the difference in temperature between the gas temperature and the surface temperature of the target. The gas pressure was about 23 torr and the gas velocity was about 25 m/s.

2.1 Test set-up

A photograph of the external view of the test set-up is shown in Figure 2-2. The dummy target was suspended off a cantilevered tube which contained the thermocouples used to measure the surface temperature is shown in Figures 2-3 and 2-4. The dummy test target is comprised of a hollow macor shell with holes drilled to permit the insertion of thermocouples through the inner core, through the drilled holes and mounted flush with the shell surface as shown in Figures 2-4 and 2-5. Thermocouples used to measure the gas temperature were held with a supporting rod as shown in Figures 2-3 and 2-4. A clam-shell heater was wrapped around the flow tube and was used to heat the apparatus to its initial temperature of about 865K prior to the gas flow. A vacuum pump pulled ambient air through the critical orifice located at the inlet of the flow tube. Since the flow was choked as it traversed the critical orifice, the flow rate was dependent on the upstream pressure, in this case, atmospheric pressure. The flow rate through the flow tube was measured by the Bernoulli’s differential pressure technique between the static and dynamic pressures.

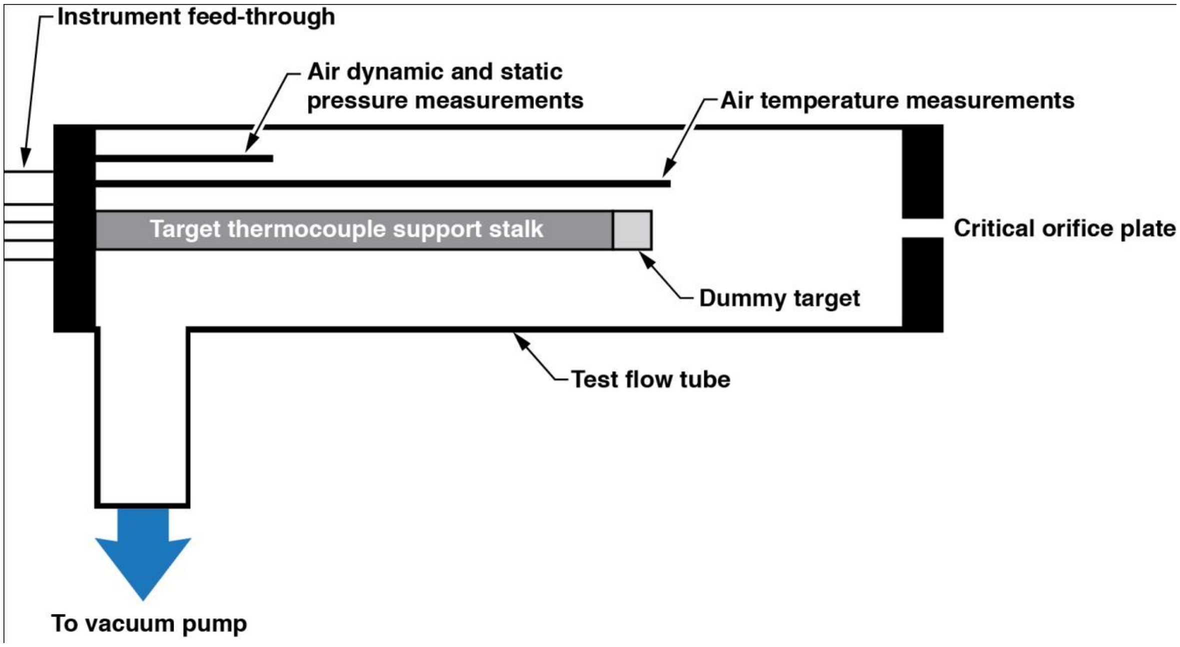
Instrument feed-through
Air dynamic and static pressure measurements
Air temperature measurements
Target thermocouple support stalk
Critical orifice plate
Dummy target
Test flow tube
To vacuum pump

Figure 2-1. Schematic for test 2 set-up to measure external heat transfer coefficient

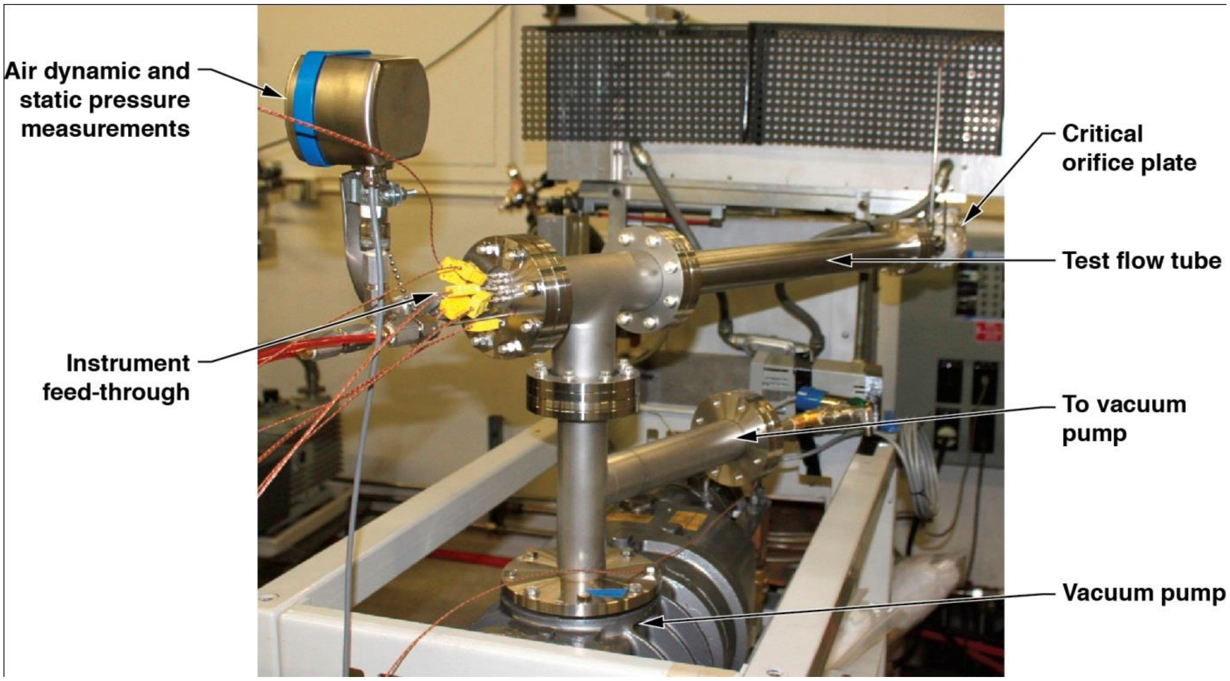
Air dynamic and static pressure measurements
Critical orifice plate
Test flow tube
Instrument feed-through
To vacuum pump
Vacuum pump

Figure 2-2. Picture of test setup used to measure the external heat transfer coefficient of the target

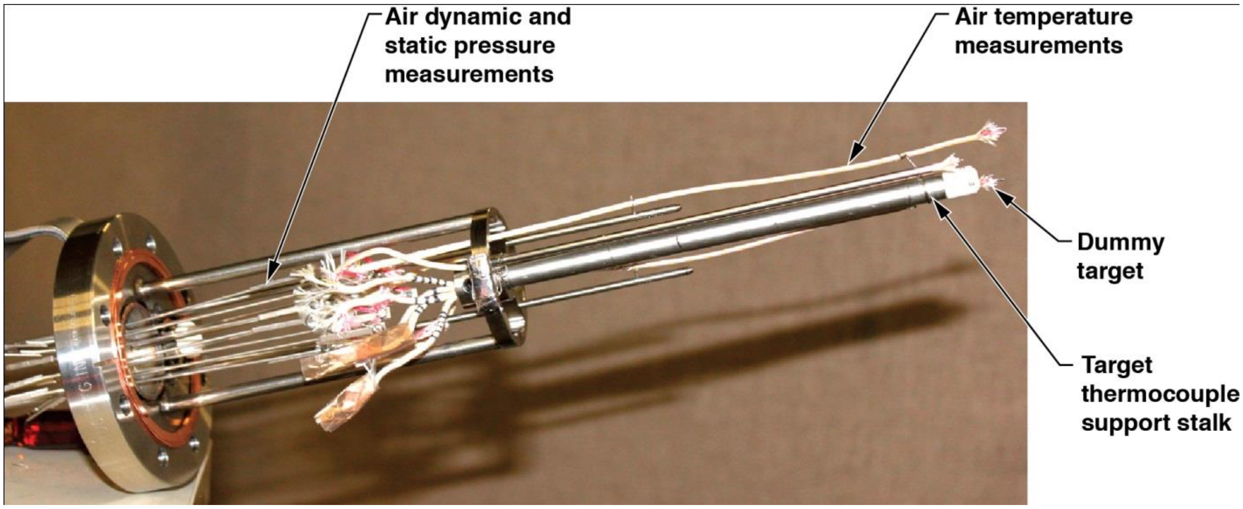
Air dynamic and static pressure measurements
Air temperature measurements
Dummy target
Target thermocouple support stalk

Figure 2-3. Dummy target assembly for external heat transfer coefficient measurements

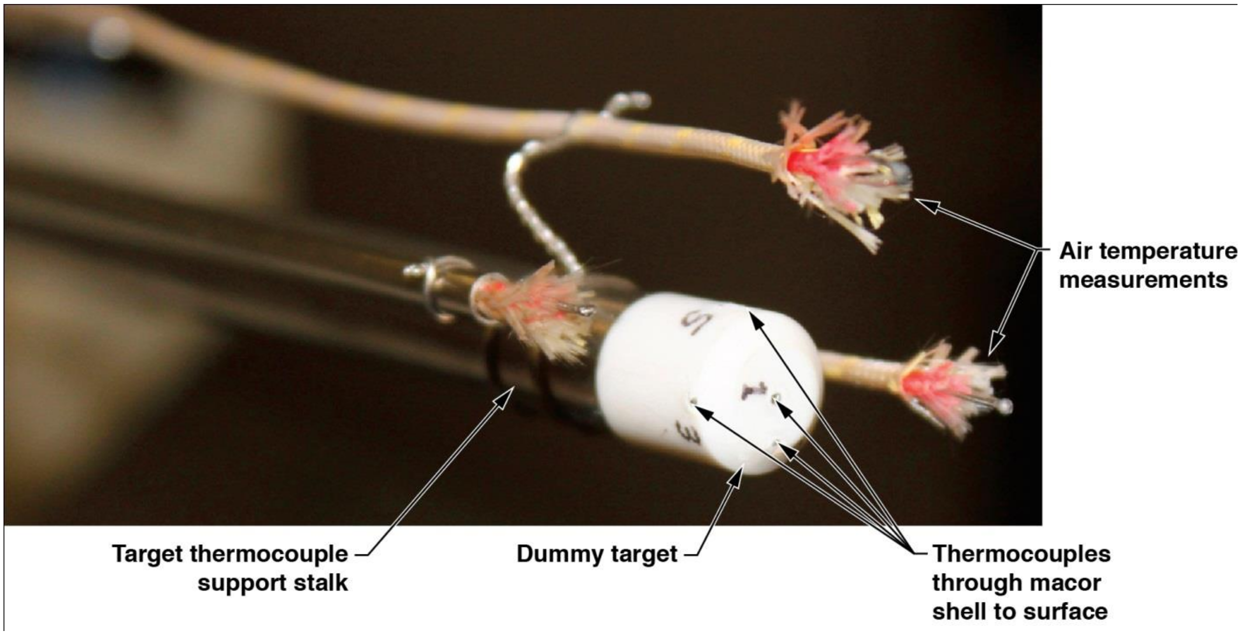
Air temperature measurements
5
1
3
Target thermocouple support stalk
Dummy target
Thermocouples through macor shell to surface

Figure 2-4. Close-up of dummy target for heat transfer coefficient measurements

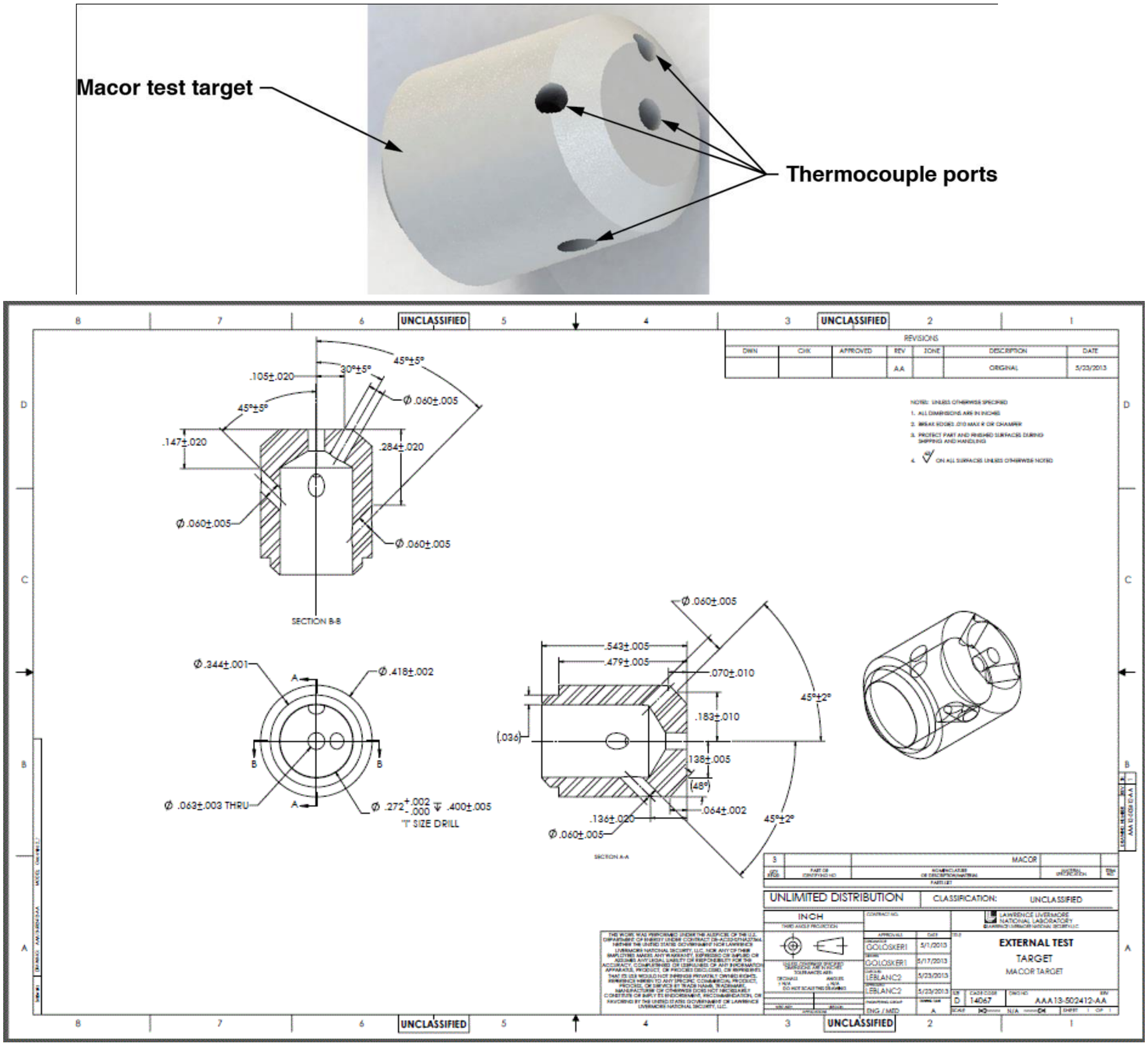
Macor test target
Thermocouple ports
UNCLASSIFIED
REVISIONS
DWN
CHK
APPROVED
REV
ZONE
DESCRIPTION
DATE
AA
ORIGINAL
5/23/2013
NOTES: UNLESS OTHERWISE SPECIFIED
1. ALL DIMENSIONS ARE IN INCHES
2. BREAK EDGES .010 MAX R OR CHAMFER
3. PROTECT PART AND FINISHED SURFACES DURING SHIPPING AND HANDLING
4. ON ALL SURFACES UNLESS OTHERWISE NOTED
.105±.020
30°±5°
45°±5°
45°±5°
Ø .060±.005
.147±.020
.284±.020
Ø .060±.005
Ø .060±.005
SECTION B-B
Ø .344±.001
Ø .418±.002
A
B
B
A
Ø .063±.003 THRU
Ø .272 +.002 -.000 ↧ .400±.005
"I" SIZE DRILL
Ø .060±.005
.543±.005
.479±.005
.070±.010
45°±2°
.183±.010
(.036)
.138±.005
(48°)
.064±.002
.136±.020
45°±2°
Ø .060±.005
SECTION A-A
3
MACOR
PARTS LIST
UNLIMITED DISTRIBUTION
CLASSIFICATION: UNCLASSIFIED
INCH
THIRD ANGLE PROJECTION
LAWRENCE LIVERMORE NATIONAL LABORATORY
APPROVAL
DATE
GOLOSKER1
5/1/2013
GOLOSKER1
5/17/2013
LEBLANC2
5/23/2013
LEBLANC2
5/23/2013
ENG / MED
A
EXTERNAL TEST
TARGET
MACOR TARGET
D
14067
AAA13-502412-AA
N/A
SHEET 1 OF 1
UNCLASSIFIED

Figure 2-5. Test target model and drawing

2.2 Analytical model results

Analytical models were used to predict the heat transfer coefficient in both the fusion chamber and in the test used to validate the models. For the Reynolds and Mach numbers of interest here there are five published heat transfer correlations of greatest interest. These are Belov and Terpigor'ev [2-1] (for the stagnation zone), Sogin [2-2] (for the rear face of the target), Hadad and Jafarpur [2-3] (an average over the body), Kang and Sparrow [2-4] (for the cylindrical outer face) and Na and Pop [2-5] (for the cylindrical face again but here varying along the face). These correlations have compared well to our CFD work concerning the target flight under the planned use conditions, as shown in Figure 2-5 below.

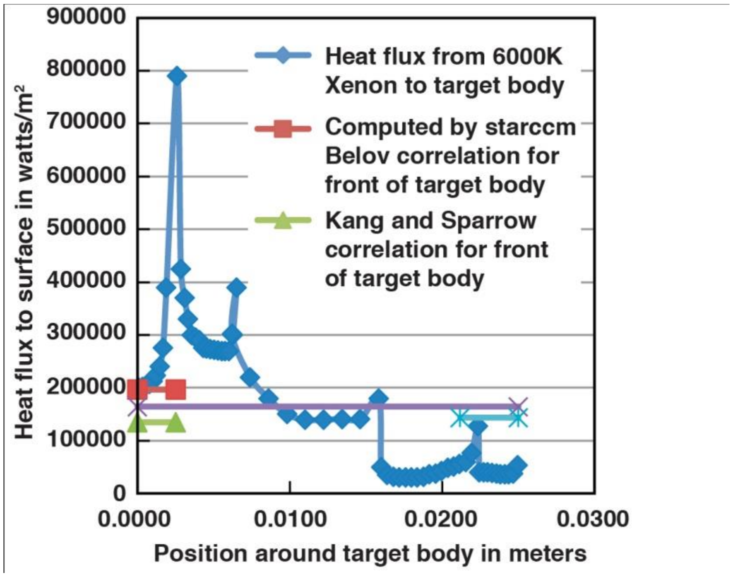

Figure 2-6. Comparison of CFD and correlations for target flight under planned use (fusion chamber) conditions

The fluid flow field around the target for a heat flux similar to that given in Figure 2-6 is shown below in Figure 2-7.

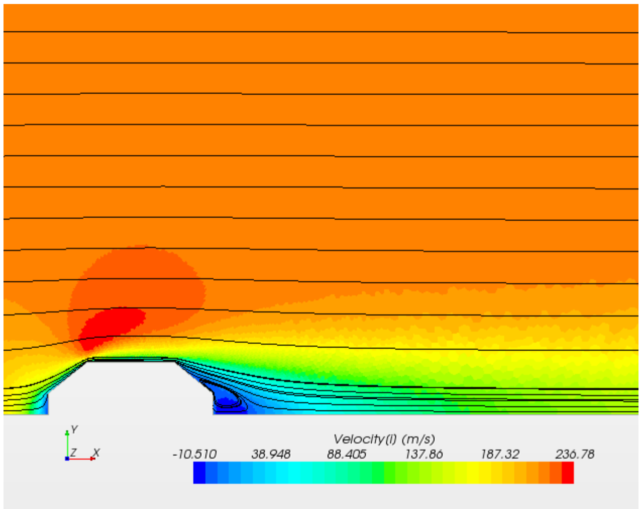

Figure 2-7. Streamlines and contours of velocity for flow around the target under expected use (fusion chamber) conditions

Simulations of flow around the test body at expected test conditions (Figure 2-8) correlate well to that shown for target under use (fusion chamber) conditions (Figure 2-7).

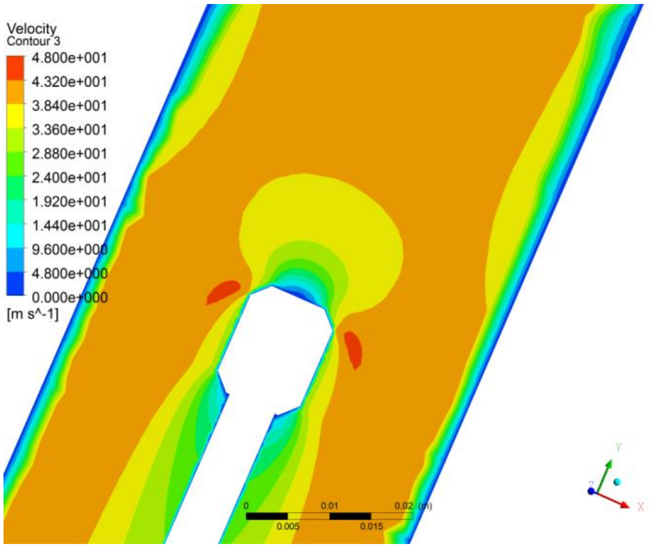

Figure 2-8. Contours of velocity for flow around the test body for expected test conditions

Both figures show the acceleration in flow around the front corners of the body where we expect high heat transfer coefficients. The frontal stagnation zones are similar between the test and planned use and the front portions of the flow fields outside the cylindrical body portion of the target are well matched. The necessity to remove instrumentation wires out the back end of the dummy target assembly made the rear of the flow field different in the test case than in the case of flight through the fusion chamber.

Of particular interest to data reduction is the transient response of the target shell for use (fusion chamber) and test. Figures 2-9 and 2-10 below show thermal profiles in the fusion target shell and test body shell after 15 seconds of exposure to convective heating as expected in test. Though the planned target exposure in the fusion chamber is only on the order of 0.080 sec, it is interesting to see both the fusion target and the test target have small thermal gradients through the hohlraum wall for the planned test exposure. The small gradients in the test body shell (macor rather than lead) mean that data reduction assuming negligible thermal gradients locally in the macor shell may be adequate.

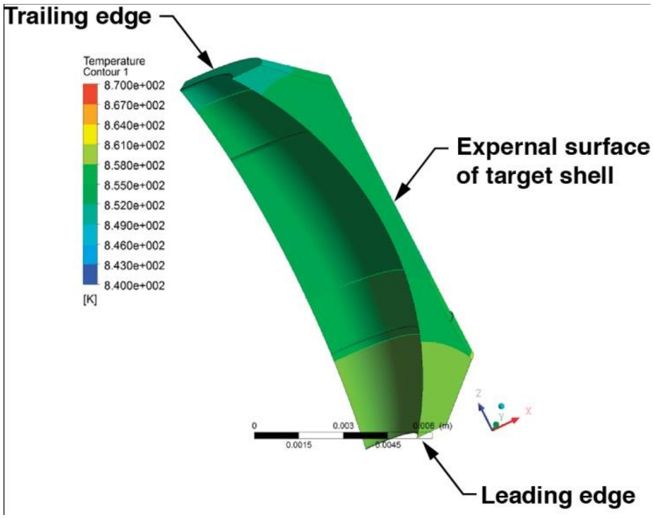
Trailing edge
Temperature
Contour 1
8.700e+002
8.670e+002
8.640e+002
8.610e+002
8.580e+002
8.550e+002
8.520e+002
8.490e+002
8.460e+002
8.430e+002
8.400e+002
[K]
Expernal surface
of target shell
Z
Y
X
0
0.003
0.006 (m)
0.0015
0.0045
Leading edge

Figure 2-9. Thermal gradients in a target shell exposed to 15 Seconds of test body heating by convection

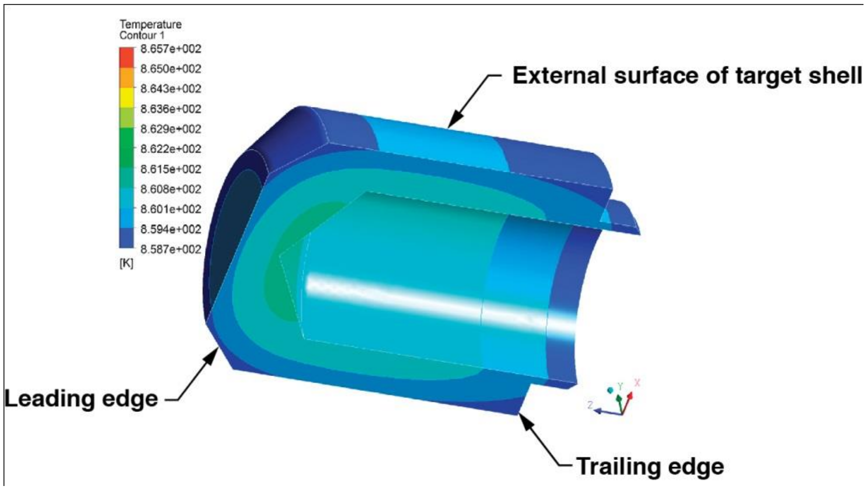
Temperature
Contour 1
8.657e+002
8.650e+002
8.643e+002
8.636e+002
8.629e+002
8.622e+002
8.615e+002
8.608e+002
8.601e+002
8.594e+002
8.587e+002
[K]
External surface of target shell
Leading edge
Y
X
Z
Trailing edge

Figure 2-10. Thermal gradients in a test body shell exposed to 15 seconds of test body heating by convection

Analysis of the tests begins with a transient heat transfer equation:

$$\rho_{bd} C_{bd} V_{bd} \frac{dT_{bd}}{dt} = h(T_\infty - T_{bd})A_{bd} - k_c(T_{bd} - T_m)A_c/\Delta x \qquad \text{(Equation 2-1)}$$

Here bd can denote the target body (the macor shell in the test apparatus) or merely the thermocouple bead. The variables are: ρ Is density , C is thermal capacity, V is the body volume, h is the heat transfer coefficient, T is the temperature, t is time, A is the area over with the heat flux is applied and x is the thickness. The subscripts are h for the mid air stream, c for the target and m for the target interior.

The conduction term on the right can represent the conductive heat loss from the thermocouple wires leaving the sensing bead or it can represent the thermal losses from the macor shell to its internal void volume. The transient simulation shown above in Figure 2-10 was done in two ways, first with the internal surfaces of the macor shell were set to an adiabatic boundary condition and second with a modest free convection loss coefficient of 10 w/m^{2}K applied to the inside surface. The transient responses of the volume average of temperature for the macor shell for the two cases are shown in Figures 2-11 and 2-12 below. The similarity in the two figures confirms that for the conditions and time scales of interest to the tests, convective losses to the test shell interior can be neglected.

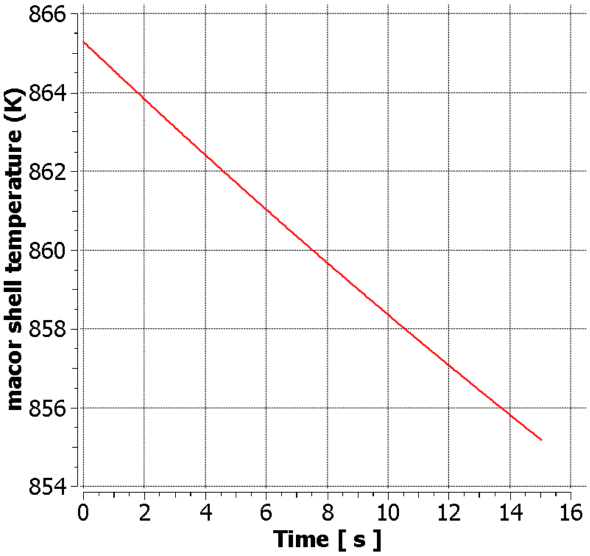

Figure 2-11. Thermal transient of test shell for adiabatic shell interior

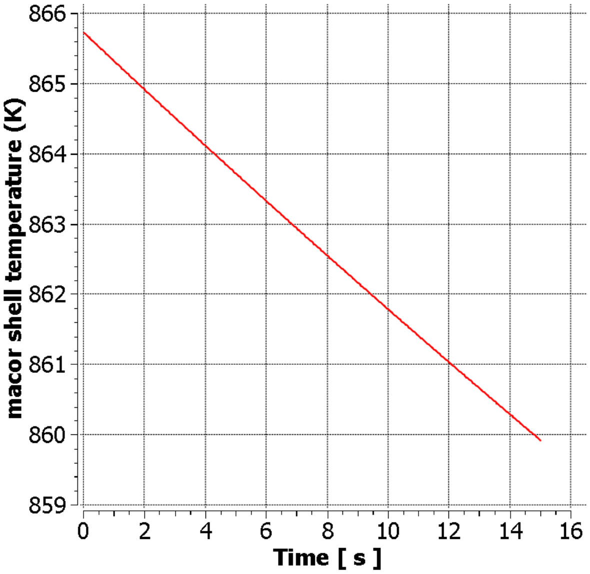

Figure 2-12. Thermal transient of test shell with modest heat loss to shell

Examining thermal gradient effects at a thermocouple bead embedded in a macor shell is useful. Figure 2-13 shows thermal gradients in a bead bonded to macor subjected to transient test conditions. The higher thermal conductivity of the bead coupled with its size (about half the macor shell thickness) makes it something of a thermal short towards the interior of the macor shell.

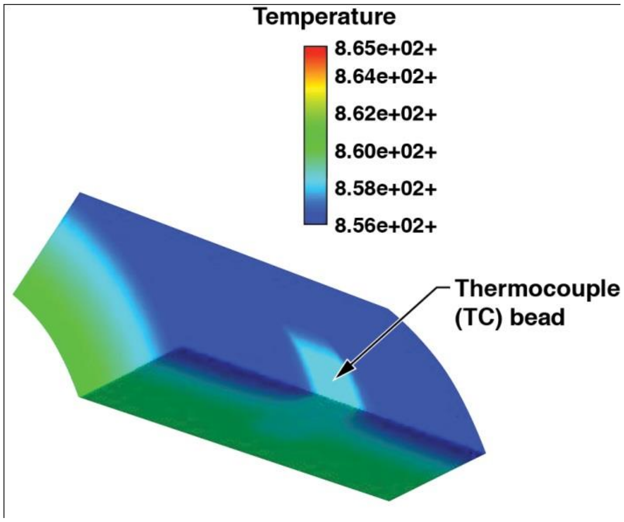

Figure 2-13. Thermal profile (at time= 8 seconds) of a chromel-alumel thermocouple bead embedded in a cylindrical macor shell subjected to test conditions

The TC bead (blue square on surface of Figure 2-13) is measuring an average of the macor temperature profile. Transient thermal effects in the test are better understood by comparing the thermal response of several items from this simulation. Figure 2-14 shows a simulated macor and TC bead local and average temperatures of interest of the key first 8 seconds of the tests.

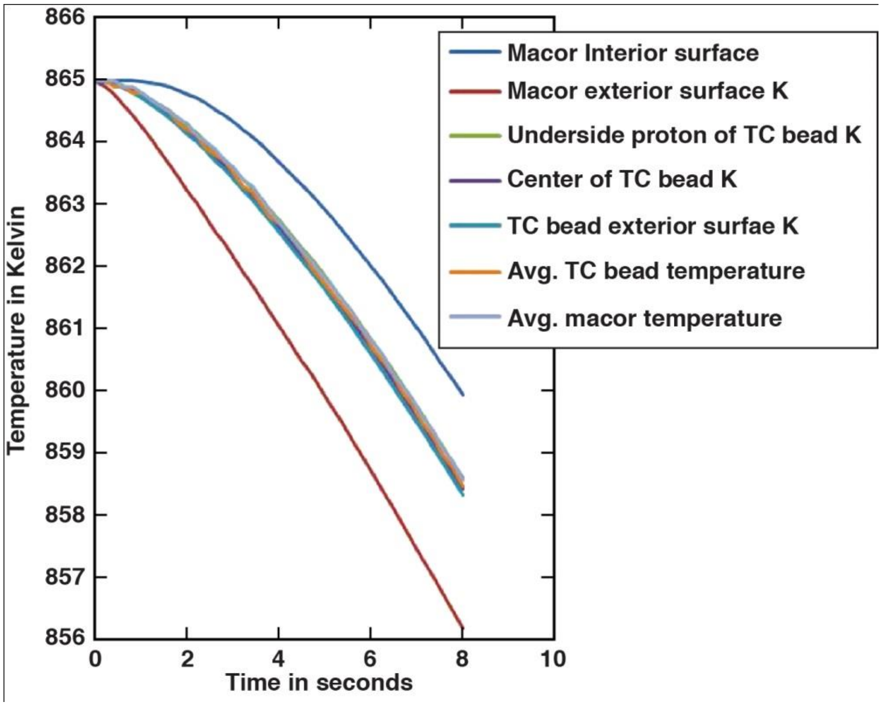

Figure 2-14. Modeled transient temperatures for macor and thermocouple bead subjected to test

The thermocouple is not measuring the macor surface temperature or its interior temperature. Temperature gradients within the metal TC bead are small and the average bead temperature follows the local average macor temperature quite well (bead response varies with location on the macor shell in the test data). Thus test data will be analyzed with the transient heat transfer equation given above, while neglecting the heat loss term to the interior and defining bd as the thermocouple bead.

The Belov and Terpigor'ev correlation, simplified for use here takes the form:

$$Nu = \frac{hD}{k} = CRe^{n(Re)}Pr^{n(Pr)} \qquad \text{(Equation 2-2)}$$

The symbols are: Nu is the Nusselt number, h is the heat transfer coefficient, k is the thermal conductivity of the gas, D is the object diameter, C and n are constants, Re is the Reynold's number, Pr is the Prandlt number. The other cited works have mostly similar forms of this equation with differing values for the exponents. When we apply this correlation to both planned target use in the fusion chamber and our test conditions described above we get moderately different results for the convective heat transfer coefficient, h. Test and use heat transfer coefficients and other conditions for the stagnation point are compared in Table 2-1 below. So while the test conditions differ from the planned use fusion conditions, the measured heat transfer coefficients are comparable.

Table 2-1. Comparison of conditions at the stagnation point

	Planned use	Test	Item
	stag. Pt.	stag. Pt.	units
Surface Temperature	20	800	K
Gas Temperature	6000	800	K
Gas pressure	3040	4400	Pa
Gas molec weight	131	29	kg/kmol
Prandtl	0.8	0.76	-
Reynolds	280	270	-
Nu	12	9	-
h	31	40	w/(m2K)
mach	0.31	0.044	-

The heat transfer coefficient can be calculated using the constants found in the other cited works as shown in Table 2-2 below, where the fluid properties have been evaluated at the “film” values, the average of the surface and free stream temperatures similar to Table 2-1. The range of possible heat transfer coefficients is shown in the far right-hand column. Thus, for test conditions we expect heat transfer coefficients to vary from 25 to 40 w/m^{2}K.

Table 2-2. Comparison of correlations for test conditions

	C	n(Re)	n(Pr)	NuFilm	h
Belov	0.76	0.50	0.40	9.04	39.54
Sogin	0.20	0.67	0.00	6.37	27.88
Hadad	0.81	0.50	0.33	18.36	34.73
Kang and Sparrow	0.20	0.67	0.33	5.79	25.34

Testing results deemed to be valid were the second and third of the three tests conducted on September 30, 2013. These tests were conducted under slightly differing but largely similar conditions. Figures 2-15 through 2-20 below show the measured heat transfer coefficient results derived from the thermocouple data at three positions on the target; the stagnation point, front corner and mid-point on the side plotted as a function of time for the two tests.

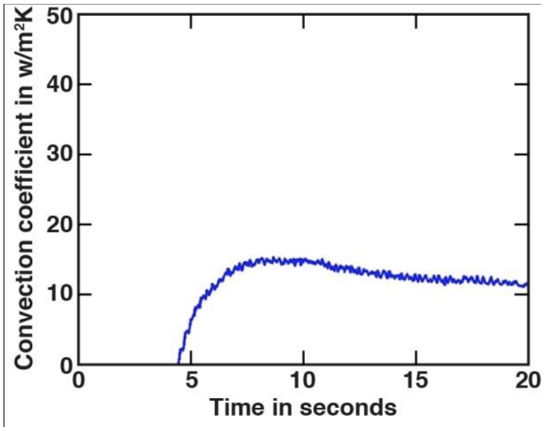

Figure 2-15. Measured convection coefficient at the stagnation point for the second test of Sept. 30, 2013

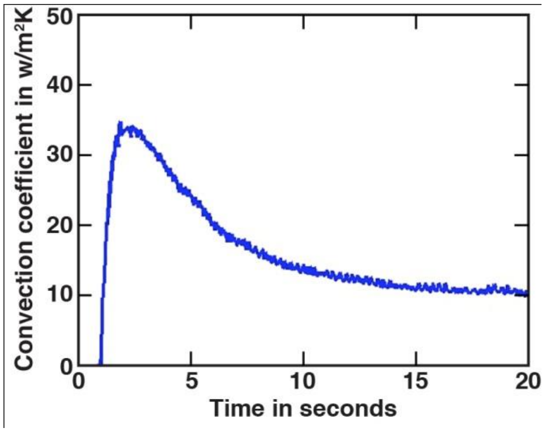

Figure 2-16. Measured convection coefficient at the front corner for the second test of Sept. 30, 2013

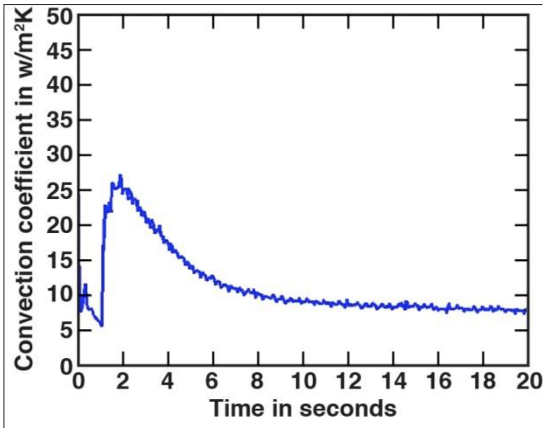

Figure 2-17. Measured convection coefficient at the target side for the second test of Sept. 30, 2013

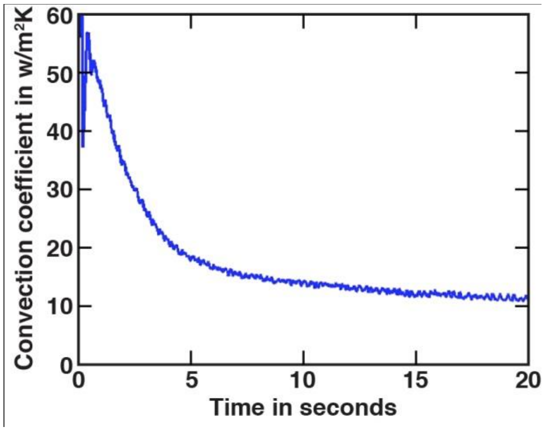

Figure 2-18. Measured convection coefficient at the stagnation point for the third test of Sept. 30, 2013

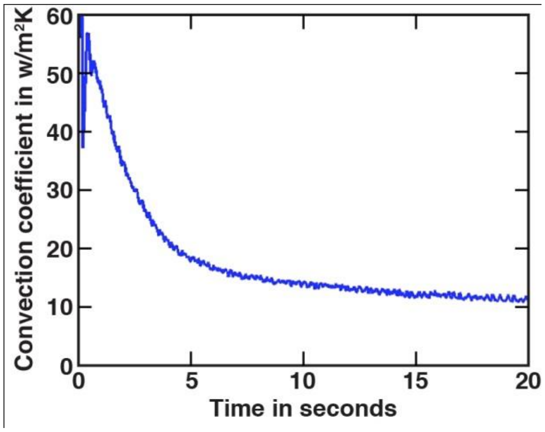

Figure 2-19. Measured convection coefficient at the front corner for the third test of Sept. 30, 2013

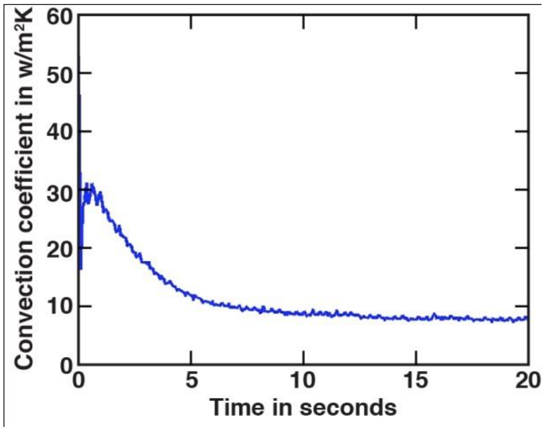

Figure 2-20. Measured convection coefficient at the target side for the third test of Sept. 30, 2013

For the plots of the second test, the first few data points plotted are actually pre-test data. Further, for all the plots the first few data points show very high scatter and should be considered unreliable. However the majority of the data over the first couple testing seconds is very good data and the results are consistent with both CFD modeling and the correlations described above. We expect that after two to four seconds of testing local conductive effects to TC bead wires and the target shell support structure are becoming more significant relative to the thermal inertia effects quantified in the transient heat transfer equation given above. For both the second and third tests the dependence of the test results on thermocouple location is mostly as anticipated from the CFD (as shown in Figure 2-1). There is a high convection coefficient at the stagnation point. A significantly higher convection coefficient is observed at the corner point, here somewhat moderated from that shown in Figure 2-1 by the presence of local conductive effects. Lastly a lower convection coefficient is observed down the cylindrical side of the target, again as shown in Figure 2-1.

2.3 Conclusions

The magnitude of these heat transfer coefficients is largely consistent between the analysis and the test. The test results shown here validate the target flow and external heat transfer modeling performed in support of LIFE target design. Further work can be conducted to measure the heat transfer coefficient for target designs incorporating a recessed front end which can be used to reduce the heat transfer coefficient to the LEH window and/or the reduced thermal effects of a using a sacrificial layer on the LEH window. Both options are discussed in Reference 1-6.

2.4 References

[2-1] Belov, I.A. and Terpigor'ev, V.S., Inzhenerno-Fizicheskii Zhurnal, **17.6**, 1106-109 (1969).
[2-2] Sogin, H. H. "A Summary of Experiments on Local Heat Transfer from the Rear of Bluff Obstacles to a Low Speed Airstream." *Transactions of the ASME: Journal of Heat Transfer* 86 (1964): 200-202.
[2-3] Hadad, Yaser, Khosrow Jafarpur. (2008, August). "Laminar Forced Convection Heat Transfer from Isothermal Bodies with Unit Aspect Ratio." Paper presented at the 6th IASME/WSEAS International Conference on Heat Transfer, Thermal Engineering, and Environment, Rhodes, Greece.
[2-4] Kang, S. S., E. M. Sparrow. "Heat Transfer from an Open- or Closed- Bore Cylinder Situated Longitudinal to a Freestream." *Transactions of the ASME: Journal of Heat Transfer* 109 (1987): 314-320.

[2-5] Na, T.Y, and Pop, I, "Flow and heat transfer over a longitudinal circular cylinder moving in parallel or reversely to a free stream," Acta Mechanica 118 (1996): 185-195.

3.0 Internal heat transfer studies

The targets are shot downward into the fusion chamber in the LIFE design. The leading LEH window is subjected to the highest heat flux due to the convective heat transfer from the chamber gases. The hot LEH window generates convective currents in the helium gas internal to the target. The objective of the internal heat transfer test was to investigate the convection currents induced by the heated leading LEH window and to note the temperature and pressure increases in the two helium chambers aft of the LEH window resulting from these currents. The configuration for the experiment is shown in Figure 2-1. A half-target was used for ease of measurement and because the leading half of the target becomes considerably hotter in the fusion chamber than the aft half and thus it is more important to study the leading half of the target. The test LEH window consisted of a rapid heater that could reach about 250-450K (starting temperature 77K) in 50-120 ms emulating the target flight LEH window which is expected to reach 1300 K in about 24 ms. The test "hohlraum" was a stainless steel block that emulated the thermal mass of the lead hohlraum. The IR window consisted of a 1 um thick polyimide membrane which supported a 5mm OD by 0.2 mm thick test "P2 shield", similar to the nominal design. The "capsule" position was replaced by a very low thermal mass, fast response time temperature sensor such that the few degree expected temperature rise could be measured. The helium density was about 1 mg/cc, about 1 atm pressure at 77K, similar to densities in the fusion targets at 18K. Tests were conducted with both a sealed IR shield and with some by-pass flow around the IR shield.

3.1 Test set-up

The experiment was designed to provide experimental data (pressure and temperature) for validating a simulation of a cryogenically-cooled LIFE hohlraum subjected to a brief (~24 ms) high thermal load on the thin LEH membrane at one end of the target. As shown in Figure 3-1, the internal geometry of the apparatus approximated the leading bottom half of a LIFE target. The stainless steel housing was comp0rised of two pieces, creating an upper and lower chamber. Pressure sensors were mounted into each chamber. The chambers were separated by a 1-micron-thick polyimide membrane. The membrane was supported by and glued to two 0.125-mm-thick sheets of polyimide. A lead disc was attached to the center of the polyimide membrane. This membrane mimicked the IR shield with attached lead P2 shield in a fusion target. The lead disc was instrumented with two thermocouples. Silicon wafers with silicon-nitride membranes with dual thin-film-platinum serpentine traces patterned on the membranes were located on the top and bottom of the housing. One of the traces on the bottom membranes was used as a heater to mimic a fusion target LEH window heated by the hot gases of a fusion chamber; the other trace was used to measure the temperature. The traces on a second membrane became a sensor used to measure the temperature at the position where a capsule in a fusion target would be mounted. The desired test environment was a helium atmosphere at 77K and atmospheric pressure to mimic the effect of the convection currents in a helium filled target. A mechanism with indium seals was used seal the top and bottom chambers once the test conditions of the internal helium atmosphere were achieved.

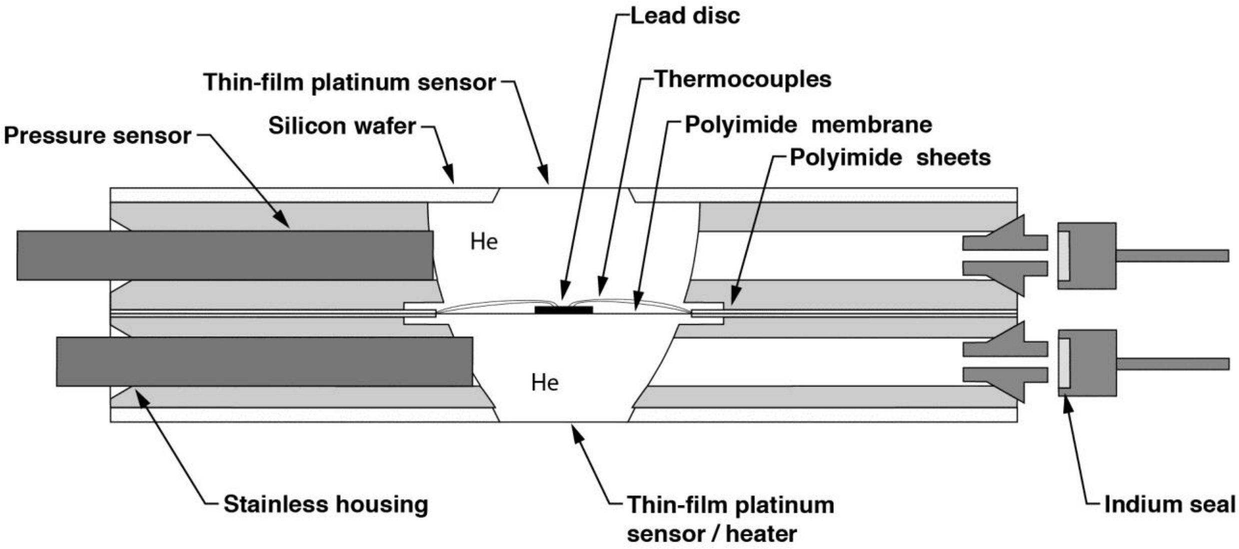
Lead disc
Thin-film platinum sensor
Thermocouples
Silicon wafer
Polyimide membrane
Pressure sensor
Polyimide sheets
He
He
Stainless housing
Thin-film platinum sensor / heater
Indium seal

Figure 3-1. Cross-sectional schematic view of the experiment.

3.2 Fabrication of the apparatus

Hohlraum pieces

The stainless hohlraum pieces (AAA13-501013-AA and AAA13-501013-AA) were fabricated at LLNL. Following the machining, the outer surfaces (sides without the counterbore) were lapped flat and smooth so that a seal could be achieved against the silicon wafers without adhesive.

Chamber seals

The indium seal design was developed via trial and error; the final shapes are as shown in Figure 3-1 above. The stainless inserts were bonded to the housing using Hardman double bubble epoxy. A fixture was used to ensure that both inserts protruded the same distance from the housing. The indium seats were punched from 0.25mm-thick sheet and pressed into the stainless holders. The indium seats were replaced each time the apparatus was brought up to atmosphere after each use.

Seal mechanism

A manually operated, rotary to linear motion mechanism was designed to close the seals once the apparatus had achieved the desired environment, 1 atmosphere of helium at 77K (Figure 3-2). Rotation of the cam causes the indium seals to be pressed into the mating pieces on the stainless housing.

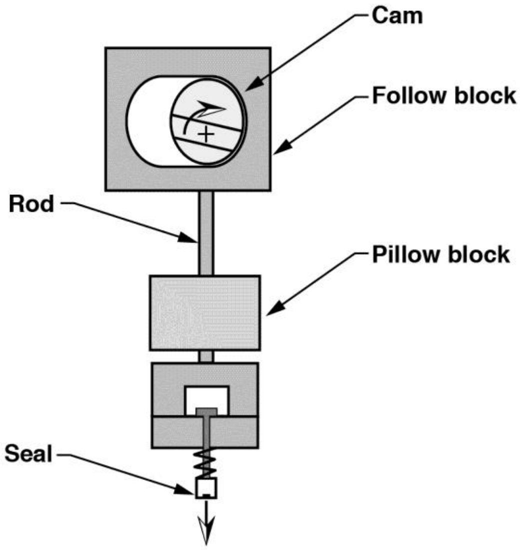

Figure 3-2. Seal Mechanism. Rotation of the cam about its off-center axis causes the follow block and rod to move downward as shown.

Membrane assembly

The membrane assembly consists of a thin polyimide membrane supported by thicker sheets of polyimide on both sides. A 5-mm-dia. lead disc instrumented with two thermocouples was bonded in the center.

The lead discs were instrumented at LLNL. A sharp knife was used to lift up “flaps” of material from the surface. Two 12.7-um-dia, type E (chromel – constantan), pre-beaded bare wire thermocouples were inserted into the flaps and the flaps pressed down to hold the beads in place.

The outer sheets of the membrane assembly were laser cut from 0.125-mm-thick Kapton HN at LLNL. Two types were fabricated – one having three slots around the center hole (bypass configuration) and one without (solid configuration). The bypass configuration in shown in Figure 3-3. The Kapton was prepared for adhesive bonding by lightly abrading the surfaces with 12 micron alumina film. The prepared frames were cleaned and sent to Luxel[*] who fabricated and bonded the 1-micron-thick, Upilex-type polyimide to one side using epoxy. Luxel also bonded the lead disc / thermocouple assembly to the center of the membrane. At LLNL, the second sheet of Kapton was bonded to the 1-micron-thick membrane using Epon 828 / Versamid 125 epoxy, sandwiching the thermocouple wires between the two Kapton layers.

---

[*] Luxel Corporation, Friday Harbor, WA

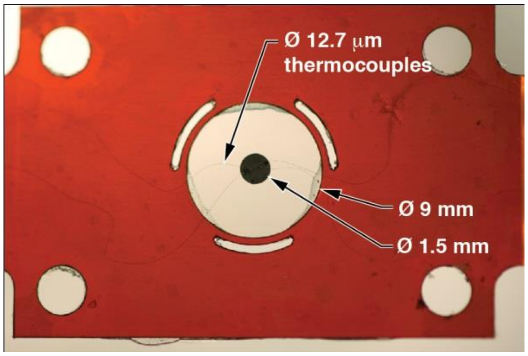

Figure 3-3. Bypass membrane assembly. The lead disc is glued to the 1-micron-thick polyimide membrane. Thermocouple wires are bonded between the sheets of Kapton.

The small-diameter thermocouple wires were spot-welded to thermocouple alloy tabs (Figure 3-6). Larger diameter (127 um) thermocouple wire was welded to the tabs and routed to through the patch panel on the underside of the apparatus to the type E thermocouple feed-throughs (Figure 3-5).

Because the assembled membrane assemblies were not sufficiently flat to achieve a good seal to the hohlraum pieces, rings of thin, rubber double-stick adhesive were used to form the seal.

Platinum sensor/heater

The platinum sensor/heater consisted of a set of two thin film platinum strips that are each 100 μm wide and 200 nm thick, and arranged in a serpentine pattern (Fig. 3-4). Each end of the platinum serpentine strips was connected to a large pad, and electrical wiring can be soldered onto the pads to make connection with the sensor/heater. Each platinum serpentine strip had an electrical resistance of around 220 Ω at room temperature.

The thin-film sensor/heaters were fabricated on 500 nm of silicon nitride thin film on 0.5mm-thick silicon wafers by photolithography. A KOH etch process was used to open a hole through the silicon underneath the sensor/heater, such that the sensor/heater were suspended on a 5 mm x 5 mm silicon nitride membrane.

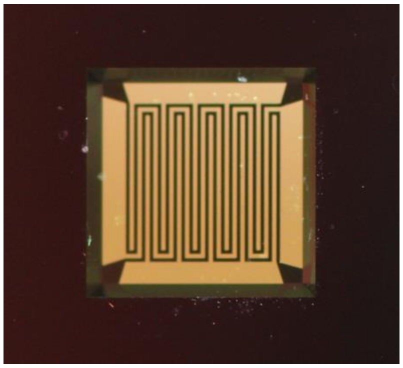

Figure 3-4. Photograph of a thin film platinum sensor / heater as would be viewed from inside the hohlraum.

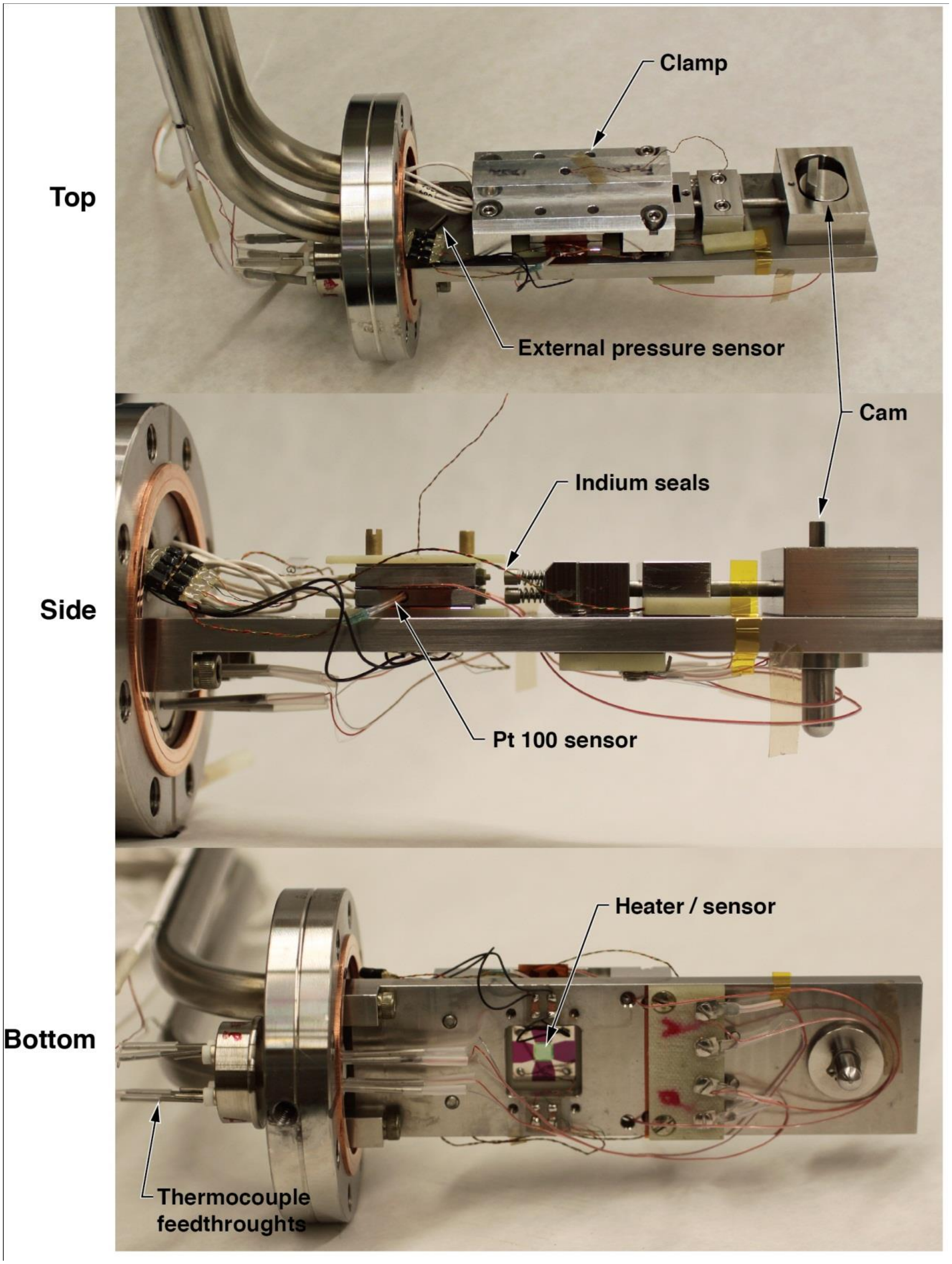
Top
Clamp
External pressure sensor
Cam
Side
Indium seals
Pt 100 sensor
Bottom
Heater / sensor
Thermocouple feedthroughts

Figure 3-5. Three views of the assembled apparatus.

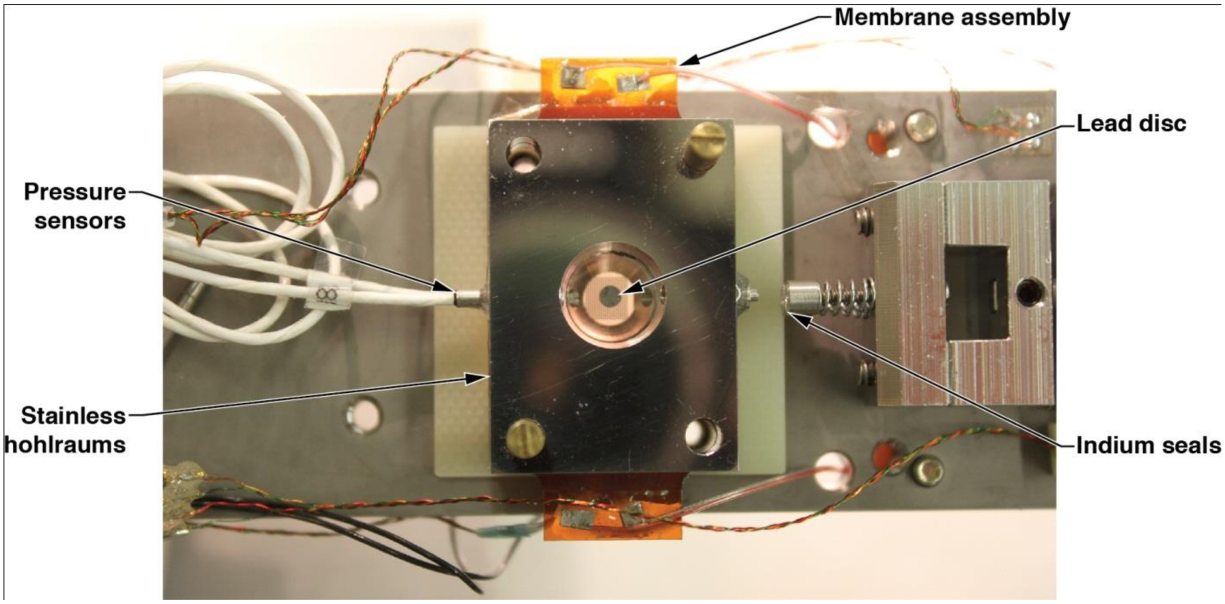
Membrane assembly
Lead disc
Pressure sensors
Stainless hohlraums
Indium seals

Figure 3-6. The assembled apparatus with the clamp and top silicon piece removed.

Housing

The experiment was mounted inside a sealed can submerged in a dewar of LN. As shown in Figure 3-7, the instrumentation feed-throughs and cam actuator were mounted in tubes long enough to keep the seals close to room temperature.

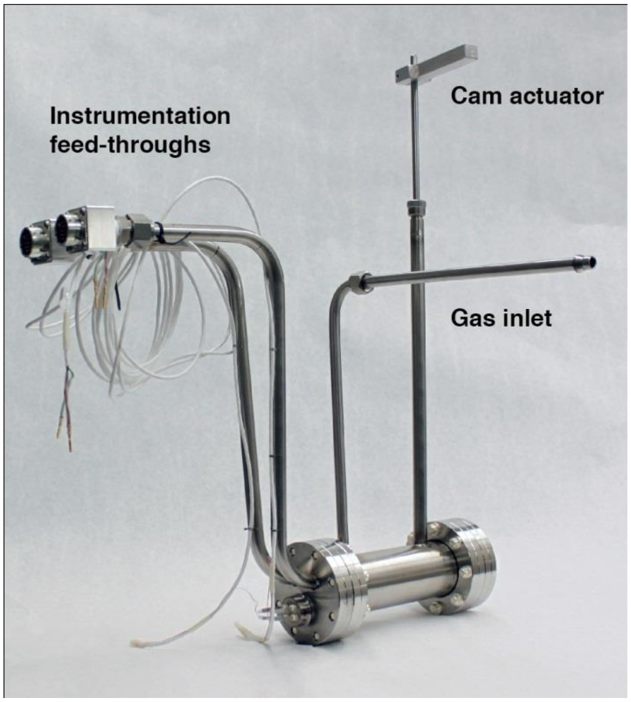
Instrumentation feed-throughs
Cam actuator
Gas inlet

Figure 3-7. Outer housing. The experiment is contained in a can so that it can be submerged in a dewar of LN. The feed-throughs are on tubes that extend outside of the dewar.

3.3 Sensors and instrumentation

Pressure Sensors

The experiment was instrumented with three Kulite pressure sensors. Two were mounted in the stainless hohlraum chambers as shown in Figures 3-1 and 3-5 using Hardman epoxy. A third sensor was installed in the area immediately outside the hohlraum (Figure 3-5). The pressure sensor specifications and instrumentation settings are shown in Table 3-1. Micromeasurements 2210 signal conditioners with an excitation of 10V were used. Because the zero balance of the sensors was not particularly precise, the bridge output was balanced at ambient atmosphere and measurements were made relative to ambient instead of absolute pressure. The sensors also exhibited a significant zero shift with temperature. The zero shift was subtracted once the system reached steady state at 77K.

Table 3-1. Kulite Pressure Sensor Data

Sensor location	Top hohlraum (away from heater)	Bottom hohlraum (near heater)	Inside can
Sensor model	CCQ-062-7BARA	CCQ-062-7BARA	CCQ-062-1.7BARA
Range (Bar)	7	7	1.7
S/N	384	383	540
Excitation used	10.002 V	10.040V	10.040V
Sensitivity	14.214 mV/BARA	14.237 mV/BARA	54.841 mV/BARA
Zero offset (typ.)	± 352 mB	± 351 mB	± 91 mB
Atmospheric pressure (as-measured, unbal-anced output)	880mB	924 mB	995 mB
Thermal zero shift (typ.) RT to 77K	± 280 mB	± 280 mB	± 68mB
Nat. Freq. (typ.)	380 kHz	380 kHz	240 kHz
Amplifier gain used	100	100	100
Nicolet scale used	704.6 mB/V	700.7 mB/V	184.9 mB/V

Lakeshore temperature sensors

Two Lakeshore[†] sensors were used ; a wire-wound platinum (PT-111-2S) sensor placed into a recess in the lower stainless hohlraum, and a Cernox bare chip sensor (CX-1070-BC-HT-4L) mounted on a G-10 rod. The Cernox sensor was originally intended to be placed inside the hohlraum to calibrate the thermocouples in-situ. When the seals were re-designed with indium seats there was not room to install it. Instead, it remained inside the can but outside the hohlraum. The temperature data collected during the gradual warm-up of the experiment showed that the PT-111 sensor was a closer match to the thermocouples and thin film Pt sensors. Therefore the PT111 sensor was used to derive the calibration scaling for both the thermocouples and thin film Pt sensors.

[†] Lakehore Cryotronics, Westerville, OH

The PT-111-2S was ordered with 3-point SoftCal data. The output of both sensors was monitored with a Lakeshore 218 temperature monitor.

Thin-film platinum sensor/heaters

The thin film Pt sensors were connected with four leads: two for the constant current source, and two for the voltage measurement. A constant current excitation of 100 uA was provided by Lakeshore 120 current sources. The output voltages were amplified by 100 using Stanford Research Systems SR560 low-noise amplifiers.

The sensors were calibrated by comparing the output to the Pt-111 sensor output during the gradual warm-up of the apparatus. The response of the upper sensor, which was not exposed to temperatures above 300K, remained repeatable throughout our series of experiments (Figure 3-8). The lower sensor showed a permanent change in resistance following exposure to elevated temperature. In order to ensure that an accurate calibration was available for every test, a warm-up experiment was performed following experiments in which a resistance change was noted.

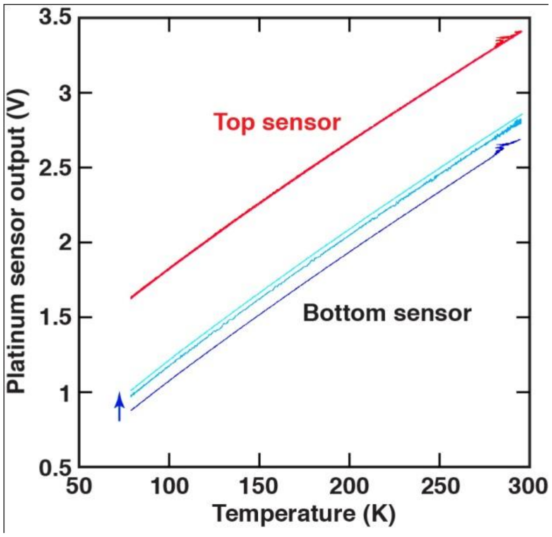

Figure 3- 8. Thin-film platinum sensor output as a function of temperature, measured after several series of experiments. The bottom sensor was exposed to elevated temperature during the experiments, causing an increase in resistance and an upward shift in the calibration curve.

Because calibration data was not available for temperatures exceeding room temperature, the linear portion of the calibration curve (above 175K) was extrapolated (Figure 3-9). A third degree polynomial accurately represents the measured data from 77 to 300K.

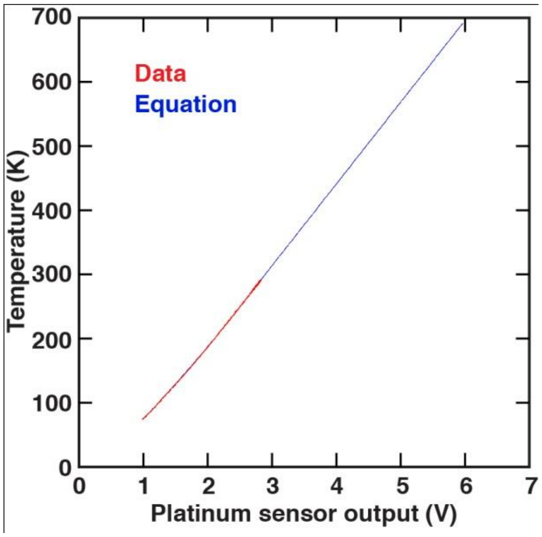

Figure 3-9. A third degree polynomial fit was used to calculate temperature from the platinum sensor output over the range of 77K to 300K. Temperatures above 300K were estimated by extrapolating a linear fit to the data above 175K.

Thermocouples

The thermocouple cold junction was formed where thermocouple wire welded to the outside thermocouple feed-throughs was connected to the copper cable. This junction was submerged in the LN during the tests. The output voltages were amplified by a gain of 200 using SRS560 amplifiers.

The thermocouple output voltage was calibrated against the PT111 sensor temperature during warm-up of the apparatus. Since the measured temperature excursions of the thermocouples were small (less than 10K), a linear fit was used (Figure 3-10). The fit as calculated is within 4% of the NIST table values.

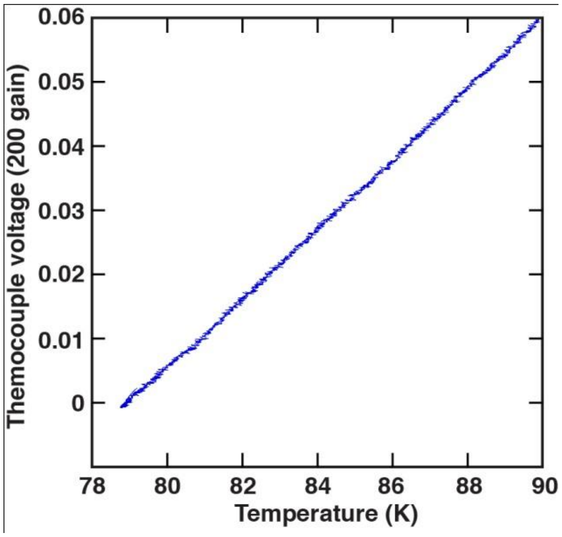

Figure 3-10. Thermocouple output vs. temperature. A linear fit was used over the range of 78-90K.

3*.4 Experimental Procedure*

The apparatus was assembled and lowered into the dewar with the internal seals in the “open” position. The manifold connecting the vacuum pump and helium source was connected. The pressure sensors were then zero balanced at ambient pressure. The helium regulator was set to apply pressure just slightly above atmosphere. The system was then evacuated and back-filled with helium several times. After the final fill the helium valve was left open to add additional gas as needed as the system was cooled.

Liquid nitrogen was poured into the dewar until the can of the apparatus was completely submerged. A foam lid was used to retard the loss of liquid nitorgen. The temperature inside the can was monitored to indicate when the apparatus had fully cooled. The external lever was then used to seal the hohlraum chambers in preparation for testing. A photograph of the cooled apparatus is shown in Figure 3-11.

Tests were conducted by applying a 60 – 250 ms voltage pulse to the heater and recording the output of the pressure and temperature sensors. The voltage pulses were generated using an HP 33120A function generator. A Trek 2100HF Piezo Driver was used to increase the current in order to drive the heater. A summary of the tests conducted is shown in Table 3-2.

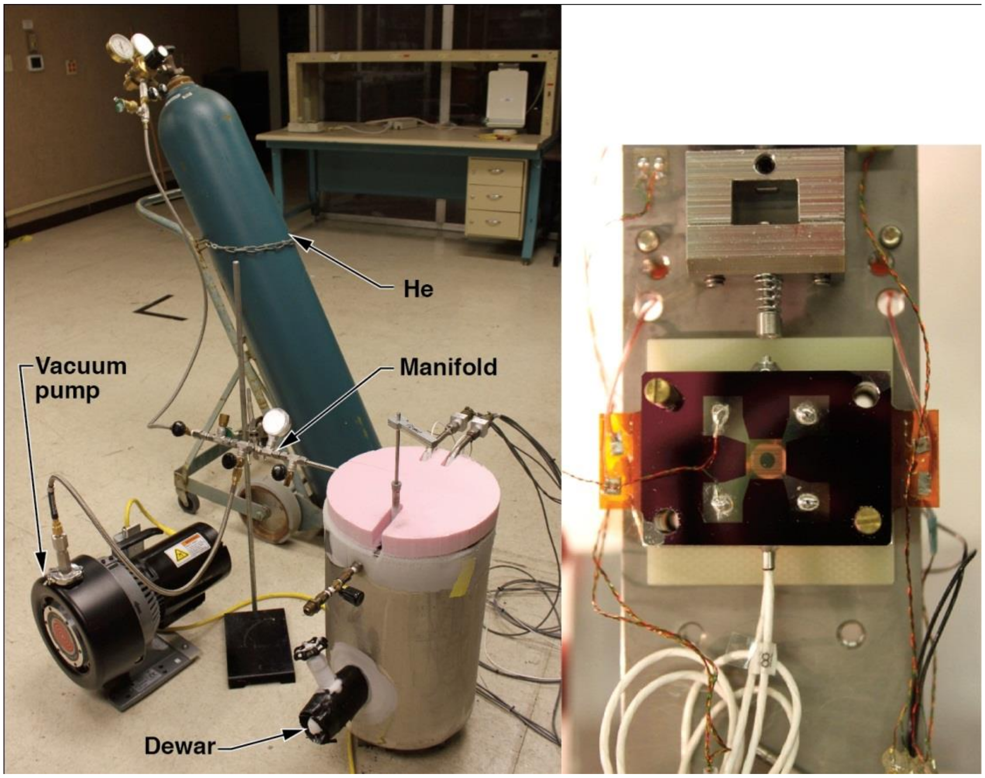
He
Vacuum pump
Manifold
Dewar

Figure 3-11. Apparatus is installed in the dewar and ready for test.

3.5 Analysis and results

The analytical model for the internal heat transfer test with helium gas "bypass" is shown in Figure 3-12 below. Models with "bypass" mean that flow of the internal helium gas was permitted between the target helium compartments. Key parts of this half symmetry model are the steel shells which contain the helium gas, the central assembly membrane and the P2 shield.

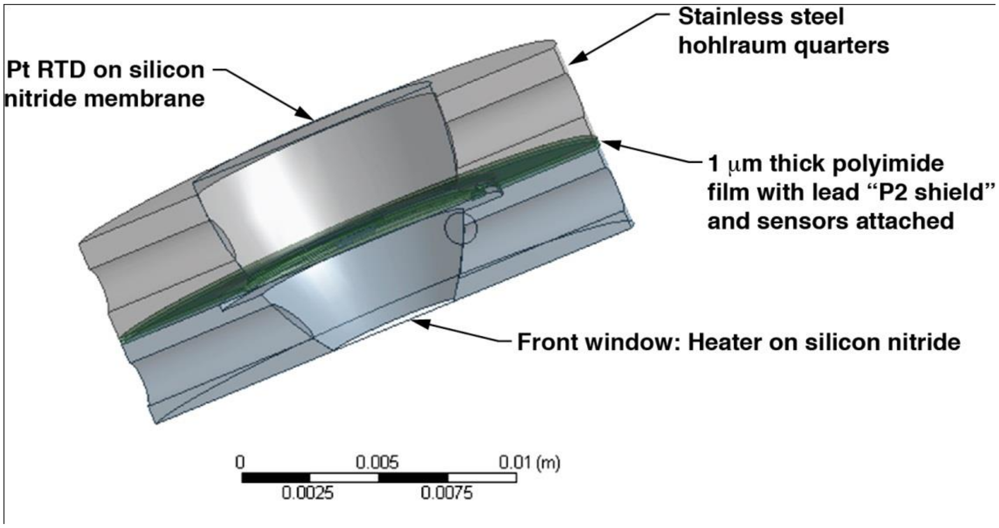
Stainless steel hohlraum quarters
Pt RTD on silicon nitride membrane
1 μm thick polyimide film with lead "P2 shield" and sensors attached
Front window: Heater on silicon nitride
0
0.005
0.01 (m)
0.0025
0.0075

Figure 3-12. Finite element model of internal heat transfer test assembly with helium "bypass"

The central membrane of this assembly is shown in Figure 3-13 below. The small central yellow disk in this figure is the P2 shield. The darker gray outer portion of this item is the membrane area that is sandwiched between the steel shells. The lighter gray central circular portion of this item is the IR shield portion of this item. The arcing 60° and 30° cutouts of this item are the "bypass" features, the cutouts for helium to move freely between the two sides of the IR shield so that frontal helium pressure does not cause the thin LEH and IR shield membranes to rupture.

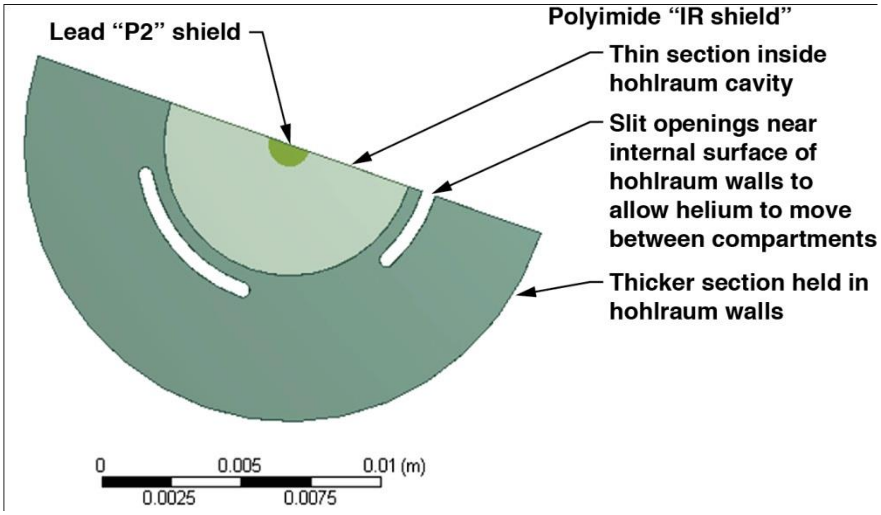
Lead "P2" shield
Polyimide "IR shield"
Thin section inside hohlraum cavity
Slit openings near internal surface of hohlraum walls to allow helium to move between compartments
Thicker section held in hohlraum walls
0
0.005
0.01 (m)
0.0025
0.0075

Figure 3-13. Central membrane of test with "bypass" assembly

The portion of the model which is the helium gas fill is shown in Figure 3-14 below. This is a single connected helium zone with boundaries on the P2 shield, the upper and lower steel shells and the central membrane.

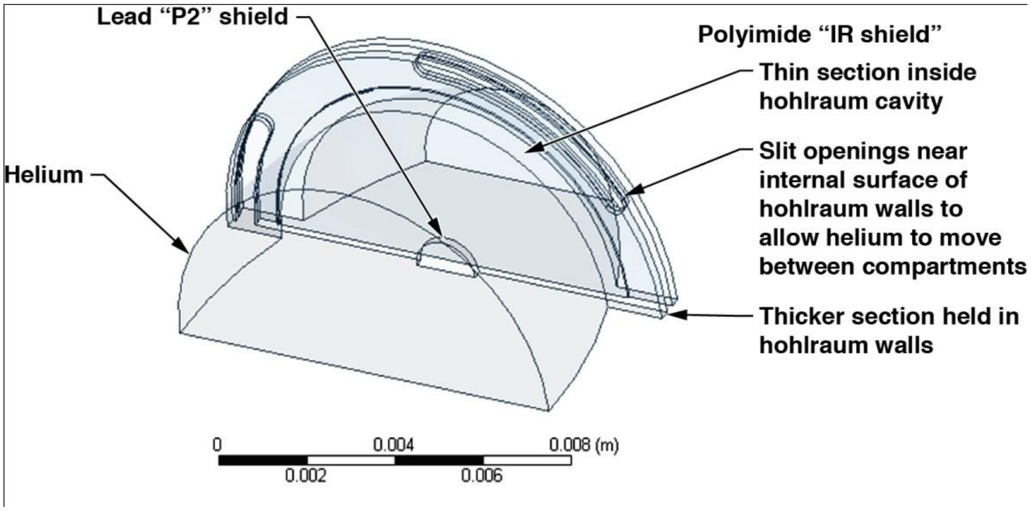
Lead "P2" shield
Polyimide "IR shield"
Thin section inside hohlraum cavity
Helium
Slit openings near internal surface of hohlraum walls to allow helium to move between compartments
Thicker section held in hohlraum walls
0
0.004
0.008 (m)
0.002
0.006

Figure 3-14. Helium zone within model of test assembly with helium "bypass"

The semicircular face of the helium zone closest to the viewer in this picture is actually the "top" face of the assembly in the "as tested" configuration and is the equivalent of the cold capsule-support membrane surface in the target design concept. The test is meant to confirm the prior modeling regarding heat flow to this area and thus to confirm or refute the assertion that the DT ice heating in the target design is less than the specified maximum of 0.1 K. The semicircular face of the helium zone furthest from the viewer in the view of Figure 3-14 is the surface of the helium in intimate contact with the front LEH window membrane, where the platinum heater applies a precise thermal pulse qualitatively but not quantitatively similar to the heating of hot xenon during flight through the target chamber.

This model was created using ANSYS workbench and its geometry and meshing tools. Thermal and fluid calculations were done using the CFX option of ANSYS. A few details of the model are given in Table 3- 3 below.

Table 3-3. Some modeling parameters for the internal heat transfer test with "bypass" assembly

Simulation information	
Nodes	**471153**
Time step size	**0.00002 sec.**
Steel external convection coefficient	**5 w/m^{2}K**
Assembly external fluid temperature	**77K**
Cold top convection coefficient	**5 w/m^{2}K**

The choice of external convection coefficients has not been rigorous, or checked. It is expected that these parameters have weak influence on the results since the thermal inertia of the steel shells is large compared to the product of the test time and the other heat input terms of the test. Material properties used in the simulations discussed here are given in Table 3-4 below.

Table 3-4. Material properties used in simulations

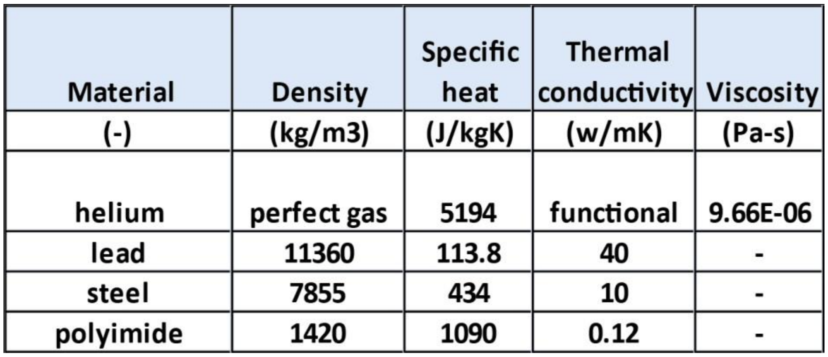

Material	Density	Specific heat	Thermal conductivity	Viscosity
(-)	(kg/m3)	(J/kgK)	(w/mK)	(Pa-s)
helium	perfect gas	5194	functional	9.66E-06
lead	11360	113.8	40	-
steel	7855	434	10	-
polyimide	1420	1090	0.12	-

The constant values shown for most of the entries in the table were selected based on the range of test temperatures expected, i.e. 77K for steel, 77K and slightly warmer for lead, and 77 to 650K for polyimide. The specific heat of helium is very insensitive to temperature over the expected range for the tests. The functional form used for the thermal conductivity of helium is a simple linear fit: k = (4.3263e-5*T+.030264) w/mK. A similar or more complex fit to the viscosity of helium may be a useful improvement. Lastly, the actual specific heat of polyimide used in the model is reduced from the value shown in Table 3-4 by the ratio of the actual test membrane thickness divided by the model membrane thickness. The model membrane thickness is larger to facilitate meshing and computation. To compensate, the specific heat is reduced so that membrane thermal inertia is correctly modeled.

The face of the helium zone adjacent to the platinum heater (and/or the LEH) has been given a range of temperature boundary conditions depending on the joule heating pulse applied to the heater in particular tests. These boundary conditions take the form of fourth and fifth order polynomial curve fits to the measured heater membrane temperatures. Figure 3-15 below compares measurements and curve fit for one such test. The fit is good and use of the fit in the modeling simplifies the simulation work. It eliminates both the need to model the “LEH window” in the test and to resolve the interaction between the solid membrane and the helium beside it. Table 3-5 below lists the curve fits for all five of the “without bypass” tests for the test configuration. “Without bypass” means that there is no helium flow between internal compartments.

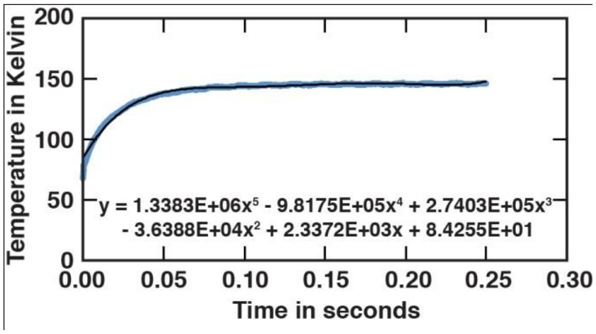

Figure 3-15. Comparison of platinum heater measured temperature history and curve fit used to drive thermal simulation of assembly heating transient

Table 3-5. Curve fitting constants for the LEH membrane heater deployed on the "without bypass" (solid membrane) tests

Test	Peak temperature	C5	C4	C3	C2	C1	C0
(-)	(K)	(K/s5)	(K/s4)	(K/s3)	(K/s2)	(K/s)	(K)
SM1	146	1.33830E+06	-9.81750E+05	2.74030E+05	-3.63880E+04	2.33720E+03	8.42550E+01
SM2	256	1.10590E+08	-4.10040E+07	5.79530E+06	-3.91020E+05	1.28450E+04	8.13760E+01
SM3	460	7.60380E+09	-1.41880E+09	1.01220E+08	-3.45920E+06	5.77760E+04	5.72780E+01
SM4	613	1.70190E+10	-3.09350E+09	2.11910E+08	-6.77230E+06	1.00590E+05	4.06790E+01
SM5	626	7.14140E+10	-1.01080E+10	5.36490E+08	-1.31300E+07	1.46550E+05	-1.84390E+00

The model for the test without helium gas "bypass" is shown in Figure 3-16 below.

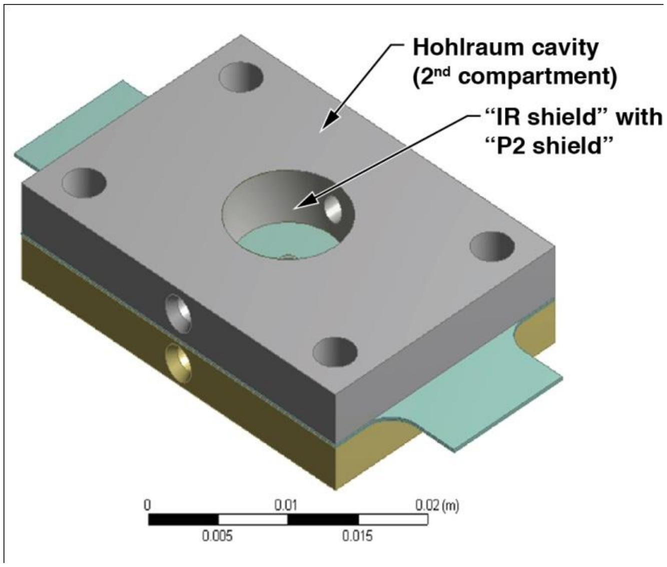

Figure 3-16. Finite element model of test #1 assembly without helium "bypass" (no helium flow between compartments)

In contrast to the "bypass" model this model assumes no symmetry. The steel shells sandwiching the central membrane (IR shield) are essentially the same as in the "bypass" model. Further details of this model are shown in Figures 3-17 through 3-19. Figure 3-17 shows the shape of the lower helium compartment (nearest the Pt heater) and Figure 3-18 shows the upper helium compartment. Figure 3-19 shows both helium compartments. These are the two separate fluid zones of the model, each of which interacts with the steel shells shown in Figure 3-16. Boundary conditions and model evaluation are similar to those applied to the "bypass" model.

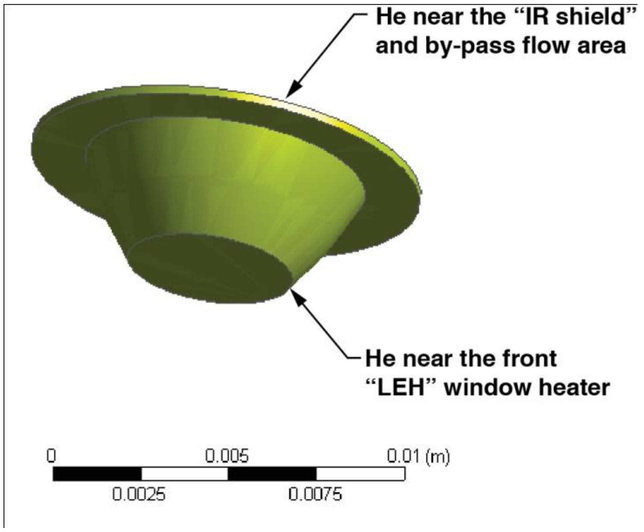
He near the "IR shield" and by-pass flow area
He near the front "LEH" window heater
0
0.005
0.01 (m)
0.0025
0.0075

Figure 3-17. Model of lower helium zone of internal heat transfer test (without "bypass")

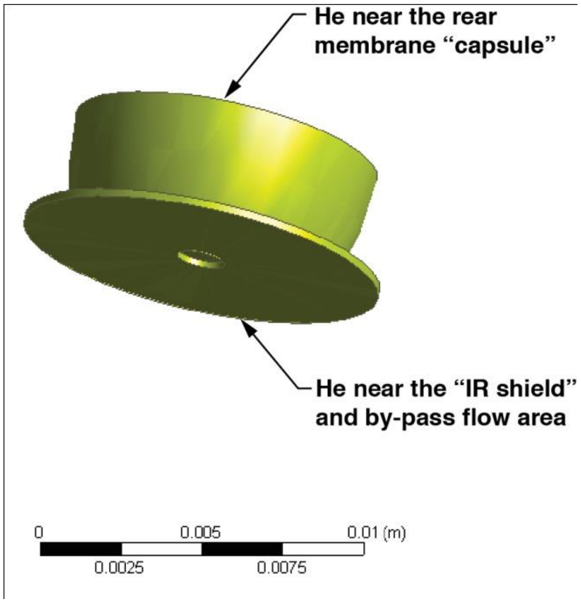
He near the rear
membrane "capsule"
He near the "IR shield"
and by-pass flow area
0
0.005
0.01 (m)
0.0025
0.0075

Figure 3-18. Model of upper helium zone of internal heat transfer test (without "bypass")

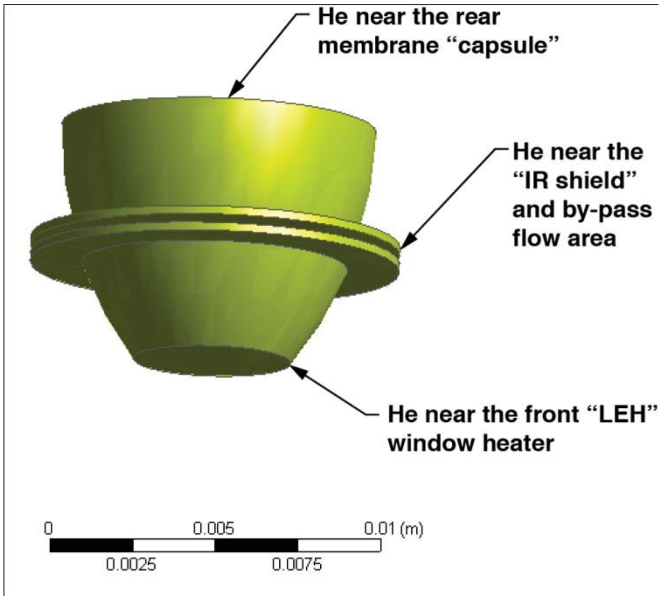
He near the rear
membrane "capsule"
He near the
"IR shield"
and by-pass
flow area
He near the front "LEH"
window heater
0
0.005
0.01 (m)
0.0025
0.0075

Figure 3-19. Both helium zones of internal heat transfer test "without bypass"

The "without bypass" model uses the same material property data and similar Pt heater histories as those given above for the "bypass" model.

3.5.1 Comparison of the test results with the model results

3.5.1.1. Comparison of test and data for internal heat transfer test with "bypass" (with helium flow between compartments)

Results for the "bypass" model with the LEH driven rapidly to 450K (corresponding to test BP3 performed on 8/27/2013) will be discussed here. The temperature transient for the maximum temperature on the LEH face is shown in Figure 3-20. The small oscillation in the maximum beyond 0.08 seconds is due to the use of a polynomial fit for this driving boundary condition and should not significantly degrade the results.

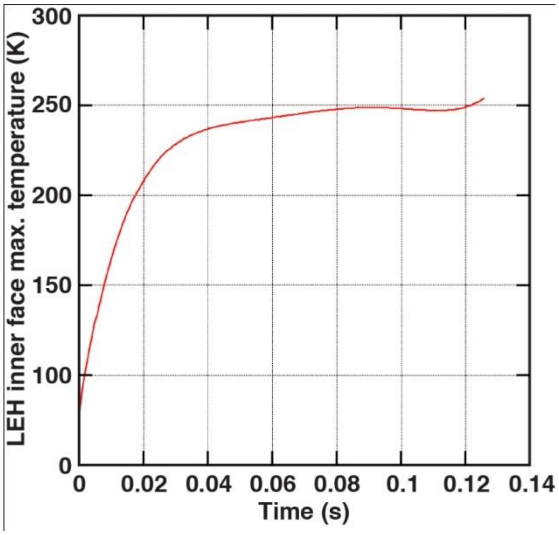

Figure 3-20. Simulation transient maximum temperature on the LEH face from the "bypass" model

Figure 3-21 shows the temperature profile on the central membrane (P2 shield) late in the simulation. The variation in temperature, due to the flow patterns developed around and through the bypass passages, is not large. The hot spots are from upwelling convection currents impinging upon the membrane.

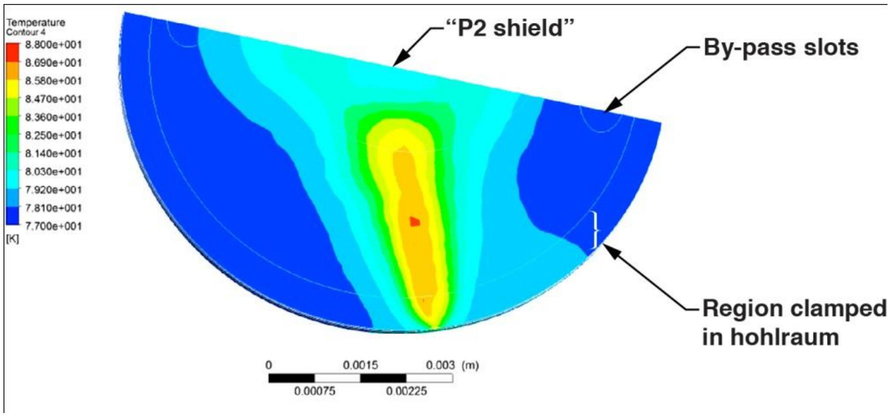
Temperature
Contour 4
8.800e+001
8.690e+001
8.580e+001
8.470e+001
8.360e+001
8.250e+001
8.140e+001
8.030e+001
7.920e+001
7.810e+001
7.700e+001
[K]
"P2 shield"
By-pass slots
Region clamped in hohlraum
0
0.0015
0.003 (m)
0.00075
0.00225

Figure 3-21. Simulation result for temperature profile on central membrane of the "bypass" model.

Figure 3-22 shows the transient of the average value of the absolute pressure in the helium charge in the model. This contrasts to the measured pressure of the charge shown in Figure 3-23. Given that pressure rise in testing is almost twice (~8 kPa vs. ~4 kPa) that of simulation this is not good agreement between simulation and test.

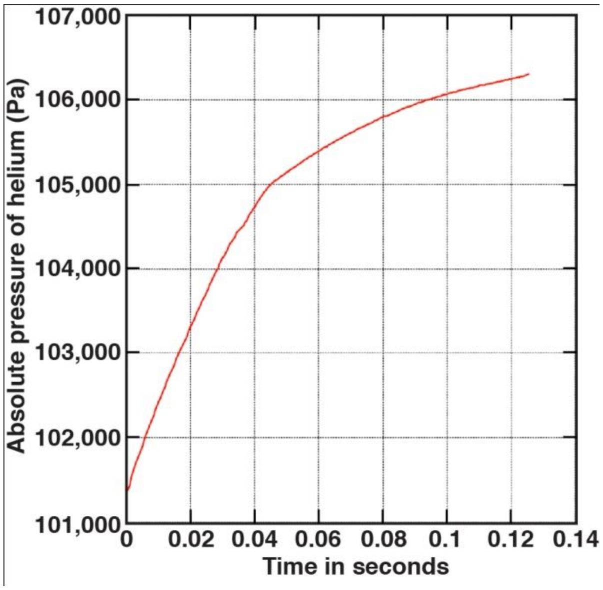

Figure 3-22. Simulation transient of the average value of the absolute pressure in the helium charge of the "bypass" model

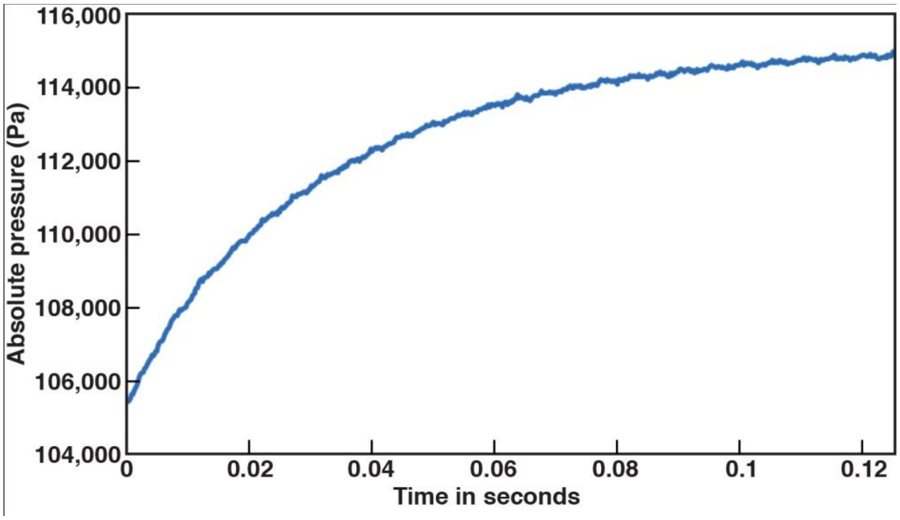

Figure 3-23. Measured transient of the absolute pressure in the helium charge of the "bypass" test

Figure 3-24 below gives the simulation transient for the average temperature of the P2 shield, which should be compared to the measured transient for the temperature sensor attached to the P2 shield shown in Figure 3-25. The simulation result, about a 0.6 K rise in temperature after about a 0.04 second lag period contrasts to about a 1.4 K rise in the measured (estimated on the sinusoidal time varying curve) which also has about a 0.4 second lag in response as well. Despite the similar lag times one would not describe this as good agreement between simulation and test.

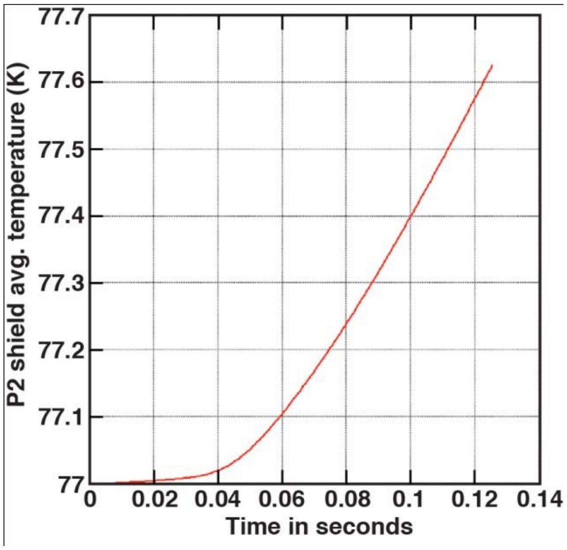

Figure 3-24. Simulation transient of the average temperature of the P2 shield of the "bypass" model

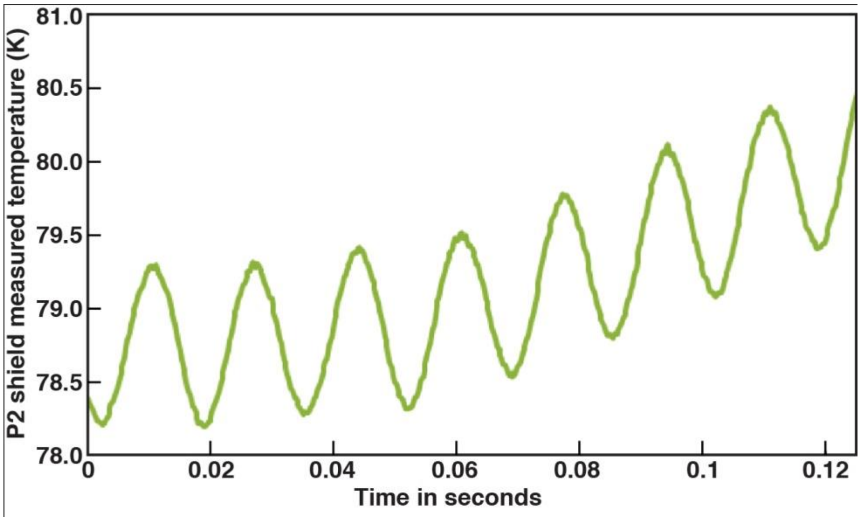

Figure 3-25. Measured transient of the sensor at the P2 shield of the "bypass" test

Figure 3-26 shows the simulation transient maximum temperature on the top face of the "bypass" model, which compares to the measured transient response of the thermal sensor at the top membrane of the test where the target capsule would be located. The simulation result, with temperature rising until ~.042 seconds and then falling afterwards, seems in error. If one considers only the first 0.04 seconds, the simulation has a 0.44 K temperature rise and over the same time period the test shows a 0.7 to 0.8 K temperature rise, about twice the simulated value. Again, this is not good agreement.

The overall results for the "bypass" model indicate a discrepancy between the test results for pressures and temperatures and the predicted results of about a factor of 2. More work would be required to determine the source of these discrepancies.

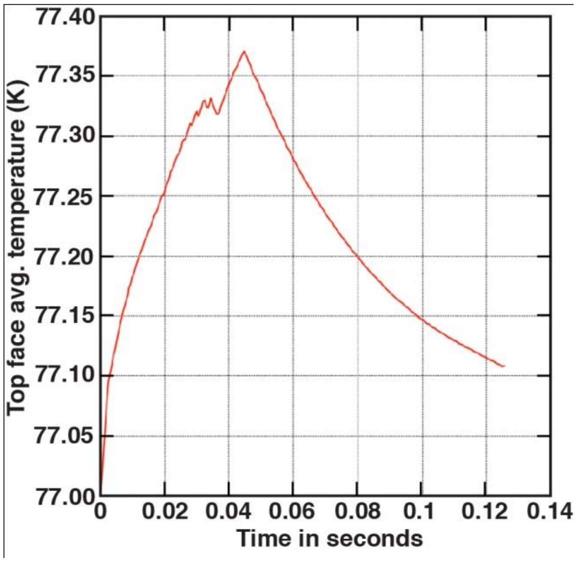

Figure 3-26. Simulation transient of the maximum temperature of the top face of the "bypass" model

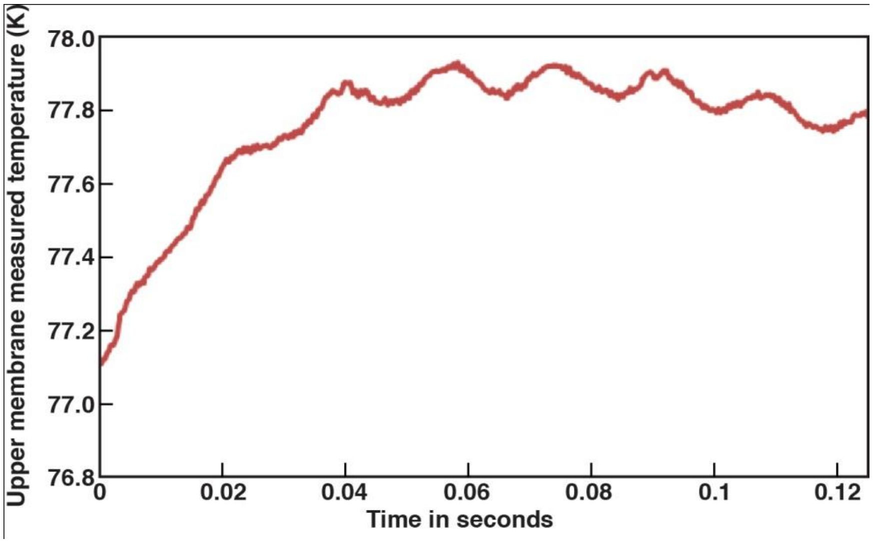

Figure 3-27. Measured transient of the sensor at the top membrane of the "bypass" test

3.5.1.2 Comparison of test and data for internal heat transfer test without "bypass" (no helium flow between compartments)

Results for the "without bypass" model with the LEH driven rapidly to 250K will be discussed here (corresponding to test SM3 performed on 9/14/2013. Figure 3-28 shows the transient average temperature for the LEH. The polynomial fit used to get this time history clearly fails after 0.045 seconds so only results to 0.05 will be shown and discussed here.

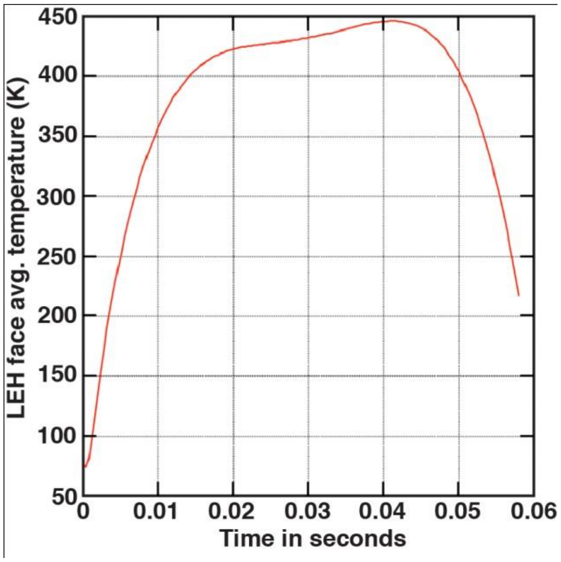

Figure 3-28. Simulated transient average temperature on the LEH face from the "without bypass" model

The simulated transient pressure history in the helium compartment adjacent the LEH is shown in Figure 3-29. This result contrasts to the measured transient histories in both helium compartments shown in Figure 3-30. Strongly opposite to the "with bypass" case, here the simulation pressure rise beside the platinum heater membrane is much higher than measured (~ 35 kPa vs. ~14 kPa). Also of note here is how the measured pressure in the top helium compartment rises rapidly (as fast as the bottom compartment for the first 0.006 seconds) without a thermal lag period. One expects no thermal lag if membrane deflection is the mechanism creating pressure rise but deflection requires a pressure differential.

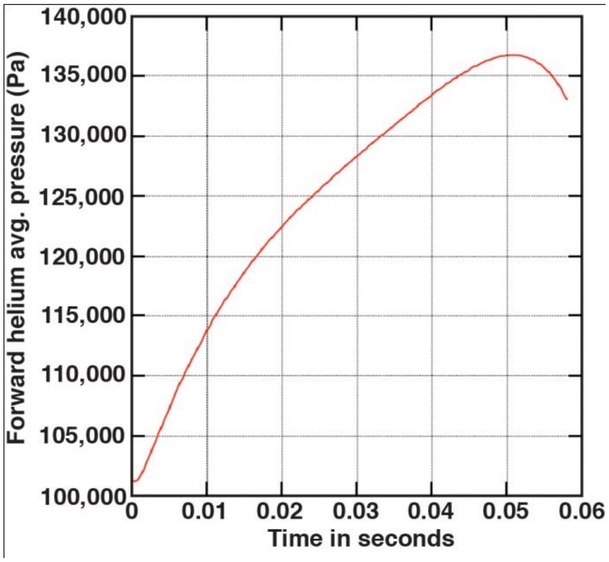

Figure 3-29. Simulated transient average absolute pressure in the bottom helium compartment of the "without bypass" model

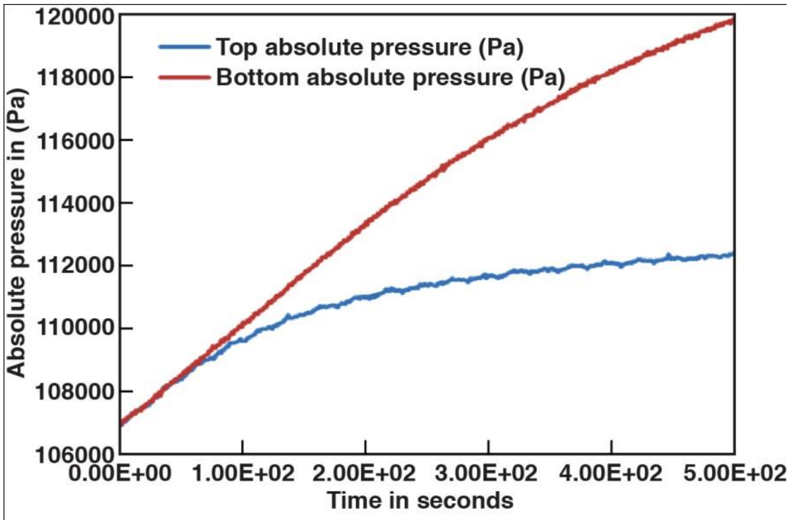

Figure 3-30. Measured transient absolute pressure in the helium compartments of the "without bypass" test

The simulation result for the absolute pressure in the top helium compartment is shown in Figure 3-31 below. This result has a time lag of about 0.003 seconds and the magnitude of the response is far lower than that measured for the top compartment (< 1 kPa vs. ~5 kPa). A leak between compartments is only one of several possible explanations for the discrepancy here between test and simulation. Flashing some surface adsorbed molecules during the initial stage of platinum wire heating can contribute to higher than expected pressure response but not fully explain the simultaneous rise of pressure of both helium compartments. Bulging of the target membranes due to the pressures may also contribute to the discrepancies. The magnitude of the time lag in response of Figure 31, about 0.004 seconds, is of note to more discussion below.

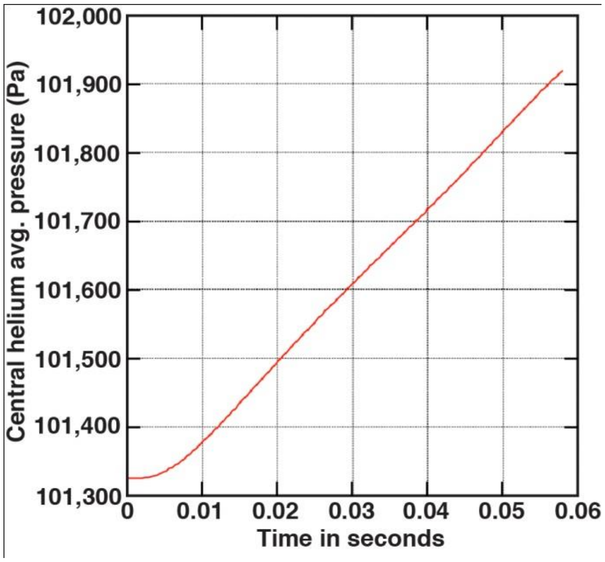

Figure 3-31. Simulated transient average absolute pressure in the central helium compartment of the "without bypass" model

The simulated transient response of the P2 shield (average temperature) is shown in Figure 3-32 below. The time lag for the P2 shield response is somewhat greater than for the central helium gas compartment and the magnitude of the response is small, only 0.17 Kelvin. The measured response at the P2 shield, shown in Figure 3-33 below, is most likely noise or drift in the sensor, which may be on the order of the simulation result.

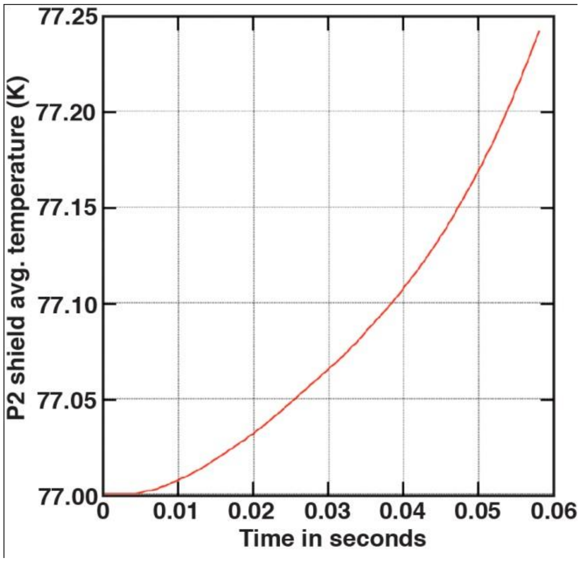

Figure 3-32. Simulation transient average temperature of the P2 shield of the "without bypass" model

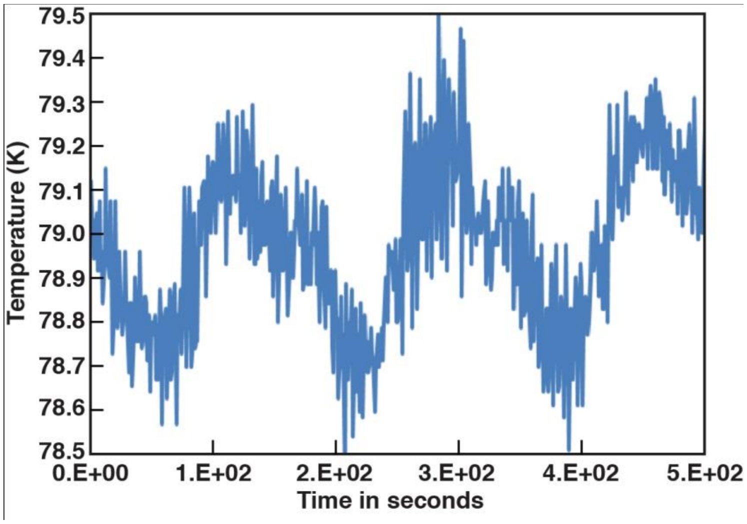

Figure 3-33. Measured transient of the sensor at the P2 shield of the "without bypass" test

Simulation transient response at the top membrane is shown in Figure 3-34 below. Both the membrane surface average and maximum temperature are shown in the plot. The temperature rise here is about two thirds that observed for the volume average of the P2 shield although temperature rises are low (<1K). One might expect the top membrane temperature rise to be a smaller fraction of the P2 shield rise because the top membrane is farther removed from the heating source, but the thermal inertia of the lead is holding its rise down despite the heating helium gas around it. Figure 3-35 below gives the measured transient response of the thermal sensor at the top membrane. This sensor has significant noise in its response and does not show a time lag in response from the test start. This is unexpected and may result from an error in the test or other some unknown factor.

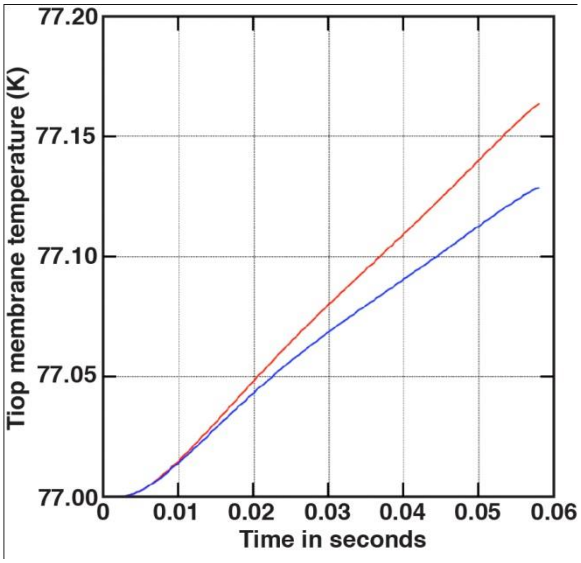

Figure 3-34. Simulated transient average temperature and maximum temperature of the top membrane of the "without bypass" model

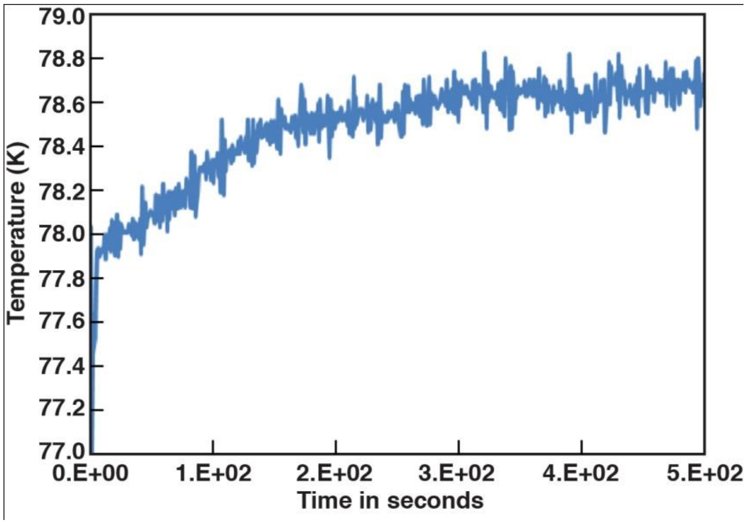

Figure 3-35, Measured transient temperature at the top membrane of the "without bypass" test

3.6 Conclusion

The tests have shown that the trends expected by the predictions, the increased pressure in the cavity near the LEH window due to heating of the window and the convection currents driving temperature changes in near the IR shield and the compartment near the capsule are confirmed by experiment. More effort is required to determine the causes of the numerical discrepancies between the test values and the models. Since the test values were generally higher than predicted, the predicted values for the fusion target in flight may also be low. The models with "bypass" are closer to predicted. The fusion target will likely require "bypass" to prevent rupture of the membranes. The factor of 2 in actual results over predicted, if that proves to be real, could be accommodated in the actual fusion target using a sacrificial layer on the LEH window which will likely be required.

4.0 IR properties of aluminum and carbon thin-films

The reflective layer of aluminum on the 500 nm thick IR shield must be sufficient to block the radiation emanating from the ~900K chamber walls yet be sufficiently thin to not interfere with propagation of either the laser light or the x-rays in the target during the implosion process. The specification is that less than 30 nm of aluminum coating is allowed on the shield. We sought to verify the reflectance of such a thin film at the cold temperatures of interest. In addition, we tested the absorption of carbon-containing thin films as carbon could be a component in either the LEH window or the capsule-support membrane to provide sufficient strength to support the capsule during the acceleration phase of injection. The optical parameters measured in these tests were used in the thermal models of the target flight through the fusion chamber.

4.1 Test set-up

For high-temperature measurements, samples were loaded onto a commercially-available heat stage, the Linkam TS1500 heat stage, capable of heating the sample up to 1500 ^{0}C at controllable heating rate (Figure 4-1). The stage consisted of a resistively-heated ceramic crucible. The temperature in the crucible was measured in real-time using a thermocouple. Sapphire windows mounted at the top and bottom of the crucible were used to allow both the transmission and reflection of the sample to be measured. The sapphire windows can transmit infrared light up to a wavelength of around 4.5 μm. The crucible was sealed inside the chamber which was nitrogen-purged to create an inert ambient atmosphere. The exterior of the stage was water-cooled. Infrared data were taken 3 minutes after each temperature point was reached to allow the system to thermally equilibrate between each temperature reading.

Infrared measurements were carried out using a Perkin-Elmer Spectrum 2000 FTIR. This spectrometer was equipped with an infrared microscope, allowing the beam to be focused onto the sample. For graphene, the samples were typically 7mm in diameter. A custom-built stage was made to mount the Linkam sample stage into this microscope setup. Both transmission and reflection (normal-incidence) of the sample could be measured. The microscope-heat stage setup was placed in nitrogen-purged chamber. However, since there were electrical cables and water lines running out of the Linkam stage, the chamber could not be tightly sealed. This resulted in residual gases in the chamber which resulted in peaks appearing in the measurement data due to these residual gases. The lower limit of measurable wavelength was around 2 μm, limited by the detector in the spectrometer. The upper limit was around 4.5 μm, limited by the transmission limit of the sapphire windows.

Graphene films were grown by chemical vapor deposition on nickel substrates. The graphene films were then transferred onto sapphire windows 7 mm in diameter. The sapphire window provided an infrared-transparent structural support for the thin graphene film and served to protect the Linkam sample stage from excessive contamination. For high-temperature transmission measurements, the temperature-dependent transmission characteristics of the sapphire window were compensated for as a background signal. The infrared transmission of the sapphire window at various temperatures were measured and shown in Figure 4-2. This set of data was used to normalize the high-temperature transmission data of graphene.

For low-temperature infrared measurements of thin aluminum film on glass substrate, samples were loaded into a commercially-available cold stage, the Linkam THMS 600 temperature-controlled stage, capable of cooling the sample down to liquid nitrogen temperature of -197 ^{0}C at controllable rate (Figure X). The cooling was achieved by flowing liquid nitrogen beneath the sample stage. Real-time temperature in the crucible was obtained by a thermocouple.

4.2 Test results

The measured temperature dependent IR transmission of a 1000 nm thick polyimide film is shown in Figure 4-3. As the temperature is increased from room temperature to 200 ^{0}C, the film's IR transmission is decreased by around 10 %.

For a 100 nm graphene film, the IR transmission decreases from 10 % to 8 % as the temperature is varied from room temperature to 1300 ^{0}C (Fig. 4-4). After cooling back down to room temperature, the IR transmission largely recovers to its original value. This result shows that the graphene film has excellent thermal stability. The IR reflectance of the film decreases from around 40 % to 20 % as temperature varies from room temperature to 1300 ^{0}C. We can thus deduce that the IR absorption (assuming no scattering) increases from 50 % to 70 % during this thermal test.

For a 30 nm aluminum film, it is verified that the film maintains a high IR reflectance of above 90 % down to liquid nitrogen temperature (Fig. 4-5).

The values for the reflected radiation off the aluminized film were used in the calculations cited in Table 1-1.

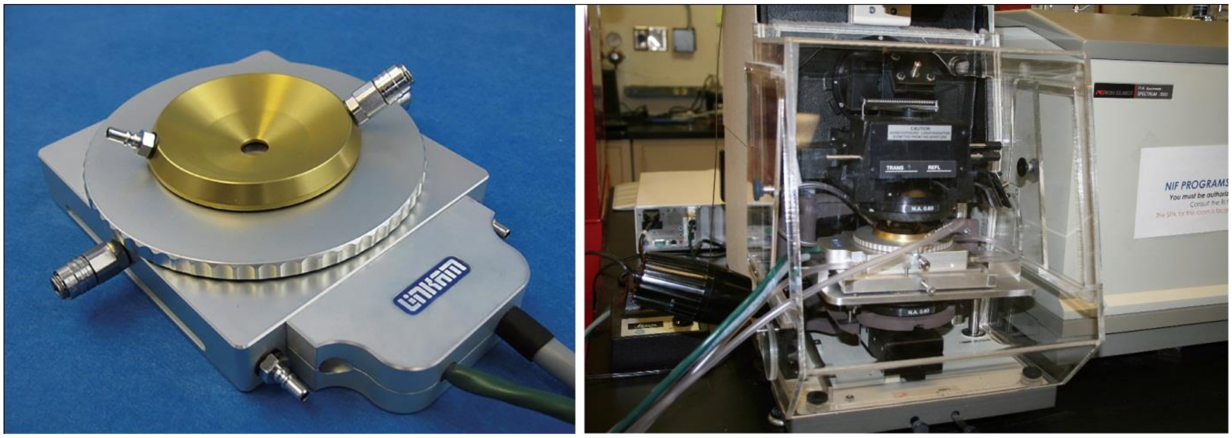

Figure 4-1. Experimental Setup for IR characterization of polyimide, graphene and aluminum films

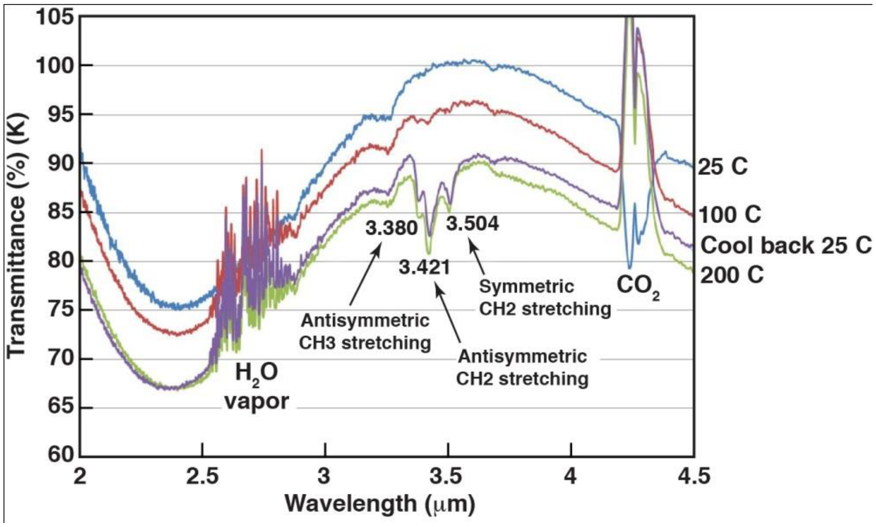

Figure 4-2. Measured transmission of 1000 nm thick polyimide at room temperature

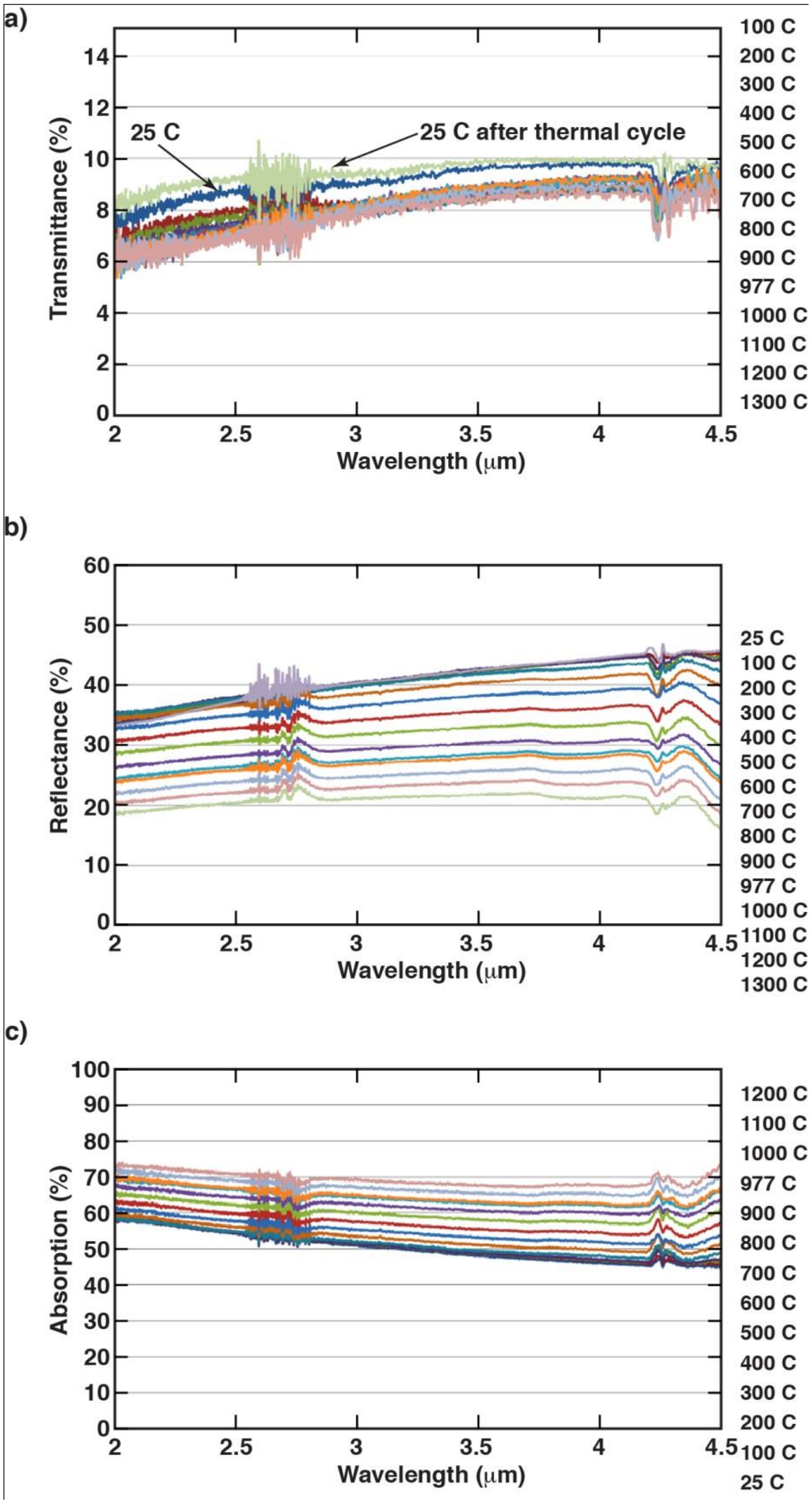

Figure 4-3. Measured transmission (a) reflection (b) and calculated absorption (c) of 100nm thickness graphene as a function of temperature

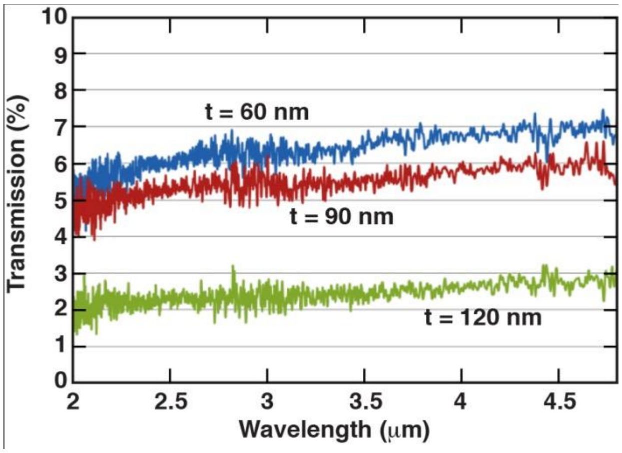

Figure 4-4. Transmission of graphene as a function of thickness

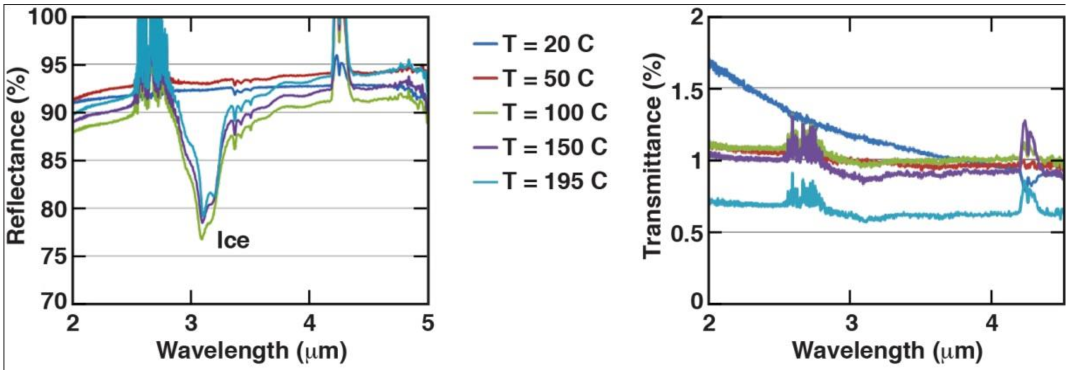

Figure 4-5. Measured reflection/transmission of 30 nm aluminum on a glass substrate as a function of temperature

5.0 Conclusion

The tests of the external heat transfer coefficient suggests that the values used in the numerical analysis for the temperature distribution within the fusion fuel target following flight into the target chamber are probably valid. The tests of the heat transfer phenomena occurring within the target due the rapid heating of the LEH window for the hot gasses within the fusion chamber show that the heat does indeed convect via the internal helium environment of the target towards the capsule and that the pressure in the front compartment of the target adjacent to the LEH window increases such that t bypass venting of the internal helium into the second chamber adjacent to the capsule is needed to prevent rupture of the membranes. The bypass flow is cooled by the hohlraum during this venting. However, the experiments suggest that our internal heat flow calculations may be low by about a factor of 2. Further studies need to be conducted to investigate the differences between the experiment and the numerical analysis.

Future studies could also possibly bring the test conditions closer to those expected in the fusion chamber to better validate the results. A sacrificial layer will probably be required on the LEH window o

Appendix FINAL REPORT

Chemical Vapor Deposited (CVD) Diamond Process for Laser Inertial Fusion Energy (LIFE) Fuel Targets

PI: Yogesh K. Vohra, University of Alabama at Birmingham (UAB)

Period: 10/01/2011 to 09/30/2013

We have investigated the possibility of producing nanodiamond spheres grown by chemical vapor deposition process.

Research methodology: Chemical vapor deposition process has been utilized to carry out experiments on titanium alloy, flat and spherical silicon substrates. In situ temperature monitoring has been utilized to calculate nanodiamond growth rate. Roughness of the grown nanodiamond films has been measured by atomic force microscopy. XPS (x-ray photoelectron spectroscopy) has been utilized to estimate sp2 content in the diamond films. Raman spectroscopy has been utilized to study the diamond films.

Experimental details: In the earlier stages of this project, effort has been put in to select a suitable substrate to carry out experiments. The important requirement that the substrate should be easy to remove after the completion of CVD growth step has been taken into consideration. Titanium alloy (Ti-6Al-4V) has been used as substrate in the initial stages and silicon has become the choice of substrate since then.

A standard gaseous chemistry of 18% CH_4/H_2 and 10% N_2/CH_4 has been utilized initially and emphasis has been placed on modifications to CVD system to increase the power density, which in turn was believed to increase growth rate. We have been successful in increasing the growth rate from below 1 micron/hr to 4 microns/hr with the help of this approach. We have then undertaken a systematic study of effects of various internal parameters on the growth rate. As part of this study various gaseous chemistries have been utilized for CVD growth experiments and their effects on resulting diamond films have been studied using various spectroscopic techniques.

Substrate temperature: With the aforementioned chemistry, we have varied the substrate temperature in the range of 750 C to 900 C. We have determined 850±20 C is ideal to carry out CVD depositions on silicon substrates. At still higher substrate temperatures, the quality of nanodiamond grown was simply unacceptable.

Modified gaseous chemistry: At elevated substrate temperature of ~ 900 C, a chemistry of 6% CH_4/H_2 and 8% N_2/CH_4 has yielded an increase in growth rate to 4.55 microns/hr (Figure 1a). Continued experimentation with gaseous chemistry and substrate seeding mechanism led to a growth rate of 5.5 microns per hour with this chemistry (Figure 1b). While this increase in growth rate is a welcome result, the roughness of the nanodiamond grown on silicon also increased. Figure 2 shows the AFM image of a 10 micron X 10 micron square area from the nanodiamond film grown with this high growth rate. The roughness of this film is around 27 nm.

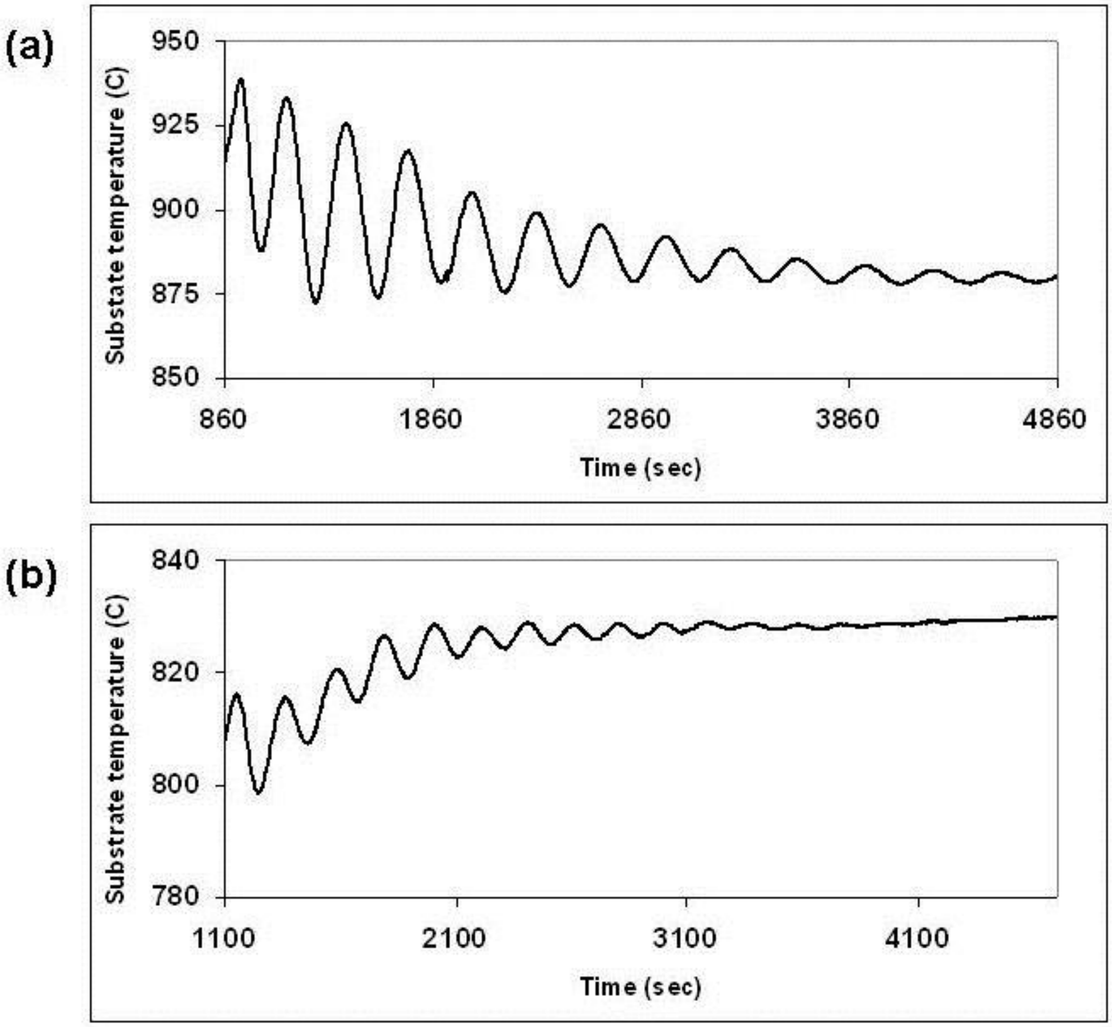

Figure 1: (a) Shows the growth rate of 4.55µm/hour with a gaseous chemistry of 6% CH4/H2 and 8% N2/CH4. (b) Shows a growth rate of 5.5µm/hour with the same gaseous chemistry at a different substrate temperature.

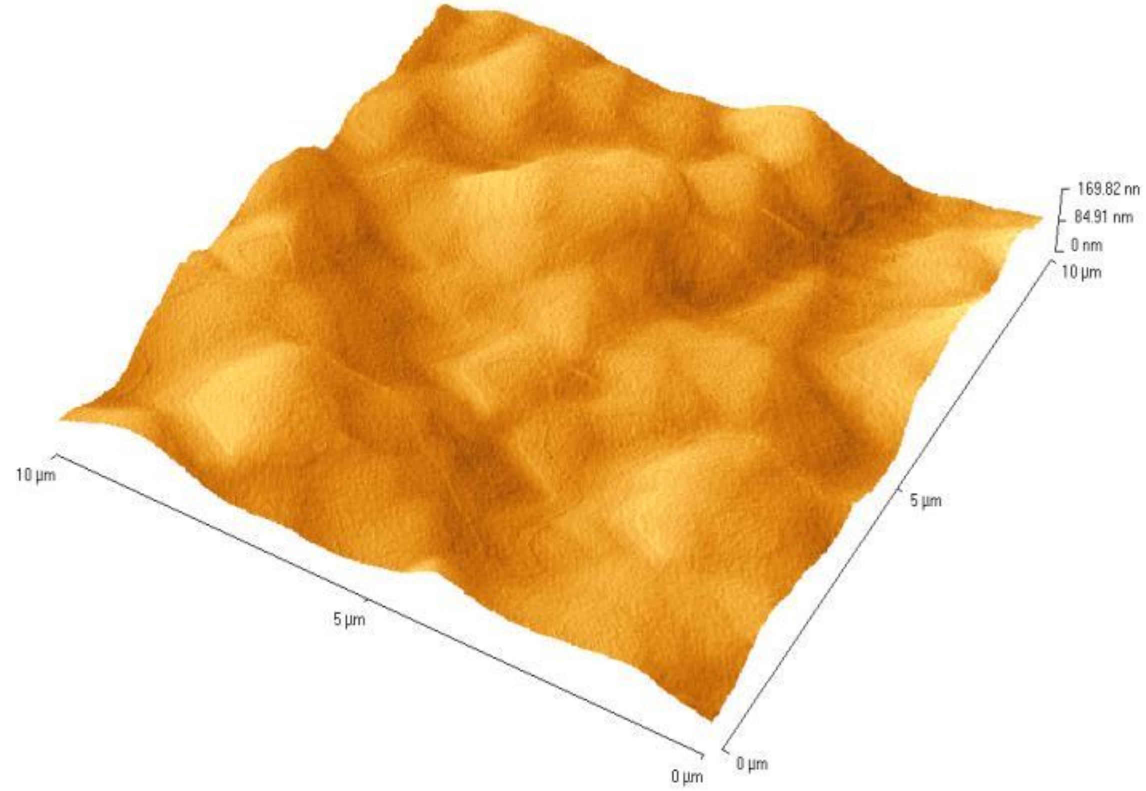

Figure 2: AFM image from a 10 µm X 10 µm area of a nanodiamond film grown on silicon with a growth rate of 5.5µm/hr.

A still higher growth rate of 6 microns/hr has been seen with a chemistry of 6% CH_4/H_2 and 20% N_2/CH_4. The resulting nanodiamond film quality is poor (Figure 3). Multiple islands of carbon aggregates have been noticed in the diamond film. But it is to be seen whether this film can be polished to achieve a smooth surface.

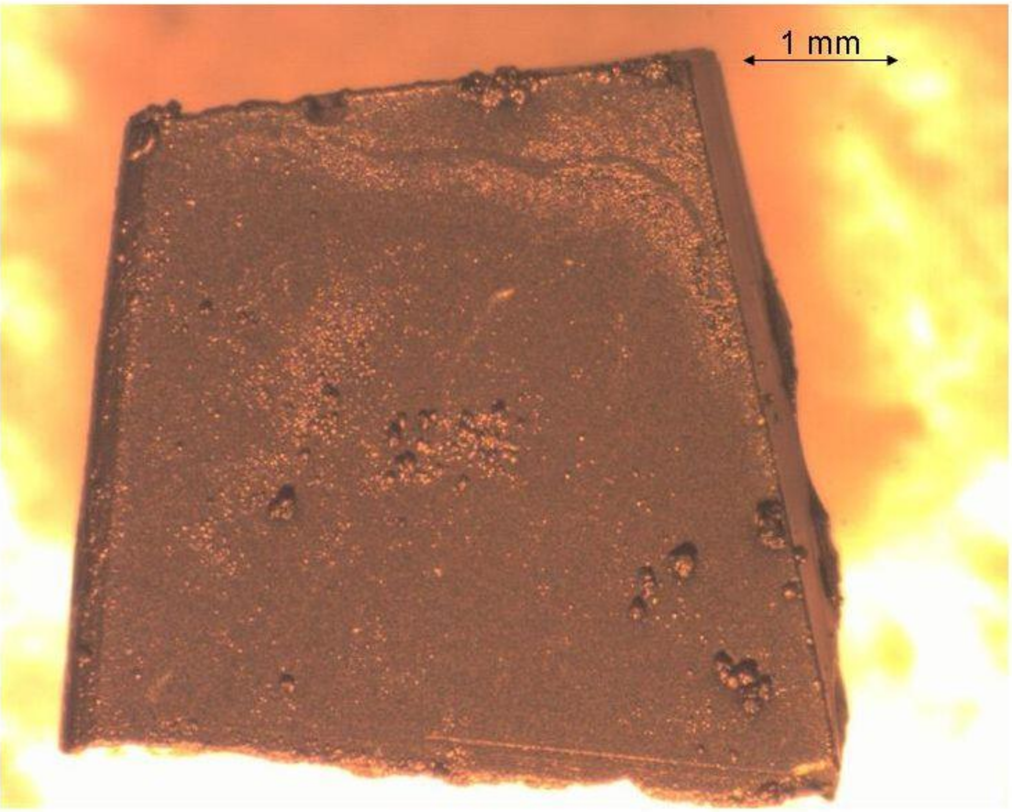

Figure 3: Nanodiamond film grown at 6µm/hr on silicon. Film quality is poor due to the multiple carbon-nitrogen aggregates.

With the aim of growing nanodiamond on silicon spheres, experiments were carried out on 4mm diameter silicon spheres. Utilizing the higher power densities that could be achieved in the 30 kW microwave plasma CVD system, we have carried out experiments in an effort to grow smooth nanostructured diamond on silicon spheres.

The average growth conditions are as follows. Microwave power of 4 kW, chamber pressure of 45 torr, and substrate temperature in the range of 750 – 800 C has been employed in the experiments. With a gas phase chemistry of 6% CH_4/H_2 and 20% N_2/CH_4, a growth rate of ~ 1 micron/hr was noticed at a substrate temperature of 775 C.

We have continued the experiments by varying the growth chemistry and growth conditions and have achieved a growth rate of 2.5 – 2.75 microns/hr at a substrate temperature of 810 C. To avoid uneven nucleation across the surface of a given sphere (Fig 4), stage design has to be modified to enable uniform coating of the sphere in single CVD growth run. We also believe this problem could be addressed by changing the seeding mechanism of sample prior to CVD growth.

We have also examined the cross-section of a sphere to examine the presence of any intermediate layers such as silicon carbide. Our SEM results show absence of any thick interface layer between silicon substrate and nanodiamond layer (Fig 6).

We have carried out density measurement on the nanostructured diamond layer to determine its density. A 3.55 mm X 3.55 mm silicon flat substrate has been selected and carefully weighed before and after the CVD deposition. Both in situ monitoring of growth rate and SEM have been employed to determine the exact thickness of the CVD grown nanodiamond layer (Fig 7). From the calculation we found that the density of nanostructured diamond is 3.565 ± 0.4 gm/cm^3.

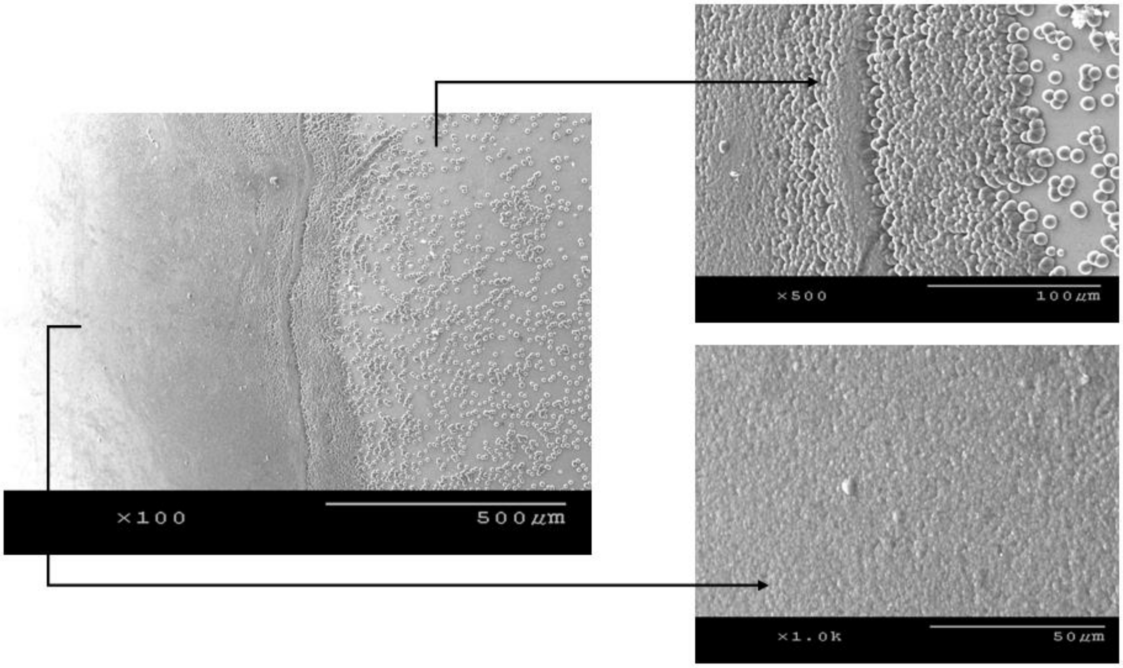

Figure 4: Uneven nucleation across the surface of the sphere. The low nucleation region is the top of the sphere exposed directly to the plasma during CVD deposition.

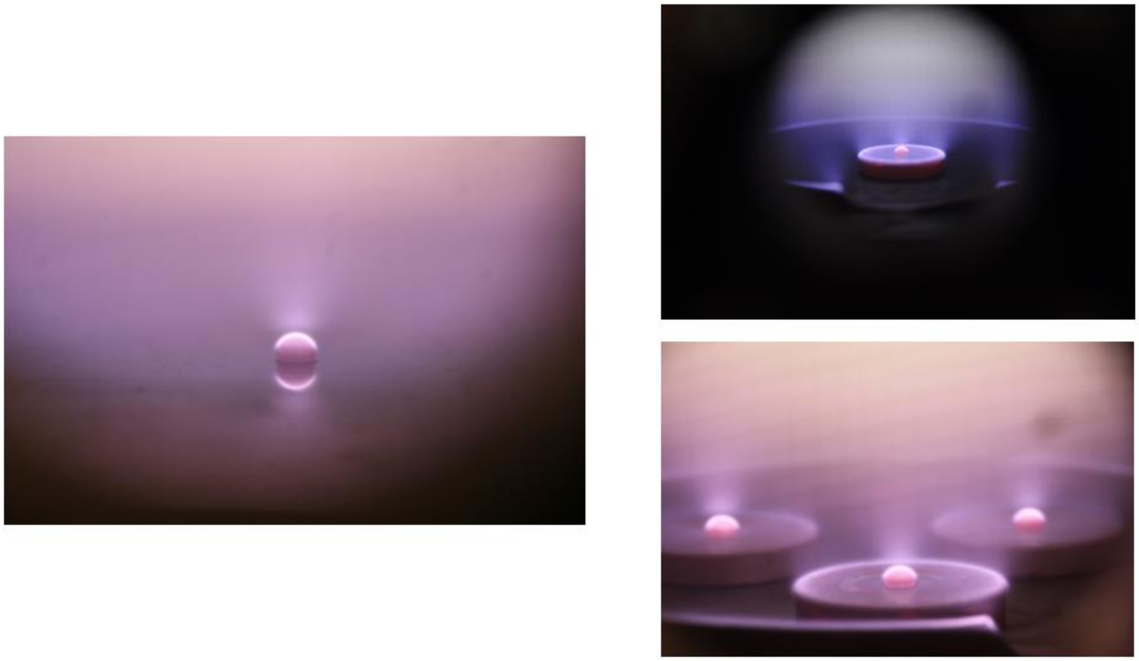

Figure 5: Substrate holder designs used to carryout CVD deposition on silicon spheres. Each half of the sphere is being coated separately. A design which will ensure coating on the entire sphere in a single run is needed.

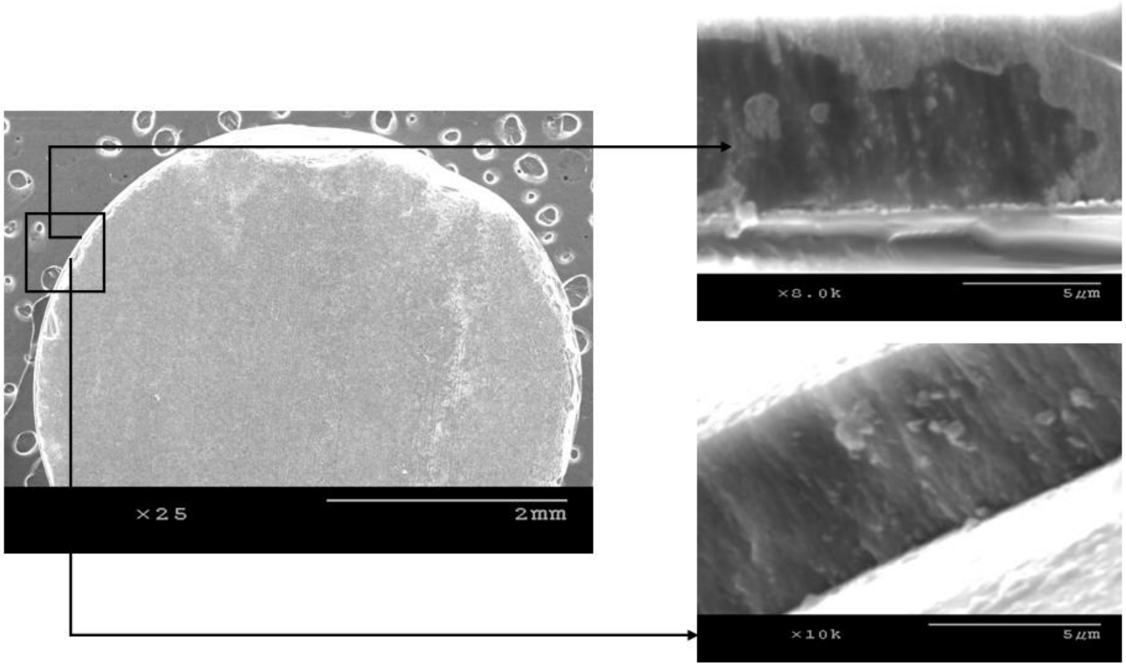

Figure 6: SEM images of cross-section of a sphere examining the area between silicon sphere and nanodiamond layer. No evidence of an interface layer could be found.

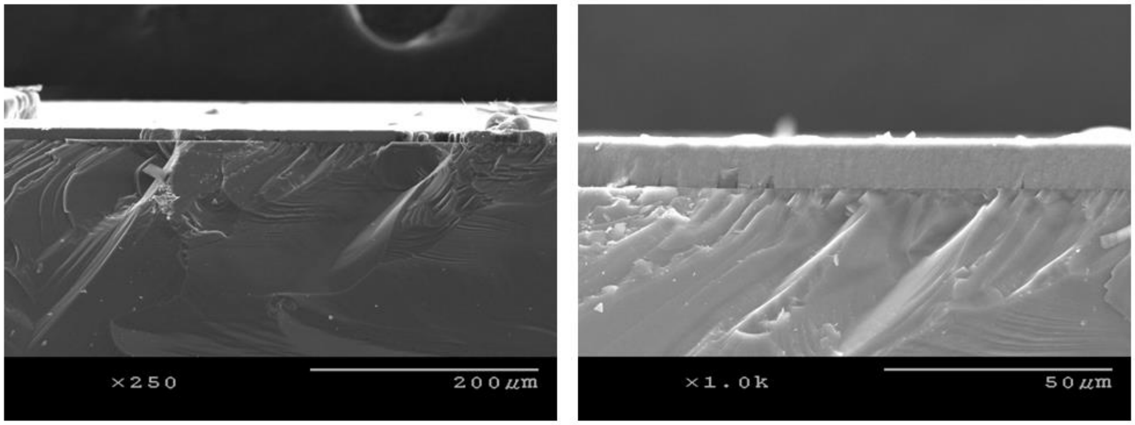

Figure 7: Cross-section SEM image showing the silicon substrate and the CVD grown nanodiamond layer on the flat silicon substrate utilized in density measurement.

All spectra shown in Figure 8 have been collected at the same time using identical laser power and collection times. The top two spectra in figure 3 have been collected from NSD film grown using low methane chemistries and the bottom spectrum has been collected from NSD film grown using high methane chemistry. The bottom spectrum shows the characteristic diamond peak at 1332 cm^{-1}, the D, G bands associated with amorphous carbon centered around 1350 cm^{-1} and 1550 cm^{-1} respectively. There are the peaks at 1150 cm^{-1} and 1480 cm^{-1}, which are associated with sp^2 bonded carbon in the form of TPA – transpolyacetylene. All these peaks are still present in the top spectra. However, the TPA peaks have less intensity, which leads us to make a qualitative assessment that it could be due to the presence of low amount of sp^2 bonded carbon.

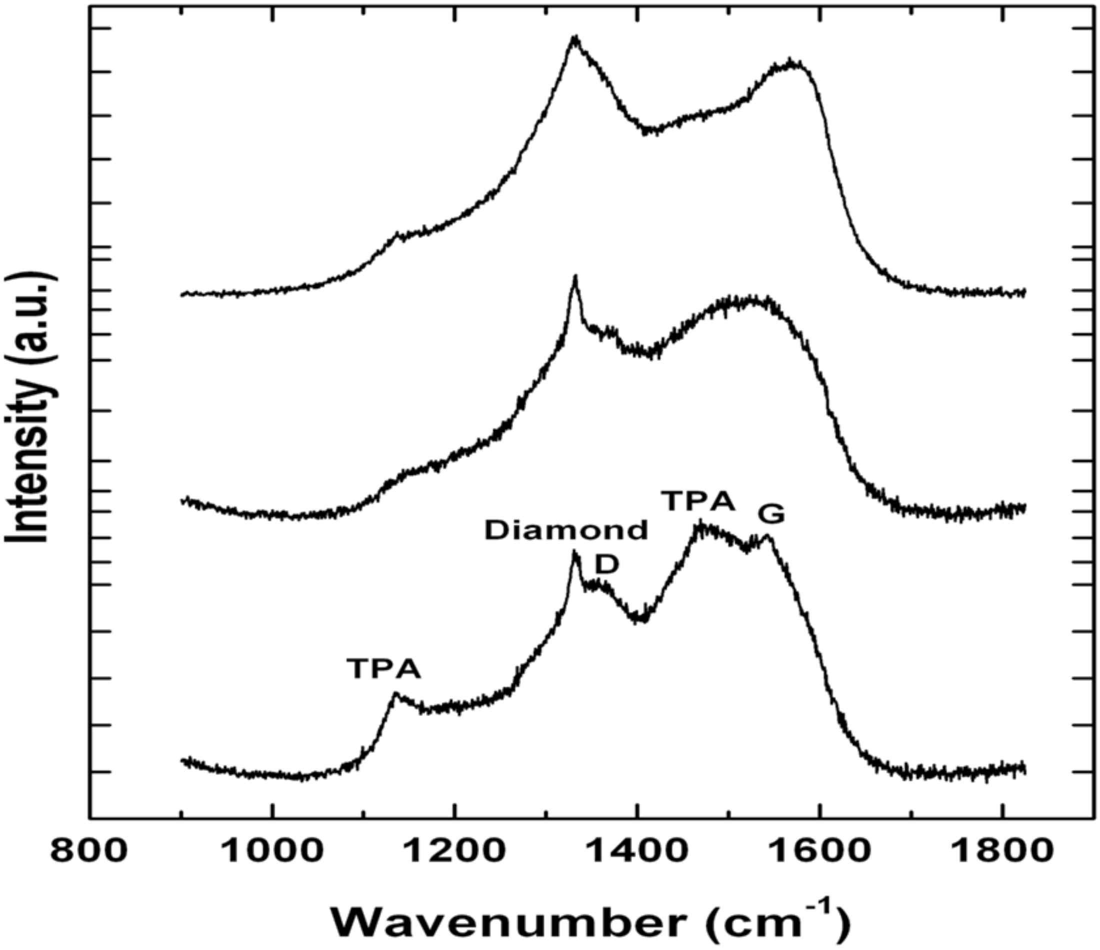

Figure 8. Raman spectra from NSD films grown on silicon using high methane chemistry (bottom), low methane chemistries (middle), (top) are shown. A low level of amorphous carbon is apparent from the middle, top spectra.

X-ray photoelectron spectroscopy has been utilized to accurately determine the sp^3 content in the NSD films we have grown. Figure 9 shows the survey scans taken on the NSD film grown on Ti-6Al-4V (pre and post etching). There is no evidence of any major impurities in the film. Especially, no evidence of large amounts of nitrogen or other impurities could be seen confirming that these NSD films are indeed diamond crystals embedded in sp^2 bonded carbon matrix. However, without conducting a more thorough study we cannot rule out presence of nitrogen in the ppm level. We performed XPS on our samples in order to determine sp^2 content in our NSD films. When analyzing the data, the residual curve, χ^2 value, FWHM were all observed carefully to ensure that the fittings are meaningful. As expected, films grown with high methane showed 25% to 30% sp^2 bonded carbon. Switching to low methane chemistry proved very beneficial, as we have consistently grown films which have only 10% to 14% of sp^2 bonded carbon as shown in figure 10. The drop in sp^2 content is more pronounced in NSD films grown on Ti-6Al-4V compared to the films grown on silicon when utilizing high and low methane chemistries. Further investigation is needed into the combined effects of N_2/CH_4 ratio, substrate temperature to achieve the goal of producing diamond films with low sp2 content at high growth rates.

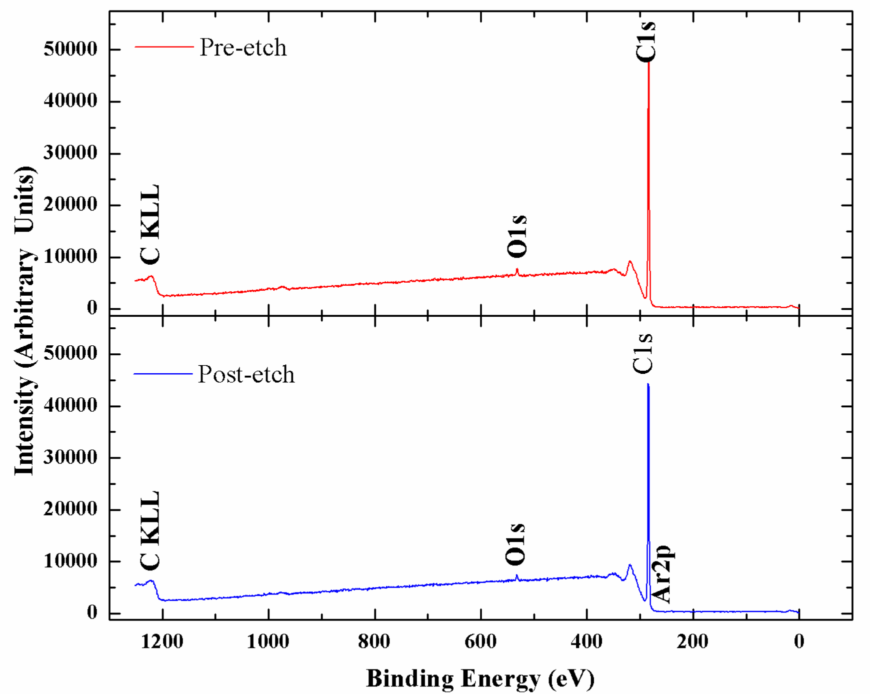

Figure 9. XPS survey scans of NSD film grown on Ti-6Al-4V utilizing a gaseous chemistry of 500 sccm of H_2, 88 sccm of CH_4 and 8.8 sccm of N_2.

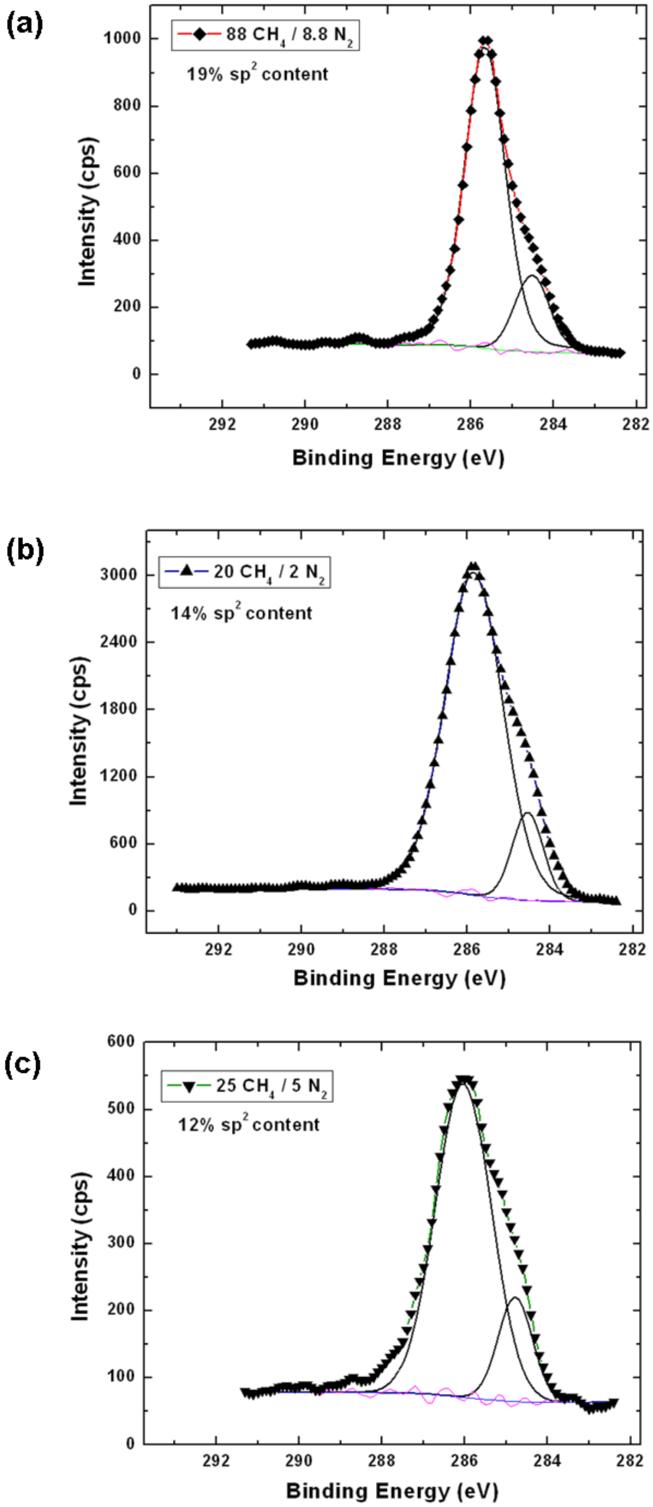

Figure 10. XPS high resolution spectra (C1s) of NSD films grown on silicon with different gaseous chemistries showing different sp2 contents. Low methane chemistry resulted in NSD films with less sp2 content.

Significant results achieved in this study are:

- Increase in growth rate of nanostructured diamond (NSD) films from 1 μm/hr to 5 μm/hr on silicon.
- Production of thick NSD films on flat silicon substrates.
- NSD films with significantly lower sp2 content have been produced by chemical vapor deposition process.
- Technique to coat spherical silicon substrates with NSD films has been demonstrated.

Dynamic Response of Liquid Saturated Nanofoam Under Extreme Acceleration for LIFE Target Design

David Dawson
Thermal-Fluids Group
Engineering Technologies Division
dawson24@llnl.gov
February 17, 2012

Abstract

Analysis of the dynamic response of liquid Deuterium-Tritium (LDT) saturated nanofoam coating the inside of a small spherical shell under the acceleration profile for the Laser Inertial Fusion Energy (LIFE) target injection system is performed. The primary quantity of interest is the maximum radial displacement from nominal, of the LDT/nanofoam layer at the time of ignition. The LDT/nanofoam combination is modeled as a poroelastic material using the COMSOL multi-physics analysis software. A grid resolution and time step convergence study is performed. It is also demonstrated that the poroelastic model reduces to the linear elastic model under specific conditions. Results are compared against a simplified linear elastic model and it is found that the two models produce fundamentally different qualitative behavior. A sensitivity study is performed on both the porosity and the permeability of the nanofoam. Preliminary results from the study of the dynamic response of LDT in a spherical capsule without nanofoam are presented and future work discussed.

I. Introduction

The LIFE target injection process consists of firing a small hohlraum assembly (target) into the chamber at velocities of about 250m/s. Regardless of the final injection mechanism used, the target will experience accelerations equivalent to hundreds to thousands of times that of earth's gravitational acceleration ($1g = 9.8\frac{m}{s^2}$). The target contains a small spherical shell (capsule) which contains the LDT fuel. At the time of ignition the LDT needs to coat the inside of the sphere with a uniform layer. Perturbations in the layer are required to be less than 1µm. The capsule will begin with enough LDT to coat the interior with a nominal thickness of 150µm. To stabilize the LDT layer the interior of the capsule is lined with a very low density, high porosity, nanofoam. The foam holds the LDT in place and it is this dynamic response of the combination of LDT and nanofoam that is the primary focus of this study.

The complex material behavior of the LDT/nanofoam layer cannot be described entirely by either the linear elastic model (for purely solid materials) or Darcy's law (fluid flow through a rigid porous material) as both of these models neglect the coupling between the motion of the pore fluid and the structural dynamics. For this reason we utilize the poroelastic model to describe the LDT/nanofoam dynamics. This model couples linear elastics with Darcy flow via the pore pressure and volumetric stress. A more detailed description of the model will be given in a later section.

A detailed description of the material properties, geometry, and physical conditions is presented in Section II. Section III gives a brief review of poroelastic theory. Section IV presents the results of the analysis and discussion, followed by concluding remarks in Section V.

II. Model/Setup/Geometry

For our analysis we assume an injection acceleration of 1000g for 45ms followed by 40ms of zero acceleration drift before target ignition. A diagram illustrating these features of the injection process is shown in figure 2.1. The acceleration profiles used in the poroelastic and linear elastic calculations include 3ms "ramp up" and "ramp down" periods during which the acceleration transitions from 0g to 1000g and from 1000g to 0g respectively. This is done for numerical considerations as well as physical considerations related to other target design features.

The target consists of a "rugby" shape Hohlraum which contains a $4mm$ diameter spherical capsule containing the LDT fuel. The capsule is considered to be perfectly rigid. On the inner surface of the capsule is a thin layer of very low density nanofoam saturated in LDT. Its thickness is nominally 150µm. The remainder of the sphere is filled with gaseous Deuterium-Tritium (GDT). The properties of the capsule, nanofoam, LDT, and GDT are summarized in table 2.1.

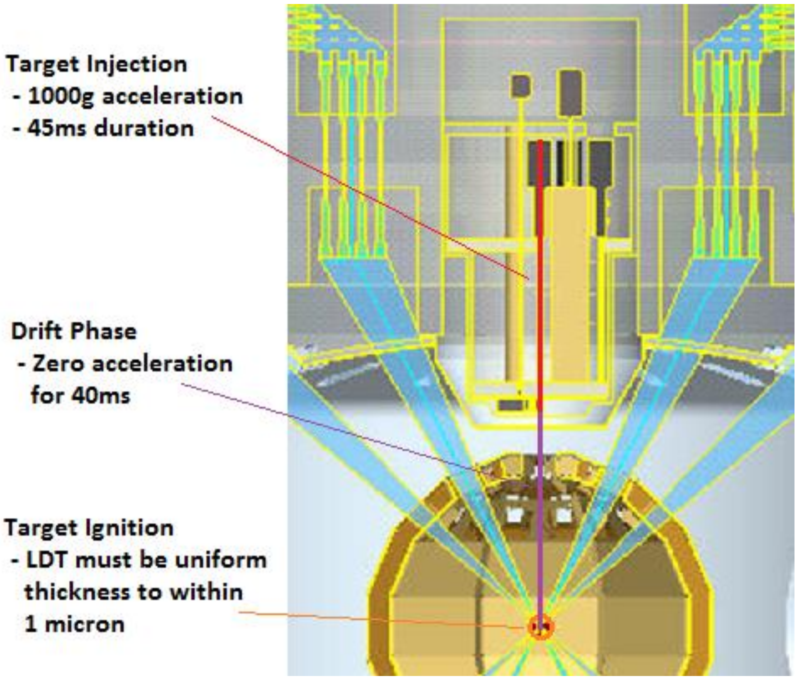
Target Injection
- 1000g acceleration
- 45ms duration
Drift Phase
- Zero acceleration for 40ms
Target Ignition
- LDT must be uniform thickness to within 1 micron

Figure 2.1: Illustration of the target injection process.

Quantity	Symbol	Value
Capsule Properties		
Inner capsule radius	r_{in}	2mm
Nanofoam Properties		
Nanofoam layer thickness	d_{foam}	0.15mm
Density of nanofoam	ρ_s	20mg/cc
Porosity of nanofoam	α	0.975
Young's Modulus	E	0.1MPa
Poisson's Ratio	ν	0.2
Mean pore diameter	d_{pore}	10-50nm
Permeability	κ	?
LDT Properties		
Density	ρ_f	221.88mg/cc
Dynamic Viscosity	μ	5.03e-5 Pa·s
Surface Tension	σ	4.1e-3 J/m^2
Contact Angle	θ	0°
Compressibility	χ	4.5e-11/Pa
GDT Properties		
Density	ρ_g	0.3mg/cc
Dynamic Viscosity	μ_g	9.4e-7 Pa·s

Table 2.1: Properties of Capsule, Nanofoam, Liquid Deuterium-Tritium, and Gaseous Deuterium-Tritium.

III. Poroelastic Theory

The LDT/nanofoam layer consists of a deformable elastic porous solid that is saturated by LDT. The LDT can flow relative to the deforming solid. On their own, linear elastic theory and Darcy's Law are insufficient to describe the behavior of these two materials as they do not account for the coupling between the dynamic response of the two phases. An increase in pore pressure induces a dilation of the porous solid and conversely, compression of the porous solid causes a rise in pore pressure if the fluid is prevented from escaping the porous network. The porous solid is more compliant under drained conditions (when excess pore pressure is completely dissipated) than undrained conditions (when the fluid cannot escape the porous network). Biot 1935 and 1941 [1,2] was the first to develop a linear theory of poroelasticity that captures this behavior. It has since been extended and generalized for a wide range of problems. We begin by defining the small strain tensor, ϵ_{ij}, and variation of fluid content, ζ, as

$$\epsilon_{ij} = \frac{1}{2}\left(u_{i,j} + u_{j,i}\right) \tag{1}$$

$$\frac{\partial \zeta}{\partial t} = -q_{i,i} \tag{2}$$

where the variation of fluid content is the variation of fluid volume per unit volume of porous material. Positive ζ corresponds to a "gain" of fluid by the porous solid. q_i is the specific discharge which describes the motion of fluid relative to the solid.

The governing equations for a linear poroelastic material can be summarized as:

The constitutive equation for the porous solid

$$\sigma_{ij} + \alpha p \delta_{ij} = 2G\epsilon_{ij} + \frac{2G\nu}{1-2\nu}\epsilon\delta_{ij} \tag{3}$$

The constitutive equation for the pore fluid

$$p = M(\zeta - \alpha\epsilon) \tag{4}$$

Darcy's Law

$$q_i = -\frac{k}{\mu}\left(p_{,i} - f_i\right) \tag{5}$$

Equilibrium equation

$$\sigma_{ij,j} = -F_i \tag{6}$$

Continuity equation

$$\frac{\partial \zeta}{\partial t} + q_{i,i} = \gamma \tag{7}$$

where the total stress tensor σ_{ij} is the total force in the x_j direction per unit area whose normal is in the x_i direction, and α is the ratio of the fluid volume gained in a material element to the volume change of that element and is often called the Biot-Willis coefficient. p is the pore pressure, δ_{ij} is the Kronecker delta which takes the value of one if $i = j$ and zero if $i \neq j$, and G is the shear modulus of the drained porous material. ν and ν_u are the drained and undrained Poisson's ratios respectively, defined as

$$\nu = \frac{3K - 2G}{2(3K + G)} \tag{8}$$

$$\nu_u = \frac{3K_u - 2G}{2(3K_u + G)}. \tag{9}$$

ϵ is the volumetric strain defined as $\epsilon = \epsilon_{kk}$, M is the Biot Modulus defined as $M = \frac{K_u - K}{\alpha^2}$, K and K_u are the drained and undrained bulk moduli, k is the intrinsic permeability, μ is the dynamics viscosity of the pore fluid, $f_i = \rho_f g_i$ is the body force per unit volume of the fluid in the x_i direction, $F_i = \rho g_i$is the body force per unit volume of the bulk material, $\rho = (1 - \phi)\rho_s + \phi\rho_f$ is the porosity weighted density of the biphasic material, ϕ is the porosity of the porous solid, and γ is a pore fluid source term. In summary, the porous material is completely described by seven material properties, $\alpha, G, K, K_u, \rho_s, k, and\ \phi$, while the pore fluid is completely described by just $\mu\ and\ \rho_f$.

These equations can be solved using a number of numerical techniques including the Method of Potentials [3, 4, 5, 6], Finite Element Method (FEM) [7, 8, 9, 10, 11, 12], and Boundary Element Method [13, 14,15, 16, 17, 18, 19, 20, 21].

In the present analysis, the FEM capabilities of COMSOL Multiphysics (v4.2.0.150) were used to solve the linear poroelastic governing equations for the geometry considered. The inner surface of the biphasic layer is considered completely deformable and impermeable (no flow). We justify the impermeable condition based on the capillary forces as calculated for the nanofoam by Sacks and Darling 1987 [22]. The capillary pressure for a random porous medium can be expressed in terms of mean pore radius r, by $p_c = \frac{2\gamma}{r}$ [23] where γ is the liquid surface tension. To ensure that the pore remain filled we must restrict the mean pore radius to give us sufficient capillary pressure to withstand the accelerations involved. This requires

$$r < \frac{2\gamma}{\rho_f a d} \tag{10}$$

where a is the maximum acceleration imposed during capsule injection and d is the capsule diameter. A $4mm$ diameter capsule with pore radius of $100nm$, for example, can withstand up to $9400g$ of acceleration before unwetting. The proposed maximum acceleration for the LIFE injection system is 1000g giving us a significant margin of confidence that the nanofoam will not unwet. In addition, the mean pore radius will more likely be closer to $10nm$, making the safety margin even larger.

To justify the use of the poroelastic model, we must assume that the nanofoam behaves as a linear elastic material when drained and that flow through the nanofoam obeys Darcy's law. Without a detailed study of the nanofoam's structural properties and its permeability properties we are unable to utilize the more general theory of porohyperelasticity which has been applied successfully to very complex saturated porous materials [24] such as soft biological tissues.

IV. Results

Our geometry consists of a spherical shell with a thin layer of LDT saturated nanofoam of $150\mu m$ thickness. The properties of the nanofoam and LDT are given in table 2.1. Because the acceleration is only in one direction, we can take advantage of the axisymmetric nature of the problem. We therefore model the system as 2-D axisymmetric. In both the poroelastic model and linear elastic model the effects of the GDT are neglected. The acceleration profile consists of a rounded top hat function. The smoothed transition occurs over $3ms$ at both the beginning and end of the acceleration period. There is a $2ms$ period at the beginning in which there is no acceleration. The duration of the acceleration is $45ms$ followed by a zero acceleration drift period of $40ms$. The total flight/runtime is $87ms$. For clarification, we will sometimes refer to the beginning of the top hat, in which the acceleration rapidly increases, and the end of the top hat, in which the acceleration rapidly decreases, as the ramp up and ramp down periods respectively. The acceleration profile is shown in $figure\ 4.1$.

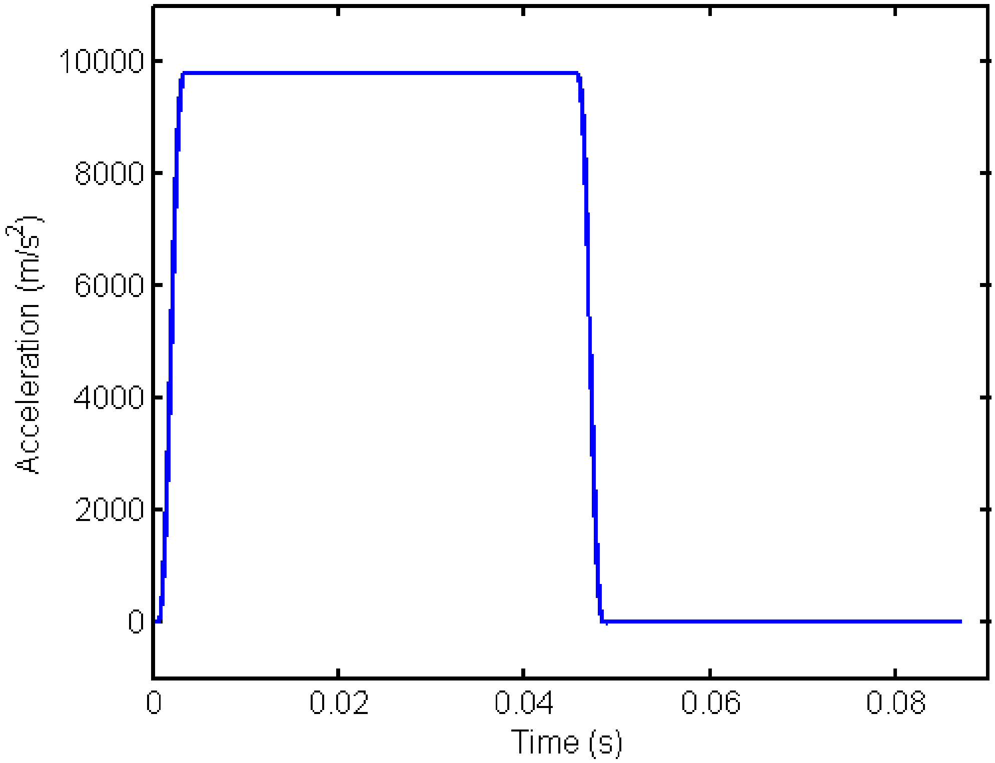

Figure 4.1: Acceleration profile used for poroelastic and linear elastic calculations.

Before any meaningful analysis can be performed it is important that we establish confidence in the quality of our solutions. We begin by performing a time step refinement study followed by a grid refinement study. In all runs, two time steps are used. At the beginning and end of the acceleration top hat, Δt_1 is used, while Δt_2 is used during the constant acceleration periods during and after the acceleration. Only Δt_1 is varied as very little change in the solution occurs outside of the ranges in which the acceleration is changing. The time step profile is depicted in $figure\ 4.2$.

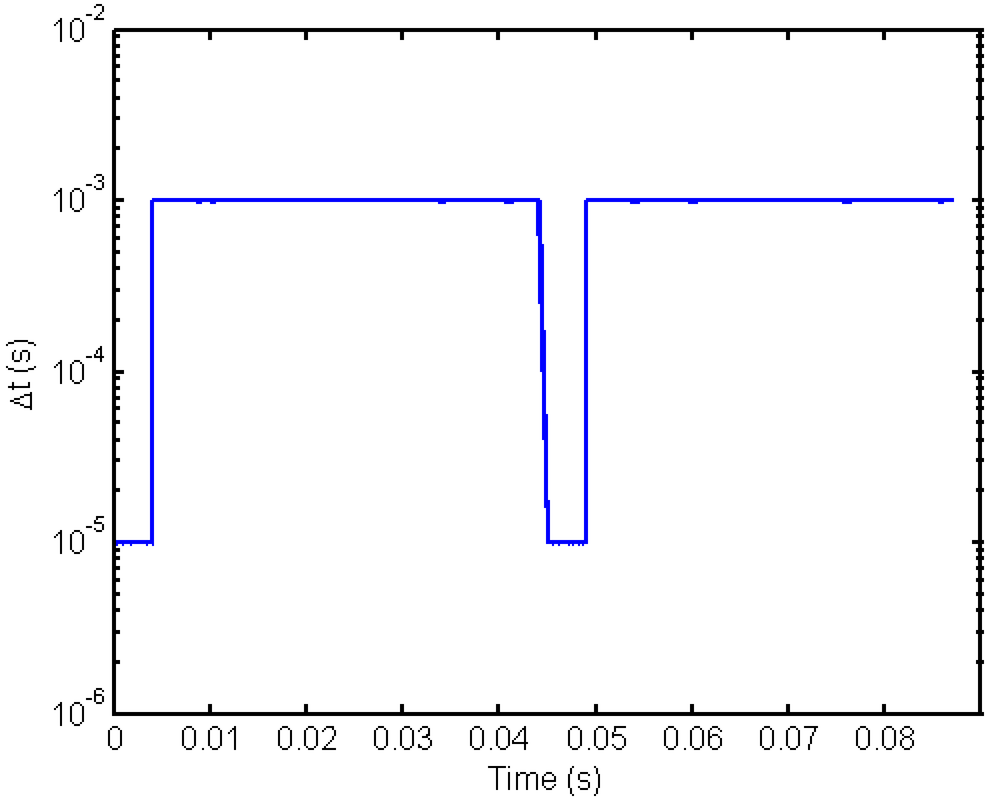

Figure 4.2: Time step profile.

Three time steps are used in the time step refinement study, $\Delta t_1 = 10^{-3}s,\ 10^{-4}s,\ and\ 10^{-5}s$. Δt_2 is held constant at $10^{-3}s$. From here on we drop the subscripts on Δt with the understanding that any reference to Δt refers to Δt_1 unless indicated otherwise. $Figure$ 4.3 shows time histories of pore pressure at $point\ A$ in $figure$ 4.4 for the poroelastic model at varying time step sizes. Pore pressure at $point\ A$ is chosen for the time step refinement study because it exhibits the greatest variation with changing time step. It is obvious from the figure that the smallest time step is entirely insufficient to resolve the changes in acceleration and produces non-physical spurious oscillations at both the beginning and end of the top hat. These oscillations also appear in radial displacement at $point\ A$, volumetric stress at $point\ A$, and maximum von Mises stress. For the intermediate time step case, the oscillations go away, but we observe too much rounding of the solution near the end of both the ramp up and ramp down periods. This is also observed in other quantities. The smallest time step solution shows little change in the solution relative to the intermediate time step solution except at the end of the ramp up and ramp down periods in which a sharper transition is captured by the finer time step solution. Unless otherwise indicated all subsequent calculations are performed with $\Delta t = 10^{-5}$s.

A curvilinear mapped mesh is used with grid spacing values, Δx, representing the longest side on any element in the domain. Four levels of mesh refinement are used in conducting the grid refinement study, $\Delta x = 40\mu m, 20\mu m, 10\mu m, and\ 5\mu m$. $Figure\ 4.4$ shows an example of the meshes used, in this case the coarsest mesh is plotted. The location, $point\ A$, refered to throughout this paper is also indicated in $Figure\ 4.4$. This point is chosen as a probe location because most of the values of interest attain their maximum amplitude at either the top or bottom of the capsule. $Figure\ 4.5$ shows the time history of volumetric strain at $point\ A$. This value is chosen for the grid refinement study because it exhibits the largest variation with grid refinement. The coarsest mesh shows a large difference from the rest throughout most of the solution. The remaining three solutions show only small differences between them. The solution is considered sufficiently converged by $\Delta x = 10\mu m$ and all calculations are performed on this mesh unless otherwise indicated.

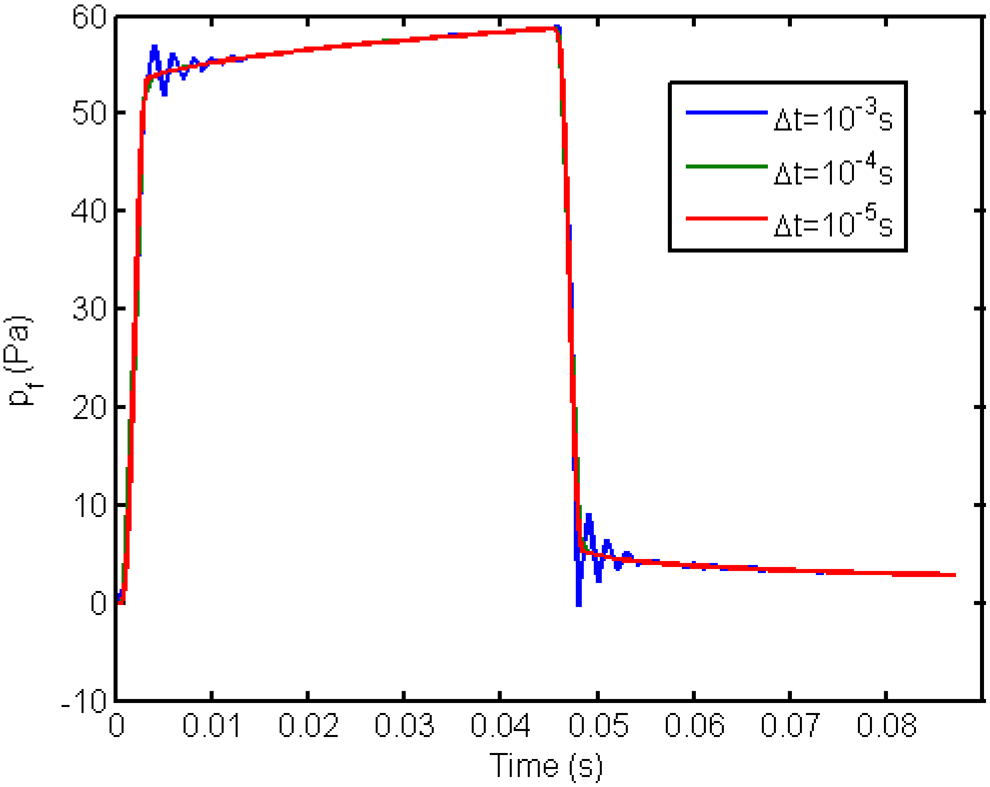

Figure 4.3: Pore pressure at Point A at several time step sizes.

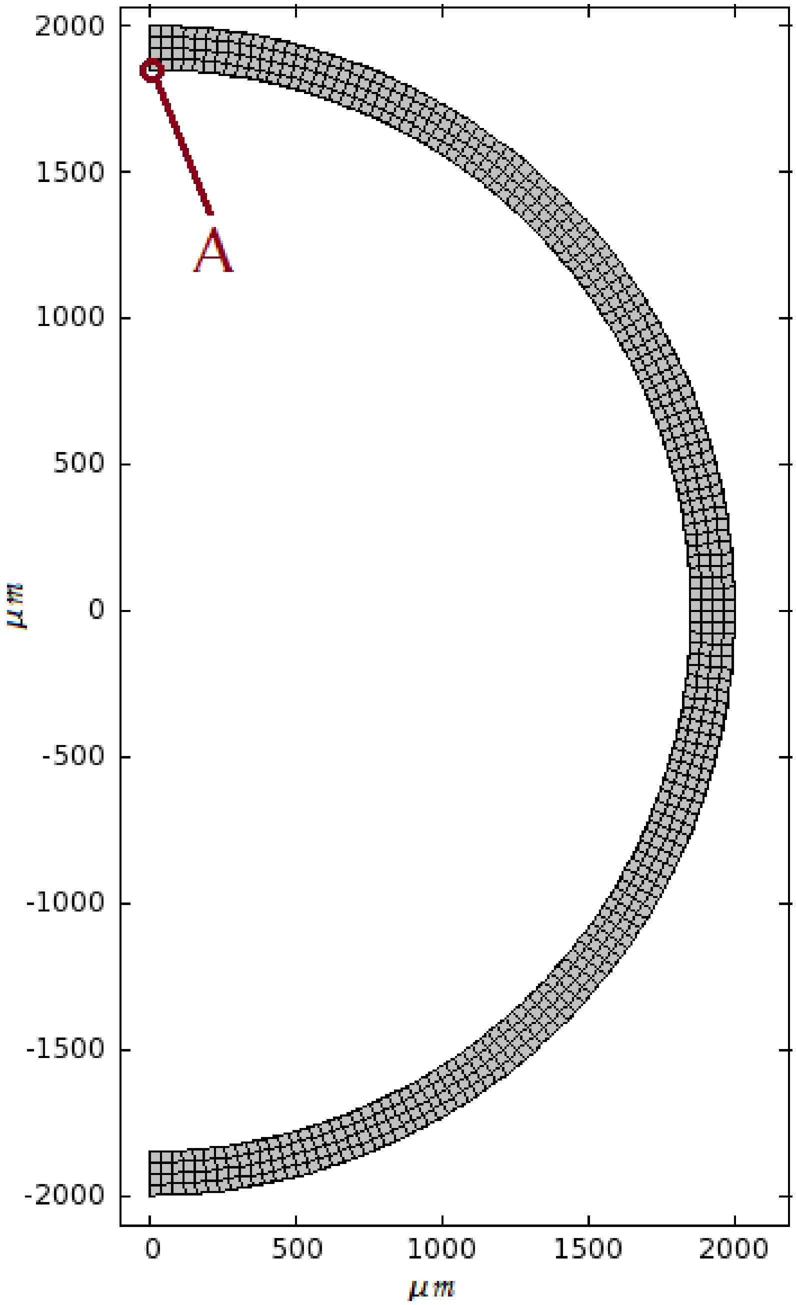
2000
1500
1000
500
0
-500
-1000
-1500
-2000
0
500
1000
1500
2000
μm
μm
A

Figure 4.4: Example of mesh used for poroelastic and linear elastic calculations. Coarsest mesh displayed.

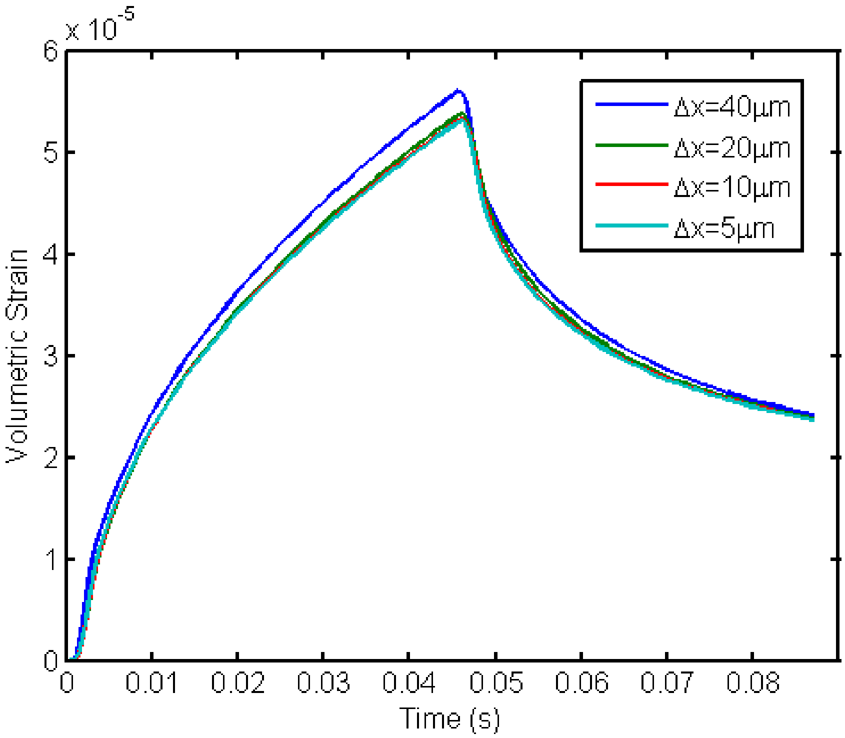

Figure 4.5: Volumetric strain at Point A for several mesh sizes.

The poroelastic model is a coupling between Darcy's Law and linear elastic theory, therefore, if the effects of the pore fluid are neglected, the linear elastic theory should be recovered. This provides us with an additional method of verifying the poroelastic model. The physical difference between the linear elastic model and poroelastic model is that 1) the linear elastic model does not account for inertial forces due to the added mass of the pore fluid, and 2) the pore fluid imparts on the material, additional rigidity, especially if the pore fluid is nearly incompressible (as is the case with LDT), thereby altering its structural response. Based upon these two physical phenomena, if we eliminate the inertial and compressibility effects from the pore fluid, we should recover the behavior of the linear elastic model applied to just the porous material. We achieve this by reducing the density and increasing the compressibility of the pore fluid, thus reducing the inertial effects and the added rigidity provided by the pore fluid respectively. $Figure\ 4.6$ and $figure\ 4.7$ show the displacement and volumetric strain respectively at $point\ A$ for several densities and compressibilities as well as for the linear elastic model of just the porous material. The density and compressibility for each plot are calculated by dividing and multiplying respectively, the nominal values by a factor β. Different values of β were chosen between the two plots to highlight the quantity's dependence on β. As density decreases and compressibility increases the poroelastic solution converges to the linear elastic solution in both displacement and strain. However, we note that displacement changes very rapidly for small β whereas strain doesn't begin to change significantly until larger β. The changes in density are large for smaller β, indicating that displacement is most sensitive to changes in the inertial forces (density) whereas changes in compressibility are largest when β is large indicating that volumetric strain is most sensitive to the additional rigidity provided by the pore fluid (compressibility).

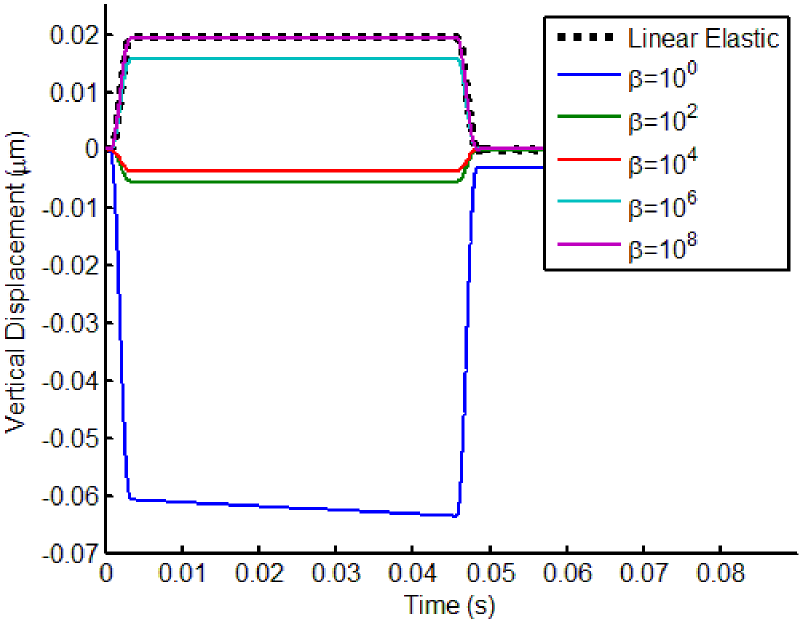

Figure 4.6: Displacement at Point A for several values of β.

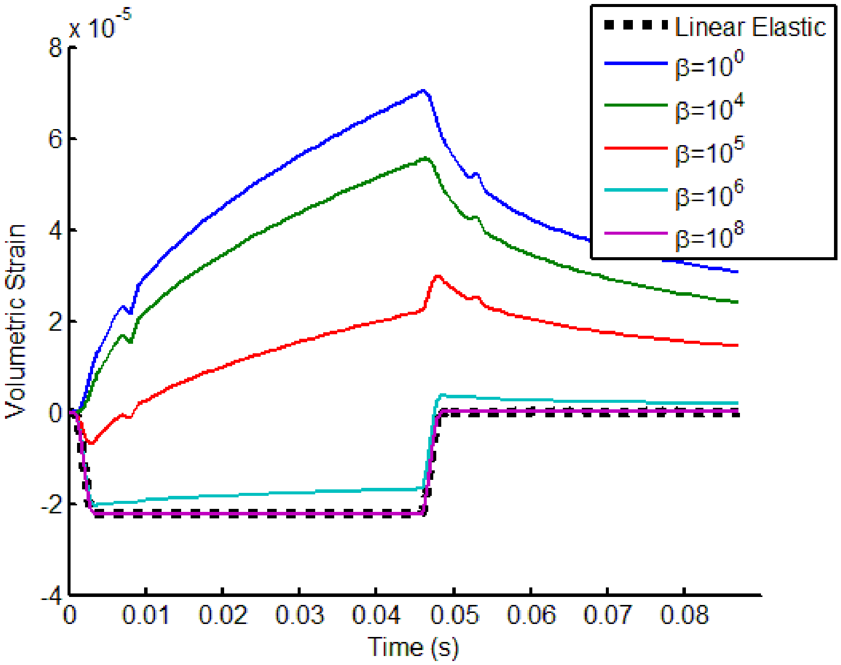

Figure 4.7: Volumetric strain at Point A for several values of β.

Having established confidence that our results are converged and that the model is a consistent extension of the linear elastic model, we now analyze the physical response of the LDT saturated nanofoam to the acceleration profile shown in $figure$ 4.1. $Figure$ 4.8 shows a series of snapshots of the LDT/nanofoam layer throughout the flight profile. The displacements are scaled up by a factor of 1200 to make them more obvious. The plots are colored by the magnitude of radial displacement. The layer begins uniform in thickness. Once the acceleration begins the layer quickly becomes thicker/thinner at the top/bottom with this trend increasing slightly during the acceleration period. Once the acceleration ends, the layer quickly returns to near-nominal thickness everywhere.

T=0.000 s	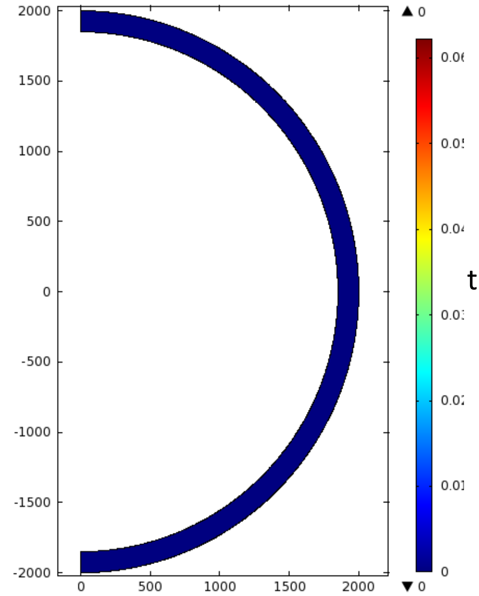	t=0.045 s	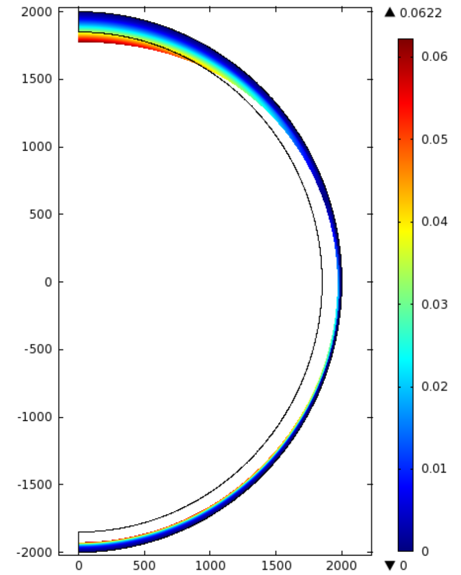
t=0.004 s	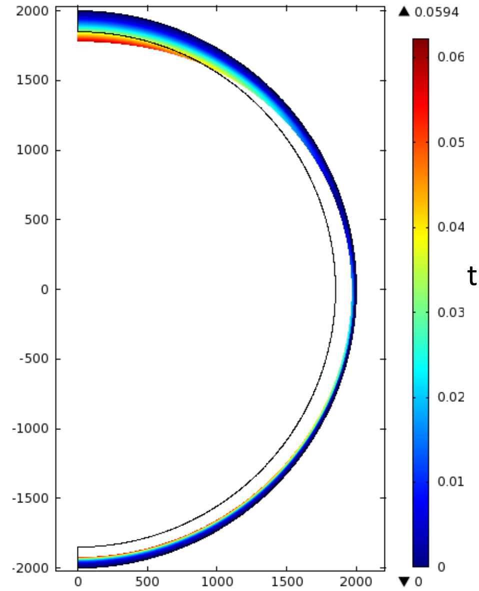	t=0.087 s	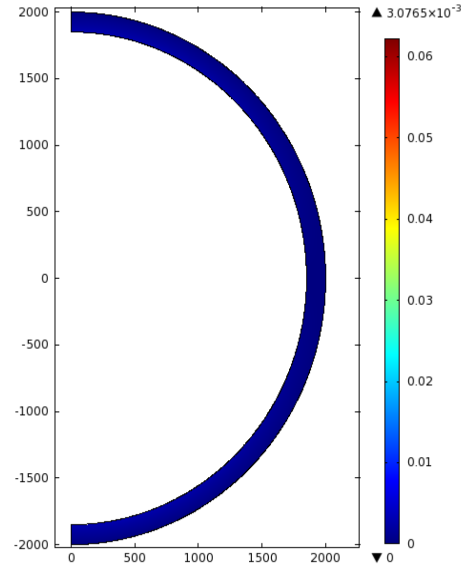

Figure 4.8: Snapshots of deforming LDT/nanofoam layer colored by radial displacement magnitude. Displacement is scaled up by a factor of 1200.

The results of the poroelastic model are compared to the results of a simplified linear elastic model in which the material properties of the nanofoam and the density of the LDT are used. This simplified model is a worst case scenario (WCS) as the material suffers from the increased inertial forces induced by the presence of the dense LDT without the additional structural rigidity provided by the nearly incompressible pore fluid. $Figure\ 4.9$ shows the displacement at $point\ A$ for both models. The two solutions show very different qualitative behavior in that the sign of the displacement differs between the two models. A similar difference in qualitative behavior is observed in the volumetric strain shown in $figure\ 4.10$. Under acceleration, the linear elastic model predicts that the material will simply expand or collapse under its own weight. This is the fundamental behavior of the model and is really the only physics that it captures. The poroelastic model, however, predicts that inertial forces drive the pore fluid from the bottom to the top of the capsule. As a result a hydrostatic pressure difference is established between the top and bottom of the capsule with the pore pressure increasing at the top and decreasing at the bottom. This high pore pressure at the top expands the porous material while the low pressure at the bottom collapses the material. This translates to a negative displacement at $point\ A$ as the material expands (positive volumetric strain) downward, whereas the linear elastic material collapses (negative volumetric strain) upward under its own weight.

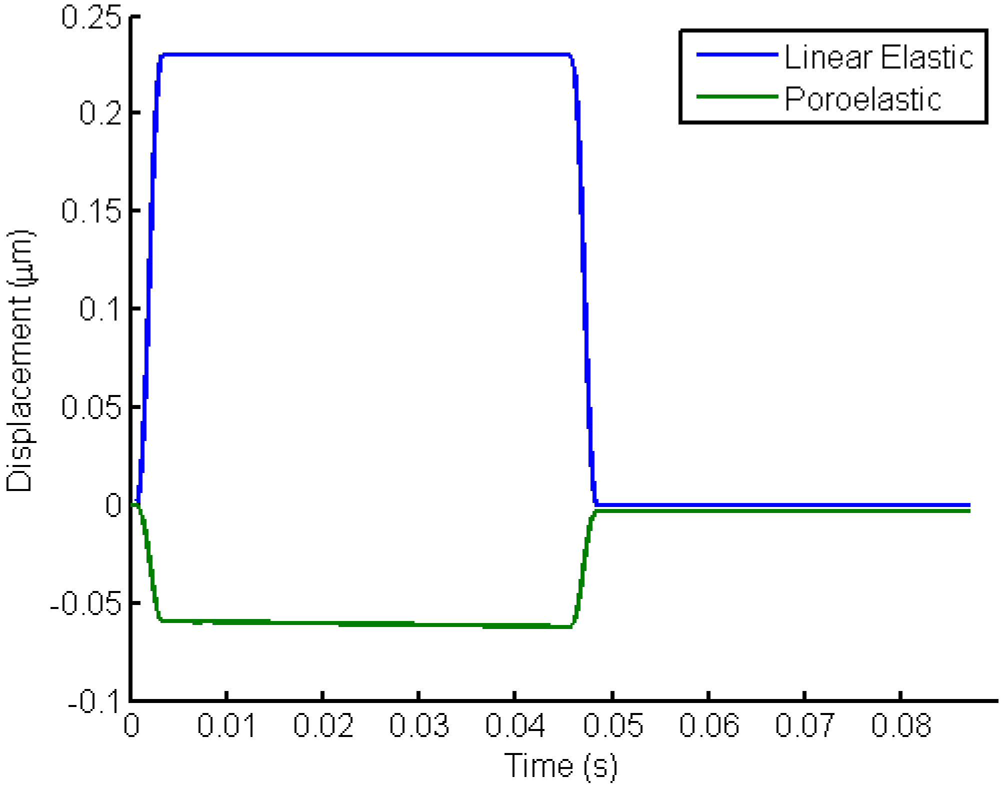

Figure 4.9: Displacement at Point A for poroelastic model and WCS linear elastic model.

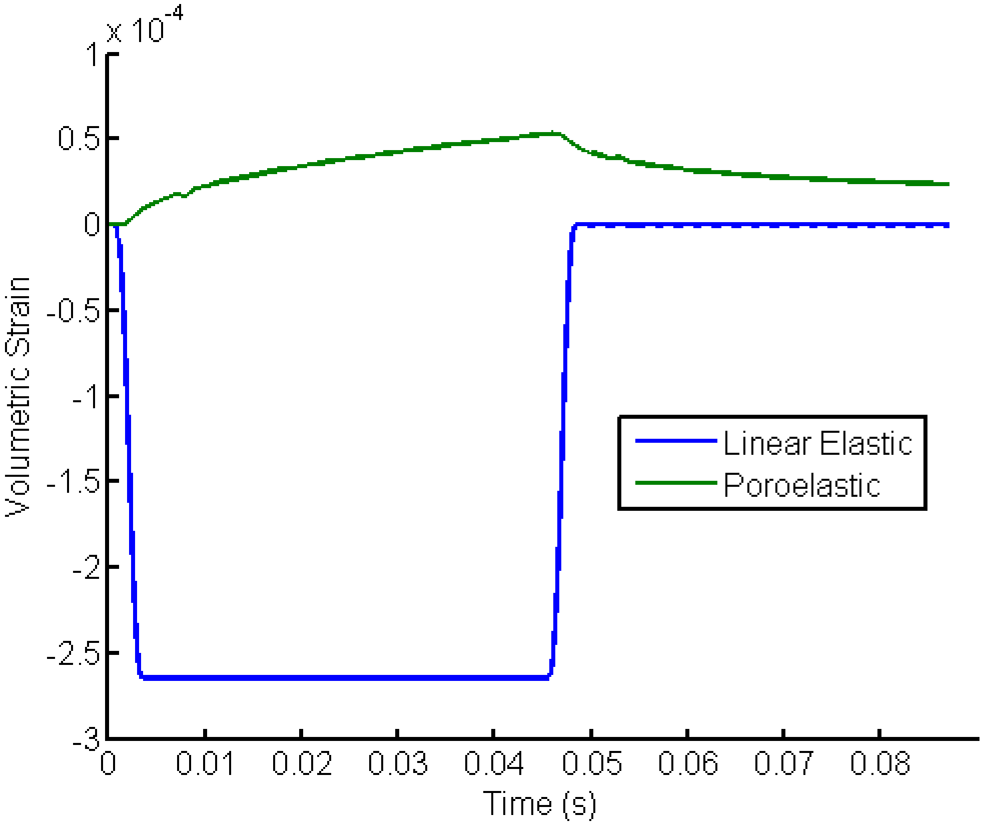

Figure 4.10: Volumetric strain at Point A for poroelastic model and WCS linear elastic model.

These results paint a positive picture for the technology of interest. The maximum radial displacement (located at $point\ A$) for either model at the time of ignition is well below (at least two orders of magnitude) the $1\mu m$ tolerance. In fact, according to both models, the LDT/nanofoam layer never, at any point in the flight profile, deforms beyond the specified tolerance. A summary of key displacement values is given in $table\ 4.1$.

	Max During Flight	At Ignition
Poroelastic	$0.0622\mu m$	$0.0031\mu m$
WCS Linear Elastic	$0.2302\mu m$	1e-13μm

Table 4.1: Summary of displacement at Point A for poroelastic model and WCS linear elastic model.

Both of these models (poroelastic and linear elastic) have been used with the assumption that the nanofoam will not fail structurally (no tearing, cracking, or separating). Although a detailed investigation into the nanofoam's structural integrity under these conditions has not been performed, preliminary qualitative tests of saturated nanofoam under acceleration indicate that the nanofoam will maintain its structural integrity and remain attached to the inner surface of the capsule. A chief quantity used to determine if a material will fail is the von Mises stress. If this quantity exceeds an experimentally determined failure threshold, than the material is at risk for failure. $Figure\ 4.11$ shows the von Mises stress at $point\ A$ for both models. The two models do not show significantly different results with a maximum stress of $508.8\ Pa$ for the poroelastic model and $530.6\ Pa$ for the linear elastic models. For standard building materials these values are incredibly low, however, without proper testing of the nanofoam considered, the context for these values remains unclear.

The final properties of the nanofoam to be used in the LIFE target are still very uncertain. Additionally, some of its properties are not easily measured or are difficult to reproduce consistently over the course of multiple batches. Two values in particular prove difficult to define/measure with certainty and as such a sensitivity study with respect to these quantities is performed. The two values of particular interest are the nanofoam porosity, α, and the nanofoam permeability, κ. For these sensitivity studies two quantities are considered. The first is the displacement at $point\ A$, which is the quantity of chief concern in this study, as it has the greatest impact on the viability of this technology. The second quantity is the volumetric strain at $point\ A$ and the maximum liquid velocity for porosity and permeability respectively. These latter quantities were chosen because they exhibit the greatest sensitivity to the parameters being investigated. $Figures\ 4.12$ and 4.13 show the displacement and volumetric strain at $point\ A$ for three values of porosity. As the porosity decreases, there is less LDT to force the nanofoam to expand/contract per volume of nanofoam. We observe that as the porosity decrease both the displacement magnitude and the volumetric strain decrease. Although the volumetric strain appears to be quite dependent on porosity, this does not translate to the displacement being equally dependent.

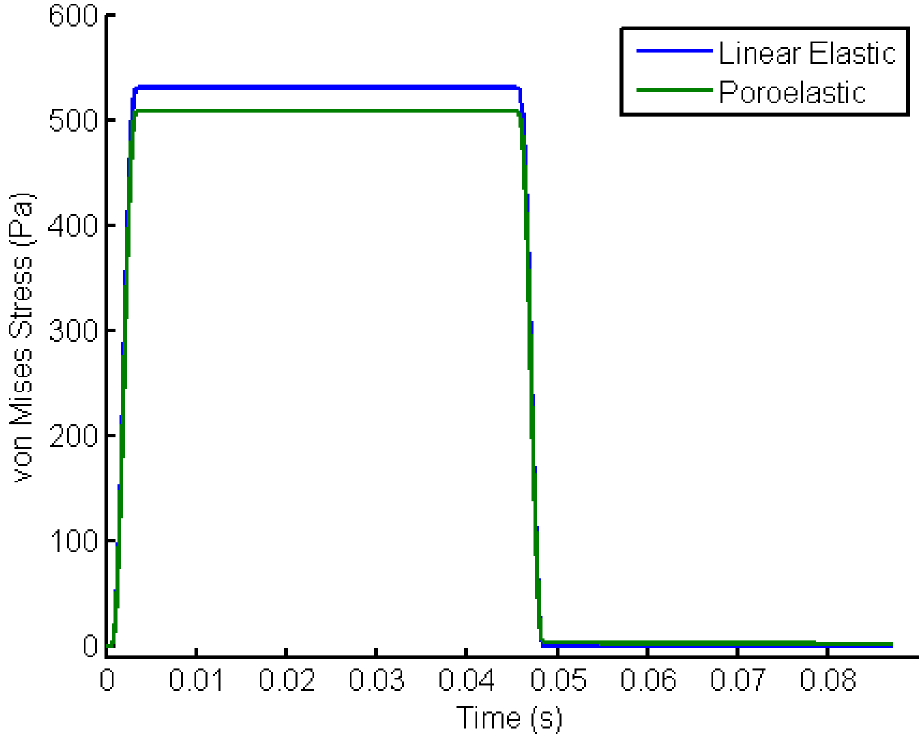

Figure 4.11: Maximum von Mises stress for poroelastic model and WCS linear elastic model.

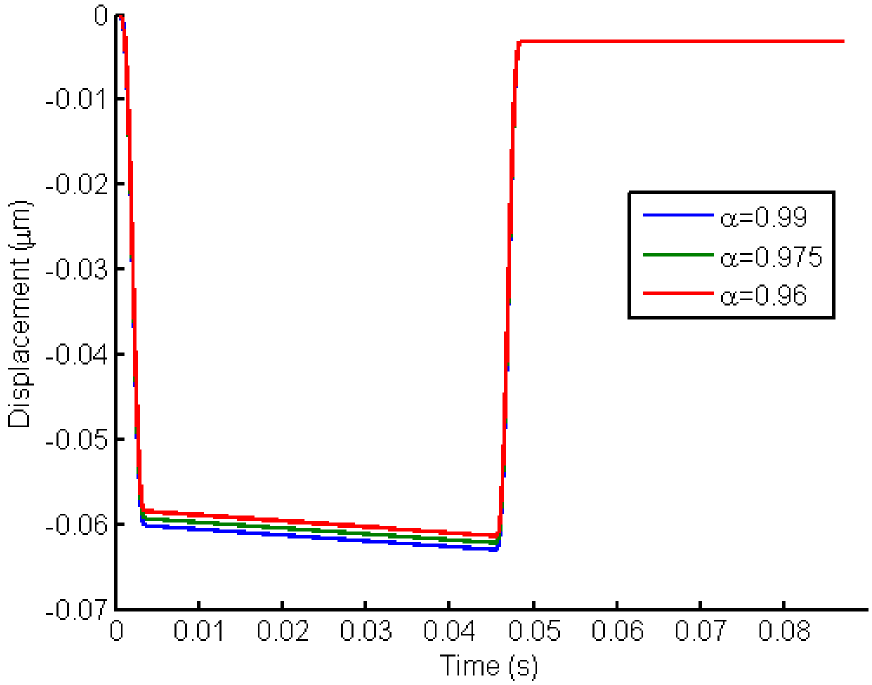

Figure 4.12: Displacement at Point A for several porosities.

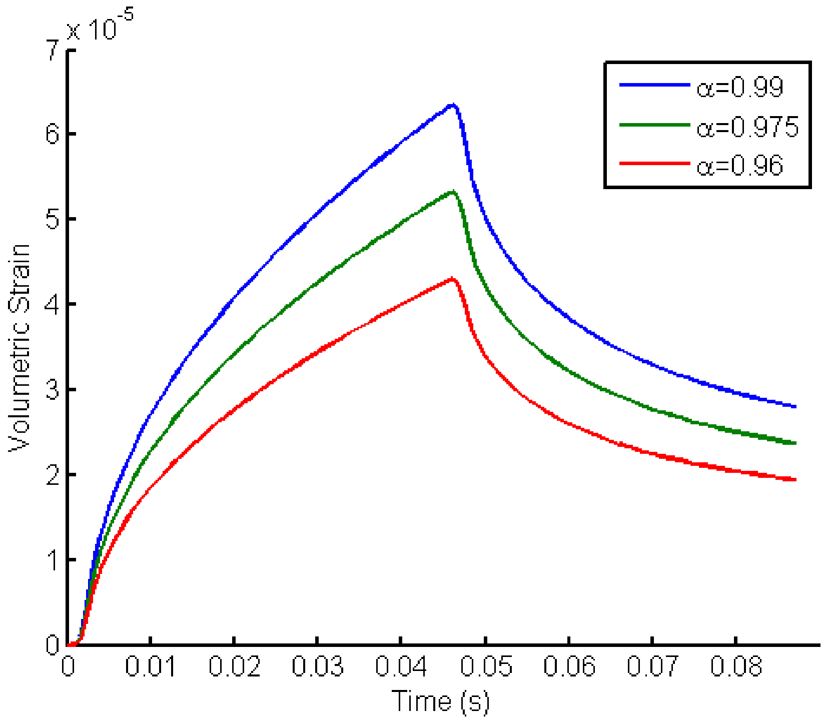

Figure 4.13: Volumetric strain at Point A for several porosities.

The velocity of the pore fluid is a critical parameter in determining the relevant time scale for the pore fluid motion in the system. The pore fluid velocity is proportional to the permeability according to Darcy's Law and so we expect the pore fluid velocity, as well as the displacement to be closely linked to the permeability of the nanofoam. The exact value of the permeability is unknown, although experiments are underway to measure this. However, based on the simple empirical relationship

$$k = Cd^2 \tag{11}$$

where d is a characteristic length scale of the pore structure (i.e. mean pore diameter or, in the case of packed grains, mean grain diameter) and C is a dimensionless coefficient highly dependent on the pore microstructure, we can estimate a range for the permeability based on a range of pore diameters. Harleman et al. 1963 [25] found the value of $C = 6.54 \times 10^{-4}$when d is measured in cm and k in cm^2, to give fairly good agreement with experimental values. We must emphasize, however, that the coefficient C is dependent on the microscale structure of the porous material and therefore, these results should be considered to be order of magnitude estimates. Using $equation$ 11 with a range of pore sizes of $d = 10nm\ to\ 300nm$ gives a range of permeabilities of $k = 7 \times 10^{-20}m^2$ to $6 \times 10^{-17}m^2$. Because of the large uncertainty in these estimates we choose to investigate a wider range of permeabilities of $k = 1 \times 10^{-20}m^2$ to $1 \times 10^{-16}m^2$. $Figures$ 4.14 and 4.15 show the radial displacement at $point\ A$ and the maximum LDT velocity respectively. As the permeability increases, the pore fluid can flow with a faster velocity through the nanofoam. This means that more fluid will move from the bottom of the capsule to the top, causing a larger differential in pore pressure. This higher/lower pressure causes the nanofoam to expand/collapse more. We observe that as the permeability increases, the maximum displacement as well as the final displacement both increase. We also note that during the acceleration, the nanofoam continues to expand thereby increasing the displacement. The rate of this increasing displacement is proportional to the pore fluid velocity, which is also observed to increase (linearly) with permeability.

Having established that a LDT saturated nanofoam will maintain its shape to within the tolerances specified, we can ask the question of whether the nanofoam is even necessary. Under acceleration into the chamber, a liquid will pool at the top of the capsule. During the zero acceleration drift phase, will surface tension draw the LDT along the sides of the capsule and form a uniformly thick layer? We now present preliminary results which attempt to answer these questions.

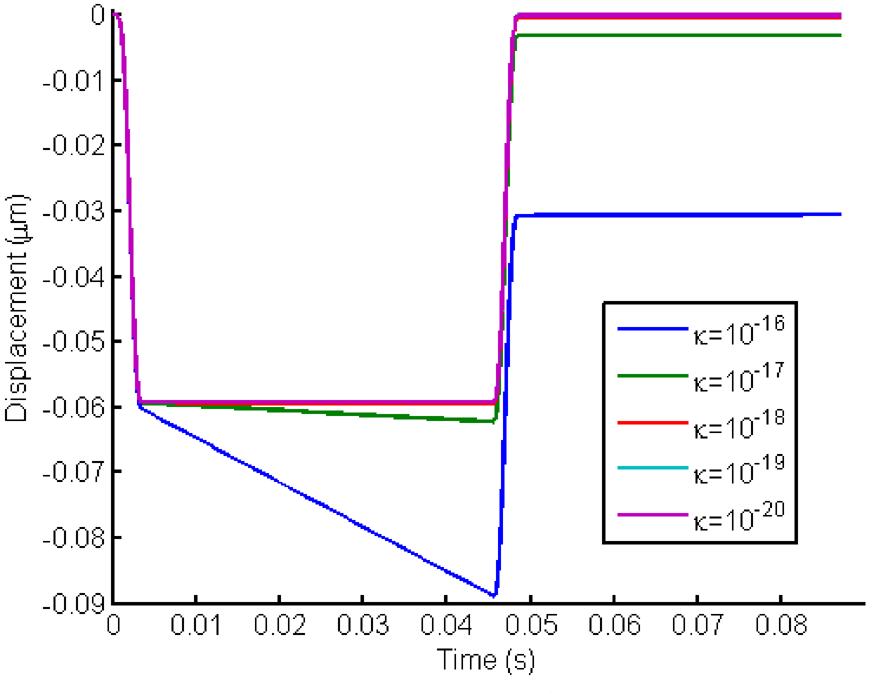

Figure 4.14: Displacement at Point A for several permeabilities.

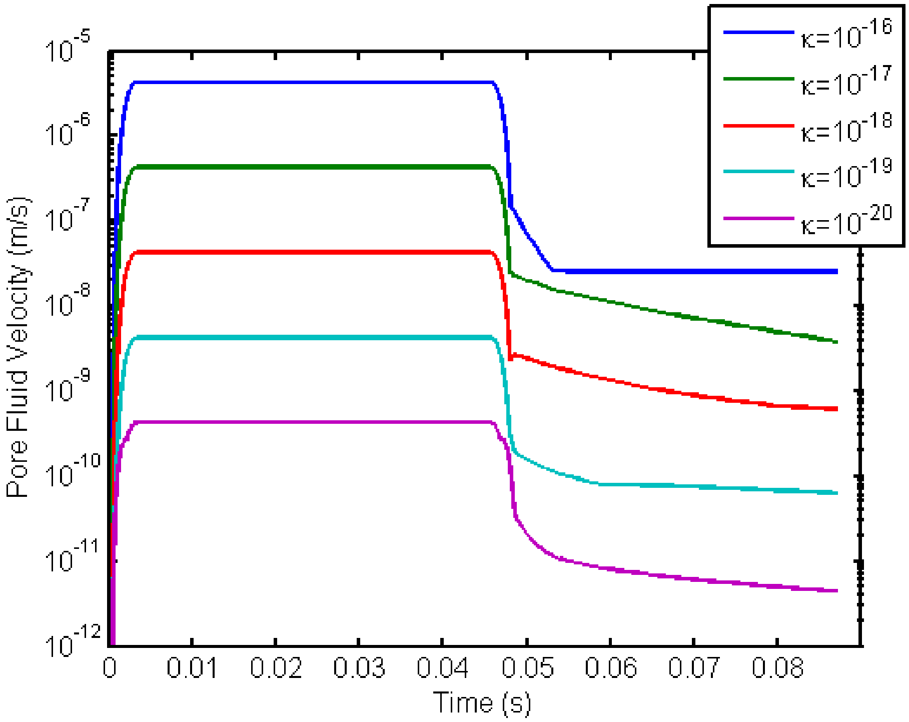

Figure 4.15: Maximum liquid velocity for several permeabilities.

We perform a 2-D axisymmetric calculation of a two phase flow under acceleration. The capsule diameter is $d = 2mm$, half that of the poroelastic calculation, to reduce the computational cost. The Volume of Fluid (VOF) technique is used to model the multi-phase flow. Capsule surface is modeled as no-slip. The LDT begins in a uniform layer of $150\mu m$ thickness at the capsule surface, with the inner region composed of GDT at conditions specified in $table$ 2.1. The acceleration is held constant at $a = 1000g$ for $0.045s$ after which it is set to zero. During this period of zero acceleration, the surface tension is allowed to reform the LDT layer. The simulation is halted at $t = 0.085s$ which is the point at which ignition occurs. The calculation is performed using the commercial CFD software STAR-CCM+. The simulation is conducted using 31,993 polyhedral elements and a time step of $\Delta t = 10^{-6}s$ is used with 30 sub-iterations. Surface tension and viscous effects are included.

LDT has an interesting behavior when in contact with both a solid surface and GDT. Under these conditions, LDT has a contact angle, the angle the LDT makes with the solid surface relative to its normal, of $\theta = 0°$ [26]. LDT will wet all surfaces it can reach with at least a monolayer. This means that if a puddle of LDT were to be placed at the bottom of a sealed room, it would spread out across the floor, climb up the walls, and across the ceiling until the entire interior of the room was wetted. This behavior is captured in the current calculation.

$Figure$ 4.16 shows contours of volume fraction of GDT at the initial conditions. From here on, the orientation of the capsule is such that the capsule accelerates to the right, thus the "top" is on the left side of the plot and "bottom" is on the right side.

$Figure\ 4.17$ shows snapshots of volume fraction of GDT during the early stages of acceleration when the LDT sloshes to the top of the capsule. $Figure\ 4.18$ shows the same contours at $t = 0.045s$ at which point the acceleration ends. $Figure\ 4.19$ shows snapshots during the recovery period when surface tension causes the LDT to recoat the entire inner surface of the capsule. Lastly, $figure\ 4.20$ shows the final configuration of the LDT at $t = 0.085s$.

Once the acceleration is applied, the liquid violently sloshes to the top of the capsule, eventually pooling at the top. When the acceleration stops, the surface tension, immediately begins to rewet the exposed surfaces, and reforms a layer of LDT. By the time of ignition, although the LDT has formed a new layer, it is not uniform in thickness. Another way of describing this is that the GDT bubble has achieved a spherical shape, however, it is not centered inside the capsule. This is not an unexpected result as there are no forces (of which the author is aware) which drive the GDT bubble to the center in this configuration. Additionally the cumulative effect of the acceleration due to gravity and the deceleration due to drag on the target as it flies through the chamber has been neglected in this analysis. The drag on the target has not yet been quantified so it is unclear what the magnitude or even the sign of this cumulative force experienced by the capsule during flight might be. Unless these two forces perfectly cancel, there will be a net force on the capsule which will serve to deform the LDT layer either towards the top or bottom of the capsule (depending on the sign of the net force). These facts prevents such a simple configuration from being utilized.

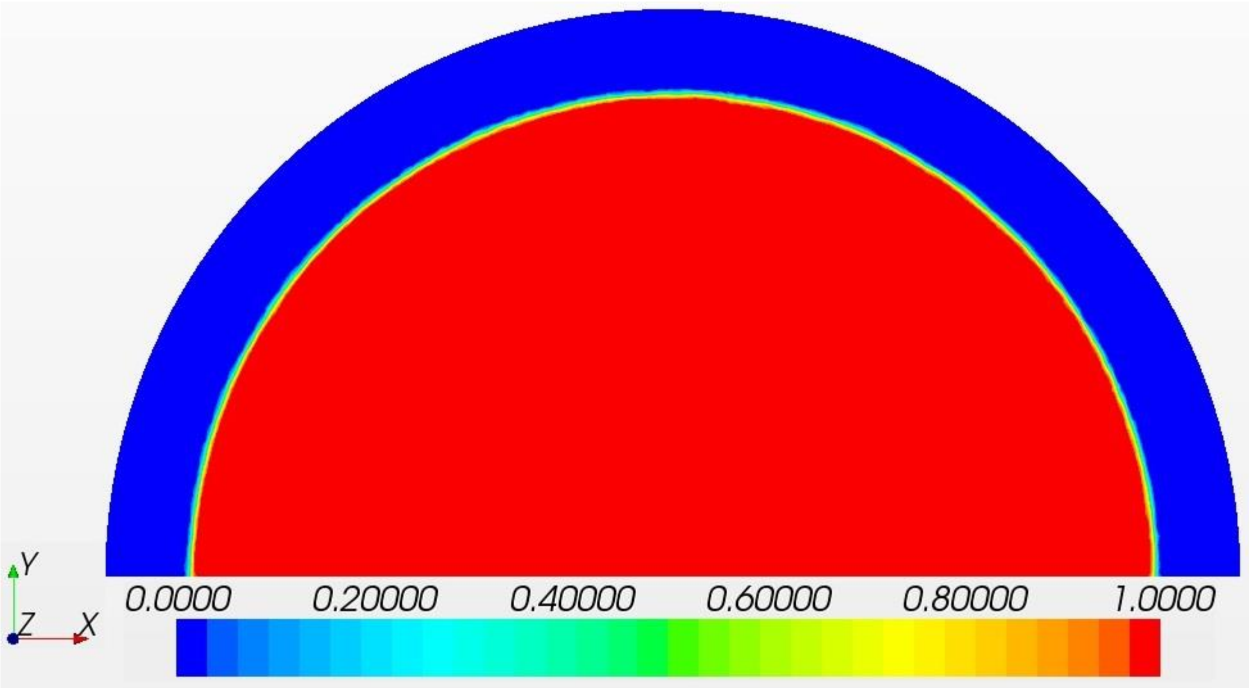

Figure 4.16: Volume fraction of GDT at the initial conditions.

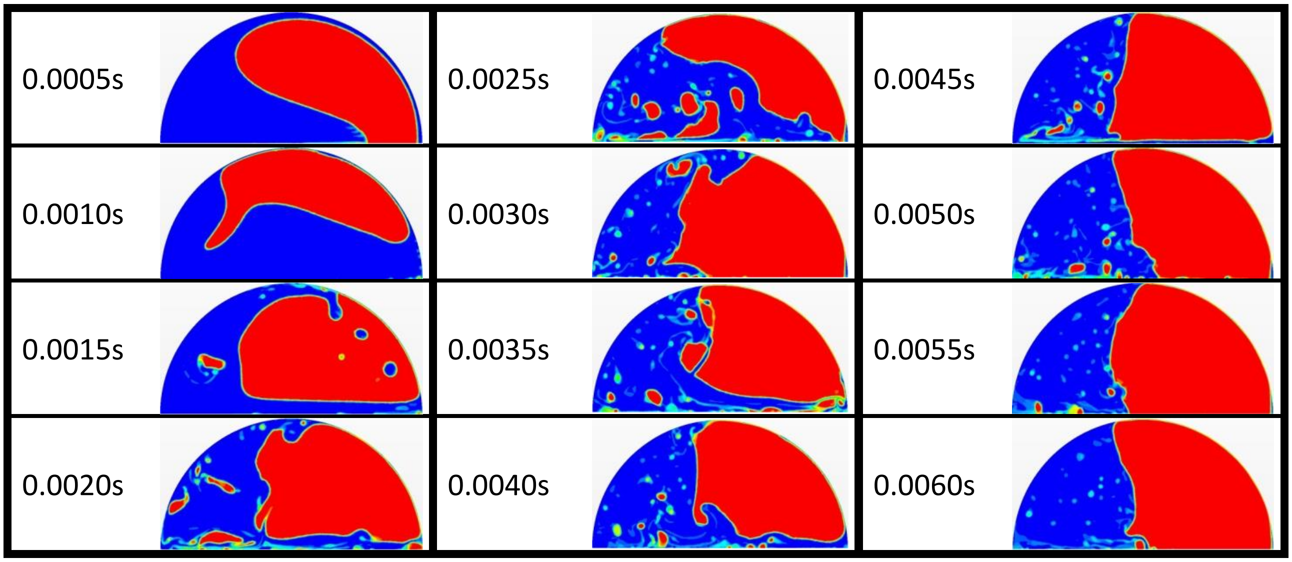
0.0005s
0.0025s
0.0045s
0.0010s
0.0030s
0.0050s
0.0015s
0.0035s
0.0055s
0.0020s
0.0040s
0.0060s

Figure 4.17: A series of snapshots of volume fraction of GDT during the initial acceleration period.

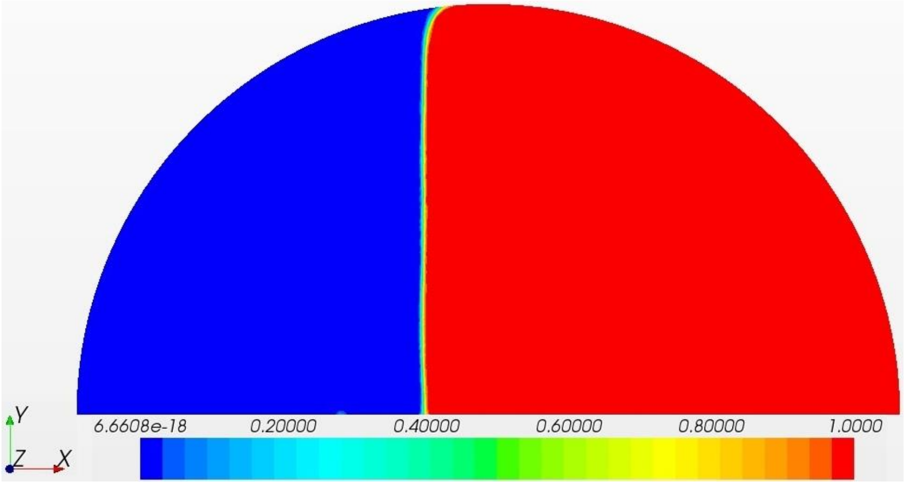
Y
Z
X
6.6608e-18
0.20000
0.40000
0.60000
0.80000
1.0000

Figure 4.18: Volume fraction of GDT at the end of acceleration (t=0.045s).

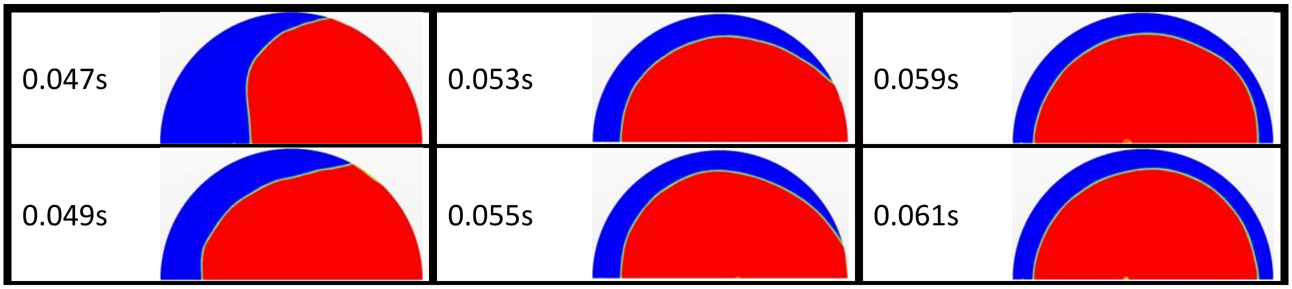
0.047s
0.053s
0.059s
0.049s
0.055s
0.061s

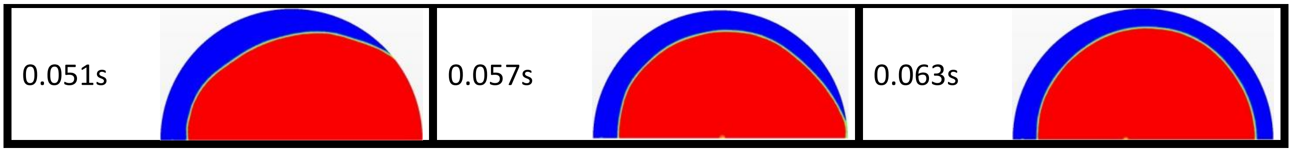

Figure 4.19: A series of snapshots of volume fraction of GDT during the recovery period.

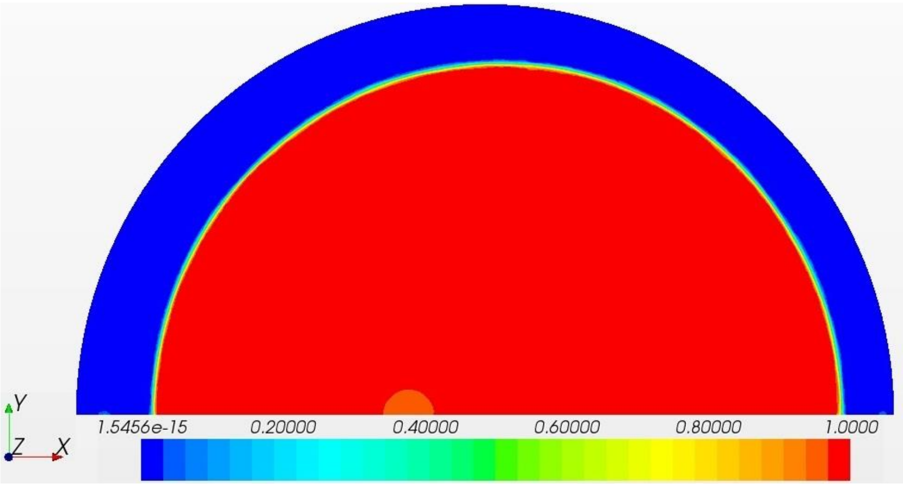

Figure 4.20: Volume fraction of GDT at the time of ignition (t=0.085s). Note that the GDT bubble is spherical but not centered.

The fact that the surface tension is so effective at reforming the spherical bubble indicates that there may be a way to drive the bubble towards the center. As long as there is a surface upon which the surface tension may act, the LDT will pull itself up that surface. In theory, all that is required to create a uniformly thick, $150\mu m$ layer of LDT would be to provide the LDT with a surface which extended $150\mu m$ into the capsule at 3 points. As long as these points are not precisely on opposite sides of the capsule, it is enough for surface tension to eventually form a spherical bubble of GDT that is perfectly centered within the capsule.

$Figure\ 4.21$ depicts a sketch of how this process might work. $Frame\ A$ shows the state of the LDT and GDT just before the acceleration ends. At this time the LDT has settled to the top of the capsule. $Frame\ B$ depicts a time after the acceleration has ended in which the LDT has reformed a layer and the GDT bubble is spherical, but it is not centered within the capsule. $Frame\ C$ depicts the LDT climbing up a surface thereby deforming the spherical bubble. This configuration is not in equilibrium because the surface tension wants to maintain as close to spherical a shape as possible for the GDT bubble but it also wants to wet the protruding surface. These two mechanisms drive the bubble to the very tip of the protruding surface. Finally in $frame\ D$ surface tension has reformed a spherical bubble whose surface is tangent to the tip of the protruding surface. This process can be applied in three directions to re-center the bubble in all three dimensions. These structures might be composed of a lattice, cilia like fibers, honeycomb, carbon nanotubes, etc. The key is to design a structure which will withstand the inertial forces during acceleration and provide a surface which extends only $150\mu m$ into the center of the capsule on which the LDT's surface tension can act. These features must all be attained without compromising the design requirements established by the fusion physics. This is essentially the purpose of the nanofoam, however, the complicated manufacturing process involved with the nanofoam, may make alternative designs more attractive. Another method of re-centering the bubble is to spin the target as it flies through the chamber. The centrifugal forces will drive the heavier LDT towards the outside of the capsule, centering the bubble. The drawback to this technique is that by spinning the capsule, the LDT now collects at the sides of the capsule causing the bubble to become ellipsoidal in shape, rather than spherical (shown in $figure\ 4.22$). Without further analysis, it is unclear whether a rate of spin sufficient to re-center the bubble in time, would be too fast for surface tension to maintain a near spherical shape.

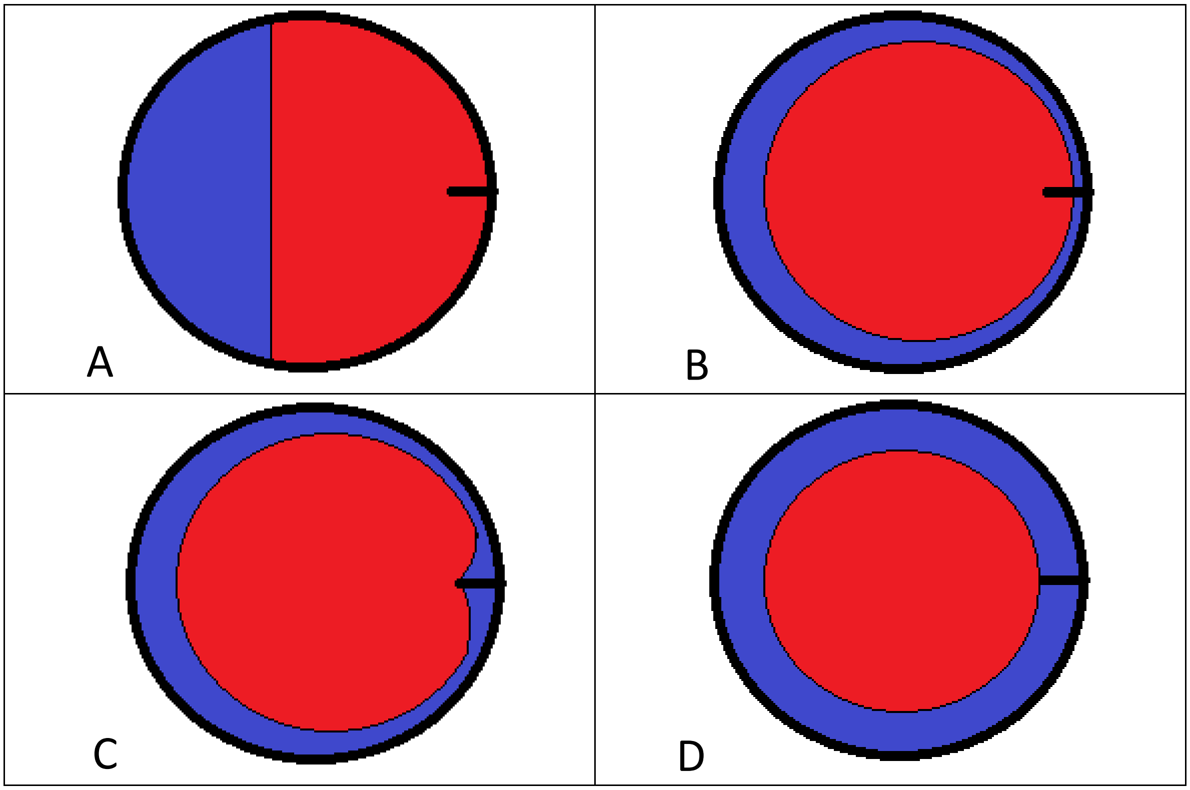

Figure 4.21: Snapshot sketches of one possible technique for centering the GDT bubble.

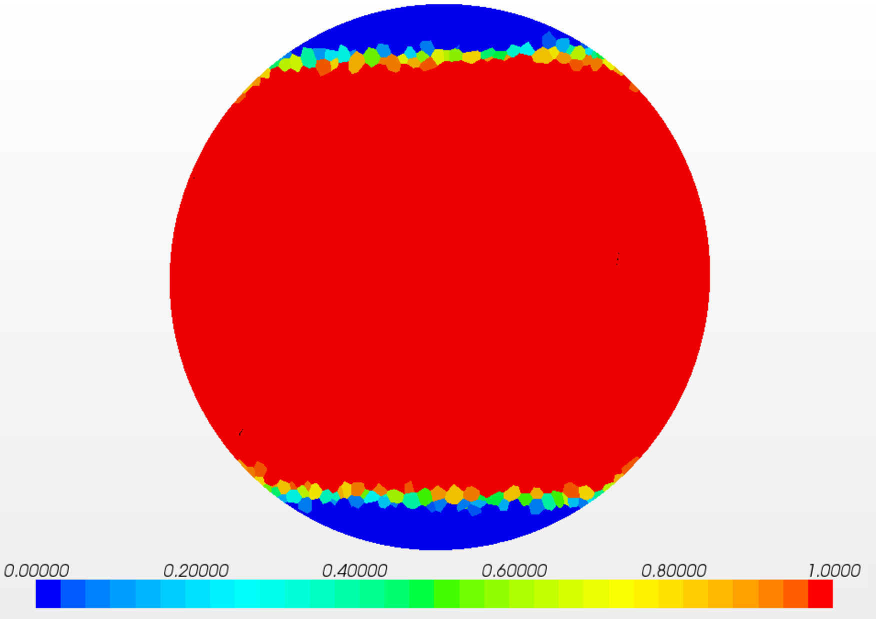

Figure 4.22: Volume fraction of gaseous DT under 80rps spin.

The main quantity of interest in this study is the displacement of the LDT from the nominal layer thickness of $150\mu m$. $Figure\ 4.23$ shows the time history of the maximum radial displacement of the LDT from nominal. We observe that once the LDT pools at the top of the capsule the maximum displacement value is around $150\mu m$. Once the acceleration ends and the LDT layer begins to recoat the inside surface of the capsule, we observe that the maximum displacement rapidly drops. However, as discussed earlier, there are no forces which drive the LDT to a uniform layer as is indicated by the displacement never returning to zero, but rather settling around $25-35\mu m$. $Figure\ 4.24$ shows the volume fraction of LDT integrated over the entire domain, normalized by the initial value. This serves as a check of how well the code is conserving the two phases, LDT and GDT. As can be seen, the volume fraction of LDT is maintained throughout the entire simulation to within 0.002%.

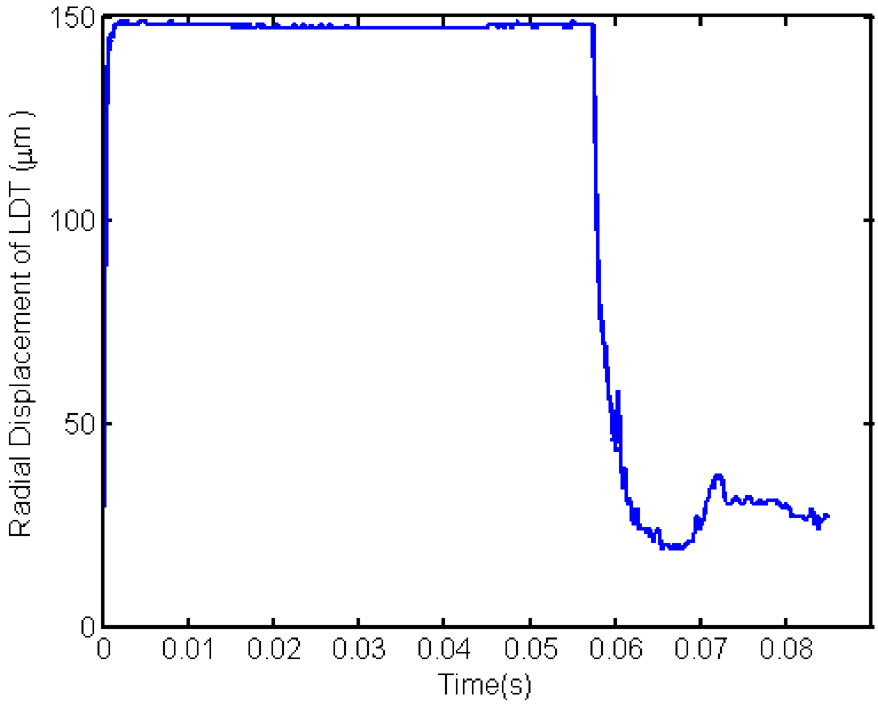

Figure 4.23: Maximum radial displacement of LDT/GDT interface. During the recovery period, the displacement does not return to zero as desired.

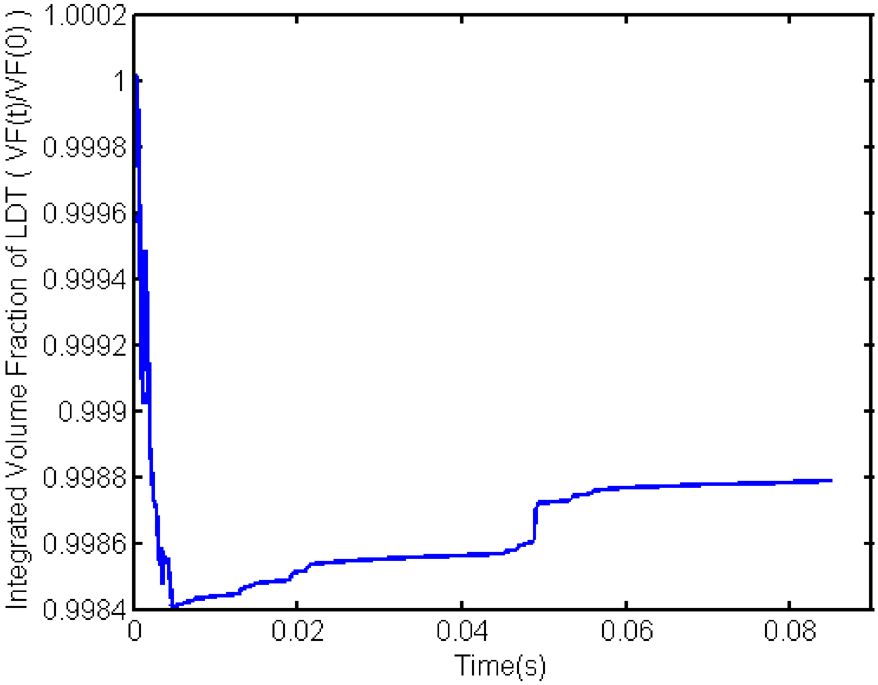

Figure 4.24: Integrated volume fraction of LDT.

V. Conclusion

We have performed a series of calculations investigating the dynamic response of a LDT saturated nanofoam coating the inside of a spherical shell under extreme acceleration. The investigation focused on the use of a poroelastic model for the saturated nanofoam. Grid and time step convergence was established. It was verified that the poroelastic model reduces to the linear elastic model if the effects of the pore fluid mass and compressibility are eliminated as expected. Comparisons against a "worst case scenario" linear elastic model, in which the material is considered to have the added mass of the pore fluid while not possessing the added rigidity provided by the pore fluid, were made. It was observed that the radial displacement is below the $1\mu m$ tolerance at all times during the flight profile, and several orders of magnitude lower at the time of ignition for both models. A sensitivity study was performed on both the porosity and permeability of the nanofoam. These studies indicated that radial displacement decreases with decreasing porosity and also decreases for decreasing permeability. The overall behavior of the poroelastic model under the conditions considered can be summarized as follows: Under acceleration the pore fluid flows from the bottom to the top of the capsule which causes the nanofoam to expand at the top and collapse at the bottom. The less LDT there is, the less of this expansion/contraction occurs. Additionally, the higher the permeability, the faster the fluid flows, and the more fluid collects at the top and drains away from the bottom, thereby increasing the amount of expansion/contraction which occurs. Over the range of porosities and permeabilities investigated, the radial displacement at the top never exceeds the allowable tolerance.

Preliminary results of a system without the nanofoam indicate that the surface tension of the LDT is sufficient to reform a spherical GDT bubble before ignition. There are, however, no forces to drive the bubble to the center of the capsule in this configuration. However, the fact that the surface tension is sufficient to reform a spherical bubble so quickly indicates that even a simple structure on which the surface tension may act, could be sufficient to create a uniformly thick LDT layer. This last point is a line of future work which holds significant potential in that it may eliminate the need for the nanofoam, and its complicated manufacturing process, entirely.

References

[1] Biot, M. A., "Le 118roblem de la consolidation des matières argileuses sous une charge:, Ann. Soc. Sci. Bruxelles, B55, 110-113, 1935.

[2] Biot, M. A., “General theory of three-dimensional consolidation”, J. Appl. Phys., 12, 155-164, 1941.

[3] Rice, J. R. and Cleary, M. P., “Some basic stress-diffusion solutions for fluid saturated elastic porous media with compressible constituents”, Rev. Geophys. Space Phys., 14, 227-241, 1976.

[4] Biot, M. A., “General solutions of the equations of elasticity and consolidation for a porous material”, J. Appl. Mech., Trans. ASME, 78, 91-96, 1956.

[5] Biot, M. A., “Thermoelasticity and irreversible thermodynamics”, J. Appl. Phys., 27, 240-253, 1956.

[6] McNamee, J. and Gibson, R. E., “Displacement functions and linear transforms applied to diffusion through porous elastic media”, Q. J. Mech. Appl. Math., 13, 98-111, 1960.

[7] Sandhu, R. S. and Wilson, E. L., “Finite element analysis of seepage in elastic media”, J. Eng. Mech. Div., ASCE, 95, 641-652, 1969.

[8] Christian, J. T., “Undrained stress distribution by numerical methods”, J. Soil Mech. Found. Div., ASCE, 94, 1333-1345, 1968.

[9] Ghaboussi, J. and Wilson, E. L., “Flow of compressible fluid in porous elastic solids”, Int. J. Numer. Meth. Eng., 5, 419-442, 1973.

[10] Booker, J. R. and Small, J. C., “An investigation of the stability of numerical solution of Biot’s equations of consolidation”, Int. J. Solids Structures, 2, 907-917, 1975.

[11] Zienkiewicz, O.C., *The Finite Element Method, 3rd ed.*, McGraw-Hill, 1977.

[12] Zienkiewicz, O. C., “Basic formulation of static and dynamic behavior of soil and other porous media”, *Numerical Methods in Geomechanics*, ed. J. Martinus, Holland, 39-56, 1982.

[13] Brebbia, C. A., Telles, J. C. F., and Wrobel, L. C., *Boundary Element Techniques–Theory and Applications in Engineering*, Springer-Verlang, 1984.

[14] Banerjee, P. K. and Butterfiled, R., *Boundary Element Methods in Engineering Science*, McGraw-Hill, 1981.

[15] Cheng, A. H-D. and Liggett, J. A., “Boundary integral equation method for linear porous-elasticity with applications to soil consolidation”, Int. J. Numer. Meth. Eng., 20, 255-278, 1984.

[16] Cheng, A. H-D. and Detournay, E., "A direct boundary element method for plane strain poroelasticity", Int. J. Num. Anal. Meth. Geomech., 12, 551-572, 1988.

[17] Badmus, T., Cheng, A. H-D., and Grilli, S., "A Laplace-transform based three-dimensional BEM for poroelasticity", Int. J. Numer. Meth. Eng., 1991.

[18] Dargush, G. F. and Banerjee, P. K., "A time domain boundary element method for poroelasticity", Int. J. Num. Meth. Eng., 28, 2423-2449, 1989.

[19] Nishimura, N. and Kobayashi, S., "A boundary integral equation method for consolidation problems", Int. J. Solids Structures, 25, 1-21, 1989.

[20] Vandamme, L., Detournay, E. and Cheng, A. H-D., "A two-dimensional poroelastic displacement discontinuity method for hydraulic fracture simulation", Int. J. Num. Anal. Meth. Geomech., 13, 215-224, 1989.

[21] Curran, J. H. and Carvalho, J. L., "A displacement discontinuity model for fluid-saturated porous media", in Proc. 6th Int. Cong. Rock Mech., Montreal, Canada, eds: G. Herget and S. Vongpaisal, Balkema, 73-78, 1987.

[22] Sacks, R. A. and Darling, D. H., "Direct drive cryogenic ICF capsules employing D-T wetted foam", Nucl. Fusion, 27, 447-452, 1987.

[23] Scheidegger, A. E., *The Physics of Flow Through Porous Media*, The Macmillan Company, New York, 1960.

[24] Simon, B.R., "Multiphase poroelastic finite element models for soft tissue structures", Applied Mech. Rev., vol. 45, no. 6, 191-218, 1992.

[25] Harleman, D.R.E., Mehlhorn, P.F., and Rumer, R.R., "Dispersion-permeability correlation in porous media", J. Hydraul. Div. Amer. Soc. Civil Eng., 89, 67-85, 1963.

[26] Good, R.J. and Ferry, G.V., "The wetting of solids by liquid hydrogen", Advan. Cryog. Eng., 8, 306-310, 1963.

Hierarchical Reinforcement of Randomly-Oriented Carbon Nanotube Thin Films by Ion Irradiation

Francesco Fornasiero[†], Mary LeBlanc[†], Supakit Charnvanichborikarn[†], Sergei O. Kucheyev [†], Swanee Shi[†], Kuangping Gong[‡], Lijie Ci, Jinseong Park[‡], and Robin Miles[†,*]

† Physical and Life Sciences Directorate, Lawrence Livermore National Laboratory, Livermore CA 94550

[b] San Jose Lab, Samsung Cheil Industries, 2186 Bering Dr. San Jose, 95131

[*] Corresponding author: tel. +1 925 422 8872; fax: +1 925 424 3295; email: miles7@llnl.gov

POINTS to be MADE:

- Nature: Hierarchical organization in nano-composite structures to give materials with extraordinary stiffness, strength and toughness with low weight
- High strength and modulus: CNT as ideal building block for artificial hierarchical structures. Can we form hierarchical structure to achieve performances superior to naturally occurring materials?
- Inefficient load transfer among adjacent bundles, CNTs in a bundle, weak interaction between shells
- DWNT can be stronger than SWNT
- Ion irradiation for efficient load transfer among different length scales
- Low doses to promote cross-linking and minimize damage
- RBM for CNT diameters
- Thin films: ion irradiation effect uniform across the film thickness
- SEM images of cracked area for CNT pull-out: YES CNTs are pulled out
- Estimate lc (transition from bending to stretching)
- AFM of dispersed mats for length measurements
- Randomly oriented good for biaxial loading
- Application: aerospace
- X-ray image of randomly oriented CNTs.
- Toughness?
- Could be combined with alignment, stronger initial mats
- Plot to compare with others rCNT
- Need table with model fitted parameters

Raman for samples above

1. Example Raman back and top surface are the same (uniform ion damage)

TEM images as a function of dose

Composition measurements

a) RBS
b) TGA (?)
c) microbalance

Abstract

Because of their outstanding mechanical, electrical, thermal and optical properties, carbon nanotubes (CNTs) are very attractive 1-D nanoscale building block for designing lightweight composites that could potentially outperform naturally occurring materials. Two challenges have been recognized to be critical for fully exploiting CNT superior elastic modulus, strength, and toughness for mechanical reinforcement of macroscopic systems: the ability to control CNT hierarchical organization and to engineer the interfacial interaction across multiple length scales to favor load transfer. Toward overcoming the latter challenge, we investigate here He^+ ion irradiation effect on the tensile strength and elastic modulus of cm^2-area, 2-D reticulated network of randomly oriented double-walled nanotubes (DWNT) samples and epoxy composites. We demonstrate that irradiation-induced reinforcement behavior is strongly connected with the formation of cross-links at the different DWNT network hierarchical levels. Our measurements show that at a rapidly increasing reinforcement at low doses, attributed to intra-bundle CNT cross-links, follows a slow mechanical reinforcement at higher doses, associated to inter-bundle cross-links. At the highest irradiation doses, DWNT-epoxy strength and elastic modulus approach ~900 MPa and 25 GPa without loss of DWNT graphitic structure. These mechanical performances are among the best ones reported for randomly-oriented CNT mats and could be further improved at higher irradiation doses. We developed also a simple mathematical model accounting for hierarchical reinforcement of DWNT films and in very good agreement with the experimental results across the entire irradiation dose range.

Introduction

Many natural materials feature remarkable structural properties, often exhibiting extraordinary toughness, strength, stiffness, and resistance to flaws in a light weight composite. Remarkably, these superior mechanical properties are realized through a complex hierarchical organization of relatively weak constituents. [1-7] In addition, functional diversity is achieved by geometrical variation of the assembly of a few building blocks, rather than relying on a large collection of different structural units.[3, 6] A remarkable example is collagen, a stiff and hard protein that represents the most abundant constituent material in the human body. At the lower hierarchical level, collagen consists of polypeptides molecules arranged in a 300-nm long, 1.5-nm wide triple-helix. At the next level, collagen molecules are quasi-hexagonally packed into ~50-nm diameter interdigitated microfibrils, which then assemble to form millimeter long fibers with ~ 1-μm diameter. Collagen molecules provide strength, elasticity and mechanical stability to diverse tissues such as blood vessels, bones, cornea, skin, ligaments and tendons as well as the extracellular matrix. The large diversity of mechanical properties of collagen connective tissues are dictated, to a large extent, by the spatial organization of the collagen fibers in 1-D (tendon and ligaments) or 2-D and 3-D network structures (skin and blood vessel) [7]. In addition, inter- and intra-fibril crosslinks [1, 3, 8] enable efficient transmission of mechanical forces across multiple length-scales, and biomineral phases and/or other biopolymers further modulate the composite mechanical properties to optimally respond to the primary tissue mechanical stresses.

The superior mechanical properties of natural materials have motivated research toward the development of artificial materials with biomimetic hierarchical design. Because of their unmatched strength and elastic modulus approaching 100 GPa and 1 TPa respectively [9-12] and outstanding optical, thermal [13, 14] and electrical [15] properties, carbon nanotubes (CNTs) are very attractive 1-D nanoscale building block for designing lightweight, bio-inspired, multiscale-structured composites that could potentially outperform naturally occurring materials. In analogy with collagen, CNTs can be organized at the macroscale in 1-D fibers/yarns [16-18] or 2-D [19-21] and 3-D structures [22-26], and they assemble spontaneously in hexagonally packed bundles [21] that are reminiscent of collagen fibrils. In spite of the considerable recent progresses in the exploiting Nature lesson, macroscopic CNT composites fail to fully deliver their promises and fall short a few orders of magnitude in their mechanical performances when compared with the pristine nanoscale building blocks [27, 28]. Strength, stiffness and toughness of CNT-based materials are indeed dictated by the weak interfacial interactions between their components, rather than by the individual CNT mechanical properties.[29-31] This deficiency is much more pronounced in 2-D and 3-D composites where requirements of isotropic stress distribution and/or thermal or electrical properties dictate the choice of a random CNT orientation[27, 32]. On the contrary, for CNT fibers[16, 33, 34] and oriented/pre-stretched CNT films[35-39], CNT contacts and stress loading is more efficient, often by nearly an order of magnitude. Thus, a critical challenge in assembling CNTs into high performance hierarchical structures is engineering the interfacial interaction across multiple length scales to favor load transfer from the nanosized constituents to the macroscale composite. Overcoming this challenge is expected to have a profound impact in aerospace and automotive applications, armor design, advanced thermal management composites, etc.

Among the proposed approaches, a promising direction is the introduction of strong covalent bonds among CNTs at multiple hierarchical levels as well as between CNTs and hosting matrix through high energy irradiation[40-42]. Electron beam irradiation has been successfully employed to dramatically enhance the mechanical performances of a single MWNT through intershell crosslinks[11], and of SWNTs and DWNTs bundles via intertube links[43, 44]. These results suggested that similar strategies could be employed to promote efficient load-bearing at even larger macroscopic scales. [45]

Motivated by these achievements and toward further expanding the toolbox for the fabrication of nanostructured, high performance composites, we investigate here He^+ ion irradiation effect on 2-D, submicron thick, cm^2 area DWNT samples and epoxy composites. Rather than aiming to the maximization of the composite mechanical properties, we design our experiment toward elucidating the mechanism of irradation reinforcement in randomly-oriented ultrathin films, i.e. for the most challenging CNT structural organization. The random CNT orientation simplifies also data interpretation by neglecting possible variation of the mechanical property enhancement due to the changes of tube alignment degree from sample to sample. Also, while thicker CNT films may enable easier handling and stronger composite fabrication by reducing the effect of nanoscale flaws, using submicron CNT films guarantee uniform properties of the irradiated CNT sample across the entire thickness. By spanning three orders of magnitude in the irradiation dose, we demonstrate here that mechanical reinforcement behavior with He^+ irradiation is strongly connected with the generation of cross-links at the different CNT hierarchical levels. The observed rapidly increasing reinforcement at low doses is attributed to intra-bundle CNT cross-links, while the following slow mechanical reinforcement at higher doses is associated to inter-bundle cross-links. At the highest irradiation doses, CNT-epoxy strength and elastic modulus approach ~900 MPa and 25 GPa, which are among the best performances reported for randomly-oriented CNT mats. Moreover, because Raman spectroscopy reveals minimum damage to the crystalline CNT graphitic structure at the highest doses, even higher stiffness and strength could be potentially be achieved in hierarchically-organized CNT films and composites with high energy He^+ irradiation. Finally, we developed a mathematical model accounting for the fundamental physics behind our data interpretation and in very good agreement with the experimental results across the entire irradiation dose range.

Results and Discussion

Randomly-oriented CNT networks were produced using a floating catalyst method in a custom-made CVD reactor using ferrocene as catalyst precursor and toluene as hydrocarbon feedstock (Figure 2.A). The nanotube network consists of long, 2-3 nm wide DWNTs of very high crystalline quality as evidenced by TEM imaging and Raman spectroscopy characterization. The intensity ratio of the G and D bands before irradiation, I_G/I_D (see Figure 1.F), is in the range 35-60 and the length of the DWNTs ranges from hundred microns to a millimeter. The as-produced network contains about 0.8-2.0 at% Fe catalyst particles (Figure 1.D), as measured by Rutherford backscattering spectrometry.

Figure 1.A-C shows the hierarchical organization of the CNTs in the network. The small-radius DWNTs form bundles with a lognormal diameter distribution in the range 5-30-nm and centered at ~15-nm. The latter was determined by TEM imaging of ~ 250 bundles. In some cases, smaller bundles merge into larger bundles and/or share nanotubes. During the floating catalysts growth, the long tubes/bundles are deposited on the collecting filter paper with no preferential orientation, thus forming a continuous, randomly entangled network. This reticulate network assembly of long, highly crystalline DWNTs is particularly favorable for the fabrication of high strength and modulus composite materials[20, 35, 36, 46, 47]. Because grown DWNTs are essentially defect-free, the individual tubes are expected to have Young modulus and strength approaching the theoretical maximum of 1 TPa and 100 GPa, respectively[9-12]. When compared with CNT-reinforced composites fabricated by mixing polymer and short nanotubes, the reticulate structure has the advantage of promoting an even distribution of applied loads over a macroscopic area by continuously transferring stresses through the network rather than merely through weak polymer/CNT interfaces [20, 36].

The as-formed DWNT mats are highly porous, as evidenced in Figure 1.D, and thus very fragile. To increase the mat density and for facile handling, the DWNT mats were first subjected to ethanol (EtOH) condensation to form films with thickness in the range 200-400 nm. CNT-epoxy composites (~300-nm-thick) were fabricated with an analogous procedure by simultaneously densifying and infiltrating the DWNT network with a highly diluted epoxy-EtOH solution. Figure 2.C-D shows typical SEM cross-sectional images of the so-formed CNT-epoxy composites, and clearly shows DWNT bundles emerging from the fractured surface. The employed infiltration protocol resulted in composites with 45~60 wt% DWNT, as estimated with a combination of Rutherford backscattering spectrometry (RBS) and elastic recoil detection analysis (ERDA). While the CNT filler percentage can be tuned by adjusting the concentration of the epoxy-ethanol solution, our infiltration method does not allow fine control of the composition in such thin samples, thus resulting in a relatively wide DWNT wt% range in the composite.

While the individual DWNT building blocks have exceptional mechanical properties, the large-scale mechanical response of CNT films and composites is largely dominated by the weak shear interactions between shells in a nanotube, nanotubes in a bundle, bundles in the network, and of nanotubes with the matrix[29-31]. Thus, to effectively exploit the outstanding mechanical properties of CNTs as nanofillers in macroscopic composite materials, strategies need to be devised to strengthen these otherwise weak shear interactions. Here, we use He^+ ion irradiation of neat DWNT networks and epoxy composites as a mean to harness the true potential of CNTs for high mechanical performance 2-D composites. The thickness of the DWNT films and composites was chosen much smaller than the expected graphite stopping power for He^+

ions (~8.8 μm, as estimated with SRIM code[48]): this criterion guarantees that the properties of the films after irradiation are uniform through the entire thickness.

Mechanical properties of un-irradiated CNT films and composites

Before studying ion-irradiation reinforcements of these materials, we quantified the strength at failure and Young modulus of the un-irradiated epoxy, DWNT networks after ethanol densification, and CNT-epoxy composites. Figure 3 clearly show that the composite material has mechanical properties that greatly surpass those of its building blocks: composite elastic modulus and strength average ~ 7.6 GPa and 210 MPa, respectively, while the corresponding metrics for epoxy and pure CNT mat are ~2-3 GPa and 70 MPa in both cases. This is in stark contrast with the typically low reinforcement achieved when short CNTs are dispersed into polymer matrices and with the expectations for conventional composite materials: the modulus of a conventional composite typically falls between that of its components according to the well-known rule of mixtures[27, 28, 36]. Our result is consistent with recent reports of mechanical properties for polymer composites with high loading of CNTs with reticulated architecture[36] and it is explained as follows. For the neat DWNT-bundle network, although load can be continuously transferred, there is no mechanism to strongly restrict the inter-tube or inter-bundle slippage within the network, so that the macroscale strain mainly comes from the deformation of the network rather than axial extension of the DWNTs, and the mechanical behavior is dominated by the weak CNT-CNT shear interaction and tubes physical entanglements. However, when the CNT reticulated architecture is coupled with the 3-D highly crosslinked epoxy network, the free deformations of the DWNT network is hindered by the polymer network[36], which essentially act as physical crosslinks. This leads to higher modulus and strength compared to the neat DWNT mat.

In spite of this synergistic reinforcement, the resulting composite (and the neat DWNT network) have mechanical properties still quite far from those of the nanotube building block, suggesting that CNT and CNT bundle sliding was only partially limited. Weak coupling between the matrix and the DWNT network is supported by cross-sectional SEM images that reveal long-CNT bundle pull-out from the cracked surface (Figures 2.C and S1.A).

Irradiation-induced reinforcement of DWNT network and composites

Efficient load transfer through the entire network requires strong interaction between adjacent CNTs and CNT shells. Electron beam irradiation at moderately low doses has proven to introduce stable links among CNTs in bundle and among shells in MWNT, thus enabling impressive enhancements in tube/bundle stiffness and strength[11, 43, 44]. To promote covalent crosslinks not only at the tube and bundle level, but also among bundles in the network, we employed here high energy He^+ ion irradiation (3 MeV) from very low doses to moderately high (10^{13}– 10^{16} ions/cm^2). Pure epoxy, ethanol-densified CNTs (CNT-EtOH), and CNT-epoxy composites were exposed to ion irradiation and their mechanical properties evaluated with tensile testing. Also, to decouple the effect of ion irradiation on the strength of the interfacial interaction between CNT and epoxy matrix in the composites, we first irradiated the CNT network and then infiltrated the network with epoxy (CNTirr-epoxy). Elastic modulus and strength for the four kinds of samples are calculated on the basis of the film thickness before tensile testing. For each sample, the latter was determined by cross-sectional SEM imaging as average of 12-25 measurements taken at different locations. Measured elastic modulus and strength for unirradiated and irradiated samples at different doses are summarized in Figure 4, while tensile stress-strain plots are given in Figure S2.

For pure epoxy films (1-μm thick) ion irradiation up to 2x10^{15} He$^+$/cm^2 did not affect significantly the material elastic modulus. Because the epoxy resin is a highly cross-linked polymer, and the Young modulus is proportional to the crosslinks density, additional irradiation-induced cross-links or damage are not expected to impact strongly the material stiffness. On the opposite, the epoxy strength steadily drops with irradiation dose, suggesting that the primary effect of irradiation is a damage of the polymer network. (reference) Epoxy films did not survive exposure to irradiation doses higher than 2x10^{15} He$^+$/cm^2 and/or resulted in too-brittle samples for further testing.

CNT containing samples show a very different behavior. CNT-EtOH elastic modulus increased very rapidly at low doses (below 2x10^{14} ions/cm^2) from 2-3 GPa to 6-7 GPa; at higher irradiation doses, we observed a steady but much slower increase. No downturn of the films mechanical performances is noticeable up to the largest dose of this study, 10^{16} ions/cm^2, which suggests that the DWNT crystalline structure is conserved in the entire irradiation dose range. Consistently, measured intensity ratio of the graphitic and defect Raman bands of our DWNT network, I_G/I_D, is ≥ 2-3 for all He$^+$ doses, and clear radial breathing modes are detectable in the Raman spectra even for 10^{16} ions/cm^2 (Figure 5.A). From the measured Raman intensity ratio I_D/I_G we can estimate the characteristic distance between defects, L_a, as a function of irradiation dose with the relation[49-51]:

$$L_a = (2.4 \times 10^{-10}) \times \lambda_{laser}^4 \left(\frac{I_G}{I_D}\right) \tag{1}$$

where λ_{laser} is the Raman laser wavelength employed for characterization (632.8-nm). The smallest calculated L_a is ~75-nm, thus confirming that the graphitic order is maintained even in the most heavily irradiation samples. Because we did not see a downturn of the films mechanical performances up to the largest dose of this study, 10^{16} ions/cm^2, further mechanical reinforcement may be achievable at higher irradiation doses. Unfortunately, our attempts to verify this claim failed because 300-nm thick films exposed to >10^{16} He$^+$/cm^2 doses were too brittle for handling.

The dose dependence of the CNT-EtOH strength mirrors that of the elastic modulus; however, recorded data suffer of a larger error especially at high irradiation doses, where early film failure was often observed. Since these films are only 300-nm thick, the presence of small defects and/or embedded foreign particles acting a stress concentrators may easily justify the large scatter of our strength measurements.

CNT-epoxy and CNTirr-epoxy films have identical mechanical properties within experimental uncertainty in the entire dose range. These results strongly suggest that the irradiation-induced mechanical reinforcement in the composite material is almost exclusively due to crosslinks forming among the CNTs in the network, whereas the creation of CNT-matrix interfacial bonds appears to be negligible. Cross-sectional SEM imaging of samples irradiated at the highest dose shows indeed DWNT bundle pull-out from the fractured surface that resembles closely the findings for un-irradiated composites (Figure S3). Mechanical properties of irradiated CNT composites follow the same trend of the neat DWNT network. The maximum recorded Young modulus and strength are however much higher, reaching 22-24 GPa and 700-870 MPa at 10^{16} ions/cm^2 dose, respectively. These mechanical performances match the best ones reported so-far for macroscopic samples of isotropic, un-irradiated CNT-composites [35, 46, 52], surpass those of electron-beam irradiated neat-SWNT films[53], and approach those of CNT yarns exposed to gamma-ray irradiation [54]. Noteworthy, reported reinforcement by He$^+$ ion bombardment has been achieved in ultrathin, isotropic, unoptimized composites without loss of the CNT graphitic structure, and has therefore still significant margin of improvement. Compare E,S with literature with other approaches: summarizing plot?

The Raman analysis performed for the CNT-EtOH samples was repeated for their epoxy composites. Since epoxy is not Raman active and measured I_D/I_G ratio did not change after adding epoxy on neat DWNT films (Figure S3), Equation (1) can be used to quantify the DWNT defect density during irradiation for epoxy composites as well. Measured I_D/I_G for CNT-Epoxy and CNTirr-Epoxy films follow the same master curve as a function of ion irradiation, as shown in Figure 5.B. The latter closely match results for the CNT-EtOH films. Thus, DWNTs that were irradiated while embedded in the polymer matrix maintain as well a high degree of crystallinity up to the 10^{16} ions/cm^2, at which L_a is ~100-nm.

Modeling ion-irradiation reinforcement of 2-D DWNT random networks

The experimental results described above revealed two regimes in the mechanical properties enhancement of randomly-oriented CNT mats when exposed to He$^+$ irradiation over three orders of dose magnitudes (10^{13}-10^{16} ions/cm^2). In the first regime, for doses up to $2\text{x}10^{14}$ ions/cm^2, CNT-mat stiffness and strength rapidly increase with irradiation dose; in the second regime corresponding to larger doses, the reinforcement proceeds at a much reduced, nearly-constant rate. We believe that the origin of these two regimes is strongly connected with the hierarchical organization of the DWNTs in the randomly-oriented mat. As show in Figure 1, DWNTs form bundles with log-normally distributed diameters in the range 5-30-nm (center ~ 15-nm); small bundles may then merge into larger bundles by sharing DWNTs or simply entangle to form the mat network structure. The reinforcement effect of ion irradiation can therefore occur at multiple levels in this hierarchically organized material. At the single nanotube level, formation of covalent bonds between the concentric shells effectively distributes stresses from the outer to the inner shell, which are otherwise weakly coupled.[11, 55, 56] At the next level (bundle), irradiation induced cross-links among DWNTs dramatically increase bundle shear strength and stiffness, and prevent tube pull-out.[29, 30, 43, 44, 57] At the network level, inter-bundle covalent bonds formed by irradiation reinforce the CNT mat by strengthening the bundle-to-bundle contact points and limiting inter-bundle slippage[30]. Because shells within a DWNT and DWNTs within a bundle are closely packed for a large part of (if not for the entire) tube/bundle length, we expect that relatively low irradiation doses will be sufficient to generate a number of inter-shell and intra-bundle covalent bonds that maximize the reinforcement achievable at tube/bundle level. Simulations of crosslinked DWNTs suggest indeed that a relatively small number of irradiation induced inter-shell crosslinks can transfer very efficiently load between shells [11, 30]. On the opposite, inter-bundle contact areas are limited to only ~1 nm^2 (for bundles that are not sharing nanotubes). Thus, it is statistically less likely to link bundles together, and saturation of the total strength of the inter-bundle contacts is expected to require much higher irradiation doses. According to this picture, the steeply increasing elastic modules and strength recorded at low doses corresponds primarily to the formation of inter-shell and intra-bundle covalent bonds, and this reinforcement at tube and bundle level saturates at ~$2\text{x}10^{14}$ ions/cm^2. A relatively small number of inter-bundle crosslinks are also created in this regime. At higher doses, any enhancement of the network mechanical properties originates from inter-bundle crosslinks that are formed at much slower rate.

This interpretation is in qualitative agreement with simulation results that suggest that the optimal cross-link linear density for SWNT bundle reinforcement is quite low, ~ 0.1/nm and decreases with increasing SWNT length. This density corresponds to an average cross-links distance of ~10-nm, significantly smaller than L_a at the largest dose of this study. further margins exist to enhance the mechanical performances of both CNT-Epoxy and CNTirr-Epoxy by increasing the irradation dose.

Based on this physical interpretation of the trends observed in our experiments, we construct a simple model that accounts for the key features of our material and irradiation process. Following reference[58, 59], our DWNT mat is modeled as a network of randomly oriented bundles of equal length, L and width, w. The bundles are assumed to be rigidly bonded at the contact points where ion-irradiation formed a covalent crosslink. If we define the segment length as the portion of the bundle length between two crosslinks, the segment length distribution is approximated by a 1-D Poisson distribution [59]. By calculating the total elastic energy of the mat as the sum of the elastic energies of the bundle segments under the assumption that the segments deform only via their least stiff mode, Åström et al. [58, 59] derived the following expression for the Young modulus of the bundle mat, E_{mat}:

$$E_{mat} = \frac{E_{bundle} w\pi}{16 l_c} z \left\{ \left(\frac{zw}{l_c}\right)^2 E_1(z) + \left(3 + \frac{1}{2(1+v)}\right) [1 - e^{-z}(z+1)] \right\} \qquad (2)$$

where E_{bundle} is the Young's modulus of the bundle; v is the mat Poisson ratio; l_c is the critical segment length above which the segments deform only by bending and below which only by stretching and shearing; and z is related to the number of irradiation-induced crosslinks per bundle, n_{links}, by $z = \frac{l_c}{L} n_{links}$. $E_1(z)$ and l_c are calculated with $E_1(z) = \int_1^{\infty} e^{-z*x}/_x \, dx$ and $l_c/L = 3.1(w/L) + 0.18$, respectively [58]. Equation (2) accounts only for the irradiation induced reinforcement associated with inter-bundle crosslinks. Since the network has a finite elastic modulus before irradiation, we assume that the as produced mat has n_0 "effective" crosslinks; thus, in our model we modify Equation (2) be replacing z with (z+z_0), where $z_0 = \frac{l_c}{L} n_0$. To represent also the reinforcement at the tube/bundle level due to the inter-shell and intra-bundle sp^3 bonds, we assumed that E_{bundle} increases exponentially with the number of crosslinks generated by ion irradiation, according to:

$$E_{bundle} = E_0 + E_{irr}(1 - e^{-c*z}) \qquad (3)$$

where E_0 is the bundle Young modulus before irradiation; E_{irr} represent the maximum enhancement of the elastic modulus of the bundle upon irradiation, and c is constant that defines the rate of bundle stiffness increase with irradiation dose. The mathematical form of Equation (3) is justified by recent experimental measurements of low-dose electron irradiation effects on DWNT bundles of sizes matching those of our DWNT mat distribution: the Young modulus and tensile strength display an "approximately exponential increase" with irradiation dose in the low-dose regime [44]. Simulations of SWNT bundles also reveal a similar trend for the bundle elastic modulus with crosslink number [60]. While higher irradiation doses may reduce bundle mechanical properties by degradation of the intrinsic crystalline structure of the DWNT shells (an effect not accounted for by Equation (3)), Raman measurements reveal that our DWNTs maintain their well graphitized walls even at highest irradiation doses of this study: the Raman G/D intensity ratio is ≥ 2 when the CNT mat is exposed to 10^{16} ions/cm^2.

Before fitting the model to our experimental data, we first need to estimate of the amount of crosslinks introduced during He$^+$ irradiation. According to simulation results[61], we assume here that the number of covalent bonds per bundle, n_{links}, is a fraction (1/6) of the number of irradiation-induced defects per bundle, $n_{defects}$. The latter is estimated with the following relation:

$$n_{defects} = L/L_a \tag{4}$$

where L_a is calculated with Equations (1) from the measured Raman intensity ratio I_D/I_G as a function of irradiation dose[49-51].

In our calculations, the number of crosslinks of the un-irradiated samples obtained with Equations (1) and (4) is subtracted out to compute the irradiation contribution to the total number of defects. Also, we set the bundle length (L=400 μm) and the bundle width (w=15 nm) to their measured average values; finally, for simplicity, we assumed the Poisson ratio to be zero. Results are not very sensitive to v and do not depend on the actual value of L for $L>>w$ since $z = \frac{l_c}{6*L_a}$ and, in this limit, $l_c \rightarrow 0.18$. To reduce the number of adjustable parameters down to 3 (z_0, E_{irr}, c), we use the measured un-irradiated DWNT mat Young modulus $E_{mat}(0)$ to express E_0 as a function of z_0 through Equation (2).

Fitting Equation (2) to our experimental data reproduces quantitatively the observed elastic moduli as function of He$^+$ irradiation dose (see Figure 6). Resulting model parameters and input constants are summarized in Table 1. The fitted $(E_0 + E_{irr})$ is ~600 GPa, remarkably close to reported maximum stiffening of DWNT bundles under electron beam irradiation [44]. The calculated un-irradiated bundle elastic modulus E_0 (~200 GPa) is, however, 3 times larger than in the quoted reference [44, 62], a discrepancy that may simply derive from their shorter bundle length (2-3 μm) and/or mat pre-irradiation treatment: our EtOH condensation step may indeed favor intra-bundle tube contact. Regardless, the agreement with our experimental data is remarkable and the fitting parameters are reasonable.

We have also estimated the mat strength with the relation $\sigma_{mat} = \varepsilon \times E_{mat}$, where ε is an adjustable constant independent of ion irradiation, and our calculation quantitatively reproduce our measurements within experimental error. As for the elastic modulus, the estimated maximum bundle strength (~14 GPa) is very close to Filleter *et al* results [44], while the calculated bundle strength before irradiation is ~6 GPa, 2-3 times higher than the reported values in references [44, 62].

Measured Young modulus and tensile strength for composites of irradiated CNTs and epoxy suggest that the polymer matrix increases the overall mechanical properties by constraining the slip of CNTs and CNT bundles in the network: the effect of the highly crosslinked polymer is essentially equivalent to introducing additional crosslinks on the CNT network before irradiation. Thus, if our model assumptions are reasonably good, Equation (2) should represent quantitatively the experimental results for the CNT-epoxy films by adjusting only z_0. We can calculate z_0 for the CNT-epoxy composite by fitting Equation (2) (with z=0) to the measured un-irradiated elastic modulus of the composite, and then employ the same equation to predict the mechanical properties of the CNT-epoxy mat as a function of ion irradiation. Remarkably, Figure 6 shows that model predictions match quantitatively the experimental results for both strength and Young modulus in the range of irradiation doses of this study. Thus, the proposed model seems to account for the essential physics dictating ion-irradiation reinforcement of randomly-oriented CNT networks; moreover, model parameters and constants have clear physical meaning and their fitted values are consistent with expectations and published experimental data. CAN EXTEND THE MODEL FOR DOWNTURN of Ebundle

Conclusions

We demonstrated a dramatic enhancement of the mechanical properties of randomly-oriented DWNT thin films and composites through irradiation with high energy He^+ ions. At the highest irradiation doses, the irradiated DWNT-epoxy composites displayed a >3-fold increase in tensile strength and elastic modulus with respect to the unirradiated composite and a 10-fold increase when compared with their unirradiated building blocks. At this ion fluence, DWNT-epoxy strength and elastic modulus approach ~900 MPa and 25 GPa without loss of DWNT graphitic structure. These mechanical performances are among the best reported for randomly-oriented CNT mats and could be further improved at higher irradiation doses.

The irradiation-induced reinforcement behavior is characterized by two distinct regimes, which are associated with the formation of cross-links at the different DWNT network hierarchical levels: at a rapidly increasing mechanical properties at low doses due to intra-bundle CNT cross-links, follows a slow mechanical reinforcement at higher doses, associated to inter-bundle cross-links. Experimental results are well represented in the entire irradiation range by a simple mathematical model accounting for the hierarchical reinforcement of DWNT films, thus supporting our data interpretation.

This study could have significant impact on the processing of ultra-strong CNT-based structures. Synthesized nanotubes are often in the form of bundles because of their large surface area and van der Waals interactions, and exfoliation of these bundles to obtain individual nanotubes is difficult. Thus, the best strategy for producing ultrastrong, macroscopic CNT composites is by growing long nanotubes, process them into sheets, ropes, or other structures and crosslink them at all hierarchical level to extract the strength and stiffness available to individual nanotubes. Application of this method to pre-aligned or stretched CNT films/fibers is expected to be even more efficient than for randomly oriented CNT networks because of the larger tube-tube contact area, and could enable fully harnessing the mechanical properties of individual CNTs in materials surpassing state-of-art carbon-fiber composites.

SERGEI Input or concluding remark: While we have demonstrate here the strong mechanical reinforcement of ion irradiation on macroscopic CNT sheets of ~ 1-cm² area, large-scale processing of nanotube composites would require dedicated high-energy ion beam sources, and achieving precise control of the crosslink densities in thick samples could be difficult.

Acknowledgments

This work was supported by Lawrence Livermore National Laboratory. Lawrence Livermore National Laboratory is operated by Lawrence Livermore National Security, LLC, for the U.S. Department of Energy, National Nuclear Security Administration under Contract DE-AC52-07NA27344. TEM experiments were conducted at the National Center for Electron Microscopy, Lawrence Berkeley National Lab, which is supported by the U.S. Department of Energy under Contract # DE-AC02-05CH11231.

Supporting Information Available: Description of Materials and Methods. This material is available free of charge via the Internet at http://pubs.acs.org

Materials and Methods

Pure CNT films and CNT/epoxy composites. The randomly-oriented CNT networks were produced with a floating catalyst CVD method. A toluene solution (carbon source) containing ferrocene (catalyst) and thiophone (co-catalyst) was vaporized with an atomizer and introduced into a custom-made horizontal ceramic-tube furnace with a controlled hydrogen stream (2 sccm). Argon was used as inert carrier gas at a flow rate of 10 sccm. The CNT growth temperature was 1100 C. Up-to-1-mm-long CNTs were collected on a nitrocellulose filter membrane at the end of the floating catalyst CVD system by applying slight vacuum. Produced CNTs are double-walled with an outer diameter of 2-3 nm as evidenced by high resolution TEM imaging and supported by the location of clear radial breathing modes in the range $\omega = 110\text{-}250\ \mathrm{cm}^{-1}$ of the Raman spectrum. According to the relation $\omega\ [\mathrm{cm}^{-1}] = 224/d\ [\mathrm{nm}] + 14$ [REF], these frequencies correspond to 1-2.5 nm inner and outer tube diameters.

Free-standing epoxy/CNT composites were prepared by first transferring the as-deposited CNT networks onto a polyimide frame (1.27x1.90-cm) with a 0.7x1.0-cm window that hosts the resulting suspended film. The transfer onto the polyimide frame was facilitated by spin-coating epoxy (EpoThin^{TM} - Buehler) on the edge of the frame (3000 rpm/1 min) and by pre-curing the epoxy for 3-h at room temperature to reach the desired tackiness. After fully curing the adhesive, 20 μl of a freshly prepared epoxy-ethanol solution (1 w% of EpoThin^{TM} resin+hardener in a 5:2 ratio) were drop casted onto the entire CNT film surface and let dry/cure overnight.

Pure CNT films for mechanical testing were prepared by first wetting the CNT film with ethanol, drying the film overnight, and then by applying the same transfer procedure to a polyimide frame described above. The ethanol treatment condenses the otherwise weak CNT film and enables easy-handling. A similar film compaction occurs during the preparation of the CNT/epoxy composites when the 1:100 epoxy-ethanol solution is allowed to dry at room temperature.

Free standing irradiated-CNT/epoxy composite films were produced by first preparing free-standing, ethanol-treated CNT-film and then by infiltrating the CNT films after ion irradiation with 20 μl of 1:100 epoxy-ethanol solution.

CNT loading in the epoxy composites was measured with a combination of Rutherford backscattering spectrometry (RBS) and elastic recoil detection analysis (ERDA). With RBS and ERDA we quantify the total mass of carbon, hydrogen, nitrogen, oxygen and Fe catalysts in the CNT networks before and after epoxy infiltration. Because Fe is originally present only in the DWNT films, the ratio (wt% Fe in the composite) / (wt% Fe in the neat CNTs) gives the weight fraction of CNTs in the composite.

RBS and ERDA [SERGEI]

Raman Spectroscopy and Electron Microscopy. Raman spectra were collected with a Nicolet Almega XR Dispersive Raman Spectrometer (Thermo Scientific) at a 632.8-nm HeNe excitation laser (1.96 eV). Every Raman measurement was conducted at room temperature and the laser power levels were kept at 1% (0.1 mW) to avoid excessive heating and subsequent CNT damage. A 100× objective lens was used to focus the laser beam on a 0.6-μm spot of the CNT forest for a 80-s total acquisition time. Raman spectra were collected at several different locations of the CNT and CNT/composite films. Reported D/G intensity ratios are averages of 3-6 spectra. Transmission electron microscopy (TEM) images were obtained using a FEI TF-20 Tecnai microscope, operated at 200 kV with a 4.0 keV extraction voltage for the field-emission gun. To prepare the samples for TEM imaging, CNTs were dry-deposited on a TEM grid by pressing/sliding the grid on the CNT film. Scanning electron microscopy images of CNT films and composites were collected at 5 or 10 kV accelerating voltage with a JEOL 7401-F SEM. For cross-sectional imaging, samples were cracked in liquid nitrogen.

Ion irradiation.* *[SERGEI]

Mechanical testing[MARY]

References

1. Buehler, M. J. Nature designs tough collagen: Explaining the nanostructure of collagen fibrils. *Proc. Natl. Acad. Sci. U. S. A.* 2006, 103, 12285-12290.

2. Espinosa, H. D.; Rim, J. E.; Barthelat, F.; Buehler, M. J. Merger of structure and material in nacre and bone - Perspectives on de novo biomimetic materials. *Progress in Materials Science* 2009, 54, 1059-1100.

3. Gautieri, A.; Vesentini, S.; Redaelli, A.; Buehler, M. J. Hierarchical Structure and Nanomechanics of Collagen Microfibrils from the Atomistic Scale Up. *Nano Lett.* 2011, 11, 757-766.

4. Giesa, T.; Arslan, M.; Pugno, N. M.; Buehler, M. J. Nanoconfinement of Spider Silk Fibrils Begets Superior Strength, Extensibility, and Toughness. *Nano Lett.* 2011, 11, 5038-5046.

5. Keten, S.; Xu, Z. P.; Ihle, B.; Buehler, M. J. Nanoconfinement controls stiffness, strength and mechanical toughness of beta-sheet crystals in silk. *Nature Materials* 2010, 9, 359-367.

6. Nova, A.; Keten, S.; Pugno, N. M.; Redaelli, A.; Buehler, M. J. Molecular and Nanostructural Mechanisms of Deformation, Strength and Toughness of Spider Silk Fibrils. *Nano Lett.* 2010, 10, 2626-2634.

7. Meyers, M. A.; Chen, P. Y.; Lin, A. Y. M.; Seki, Y. Biological materials: Structure and mechanical properties. *Progress in Materials Science* 2008, 53, 1-206.

8. Orgel, J.; Irving, T. C.; Miller, A.; Wess, T. J. Microfibrillar structure of type I collagen in situ. *Proc. Natl. Acad. Sci. U. S. A.* 2006, 103, 9001-9005.

9. Yu, M. F.; Lourie, O.; Dyer, M. J.; Moloni, K.; Kelly, T. F.; Ruoff, R. S. Strength and breaking mechanism of multiwalled carbon nanotubes under tensile load. *Science* 2000, 287, 637-640.

10. Yu, M. F.; Files, B. S.; Arepalli, S.; Ruoff, R. S. Tensile loading of ropes of single wall carbon nanotubes and their mechanical properties. *Phys. Rev. Lett.* 2000, 84, 5552-5555.

11. Peng, B.; Locascio, M.; Zapol, P.; Li, S. Y.; Mielke, S. L.; Schatz, G. C.; Espinosa, H. D. Measurements of near-ultimate strength for multiwalled carbon nanotubes and irradiation-induced crosslinking improvements. *Nat. Nanotechnol.* 2008, 3, 626-631.

12. Wei, X. L.; Chen, Q.; Peng, L. M.; Cui, R. L.; Li, Y. Tensile Loading of Double-Walled and Triple-Walled Carbon Nanotubes and their Mechanical Properties. *Journal of Physical Chemistry C* 2009, 113, 17002-17005.

13. Kim, P.; Shi, L.; Majumdar, A.; McEuen, P. L. Thermal transport measurements of individual multiwalled nanotubes. *Phys. Rev. Lett.* 2001, 87.

14. Pop, E.; Mann, D.; Wang, Q.; Goodson, K. E.; Dai, H. J. Thermal conductance of an individual single-wall carbon nanotube above room temperature. *Nano Lett.* 2006, 6, 96-100.

15. Ebbesen, T. W.; Lezec, H. J.; Hiura, H.; Bennett, J. W.; Ghaemi, H. F.; Thio, T. Electrical conductivity of individual carbon nanotubes. *Nature* 1996, 382, 54-56.

16. Behabtu, N.; Young, C. C.; Tsentalovich, D. E.; Kleinerman, O.; Wang, X.; Ma, A. W. K.; Bengio, E. A.; ter Waarbeek, R. F.; de Jong, J. J.; Hoogerwerf, R. E.; Fairchild, S. B.; Ferguson, J. B.; Maruyama, B.; Kono, J.; Talmon, Y.; Cohen, Y.; Otto, M. J.; Pasquali, M. Strong, Light, Multifunctional Fibers of Carbon Nanotubes with Ultrahigh Conductivity. *Science* 2013, 339, 182-186.

17. Zhang, M.; Atkinson, K. R.; Baughman, R. H. Multifunctional carbon nanotube yarns by downsizing an ancient technology. *Science* 2004, 306, 1358-1361.

18. Koziol, K.; Vilatela, J.; Moisala, A.; Motta, M.; Cunniff, P.; Sennett, M.; Windle, A. High-performance carbon nanotube fiber. *Science* 2007, 318, 1892-1895.

19. Zhang, M.; Fang, S. L.; Zakhidov, A. A.; Lee, S. B.; Aliev, A. E.; Williams, C. D.; Atkinson, K. R.; Baughman, R. H. Strong, transparent, multifunctional, carbon nanotube sheets. *Science* 2005, 309, 1215-1219.

20. Ma, W.; Song, L.; Yang, R.; Zhang, T.; Zhao, Y.; Sun, L.; Ren, Y.; Liu, D.; Liu, L.; Shen, J.; Zhang, Z.; Xiang, Y.; Zhou, W.; Xie, S. Directly synthesized strong, highly conducting, transparent single-walled carbon nanotube films. *Nano Lett.* 2007, 7, 2307-2311.

21. Endo, M.; Muramatsu, H.; Hayashi, T.; Kim, Y. A.; Terrones, M.; Dresselhaus, N. S. 'Buckypaper' from coaxial nanotubes. *Nature* 2005, 433, 476-476.

22. Hata, K.; Futaba, D. N.; Mizuno, K.; Namai, T.; Yumura, M.; Iijima, S. Water-assisted highly efficient synthesis of impurity-free single-waited carbon nanotubes. *Science* 2004, 306, 1362-1364.

23. Gui, X.; Wei, J.; Wang, K.; Cao, A.; Zhu, H.; Jia, Y.; Shu, Q.; Wu, D. Carbon Nanotube Sponges. *Adv. Mater.* 2010, 22, 617-+.

24. Gui, X. C.; Cao, A. Y.; Wei, J. Q.; Li, H. B.; Jia, Y.; Li, Z.; Fan, L. L.; Wang, K. L.; Zhu, H. W.; Wu, D. H. Soft, Highly Conductive Nanotube Sponges and Composites with Controlled Compressibility. *Acs Nano* 2010, 4, 2320-2326.

25. Bryning, M. B.; Milkie, D. E.; Islam, M. F.; Hough, L. A.; Kikkawa, J. M.; Yodh, A. G. Carbon nanotube aerogels. *Adv. Mater.* 2007, 19, 661-+.

26. Cao, A. Y.; Dickrell, P. L.; Sawyer, W. G.; Ghasemi-Nejhad, M. N.; Ajayan, P. M. Super-compressible foamlike carbon nanotube films. *Science* 2005, 310, 1307-1310.

27. Coleman, J. N.; Khan, U.; Blau, W. J.; Gun'ko, Y. K. Small but strong: A review of the mechanical properties of carbon nanotube-polymer composites. *Carbon* 2006, 44, 1624-1652.

28. Coleman, J. N.; Khan, U.; Gun'ko, Y. K. Mechanical reinforcement of polymers using carbon nanotubes. *Adv. Mater.* 2006, 18, 689-706.

29. Espinosa, H. D.; Filleter, T.; Naraghi, M. Multiscale Experimental Mechanics of Hierarchical Carbon-Based Materials. *Adv. Mater.* 2012, 24, 2805-2823.

30. Filleter, T.; Espinosa, H. D. Multi-scale mechanical improvement produced in carbon nanotube fibers by irradiation cross-linking. *Carbon* 2013, 56, 1-11.

31. Ajayan, P. M.; Tour, J. M. Materials science - Nanotube composites. *Nature* 2007, 447, 1066-1068.

32. Gou, J. H. Single-walled nanotube bucky paper and nanocomposite. *Polym. Int.* 2006, 55, 1283-1288.

33. Wu, A. S.; Chou, T.-W. Carbon nanotube fibers for advanced composites. *Materials Today* 2012, 15, 302-310.

34. Lu, W.; Zu, M.; Byun, J.-H.; Kim, B.-S.; Chou, T.-W. State of the Art of Carbon Nanotube Fibers: Opportunities and Challenges. *Adv. Mater.* 2012, 24, 1805-1833.

35. Cheng, Q. F.; Bao, J. W.; Park, J.; Liang, Z. Y.; Zhang, C.; Wang, B. High Mechanical Performance Composite Conductor: Multi-Walled Carbon Nanotube Sheet/Bismaleimide Nanocomposites. *Adv. Funct. Mater.* 2009, 19, 3219-3225.

36. Ma, W. J.; Liu, L. Q.; Zhang, Z.; Yang, R.; Liu, G.; Zhang, T. H.; An, X. F.; Yi, X. S.; Ren, Y.; Niu, Z. Q.; Li, J. Z.; Dong, H. B.; Zhou, W. Y.; Ajayan, P. M.; Xie, S. S. High-Strength Composite Fibers: Realizing True Potential of Carbon Nanotubes in Polymer Matrix through Continuous Reticulate Architecture and Molecular Level Couplings. *Nano Lett.* 2009, 9, 2855-2861.

37. Wang, X.; Yong, Z. Z.; Li, Q. W.; Bradford, P. D.; Liu, W.; Tucker, D. S.; Cai, W.; Wang, H.; Yuan, F. G.; Zhu, Y. T. Ultrastrong, Stiff and Multifunctional Carbon Nanotube Composites. *Materials Research Letters* 2012, 1, 19-25.

38. Di, J. T.; Hu, D. M.; Chen, H. Y.; Yong, Z. Z.; Chen, M. H.; Feng, Z. H.; Zhu, Y. T.; Li, Q. W. Ultrastrong, Foldable, and Highly Conductive Carbon Nanotube Film. *Acs Nano* 2012, 6, 5457-5464.

39. Liu, W.; Zhang, X. H.; Xu, G.; Bradford, P. D.; Wang, X.; Zhao, H. B.; Zhang, Y. Y.; Jia, Q. X.; Yuan, F. G.; Li, Q. W.; Qiu, Y. P.; Zhu, Y. T. Producing superior composites by winding carbon nanotubes onto a mandrel under a poly(vinyl alcohol) spray. *Carbon* 2011, 49, 4786-4791.

40. Banhart, F. Irradiation effects in carbon nanostructures. *Reports on Progress in Physics* 1999, 62, 1181-1221.

41. Krasheninnikov, A. V.; Nordlund, K. Ion and electron irradiation-induced effects in nanostructured materials. *J. Appl. Phys.* 2010, 107.

42. Krasheninnikov, A. V.; Banhart, F. Engineering of nanostructured carbon materials with electron or ion beams. *Nature Materials* 2007, 6, 723-733.

43. Kis, A.; Csanyi, G.; Salvetat, J. P.; Lee, T. N.; Couteau, E.; Kulik, A. J.; Benoit, W.; Brugger, J.; Forro, L. Reinforcement of single-walled carbon nanotube bundles by intertube bridging. *Nature Materials* 2004, 3, 153-157.

44. Filleter, T.; Bernal, R.; Li, S.; Espinosa, H. D. Ultrahigh strength and stiffness in cross-linked hierarchical carbon nanotube bundles. *Adv. Mater.* 2011, 23, 2855-2860.

45. Ajayan, P. M.; Banhart, F. Strong bundles. *Nature Materials* 2004, 3, 135-136.

46. Li, J. Z.; Gao, Y.; Ma, W. J.; Liu, L. Q.; Zhang, Z.; Niu, Z. Q.; Ren, Y.; Zhang, X. X.; Zeng, Q. S.; Dong, H. B.; Zhao, D.; Cai, L.; Zhou, W. Y.; Xie, S. S. High performance, freestanding and superthin carbon nanotube/epoxy nanocomposite films. *Nanoscale* 2011, 3, 3731-3736.

47. Song, L.; Ci, L.; Lv, L.; Zhou, Z. P.; Yan, X. Q.; Liu, D. F.; Yuan, H. J.; Gao, Y.; Wang, J. X.; Liu, L. F.; Zhao, X. W.; Zhang, Z. X.; Dou, X. Y.; Zhou, W. Y.; Wang, G.; Wang, C. Y.; Xie, S. S. Direct synthesis of a macroscale single-walled carbon nanotube non-woven material. *Adv. Mater.* 2004, 16, 1529-+.

48. Ziegler, J. F.; Ziegler, M. D.; Biersack, J. P. SRIM - The stopping and range of ions in matter (2010). *Nuclear Instruments & Methods in Physics Research Section B-Beam Interactions with Materials and Atoms* 2010, 268, 1818-1823.

49. Dresselhaus, M. S.; Jorio, A.; Souza, A. G.; Saito, R. Defect characterization in graphene and carbon nanotubes using Raman spectroscopy. *Philosophical Transactions of the Royal Society a-Mathematical Physical and Engineering Sciences* 2010, 368, 5355-5377.

50. Ferrari, A. C.; Robertson, J. Interpretation of Raman spectra of disordered and amorphous carbon. *Physical Review B* 2000, 61, 14095-14107.

51. Ferrari, A. C.; Basko, D. M. Raman spectroscopy as a versatile tool for studying the properties of graphene. *Nat. Nanotechnol.* 2013, 8, 235-246.

52. Shim, B. S.; Zhu, J.; Jan, E.; Critchley, K.; Ho, S.; Podsiadlo, P.; Sun, K.; Kotov, N. A. Multiparameter Structural Optimization of Single-Walled Carbon Nanotube Composites: Toward Record Strength, Stiffness, and Toughness. *ACS Nano* 2009, 3, 1711-1722.

53. Wang, S. R.; Liang, Z. Y.; Wang, B.; Zhang, C. High-strength and multifunctional macroscopic fabric of single-walled carbon nanotubes. *Adv. Mater.* 2007, 19, 1257-+.

54. Miao, M. H.; Hawkins, S. C.; Cai, J. Y.; Gengenbach, T. R.; Knott, R.; Huynh, C. P. Effect of gamma-irradiation on the mechanical properties of carbon nanotube yarns. *Carbon* 2011, 49, 4940-4947.

55. Fonseca, A. F.; Borders, T.; Baughman, R. H.; Cho, K. Load transfer between cross-linked walls of a carbon nanotube. *Physical Review B* 2010, 81, 045429.

56. Byrne, E. M.; McCarthy, M. A.; Xia, Z.; Curtin, W. A. Multiwall Nanotubes Can Be Stronger than Single Wall Nanotubes and Implications for Nanocomposite Design. *Phys. Rev. Lett.* 2009, 103.

57. da Silva, A. J. R.; Fazzio, A.; Antonelli, A. Bundling up carbon nanotubes through Wigner defects. *Nano Lett.* 2005, 5, 1045-1049.

58. Astrom, J. A.; Krasheninnikov, A. V.; Nordlund, K. Carbon nanotube mats and fibers with irradiation-improved mechanical characteristics: A theoretical model. *Phys. Rev. Lett.* 2004, 93.

59. Astrom, J. A.; Makinen, J. P.; Hirvonen, H.; Timonen, J. Stiffness of compressed fiber mats. *J. Appl. Phys.* 2000, 88, 5056-5061.

60. Cornwell, C. F.; Welch, C. R. Very-high-strength (60-GPa) carbon nanotube fiber design based on molecular dynamics simulations. *J. Chem. Phys.* 2011, 134.

61. Salonen, E.; Krasheninnikov, A. V.; Nordlund, K. Ion-irradiation-induced defects in bundles of carbon nanotubes. *Nuclear Instruments & Methods in Physics Research Section B-Beam Interactions with Materials and Atoms* 2002, 193, 603-608.

62. Naraghi, M.; Filleter, T.; Moravsky, A.; Locascio, M.; Loutfy, R. O.; Espinosa, H. D. A Multiscale Study of High Performance Double-Walled Nanotube-Polymer Fibers. *Acs Nano* 2010, 4, 6463-6476.

Figure Legends

Figure 1. Characterization of the hierarchically organized 2-D DWNT network: (A) HRTEM image of a ~2-nm wide DWNT merging into a bundle; (B) representative TEM image used to determine the DWNT bundle diameter distribution in (E) and showing the DWNT entangled network spotted with Fe particles; (C) low (main) and high (inset) magnification SEM images of the low density, randomly oriented CNT network; (D) XX; (E) Bundle diameter distribution determined by TEM imaging of ~ 250 bundles; (F) Raman spectroscopy characterization of the DWNT network with a λ=632.8-nm excitation laser showing high graphitization level and the presence of well-defined radial breathing modes in the range ω = 110-250 cm^{-1}.

Figure 2. DWNT mat and epoxy-composite fabrication: (a) Schematic representation of the DWNT network production with a floating catalyst method and subsequent ethanol densification or epoxy infiltration. Produced thin films are exposed to He^+ ion irradiation before or after epoxy infiltration. Neat DWNT networks (ii = CNT-EtOH), irradiated epoxy composites (iii = CNT-Epoxy) and composites formed by epoxy infiltration after DWNT network irradiation (i = CNTirr-Epoxy) are then probed for their mechanical properties. (b-d) SEM cross-sectional images of the neat DWNT film (b) and CNT-Epoxy composites (c-d). High resolution image in (d) clearly shows DWNT bundles emerging from the composite cross-sectional surface.

Figure 3. Tensile strength and elastic modulus of the neat DWNT network, epoxy films, and their composites before irradiation.

Figure 4. Effect of He^+ ion irradiation dose on the mechanical properties of CNT-EtOH, CNTirr-Epoxy, CNT-Epoxy, and epoxy films. While elastic modulus (a) and tensile strength (b) for pure epoxy remain unchanged or decline with irradiation dose, DWNT-containing films show a two-regime reinforcement process in which, at a rapid mechanical property increase at low doses follows a slow but steady strengthening and stiffening at high doses.

Figure 5. Raman characterization of DWNT-containing films as a function of ion irradiation: (a) Normalized Raman spectra for irradiated CNT-Epoxy films (G-band maximum intensity set =1). Similar results were obtained for CNT-EtOH and CNTirr-Epoxy films. (b) Irradiation dose dependence of the Raman bands intensity ratio, I_D/I_G, for CNT-EtOH, CNT-Epoxy, and CNTirr-Epoxy films. Nearly identical irradiation damage (I_D/I_G) is observed for the three materials.

Figure 6. Schematic representation of the hierarchical reinforcement mechanism of DWNT-containing films upon irradiation and corresponding model calculations: (A) Reinforcement due to inter-shell (1, in blue) and intra-bundle (2, in red) crosslinks are represented by Equation (3); (B) Inter-bundle cross-links at bundle contact points are accounted for by Equation (2). Bundles may (3a) share nanotubes and merge in larger bundles or (3b) simply contact at crossing points; (C) Model representation of the DWNT network as an isotropic 2-D film made of rods (bundles) with length *L* and width *w*. (D-E) Fitting of the experimental (D) Young moduli and (E) tensile strengths with Equations (1-4). The number of crosslinks at different irradiation doses (x-axis) is set equal to 1/6 of the total number of detects generated by ion irradiation and calculated with Equation (1) and (4) in a bundle of length L= 400 μm.

Figure S1. Cross-sectional SEM images of CNT-Epoxy films before (a) and after (b) irradiation at 10^{16} He^+/cm^2 dose. Surface cracking pulls out long DWNT bundles in both cases, regardless of irradiation.

Figure S2. Stress-strain behavior of (a) CNT-EtOH, (b) CNT-Epoxy and (c) CNTirr-Epoxy films during tensile loading.

Figure S3. Raman spectra before irradiation (a) and I_G/I_D intensity ratios after irradiation (b) for DWNT films before and after epoxy infiltration.

Table Legend

Table 1. Model parameters and constants. Equations (1-4) are first applied to fit CNT-EtOH Young modulus and extract the DWNT bundle parameters $E_0(z_0)$, E_{irr}, c. ε is fitted to the irradiated, neat DWNT strength data with the equation $\sigma_{mat} = \varepsilon \times E_{mat}$. For epoxy composites, z_0 is obtained from the experimental elastic modulus before irradiation, and then Equations (1-4) are used to predict the composite mechanical properties as a function of ion irradiation.

Figure 1

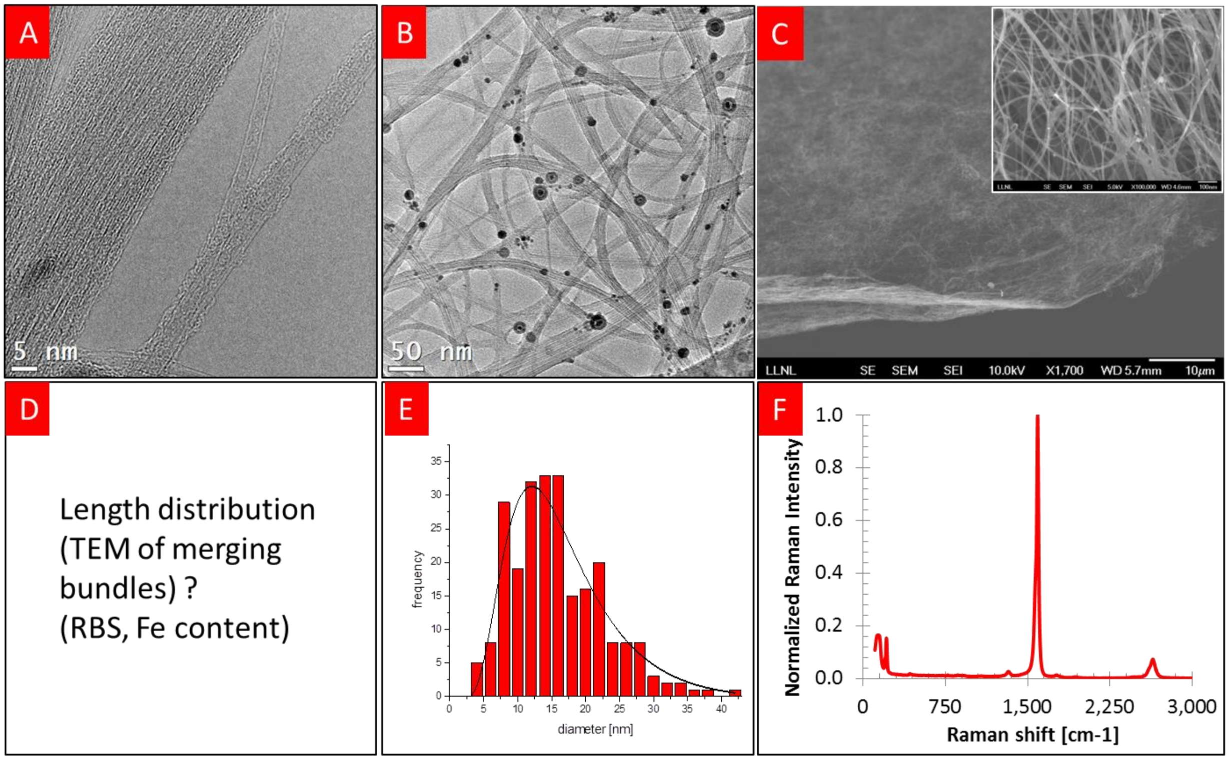

X-ray of mat??

Figure 2

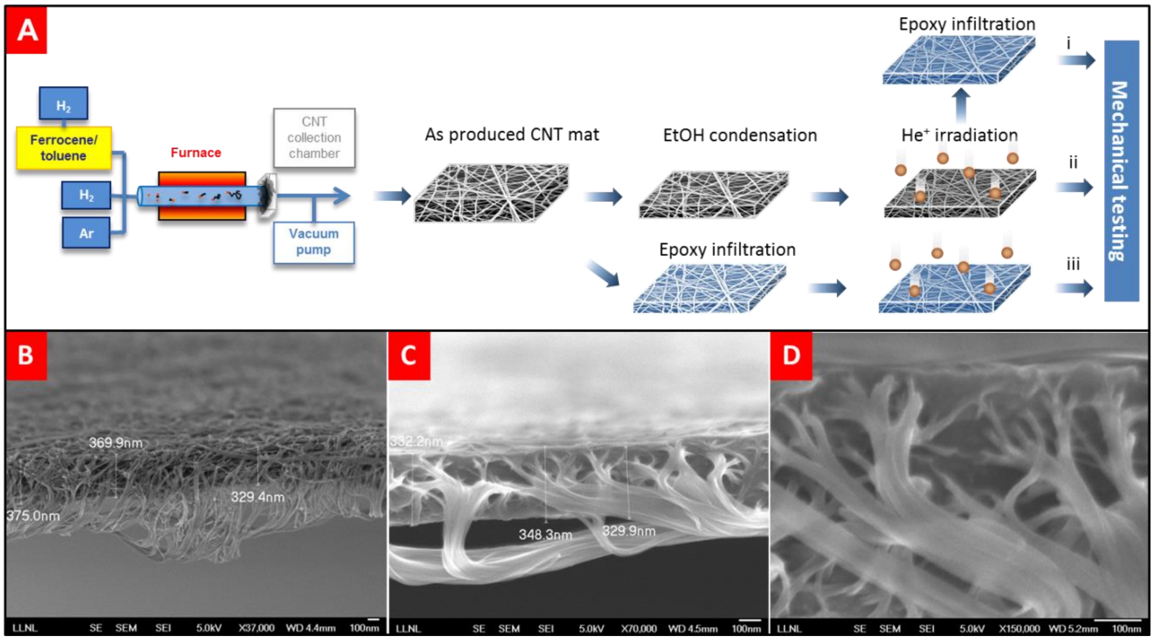
A
H2
Ferrocene/
toluene
H2
Ar
Furnace
CNT
collection
chamber
Vacuum
pump
As produced CNT mat
EtOH condensation
Epoxy infiltration
He+ irradiation
Epoxy infiltration
i
ii
iii
Mechanical testing
B
369.9nm
329.4nm
375.0nm
LLNL SE SEM SEI 5.0kV X37,000 WD 4.4mm 100nm
C
332.2nm
348.3nm
329.9nm
LLNL SE SEM SEI 5.0kV X70,000 WD 4.5mm 100nm
D
LLNL SE SEM SEI 5.0kV X150,000 WD 5.2mm 100nm

Figure 3

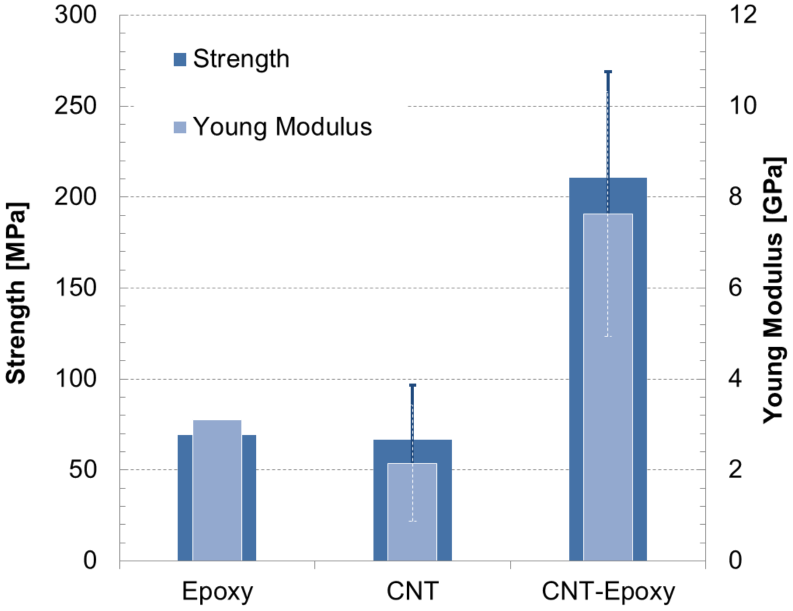

300
250
200
150
100
50
0
12
10
8
6
4
2
0
Strength
Young Modulus
Strength [MPa]
Young Modulus [GPa]
Epoxy
CNT
CNT-Epoxy

Figure 4

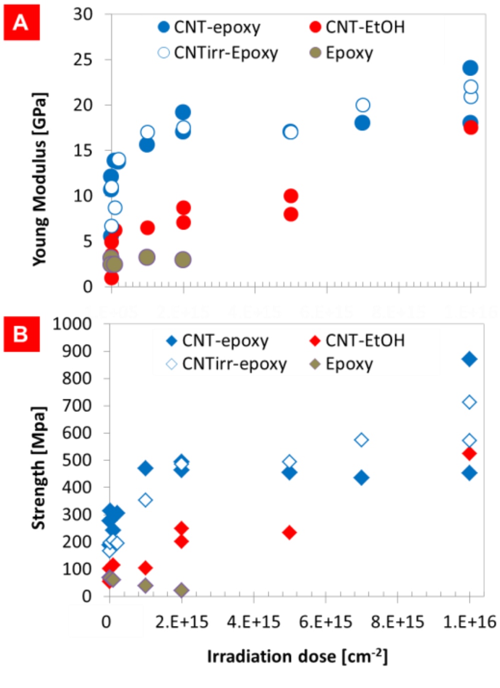
A
B
Young Modulus [GPa]
Strength [Mpa]
Irradiation dose [cm⁻²]
CNT-epoxy
CNT-EtOH
CNTirr-Epoxy
CNTirr-epoxy
Epoxy
0
5
10
15
20
25
30
100
200
300
400
500
600
700
800
900
1000
2.E+15
4.E+15
6.E+15
8.E+15
1.E+16

Figure 5

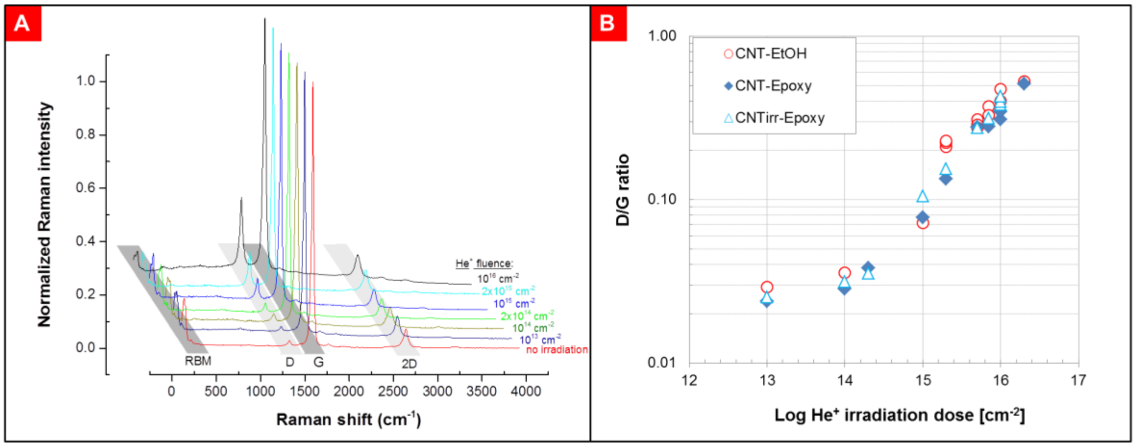
A
Normalized Raman intensity
1.0
0.8
0.6
0.4
0.2
0.0
RBM
D
G
2D
0
500
1000
1500
2000
2500
3000
3500
4000
Raman shift (cm^{-1})
He^{+} fluence:
10^{16} cm^{-2}
2x10^{15} cm^{-2}
10^{15} cm^{-2}
2x10^{14} cm^{-2}
10^{14} cm^{-2}
10^{13} cm^{-2}
no irradiation
B
D/G ratio
1.00
0.10
0.01
○CNT-EtOH
◆CNT-Epoxy
△CNTirr-Epoxy
12
13
14
15
16
17
Log He^{+} irradiation dose [cm^{-2}]

Figure 6

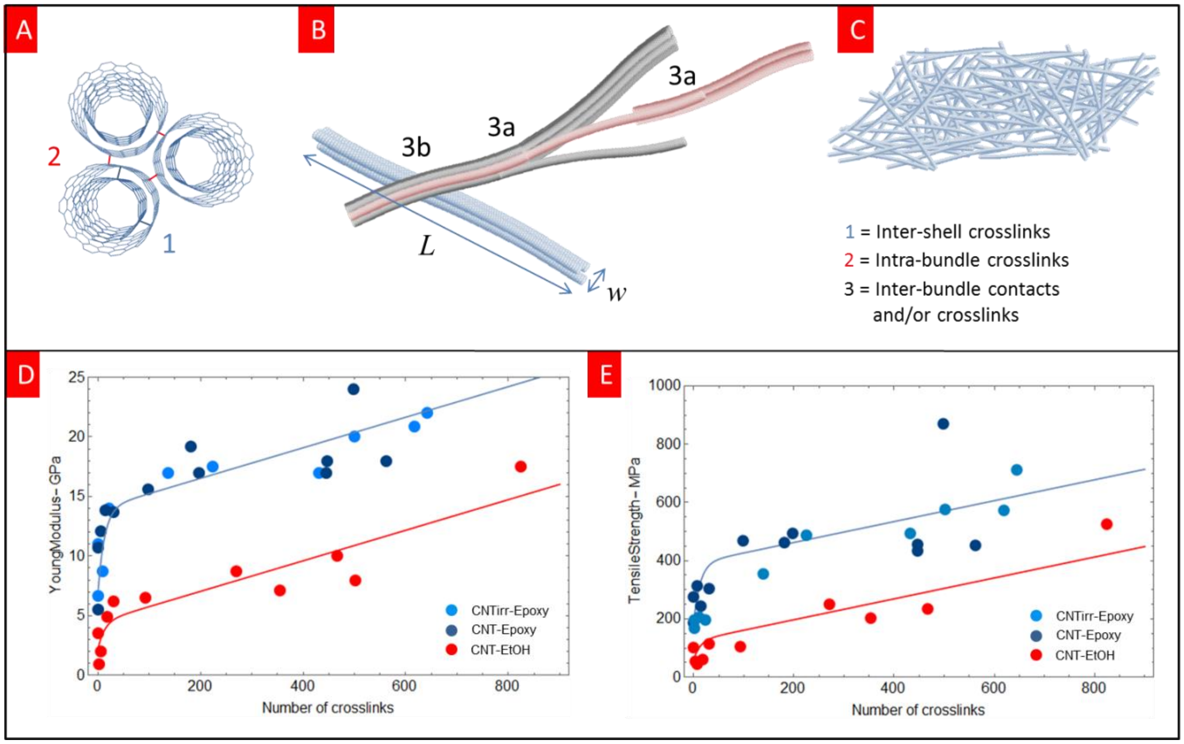
A
2
1
B
3b
3a
3a
L
w
C
1 = Inter-shell crosslinks
2 = Intra-bundle crosslinks
3 = Inter-bundle contacts and/or crosslinks
D
YoungModulus - GPa
0
5
10
15
20
25
0
200
400
600
800
Number of crosslinks
CNTirr-Epoxy
CNT-Epoxy
CNT-EtOH
E
TensileStrength - MPa
0
200
400
600
800
1000
0
200
400
600
800
Number of crosslinks
CNTirr-Epoxy
CNT-Epoxy
CNT-EtOH

Table 1

Parameter/constant	**CNT-EtOH**	**CNTirr-Epoxy**
L [μm]	400	400
w [nm]	15	15
z_0	62.9 (*)	196.1(*)
E_0 [GPa]	238.8	238.8
E_{irr} [GPa]	258.8 (*)	258.8
c	0.439 (*)	0.439
ε	0.028 (*)	0.028
$\sigma_0 = \varepsilon E_0$ [GPa]	6.7	6.7

*Quantities indicated with (*) are fitting parameters

Supplemental Info

Figure S1:

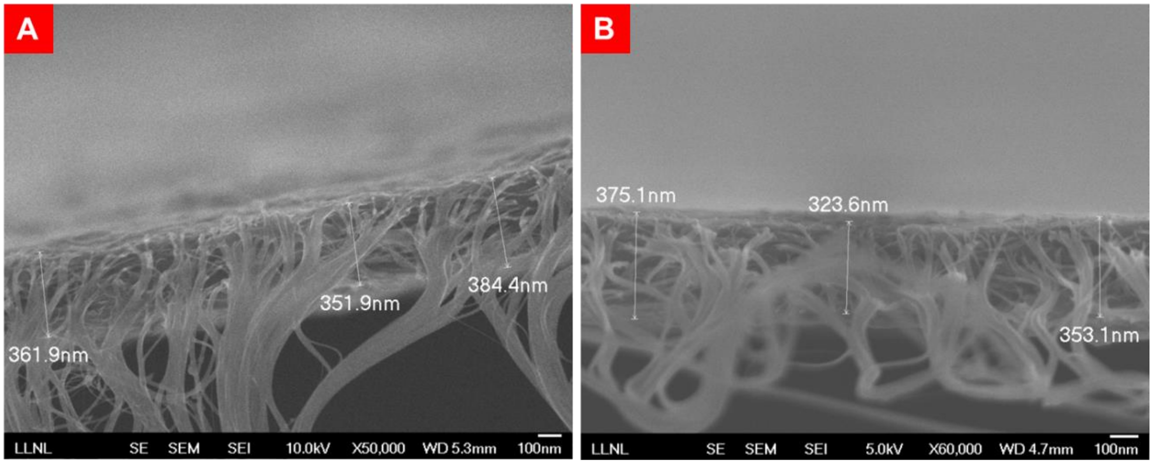
A
361.9nm
351.9nm
384.4nm
LLNL SE SEM SEI 10.0kV X50,000 WD 5.3mm 100nm
B
375.1nm
323.6nm
353.1nm
LLNL SE SEM SEI 5.0kV X60,000 WD 4.7mm 100nm

Figure S2 CNT-EtOH, CNT-Epoxy, CNTirr-Epoxy

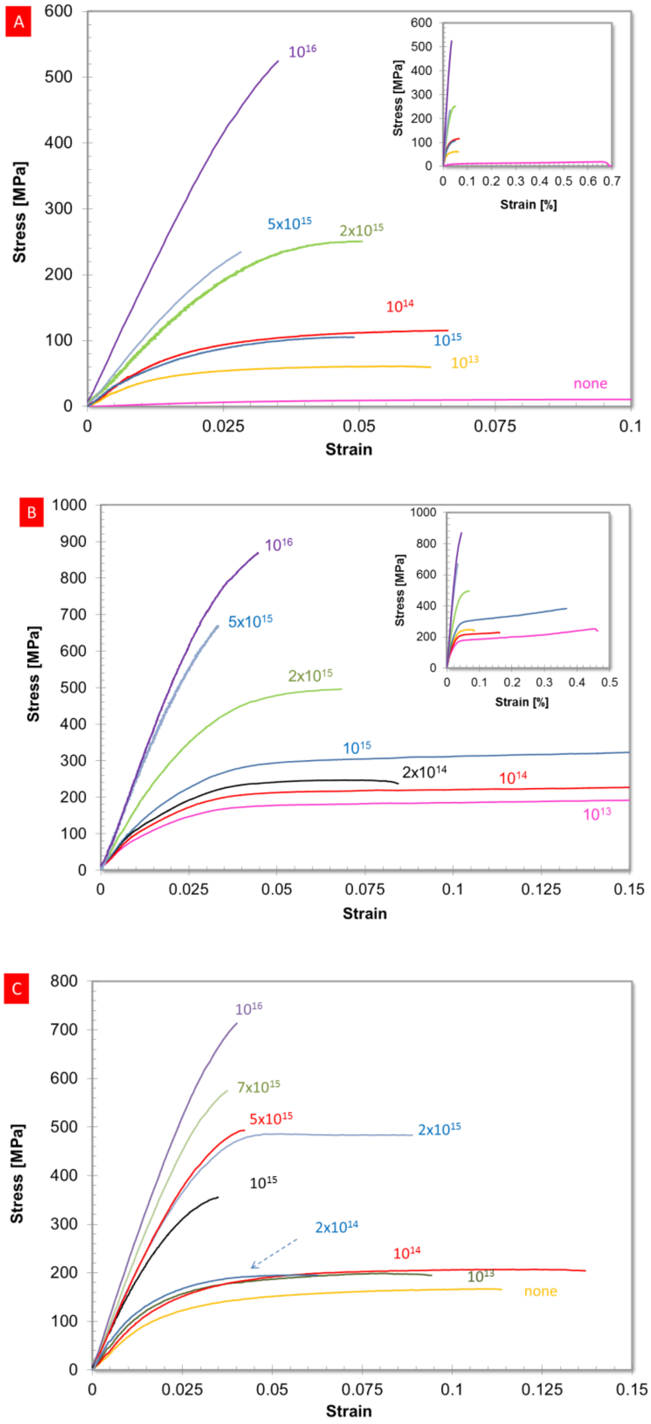

Figure S3

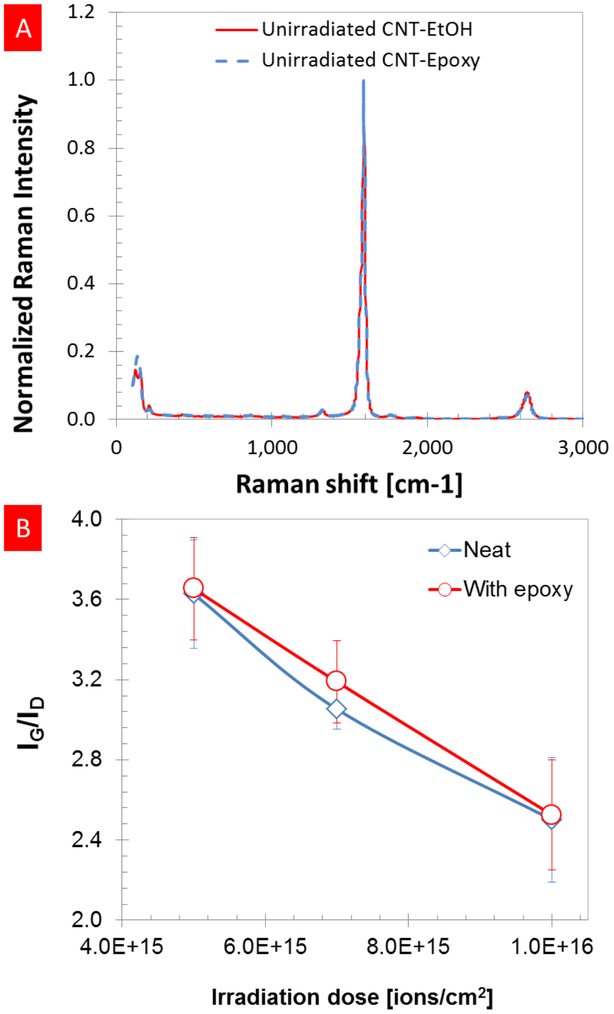
A
1.2
1.0
0.8
0.6
0.4
0.2
0.0
0
1,000
2,000
3,000
Unirradiated CNT-EtOH
Unirradiated CNT-Epoxy
Normalized Raman Intensity
Raman shift [cm-1]
B
4.0
3.6
3.2
2.8
2.4
2.0
4.0E+15
6.0E+15
8.0E+15
1.0E+16
Neat
With epoxy
I_G/I_D
Irradiation dose [ions/cm^2]

OTHER PLOTS

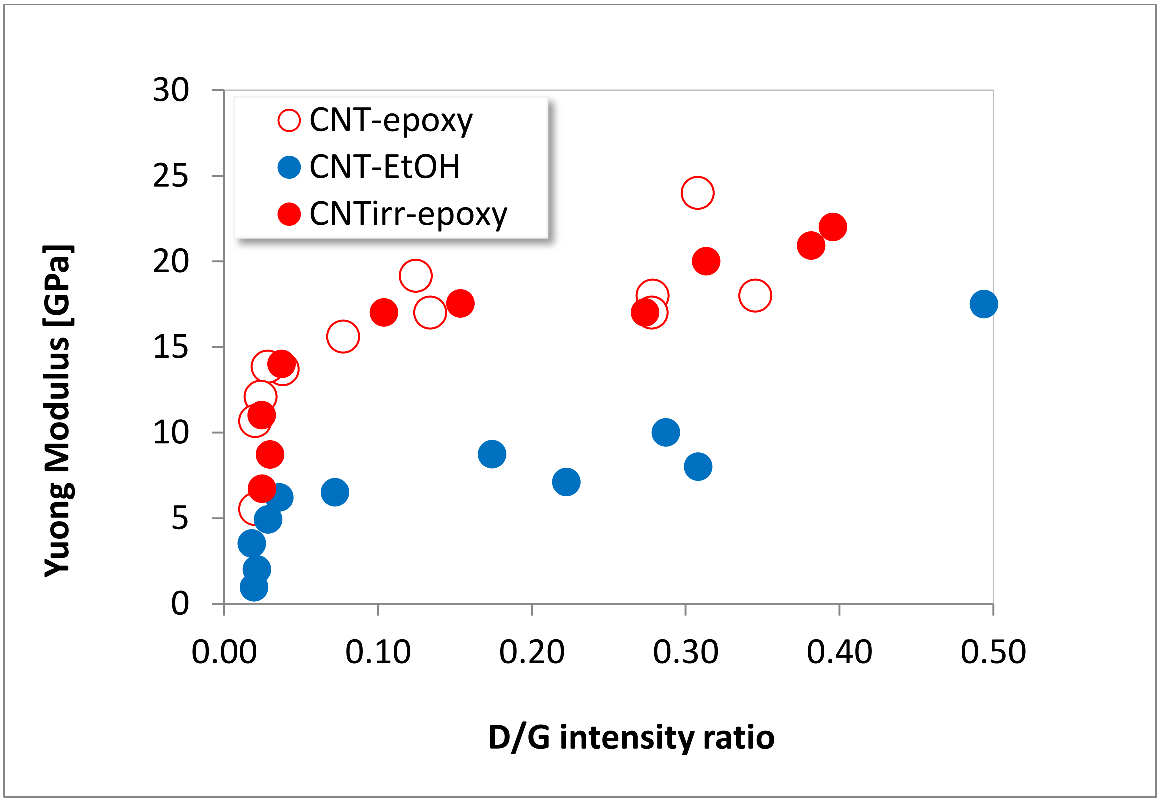
Yuong Modulus [GPa]
30
25
20
15
10
5
0
0.00
0.10
0.20
0.30
0.40
0.50
D/G intensity ratio
○ CNT-epoxy
● CNT-EtOH
● CNTirr-epoxy

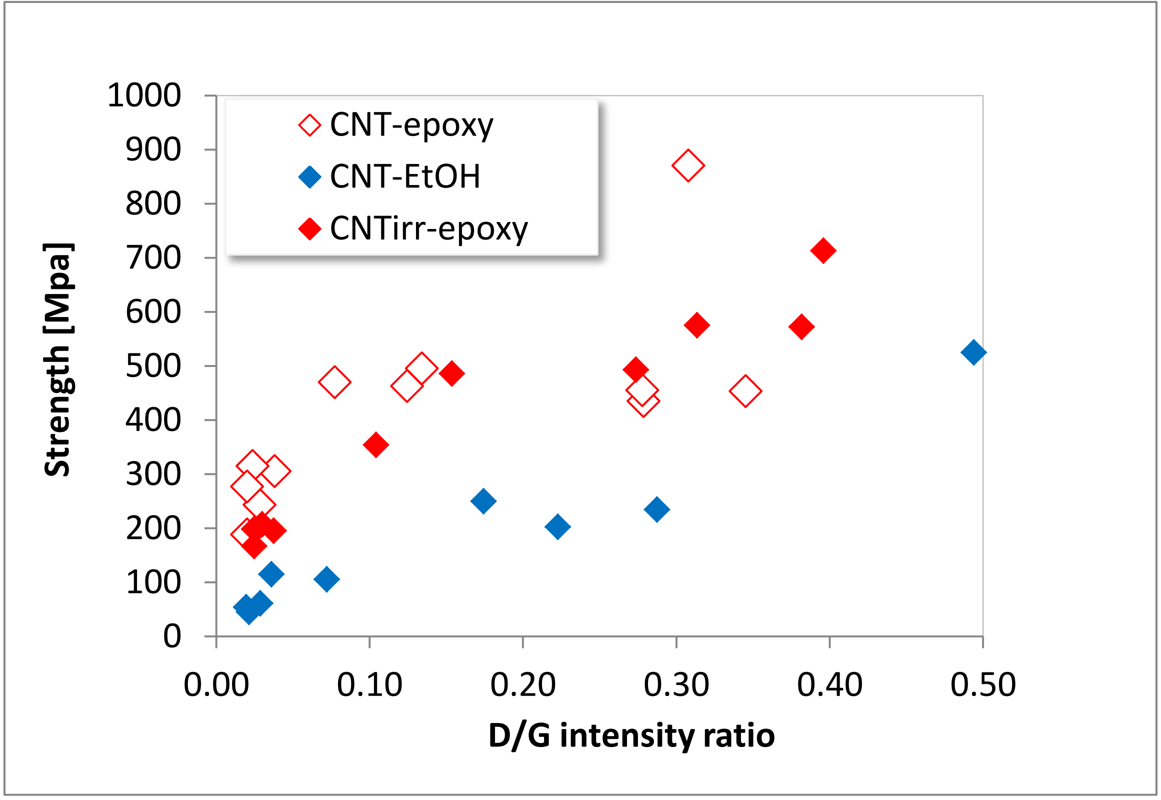
Strength [Mpa]
1000
900
800
700
600
500
400
300
200
100
0
0.00
0.10
0.20
0.30
0.40
0.50
D/G intensity ratio
◇ CNT-epoxy
◆ CNT-EtOH
◆ CNTirr-epoxy

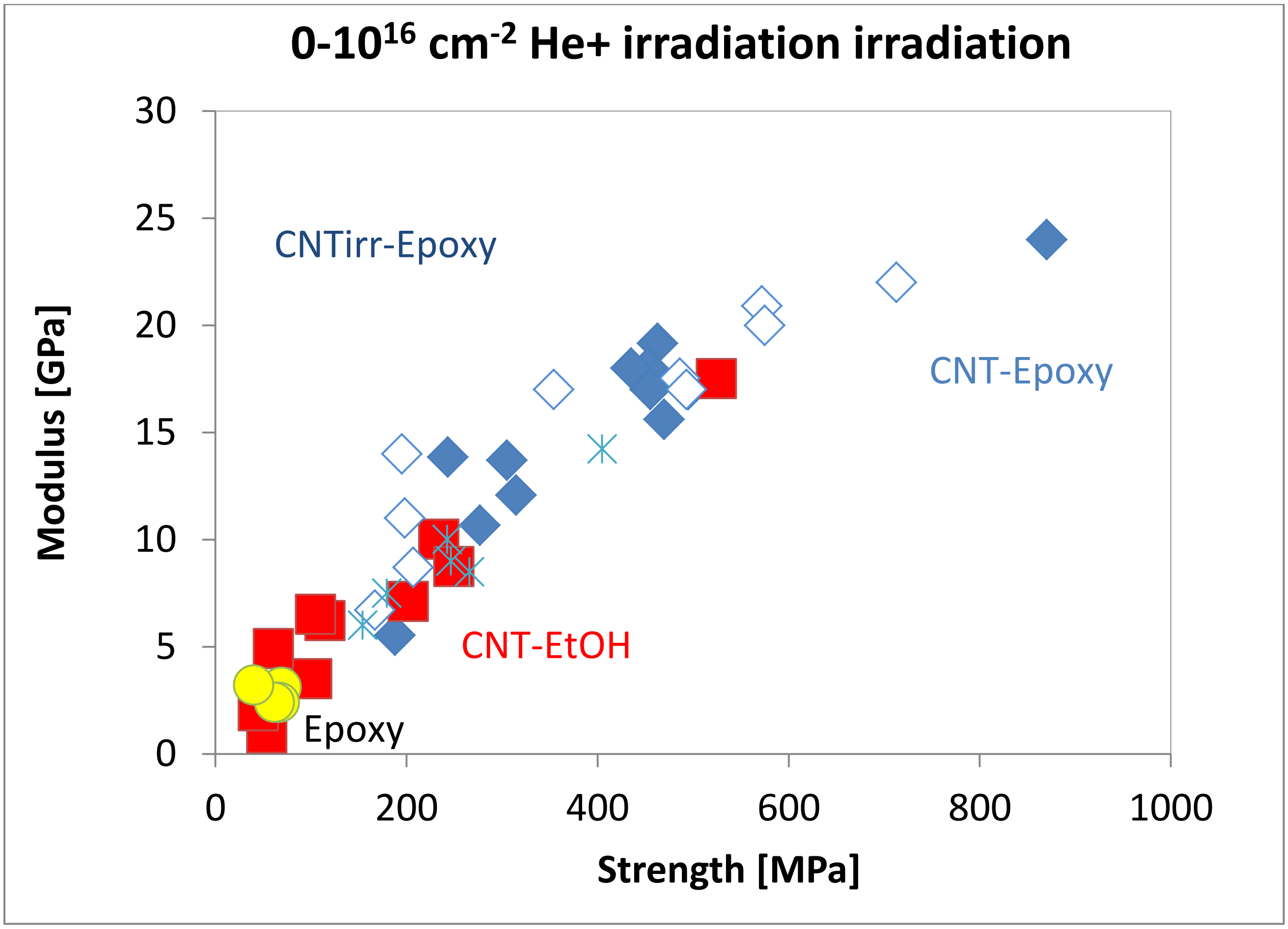
0-10^{16} cm^{-2} He+ irradiation irradiation
CNTirr-Epoxy
CNT-Epoxy
CNT-EtOH
Epoxy
Modulus [GPa]
Strength [MPa]
30
25
20
15
10
5
0
0
200
400
600
800
1000

Fitting CNT, predicting CNT-epoxy

Y0 = 238.8 GPa;   a = 62.9;   ae = 196.08;   b =258.8 GPa;   c=0.439

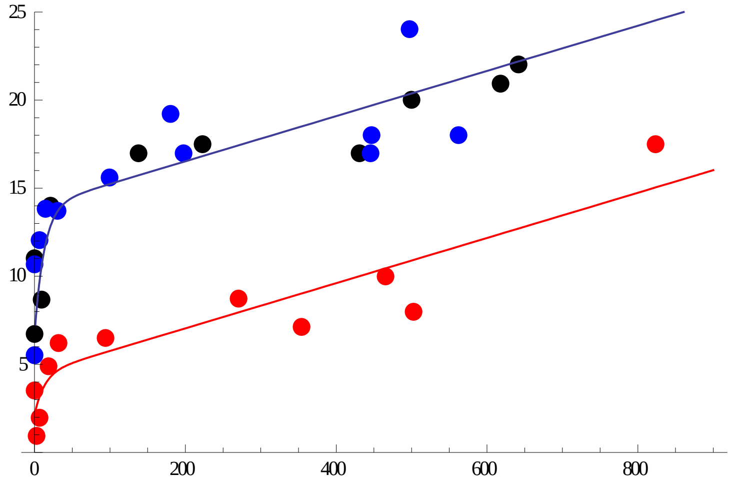

S0 = 6686.6 MPa;   S0matCNT =60.2 MPa

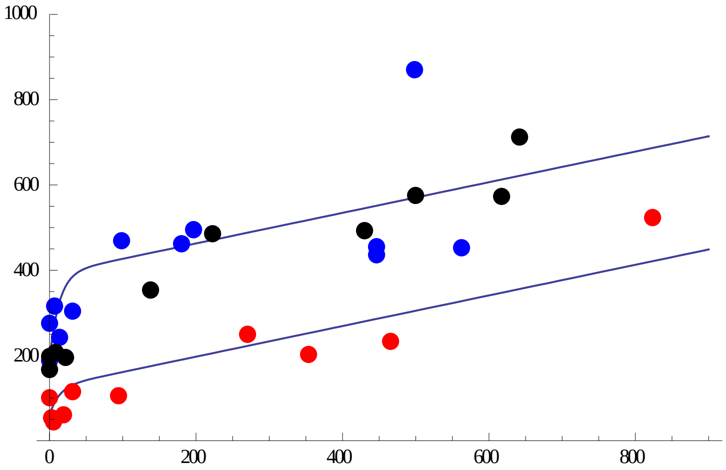

Fitting CNT-epoxy, predicting CNT

Y0 = 147.3 GPa; a = 102; ae = 317.9; b =191.357 GPa; c=0.302

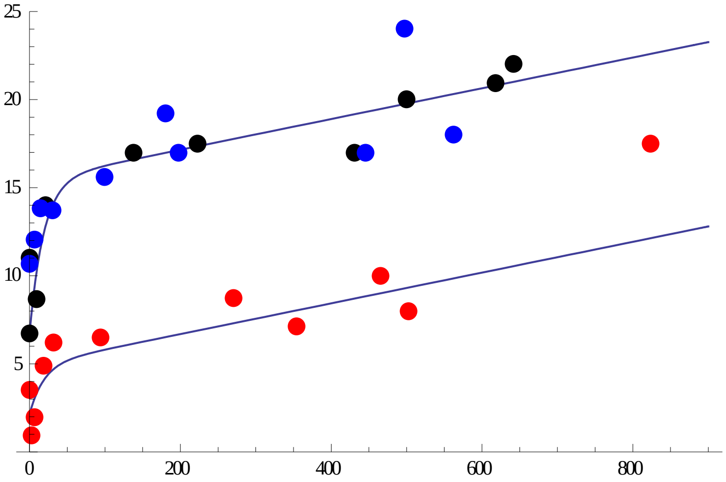

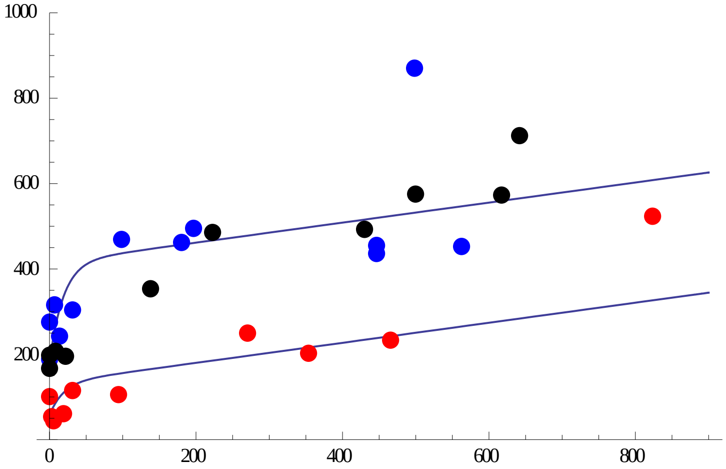S0 = 3964 MPa;   S0matCNTepoxy =180.3 MPa